Magma storage and differentiation in volcanic arcs: examples from the central Aeolian arc, Italy

Rebecca Emma Wiltshire

Thesis submitted for the degree of Doctor of Philosophy in Earth Science

October 2021

Keele University

Abstract

The Aeolian arc is characterised by its complex geodynamic setting, with a heterogeneous mantle source and differing extents of shallow-level magmatic processes. These processes result in large within arc geochemical variations influencing the magma compositions erupted and styles of volcanism in the region distinguishing it from other volcanic arcs worldwide. Intermediate to silicic volcanism dominates during the most recent eruption stages in the central Aeolian arc, on Vulcano, Lipari and Salina after the first occurrence of rhyolitic volcanism in the Aeolian archipelago. Key eruptive centres from the central Aeolian arc characterised by alternating periods of Vulcanian to Subplinian explosive events and lava flow effusion were selected as case studies including La Fossa di Vulcano and the Lentia domes on Vulcano, the southern dome field and northern rhyolitic centres on Lipari and the Pollara crater on Salina.

This study quantitatively assesses the role of crustal contamination in the generation of intermediate and silicic magmas in the central Aeolian arc, geochemically and isotopically constrains the evolution of the La Fossa di Vulcano magmatic system and identifies the shallow conduit processes during the 1888-90 eruption of La Fossa di Vulcano. We present a stratigraphically controlled dataset to elucidate magma storage conditions, magmatic processes occurring at different levels in the subvolcanic system, and the role and extent of crustal assimilation in producing intermediate to felsic magmas since the switch to dominantly rhyolitic volcanism in the central Aeolian arc. New major- and trace-element geochemistry, stable- and radiogenic-isotope geochemistry data from characteristic crustal xenoliths from the different levels within the Calabro-Peloritano basement are presented to quantify the role of crustal contamination during magmatic evolution in the central Aeolian arc. This study of the central Aeolian arc quantitatively assesses the role of source and crustal contamination at arguably the most hazardous volcanoes in Aeolian arc.

Acknowledgements

I am extremely grateful for my Ph.D. supervisors Ralf Gertisser and Ralf Halama, for not only giving me the opportunity to pursue this project, but their endless patience, knowledge, guidance, good humour (usually at my expense!) and assistance during fieldwork over the past four years. You have both made the past four years entertaining! I would also like to thank Federico Lucchi, Claudio Tranne and Roberto Sulpizio for their assistance during my first field season and for looking out for me when I am on the islands. Sara Meschiari and Silvia Massaro are also thanked for their assistance during fieldwork.

This project would not have been possible without the assistance of numerous technical staff. I greatly thank David Wilde and Peter Greatbatch for the countless thin sections and life advice. Richard Darton and Sabrina Nazzareni are thanked for their assistance with XRD sample preparation and methods, and to Adrian Boyce and Alison McDonald for letting me loose on the laser fluorination line at SUERC. I also thank Chiara Petrone and John Spratt for their assistance and advice using the microprobe at the NHM. Matthew Cooper is also thanked for his assistance with sample preparation for Sr isotopes at the NOC. I also thank Ian Wilshaw and Luke Hobson for keeping track of my PhD finances.

I would not be here if not for my best friend Jessica Goodwill and Joshua Myatt for their continued support, kindness, advice and good laughs! I thank my office neighbour Luke Hepworth for his endless entertainment, advice (on literally everything!) and friendship. Hannah Miller and Alex Anrude are also thanked. I would like to thank Siân Wiltshire, Sophie Wiltshire and Ashley Everitt for their support and understanding, and importantly Libby the lab for being an amazing (albeit sleepy) office buddy. Finally, I thank Keele for funding this PhD, and the VMSG and KPA for their additional funding. NERC is thanked for the grant to Ralf Gertisser for oxygen isotope analysis. Finally, I thank my examiners Joaquín Cortés and Richard Waller for their interesting discussions during my viva.

In loving memory of my father,

Nick Wiltshire

the most inspiring person I knew

and the person who made me who I am today.

Contents

List of Figures

List of Tables

CHAPTER 1 - Introduction

1.1 Rationale

The Aeolian Islands have been the subject of extensive research in recent years due to the complicated relationship between volcanism, geodynamics and magmatism, including the types of volcanic eruptions of differing magnitudes, the origin and evolution of magmas through time, and the hazards posed by volcanism in the Aeolian archipelago (Lucchi *et al.* 2013a). The central Aeolian arc has been selected as the main study area of this thesis due to its complex geodynamic setting, with a heterogeneous mantle source and differing extents of shallow-level magmatic processes and the subsequent influence on volcanism in the region distinguishing it from other volcanic arcs. This has resulted in many questions remaining unanswered surrounding important aspects of magma differentiation and crustal contamination, specifically, the source and extent of crustal contamination in the generation of intermediate and silicic magmas, the bulk crustal contaminations, the driving forces of explosive and effusive eruptions and the role of shallow conduit processes during single eruptions. Understanding these are important to elucidate processes operating in the subvolcanic system and insights into the pre-eruptive magmatic system of some of the most hazardous young volcanic centres in the Aeolian arc, specifically those on Lipari and Vulcano.

1.2 Arc Volcanism

Arc style volcanism is widely regarded as the geological setting associated with the highest hazard factors. Some of the largest high-energy explosive eruptions are associated with arc style volcanism, including the 1815 eruption of Tambora, Indonesia (Stothers 1984), the 1902 eruption of Mount Pelée, Martinique (Westercamp & Traineau 1983; Smith & Roobol 1990), the 1991 eruption Mount Pinatubo, Philippines (McCormick *et al.* 1995;

Hammer *et al.* 1999), the Bronze Age Minoan eruption, Santorini volcano, Greece (c.f. Druitt *et al.* 1999; Simmons *et al.* 2016) and eruptions of Soufrière Hills, Montserrat (Druitt *et al.* 2002; Clarke *et al.* 2007) . Arc volcanoes are renowned for the complex magmas erupted and often display distinct shifts in eruption style from explosive (Plinian and Vulcanian) to effusive activity, or vice versa over varying timescales (e.g. during a single eruption or the evolution of a volcano). These transitions in eruption style are commonly rapid and are accompanied by a change in eruptive products e.g. from ash/pumice to lava flows, resulting from a complex interplay of sub-surface and conduit processes such as fractional crystallisation, magma recharge, magma ascent rates, volatile loss and related crystallisation, in addition to open- versus closed-system degassing and rheological changes during magma ascent (e.g. Hildreth & Moorbath 1988; Martel *et al.* 1998; Davidson *et al.* 1990; Wilson 1997; Hammer *et al.* 2000; Adams *et al.* 2006; Clarke *et al.* 2007; Platz *et al.* 2007; Cassidy *et al.* 2015; Preece *et al.* 2016; Isgett *et al.* 2017). Arc volcanoes are characterised by long periods of quiescence (hundreds of years) coupled by abrupt phases of explosive volcanism, hence have been the subject of extensive study in recent years.

Arc volcanic suites are divided into four well-defined volcanic series; low-K (tholeiitic) series, calc-alkaline series, high-K calc-alkaline series and shoshonitic series, with the calc-alkaline series most prevalent (Wilson 1997). Arc magmatism is dominated by intermediate magmas which have undergone large degrees of differentiation resulting from fractional crystallisation and the varying involvement of crustal material during petrogenesis (Hildreth & Moorbath 1988; Davidson *et al.* 1990; Wilson 1997), including large compositional variations in erupted products (basalt – rhyolite) with varying degrees of incompatible element and radiogenic isotope (e.g. $^{87}Sr/^{86}Sr$) enrichment relative to the unmodified mantle (Hawkesworth *et al.* 1982; Thorpe *et al.* 1984).

The large array of magma compositions erupted at volcanic arcs occur due to a combination of magmatic processes including fractional crystallisation, magma mixing and or mingling, crustal contamination in addition to other factors such as magma ascent rates (Hildreth & Moorbath 1988; Davidson *et al*. 1990). The compositions of arc magmas are predominantly modified by processes of magmatic differentiation. Fractional crystallisation is widely accepted as the prevailing process in the generation or intermediate to felsic magmas at volcanic arcs, where mafic minerals are the main fractionating phases (e.g. Cashman *et al*. 2017). However, arc magmas can also be modified by the composition of the source magma, the subducting material, the degree to which the subducting material is incorporated into the arc magmas and crustal contamination processes therefore, magmatism is often complex with a large number of components involved in magma genesis. Specifically, the composition of the oceanic lithosphere, such as the interaction of melts and volatiles released by the subducting slab, sediments and crustal material from the subducted slab (e.g. Gill 1981; Arculus & Johnson 1981; Wilson & Davidson 1984; Arculus & Powell 1986).

Processes of contamination in arc magmas can broadly be divided into two models; 1) source contamination where the crustal melts, hydrous fluids, or mélange diapirs are derived from the subducted slab and added to the arc magma mantle source and 2) crustal contamination where mantle derived magmas are contaminated due to assimilation of the subducted crustal material (c.f. Wilson 1997; Marschall & Schumacher 2012). Contamination can be quantified using a combination of stable and radiogenic isotopes. Specifically, Oxygen (O) isotopes can be used to trace interaction with crustal material during magma ascent due to large variations in O isotopes between the crustal derived and mantle derived rocks (James 1981; Davidson 1985; 1986). This occurs via wall-rock assimilation or combined assimilation and fractional crystallisation (AFC) processes (Eiler *et al.* 2000), although smaller scale variations of $\delta^{18}O$ with indices of magmatic

differentiation may also be introduced through closed-system fractional crystallisation (Eiler *et al.* 2000). Furthermore, open-system magmatic processes such as magma replenishment and assimilation of crustal carbonates have been linked to rapid and frequently erratic shifts in eruption styles from effusive to explosive activity (Borisova *et al.* 2013). Significant aspects of crustal assimilation in magmatic systems, particularly in geodynamically complex volcanic arcs, including the active Aeolian arc, still remain poorly constrained such as the depth at which contamination occurs, extent of contamination at different levels in the subvolcanic system and the degree of crustal assimilation at varying stages of magma differentiation.

1.3 Tectonic and Geological setting of the Aeolian Arc

The Quaternary Aeolian archipelago, South Tyrrhenian Sea is widely considered the cradle of modern volcanology (Lucchi *et al.* 2013a), previously described by many famous naturalists including Aristotle, Pliny the Elder, Giuseppe Mercalli among others and modern volcanologists. The Aeolian archipelago is an active group of volcanic islands (Gioncada *et al.* 2003) associated with the subduction of the African plate beneath the Eurasian plate (Caputo *et al.* 1972; Gaspareni *et al.* 1982; 1985; Barberi *et al.* 1973; Keller 1982; Anderson & Jackson 1987; Faccenna *et al.* 2001; Chiarabba *et al.* 2008; Ventura 2013). The archipelago consists of seven volcanic islands (Alicudi, Filicudi, Salina, Lipari, Vulcano, Panarea and Stromboli; Fig. 1.1) and nine seamounts (Barberi *et al.* 1974; De Astis *et al.* 1997). The Aeolian archipelago is located between the Marsili oceanic basin and Calabrian arc (Boccaletti *et al.* 1984) and emplaced on Calabro-Peloritano continental crust (Barberi *et al.* 1974; Boccaletti *et al.* 1984), extending ~100 km NE - SW (Gasparini *et al.* 1982). Volcanism is associated with thermal uplift accompanying the opening of the Tyrrhenian Sea within an overall post-subduction extensional tectonic regime (Wang *et al.* 1989; Crisci *et al.* 1991; Esperança *et al.* 1992).

Recent studies identified seismicity up to 350 km in the southern Tyrrhenian Sea (Milano *et al.* 1994) suggesting the Aeolian volcanic arc formed as a result of South-East rollback of the Ionian slab beneath the Calabrian arc (Barberi *et al.* 1973; Beccaluva *et al.* 1985; Ferrari & Manetti 1993; Mantovani *et al.* 1996; Ventura *et al.* 1999). However, Westway (1993), Hyppolite *et al.* (1994), Milano *et al.* (1994), and Carminati *et al.* (1998) suggest subduction ceased c. 1Ma, when uplift and extensional tectonics started strongly influencing the Calabrian arc. Magmatism across the Aeolian arc varies from calc-alkaline to shoshonitic arc magmatism. Tomographic studies depict a continuous high-P wave velocity body, attributed to the subducting slab extends from the Calabrian arc to the Marsili basin, dipping at an angle of 70° - 80° to the NW (Chiarabba *et al.* 2008). The Aeolian archipelago is located in an anomalous high-P (Vp) and -S (Vs) wave velocity and low attenuation (Qp) region, indicating the slab is located at depths of 150 km in a fluid-rich zone, probably reflecting dehydration processes (Pontevivo & Panza 2006).

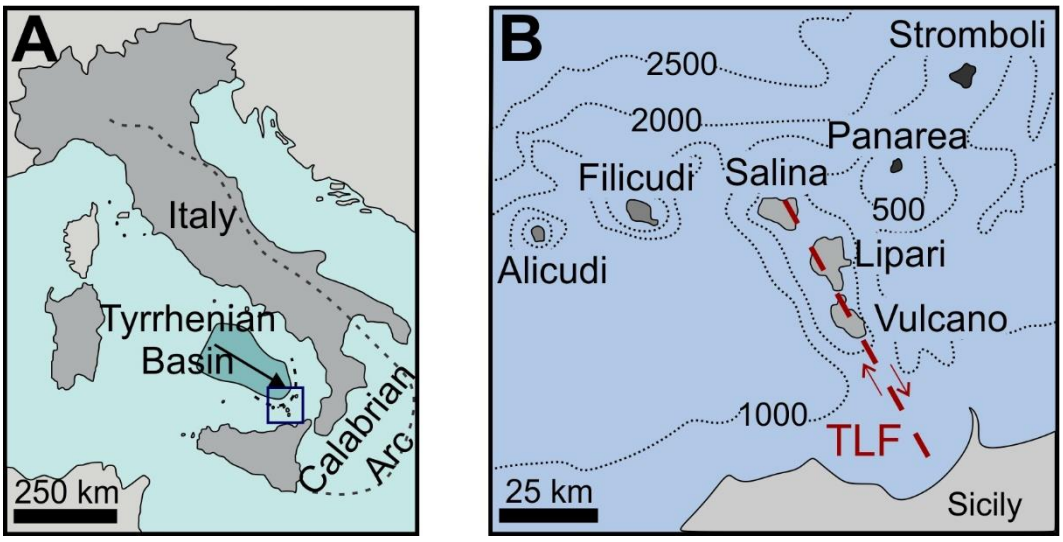

Fig. 1.1: (A) Location map of the Aeolian archipelago, southern Tyrrhenian Sea showing the location of all the islands and the location of the subducting slab (highlighted) and the Calabrian arc (dashed line) (After: Ventura 2013). (B) The central sector comprising Salina, Lipari and Vulcano is highlighted in light grey. The Tindari-Letojanni Fault (TLF) system running through the central sector. (After: Peccerillo *et al.* 2013).

The continental crust in the region is 18 to 25 km, thickening to the south (Finetti & Morelli 1973; Giese & Morelli 1973; Morelli *et al.* 1975; Schütte 1978; Beccaluva *et al.*

1985; Ellam *et al.* 1988; Mattia *et al.* 2008). The Calabro-Peloritano basement comprises a volcanic and sedimentary/metasedimentary cover (0 - 5 km) above a continental crust (5 - 20 km) composed predominantly of gneisses, metabasites and granitoids (Peccerillo *et al.* 2006; De Astis *et al.* 2013; Forni *et al.* 2013; Lucchi *et al.* 2013b). This is evidenced by the occurrence of abundant crustal xenoliths in the eruptive products (Bergeat 1910; Honnorez & Keller 1968; Keller 1980a, b; Pichler 1980; Ellam 1986; Barker 1987; Ellam *et al.* 1989; Ellam & Harmon 1990; Esperança *et al.* 1992; Del Moro *et al* 1998; Gioncada *et al.* 1998; 2003; 2005; Zanon *et al.* 2003; Frezzotti *et al.* 2004; Zanon & Nikogosian 2004; De Astis *et al.* 2013; Forni *et al.* 2013; Lucchi *et al.* 2013b), with metapelites, quartzites, granitoids, gneisses and metabasites (Ellam & Harmon 1990; Gertisser & Keller 2000).

The Aeolian archipelago comprises three sectors (Fig. 1.1); western (Alicudi and Filicudi), central (Salina, Lipari and Vulcano) and the eastern sector (Panarea and Stromboli). The central sector of the Aeolian arc has been selected for this study because these volcanoes consist of complex magma plumbing systems characterised by multiple magma storage zones at different depths within the underlying ~ 20 km thick continental crust of the Calabro-Peloritano basement, and therefore illustrate the interactions between several magmatic processes during differentiation.

Subaerial volcanism in the central sector commenced at c. 267 ka (Lucchi *et al.* 2013c). Volcanoes located in the central sector are predominantly aligned NNW – SSE to NW – SE due to the strong influence of the NNW – SSE striking, the Tindari-Letojanni Fault (TLF) System (Fig. 1.1B; Barberi *et al.* 1994; Ventura 1994; Mazzuoli *et al.* 1995; Lanzafame & Bousquet 1997). The TLF is a 100 – 150 km deep subvertical tear fault formed by a gap in the subducting lithosphere (Rosenbaum *et al.* 2008). Magmatism in the Central Aeolian arc is characterised by overlying spatial and temporal eruptive products identified by ‘typical’ island arc affinities with late occurrences of potassic alkaline series

on Vulcano (Peccerillo 2002; 2005; De Astis *et al.* 2003), indicating fault systems strongly influence volcanism in addition to subduction processes (De Astis *et al.* 2003; 2006).

The oldest (267 – 246 ka) erupted products in the Central Aeolian arc are calc-alkaline basaltic andesites forming scoriae and lavas on Lipari and Salina, followed by calc-alkaline (to high-K) basaltic andesites to andesites with minor dacites from 219 – 124 ka on Lipari and Salina (Lucchi *et al*. 2013c; 2013d). From 124 – 81 ka volcanism on Lipari and Vulcano was high-K to calc-alkaline andesites to dacites, followed by high-K dacites to rhyolites from 75 ka (Lucchi *et al*. 2013c). The latest eruptions of high-K dacites to rhyolites were responsible for some of the most explosive eruptions in the Central Aeolian arc, including; the Upper Brown Tuffs (24 – 8 ka; Lucchi *et al.* 2008; De Astis *et al.* 2013) and Intermediate Brown Tuffs (56 – 27 ka; Lucchi *et al.* 2008; De Astis *et al.* 2013) on Vulcano, Monte Pilato (AD 776; Keller 2002), Vallone del Gabellotto (8.7 – 8.4 ka; Zanchetta *et al.* 2011) and Monte Guardia (27 – 24 ka; Crisci *et al.* 1981; 1983; Forni *et al.* 2013) on Lipari and the Lower Pollara Tuffs (27.5 ka; Crisci *et al.* 1981; 1983; Keller 1980b; Lucchi *et al.* 2013b) and Grey Porri Tuffs (70 – 67 ka; Morche 1988; Lucchi *et al.* 2008) on Salina (Lucchi *et al.* 2013d).

1.3.1 Vulcano

Vulcano is the southernmost island located Aeolian archipelago and is the type location for ‘Vulcanian’ style eruptions (Ventura *et al.* 1999; De Astis *et al.* 2013). Volcanism is typically identified by a quiescent stage, ash surge eruptions and Vulcanian style eruptions ending with effusive lava flows (Arrighi *et al.* 2006). Six main volcanic centres have been identified on Vulcano; Primordial Vulcano (c. 127 – 100 ka), Piano Caldera (78 – 20 ka), Lentia Complex (28 - 8 ka), La Fossa Caldera (15 – 8 ka), La Fossa di Vulcano (< 5.5 ka) and the Vulcanello Peninsula (c. 1.9 ka) (Keller 1970; 1980a; De Astis *et al.* 1997, 2013).

Subaerial volcanism commenced c. 127 ka and has been divided into eight eruptive epochs (Fig. 1.2) by De Astis *et al.* (2013) separated by periods of quiescence and volcano-tectonic collapses. The eruptive epochs are often characterised by multiple eruptive vents and have variable magma compositions (De Astis *et al.* 2013) with eruptive products belonging to the high-K calc-alkaline and shoshonitic magma series (Keller 1980a; Ellam *et al.* 1988; De Astis 1995; De Astis *et al.* 2013). Throughout the geological evolution of Vulcano, eruption magnitudes and eruption styles have changed from large caldera forming eruptions to the explosive widespread 'Brown Tuffs' found across the Aeolian arc, to smaller explosive eruptions and effusive lava flows confined to Vulcano (c.f. De Astis *et al.* 2013). Magma compositions are also variable, changing from basalt to rhyolite with variable alkali contents (De Astis *et al.* 2013).

Eruptive Epoch 1 (Paleo-Vulcano informal unit) formed c. 127 – 113 ka (Gillot 1987; Solìgo *et al.* 2000), comprising shoshonitic lava flows of the Capo Secco shield volcano (De Astis *et al.* 2013). Eruptive Epoch 2 (Casa Grotta dell' Abate Synthem) marks the renewal of volcanism after a quiescent period in southern Vulcano, forming the Primordial Vulcano stratocone (referred to as 'Southvulcano' or 'Old Vulcano' by Keller (1980a) and 'Primordial Vulcano' by De Astis *et al.* (1997)) dated between 117 and 101 ka (Frazzetta *et al.* 1985; Gillot 1987; Laj *et al.* 1997; Solìgo *et al.* 2000). The Primordial Vulcano stratocone comprises alternating high-K basaltic andesitic and shoshonitic lava flows, scoriaceous deposits and minor fine-grained pyroclastic deposits (De Astis *et al.* 1997; 2013). Eruptive Epoch 3 (Scoglio dell' Arpa Synthem) forms shoshonitic basaltic to leucite-bearing shoshonites (Keller 1980a; De Astis *et al.* 1997; 2013) of the Scoglio Congiliara lava flows dated at 99.5 ka (Gillot 1987; Laj *et al.* 1997). These lavas were previously referred to as the 'Leucite tephrites of Caldera del Piano' by Keller (1980a). Eruptive Epoch 4 (Rio Grande Synthem) formed the Monte Aria and Timpa del Corvo fissures at c. 78 ka (Frazzetta *et al.* 1985; Gillot 1987; De Astis *et al.* 1989; 2013; Laj *et al.*

1997). These correspond to the 'older Piano caldera infill products' by De Astis *et al.* (1997) and the 'Lower Grey Tuffs' by Keller (1980a).

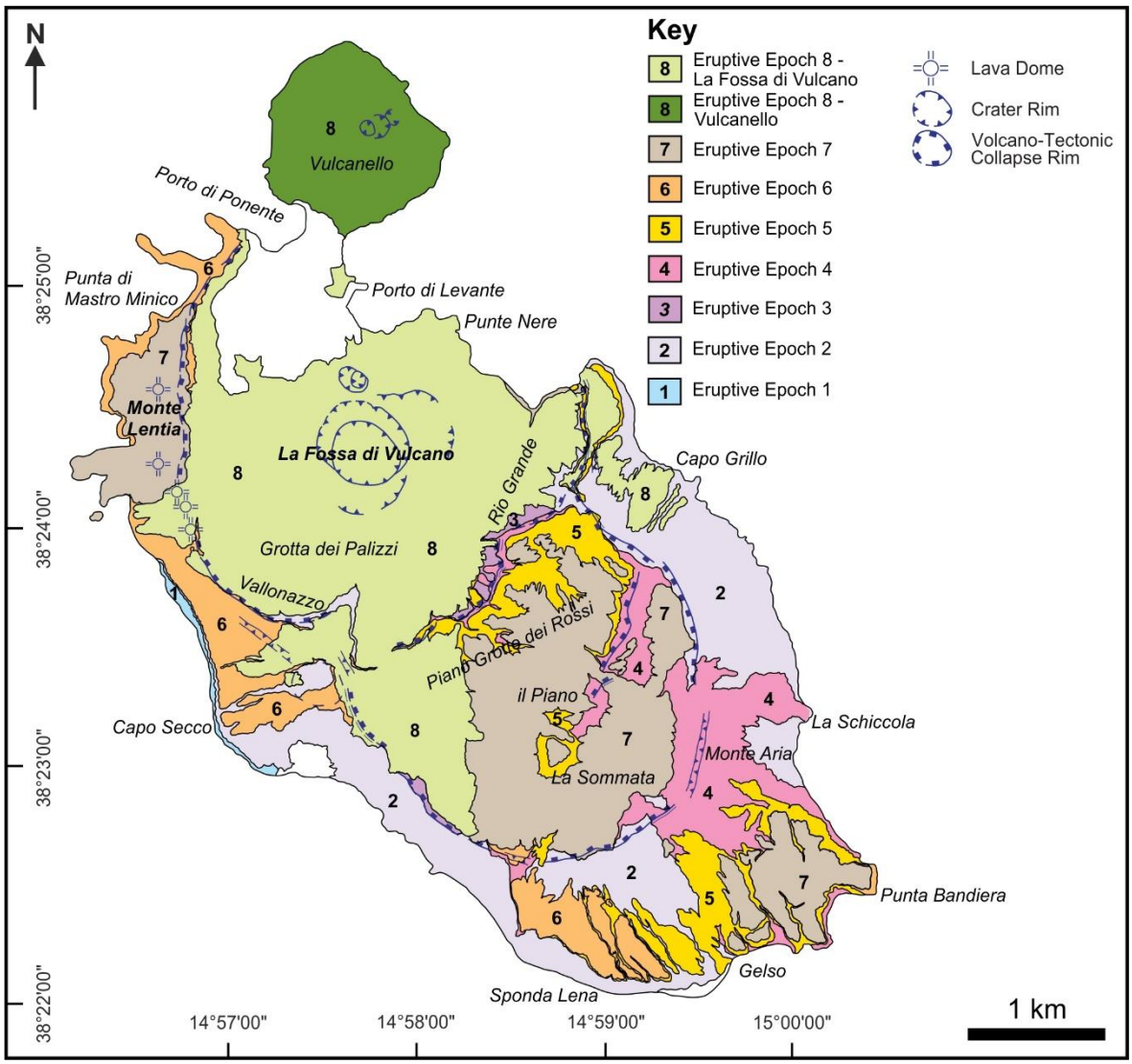

Fig. 1.2: Simplified geological map of the island of Vulcano, identifying all major eruptive epochs. Eruptive Epoch 8 forms La Fossa di Vulcano and Vulcanello Peninsula. (After: De Astis *et al.* 2013).

Eruptive Epoch 5 (il Piano di Vulcano Synthem) marked the renewal of volcanism and shift in eruptive vents to the north north-west in south Vulcano with the il Piano caldera-infill products (De Astis *et al.* 2013). Thick pyroclastic successions that progressively infilled the il Piano caldera mark this Eruptive Epoch (De Astis *et al.* 2013). Scoriaceous layers found within the pyroclastic deposits, specifically Monte Molineddo 1 and 2 Formations correspond to the 'Upper Grey Tuffs' and 'Varicoloured Tuffs' of Keller

(1980a). Eruptive Epoch 6 (Serra delle Felicicchie Synthem, 28 – 21 ka (Laj *et al.* 1997; Solìgo *et al.* 2000) formed the western eruptive fissures on Vulcano, namely the lower portion of the Monte Lentia dome field.

Renewed volcanism was marked by another shift in eruptive vents and the onset of latitic and trachytic to rhyolitic volcanism (De Astis *et al.* 2013). Eruptive Epoch 6 formed the lower portion of the trachy-rhyolitic Monte Lentia dome field ('Lentia Group' of Keller (1980a) or 'Lentia Complex' of De Astis *et al.* (1997)). Eruptive Epoch 7 (Vallonazzo Synthem, Menichedda Subsynthem) formed the Piano Grotte dei Rossi tuffs from 21 to 13 ka (Laj *et al.* 1997 Solìgo *et al.* 2000; De Astis *et al.* 2013), marking the shift in volcanism to northern Vulcano. The Piano Grotte dei Rossi Formation ('Grotte dei Rossi tuffs' by Keller (1980a), De Astis (1995) and De Astis *et al.* (1997)) forms a widespread pyroclastic succession in northern Vulcano. This Formation represents the proximal Upper Brown Tuffs (Lucchi *et al.* 2008; 2013b). Eruptive Epoch 7 also formed the main (intermediate) portion of the Monte Letia dome field dated at 15 – 13 ka (Laj *et al.* 1997; Solìgo *et al.* 2000). In contrast the older domes, the intermediate Monte Lentia dome field was not preceded or succeeded by explosive activity (De Astis *et al.* 2013). Eruptive Epoch 8 (Vallonazzo Synthem, Porto di Levante Subsynthem) forming the Vulcanello Peninsula and currently active La Fossa di Vulcano in the last 8 ky (De Astis *et al.* 2013). The erupted products from Eruptive Epoch 8 are some of the most complex on Vulcano due to single vents producing a wide range and composition of eruptive products (De Astis *et al.* 2013).

The composition of the erupted magmas on Vulcano changed with time, with volcanism switching between explosive and effusive activity, illustrating the complex intermittent magma-water interactions (phreatomagmatic) and the role of volatiles in the magmatic system (De Astis *et al.* 2013). Eruptive products belong to the high-K calc-alkaline and shoshonite series (Fig. 1.3), with varying degrees of evolution (Keller 1980a; Ellam *et al.*

1988; De Astis 1995; De Astis *et al.* 2013). Eruptive Epochs 1 - 5 (c. 127 – 42 ka; Capo Secco, Primordial Vulcano, Scoglio Conigliara lavas, Monte Aria and Timpa del Corvo fissures and the il Piano caldera) are characterised by low to intermediate SiO_2 contents and high-K calc-alkaline to shoshonitic affinities, with most rocks plotting in the shoshonitic series (Fig. 1.3; Keller 1980a; De Astis *et al.* 1997; 2013). During Eruptive Epochs 6 – 8 (< 30 ka) volcanism shifted to intermediate to high SiO_2 contents with shoshonitic affinities (Fig. 1.3; Keller 1980a; De Astis *et al.* 1997; 2013).

The currently active La Fossa di Vulcano is widely considered the most hazardous volcano in the Aeolian Islands and is characterised by alternating periods of explosive Vulcanian-subplinian events and lava flow effusion last erupting in 1888-90 (Keller 1970; 1980a; Frazzetta *et al.* 1982; Dellino & La Volpe 1997; De Rosa *et al.* 2004; De Astis *et al.* 2007). Volcanic activity at La Fossa di Vulcano alternates between explosive and effusive activity (Frazzetta *et al.* 1983; Dellino & La Volpe 1997; De Rosa *et al.* 2004; De Astis *et al.* 2007), typically commencing with pyroclastic eruptions of surges and fallout layers, with most explosive eruptions capped by lava flows (De Astis *et al.* 2007; 2013). The 391-metre high stratocone formed over the past 5.5 ky and the eruptive units are subdivided into eight eruptive units (formations, Fig. 1.4): Punte Nere (pn), Grotta dei Palizzi 1 (gp1), 2 (gp2) & 3 (gp3), Caruggi (ca), Pietre Cotte (pc) and Gran Cratere 1 (gc1) & 2 (gc2) (De Astis *et al.* 1997; 2013).

The Punta Nere activity (5.5 – 3 ka), after the widespread Piano Grotte dei Rossi tuffs (Upper Brown Tuffs) from alternating dilute pyroclastic density currents (PDCs) and periodic fallout layers (latite – trachyte) with late-stage effusive activity forming an ‘A’ā lava flow on the northern flanks of La Fossa (Frazzetta *et al.* 1985; Gillot 1987; Solìgo *et al.* 2000; De Astis *et al.* 2013). Punte Nere is subdivided into three distinct members; (1) plane-parallel to cross-laminated black ash with beds of well-sorted lapilli, (2) massive,

dense, oxidised lapilli formed by fallout and dilute PDCs and (3) metre-thick lobate trachytic lava flow (De Astis *et al.* 1997; 2013).

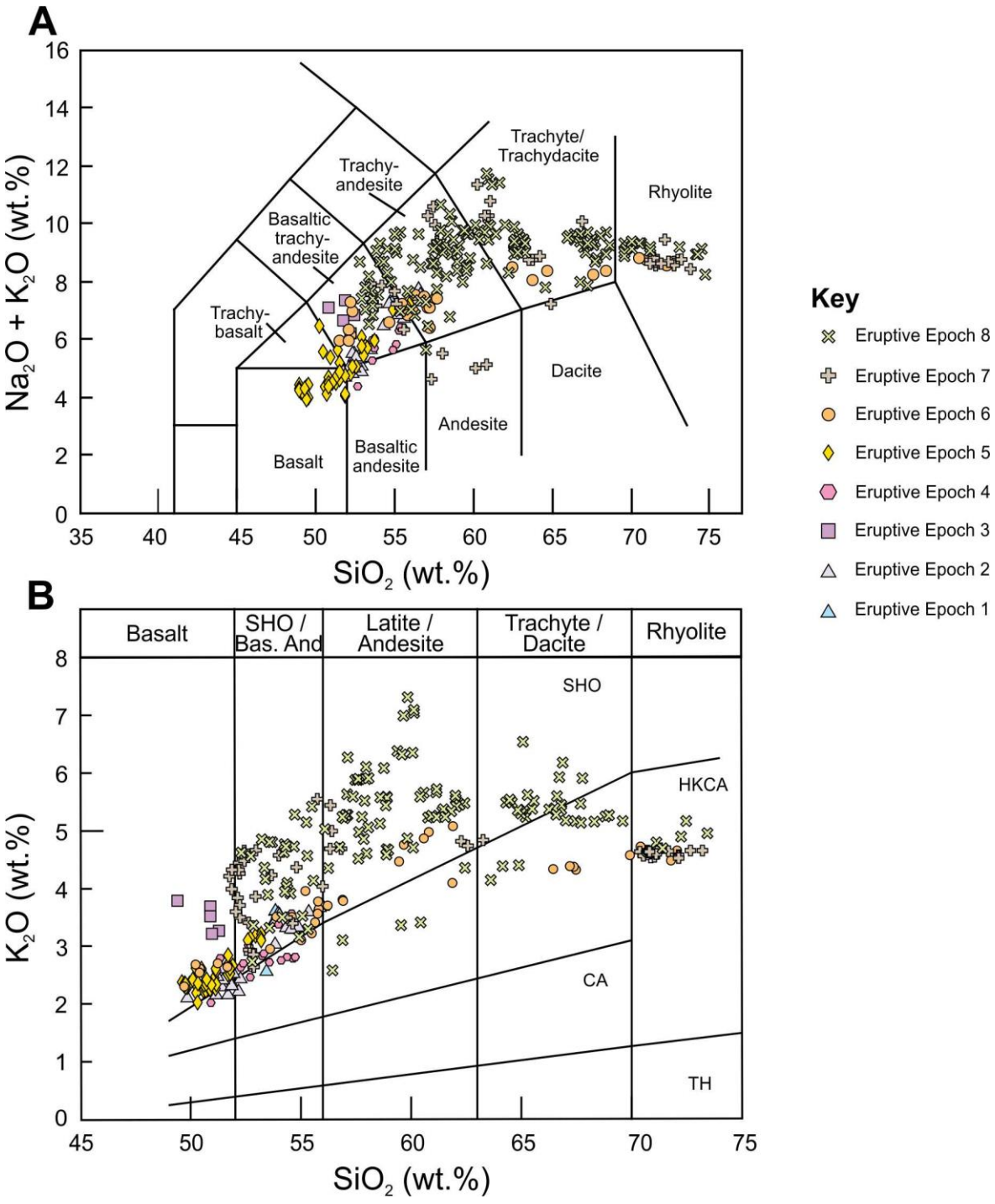

Fig. 1.3: (A) Total Alkali versus silica (SiO_2) diagram (Le Bas *et al.* 1986; Le Maitre *et al.* 2002) and (B) K_2O versus silica (SiO_2) diagram (Peccerillo & Taylor 1976) for lavas and pyroclastic rocks covering the entire eruptive history of Vulcano. Analyses are normalised to 100 wt.% and are volatile free. TH: Tholeiitic, CA: calc-alkaline; HKCA: High-K calc-alkaline, SHO: Shoshonitic. (Data from: De Astis *et al.* 2013).

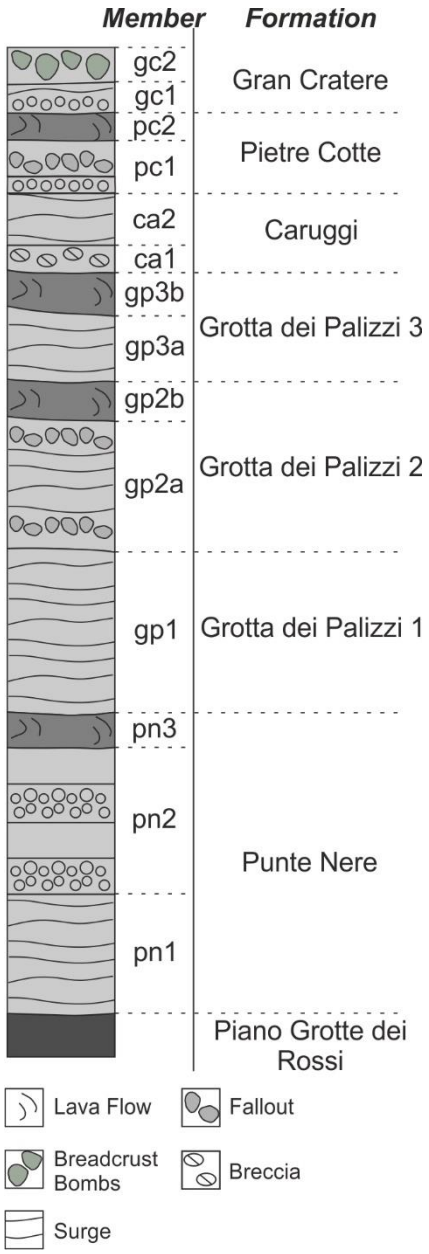

Fig. 1.4: Summary stratigraphic section for La Fossa di Vulcano, highlighting the main eruptive formations and units. (After: Dellino & La Volpe 1997; De Astis et al. 2007).

Grotta dei Palilzzi 1 is dated at 2.9 ka (Voltaggio *et al.* 1995) comprises a pyroclastic succession of PDCs from recurrent hydromagmatic eruptions, with abundant scoriaceous bombs at the base (De Astis 1995; De Astis *et al.* 2013). This was followed by early explosive phases forming PDCs of latitic to rhyolitic composition attributed to Grotta dei Palizzi 2 (2.2 – 2.1 ka; Frazzetta *et al.* 1985; Voltaggio *et al.* 1995). Pyroclastic deposits from Grotta dei Palizzi 2 form thinly bedded planar to cross-stratified tuffs (De Astis 1995) with an inversely graded pumiceous bomb and lapilli layer at the base (De Astis *et al.*

2013). The top of the succession consists of pumiceous lapilli with isolated breadcrust bombs (De Astis *et al.* 2013). These were proceeded by a late-stage rhyolitic obsidian lava flow on the southern flanks of La Fossa di Vulcano with abundant magmatic enclaves, flow banding, convolute folding and irregular fracturing (De Astis *et al.* 2013).

Similarly, Grotta dei Palizzi 3 commenced with initial explosive wet and dry type PDCs forming planar to cross-stratified tuff deposits with accretionary lapilli (De Astis *et al.* 2013). This formation ended with late-stage trachytic lava flow erupted on the southern flanks of La Fossa di Vulcano dated at 1.6-1.5 ka (Frazzetta *et al.* 1985; Voltaggio *et al.* 1995).

Renewed volcanism after a quiescent period of a few hundred years formed the Caruggi Formation, comprising a reworked tuff breccia on the southern flanks and explosive varicoloured latitic wet-type PDC deposits with accretionary lapilli and bomb sags (Dellino & La Volpe 1997; Scolamacchia 1997; De Astis *et al.* 2013).

This was followed by the activity of Pietre Cotte, commencing with early explosive phases of PDCs and subordinate fallout from a discontinuous eruption column forming dilute PDCs with minor strombolian and Vulcanian activity (De Astis *et al.* 2013). The pyroclastic succession was succeeded by the effusion of a rhyolitic obsidian lava flow (AD 1739; Keller 1970) on the northern flanks. The Pietre Cotte lava is characterised by abundant magmatic enclaves of porphyritic latitic-trachytic compositions and flow banding (Piochi *et al.* 2009; De Astis *et al.* 2013; Bullock 2015).

Lava flow effusion was then followed by intermittent explosive eruptive phases of alternating dry PDCs and fallout from a Vulcanian eruption with a pulsating eruption column (De Astis *et al.* 2013), forming the Gran Cratere 1 Formation. This Formation is identified by massive to asymmetrically laminated ash deposits, alternating with thin, massive pumiceous lapilli beds of trachytic-rhyolitic composition, exposed at Monte

Lentia (De Astis *et al.* 2013). The most recent eruption of La Fossa di Vulcano (Gran Cratere 2) was the 1888-1890 'type' Vulcanian eruption documented by Mercali & Silvestri (1891). Gran Cratere 2 formed dense lapilli tuffs with abundant bombs and breadcrust bombs from alternating PDCs and intermittent fallout pulses (De Astis *et al.* 2013). Scattered trachytic bread-crust bombs up to 1-metre diameter with abundant quartz-rich xenoliths occur close to the vent (Walker 1969; Clocchiatti *et al.* 1994; De Astis *et al.* 2013).

1.3.2 Lipari

Lipari is the largest and one of the more chemically diverse islands in the Aeolian archipelago (Crisci *et al.* 1991), located between Salina and Vulcano. Volcanism commenced c. 267 ka until AD 1220 (Forni *et al.* 2013 and references therein). The volcanic complex of Lipari has a surface area of 38 km^2 (Forni *et al.* 2013), situated ~1700 metres above the sea floor with a maximum elevation of 602 metres above sea-level at Monte Chirica (Forni *et al.* 2013). Lipari is connected to Vulcano by a shallow saddle structure; the Bocche di Vulcano, 50 metres below sea level, and to Salina by a 300-metre-deep basin (Bosman *et al.* 2013; Romagnoli *et al.* 2013).

Lipari comprises several volcanic edifices including fissures, polygenetic volcanoes, cinder cones, tuff rings and lava domes (Fig. 1.5) (Tranne *et al.* 2002; Lucchi *et al.* 2010). The composition of magmas erupted changed with time, from mafic to silicic volcanism 42 ky ago (Gioncada *et al.* 2005), with rhyolitic fall and surge deposits and lava domes from 27 ka in southern Lipari (Forni *et al.* 2013). Volcanism has been divided into four main periods by Pichler (1976; 1980), and later into nine eruptive epochs (Fig. 1.5) by Forni *et al.* (2013). Early volcanism commenced with eruptions of primitive basalts and andesites, whilst the younger deposits are high-K calc-alkaline andesites and rhyolites (Crisci *et al.*

1991). Forni *et al.* (2013) defined eruptive epochs 1 - 3 with the eruption of basalts from c. 267 – 150 ka, with eruptive epochs 4 - 6 (119 – 81 ka) associated with the eruption of low-Si andesites corresponding to the first and second periods from Pichler (1976, 1980). Eruptive epochs 7 - 9 occurred from 43 ka – AD 1220 and are associated with the eruption of high-K dacites and rhyolites, corresponding to Pichler's third and fourth periods.

Eruptive products are calc-alkaline to high-K calc-alkaline basaltic andesites-rhyolites with an apparent compositional gap in the dacite field (Fig. 1.6; Forni *et al.* 2013), and are identified by lava flows, scoriaceous deposits, hydro-magmatic deposits, subordinate marine terraces and detrital units (Forni *et al.* 2013). The island is currently in a quiescent period, identified by low-temperature fumaroles in the eastern and western sectors (Forni *et al.* 2013). The volcanism observed is attributed to the complex interplay between an alkaline and crustal-derived mantle source (Crisci *et al.* 1991), explaining the transition from mafic to silicic volcanism c. 42 ka (Crisci *et al.* 1991; Di Martino *et al.* 2010), after a 50 ky quiescent period (Di Martino *et al.* 2010).

The southern Lipari domes erupted during Eruptive Epochs 7 and 8 (Scogliera sotto il Monte and Valle Muria synthems), mark the onset of rhyolitic volcanism, and are associated with initial explosive eruption phases followed by late-stage effusion of endogenous lava domes (Forni *et al.* 2013).

The Punta del Perciato Formation forms the lowest section of the dome field consisting of two NNW-SSE aligned rhyolitic lava domes along the Scogliera sotto il Monte coastal cliff (Forni *et al.* 2013). Late-stage explosive activity associated with Punta del Perciato formed dilute and turbulent PDCs destroying the summits of the Punta del Perciato lava domes (Forni *et al.* 2013). This eruption formed a white, rhyolitic, highly vesicular pumice-rich, poorly sorted, massive and coherent lithic-rich layer close to the vent (Forni *et al.* 2013).

Tuff beds contain cross-laminations, bomb sags and accretionary lapilli and were deposited as a result of a series of explosive phases driven by magmatic fragmentation.

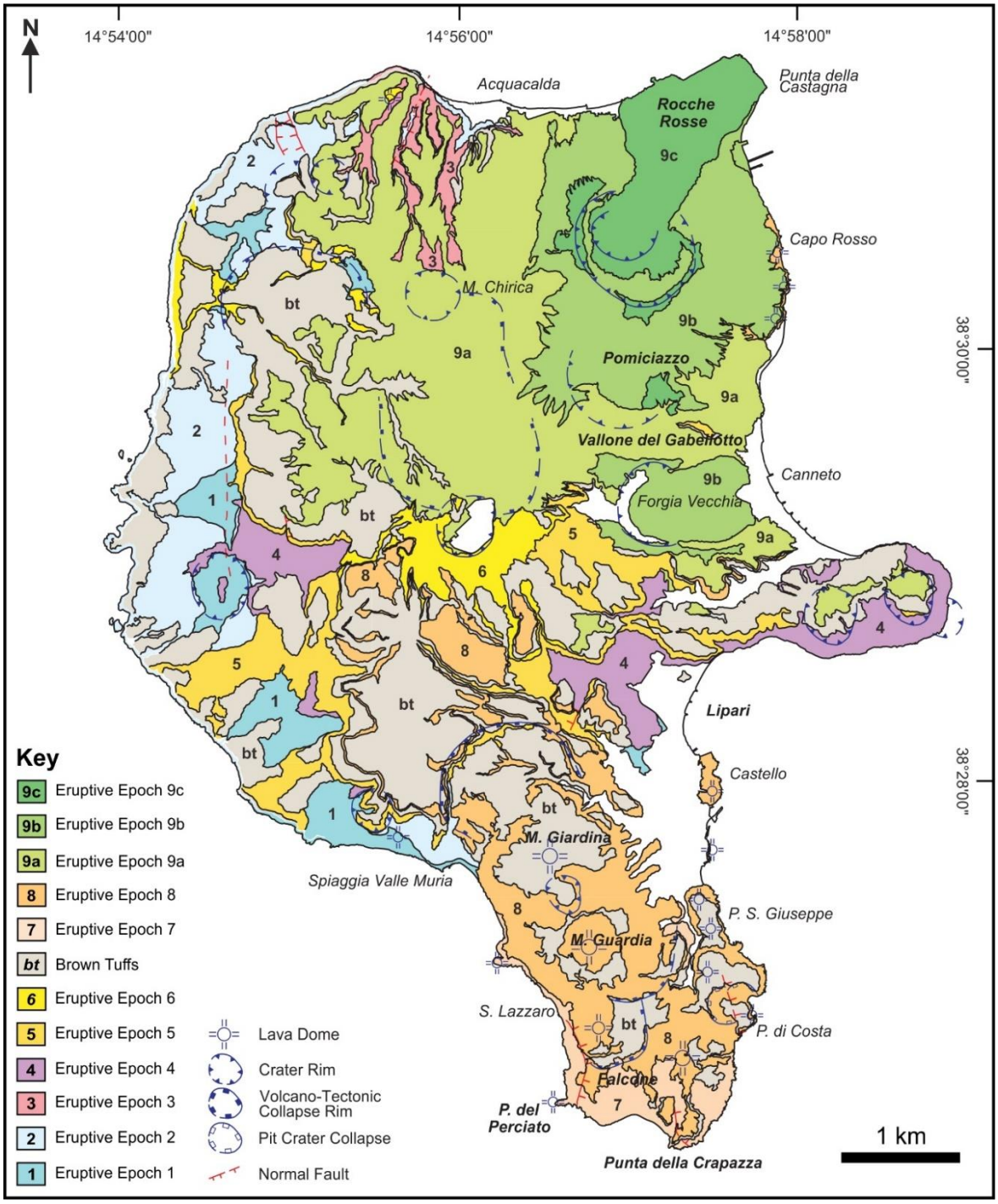

Fig. 1.5: Simplified geological map of the island of Lipari, identifying all major eruptive epochs. Eruptive epoch 8 consist of the southern dome field (Punta del Perciato, Falcone, Monte Guardia, Monte Giardina. Eruptive epoch 9 (northern rhyolitic centres) is subdivided into 3 units; 9a Gabellotto, 9b Forgia Vecchia & Pomiciazzo and 9c Rocche Rosse. (After: Forni *et al.* 2013).

The Falcone Formation (43 – 40 ka; Gillot 1987) consists of three members (Gillot 1987; Crisci *et al.* 1991) followed by a 15 ky quiescent period (Forni *et al.* 2013). The Falcone Formation is subdivided into two distinct members: pumiceous pyroclastic deposits and endogeneous lava domes. The Falcone pyroclastic activity formed due to initial explosive phases establishing an extensive succession of white pumiceous lapilli-tuffs up to 15-metres-thick, with abundant bomb sags towards the base, close to the vent, representing a northerly directed dilute and turbulent PDC (Forni *et al.* 2013). Explosive activity was followed by the effusion of rhyolitic lava domes at Capparo, Falcone, and Capistello (Forni *et al.* 2013), along the NNW-SSE tectonic lineament (Fig. 1.1). The domes represent the second stage of dome effusion in southern Lipari. A small black high-K dacitic lava dome with abundant xenoliths, enclaves and mingling textures, located close to Punta della Crapazza, crosscuts the rhyolitic domes (Forni *et al.* 2013).

Eruptive epoch 8 (Valle Muria Synthem) commenced with one of the most powerful eruptions in the Aeolian archipelago, the 27 – 24 ka subplinian Monte Guardia eruption (Urnazzo Subsynthem; Forni *et al.* 2013), producing a widespread pumiceous pyroclastic succession (Crisci *et al.* 1983; De Rosa & Sheridan 1983; Colella & Hiscott 1997; De Rosa *et al.* 2003; Lucchi *et al.* 2010). The Monte Guardia Formation consists of thick lithic-rich, massive lapilli-tuffs and tuff-breccias, with angular blocks erupted close to the vent (Forni *et al.*2013), transitioning into thickly bedded-massive lapilli-tuffs containing bomb sags and clast embedding at the base (Forni *et al.* 2013). Distal deposits located up to 6 km from the vent on Lipari consist of thin-medium bedded, laminated to cross-stratified, lapilli-tuffs and are located on Vulcano, Panarea, Salina and Bazziluzzo (Forni *et al.* 2013). The Monte Guardia Formation is associated with magmatic volatile fragmentation processes and magma-water (phreatomagmatic) interactions in the conduit (Forni *et al.* 2013). The Monte Guardia eruption was succeeded by the Monte Giardina domes and pyroclastic succession and the Punta Sella Giuseppe domes, and the Castello lava domes, the Valle ne Canneto

Dentro Formation (Vallonaccio Subsynthem) and the final activity of eruptive epoch 8 formed the Capo Rosso lava domes (Forni *et al.* 2013).

Eruptive Epoch 9 (Vallone Fiume Bianco Synthem; 8.7 ka – AD 1220; Fig. 1.5) followed a period of quiescence marked by a sharp unconformity and a shift in volcanic centres from southern Lipari to northern Lipari. Eruptive Epoch 9 is characterised by successive pumiceous and viscous obsidian-rich lava coulees.

The Vallone del Gabellotto Formation (Chirica Rasa Subsynthem; 8.7 – 8.4 ka using ^{14}C dating; Zanchetta *et al.* 2011) is one of the most powerful eruptions in the Aeolian archipelago. The formation comprises dilute PDCs forming massive to planar and cross-stratified lapilli tuffs and subordinate fallout layers comprising well sorted pumiceous lapilli tuffs (Forni *et al.* 2013). The range in erupted products from highly vesicular pumices to moderately vesicular and blocky pumices indicated both hydromagmatic processes and magma fragmentation dominated (Forni *et al.* 2013). The effusive activity associated with the Gabellotto activity formed the subphyric to aphyric Pomiciazzo obsidian lava coulee (Pomiciazzo Formation) on the eastern rim of the Vallone del Gabellotto crater, NE Lipari (Fig. 1.5). The Pomiciazzo lava has been dated at 8.6 ka (Wagner *et al.* 1976; Keller 2002; Forni *et al.* 2013).

Following a long period of dormancy, leading to the development of an erosional unconformity and development of a palaeosol and the Upper Brown Tuffs (originating from Vulcano), volcanism renewed with the formation of the Monte Pilato pumice cone (C. le S.Elmo subsynthem, Sciarra dell'Arena Formation), forming a widespread pumiceous, rhyolitic, aphyric pumiceous deposit in NE Lipari (Fig. 1.5; Forni *et al.* 2013). The eruption can be divided into four distinct lithologies; (1) well-sorted, normally graded, highly vesicular lapilli-tuffs, (2) poorly sorted matrix-supported lapilli tuffs, (3) thin beds of parallel laminated tuffs with bomb sages and (4) parallel-laminated tuffs with

accretionary lapilli (up to 30 vol.%), becoming more prevalent towards the top of the succession (Forni *et al.* 2013).

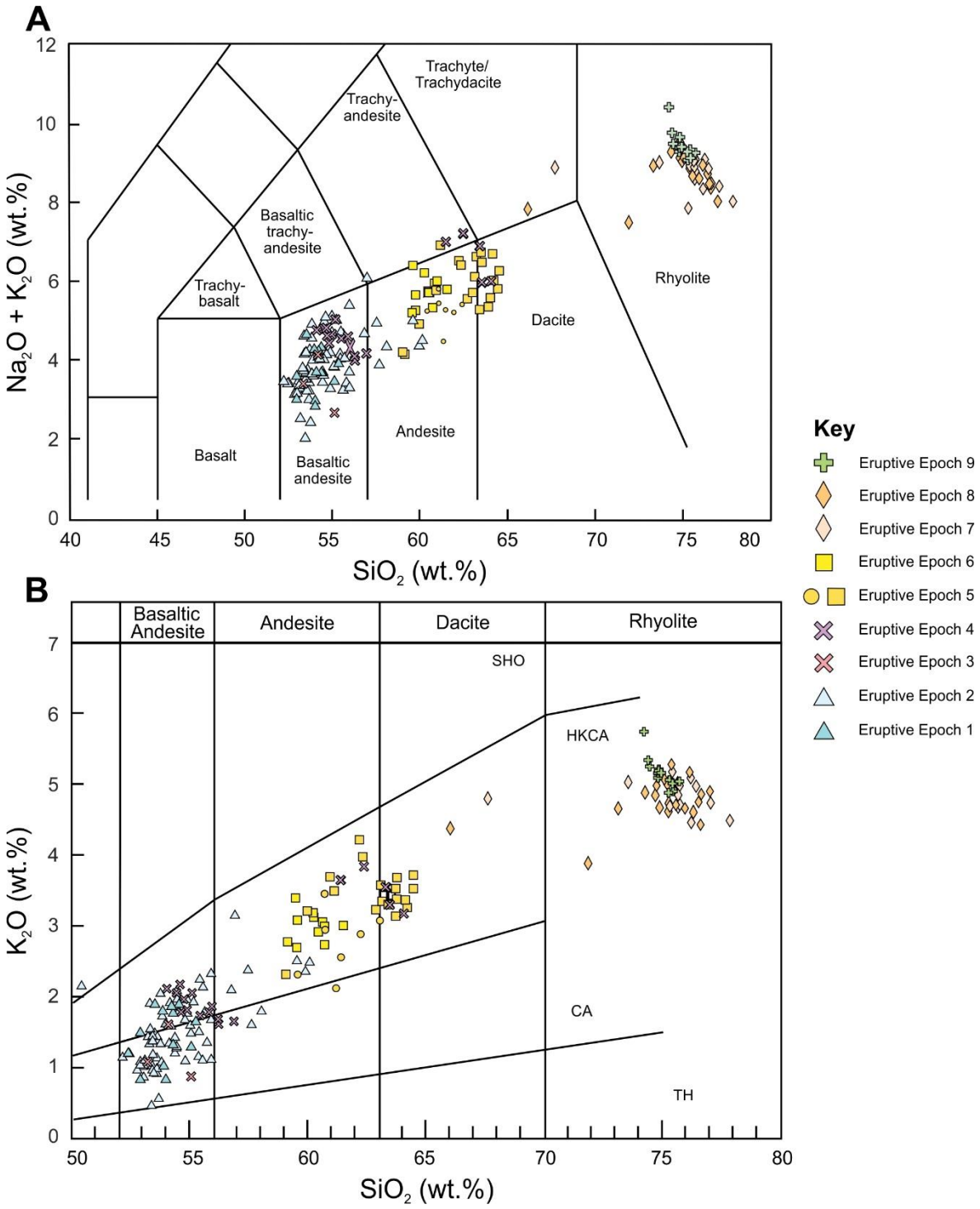

Fig. 1.6: (A) Total Alkali versus silica (SiO_2) diagram (Le Bas *et al.* 1986) and (B) K_2O versus silica (SiO_2) diagram (Peccerillo & Taylor 1976) for lavas and pyroclastic rocks covering the entire eruptive history of Lipari. Analyses are normalised to 100 wt.% and are volatile free. TH: Tholeiitic, CA: calc-alkaline; HKCA: High-K calc-alkaline, SHO: Shoshonitic. (Data from: Forni *et al.* 2013).

The changing eruptive products illustrate a shift from magmatic fragmentation during the early phases of the eruption to magma-water interactions during the latter stages (Dellino & La Volpe 1995; Dellino *et al.* 2001). Calibrated ^{14}C dates yield an age of AD 776 (Keller 2002).

The Rocche Rosse coulée (Fossa Castagna Subsynthem; Fig. 1.5) erupted following a short-lived quiescence following Monte Pilato activity. This rhyolitic obsidian coulee erupted on the NE side of Monte Pilato (Fig. 1.5), and is characterised by abundant flow ramp structures, flow foliations and blocky textures (Forni *et al.* 2013; Bullock 2015; Bullock *et al.* 2018). The age of the Rocche Rosse lava flow is widely debated, Pichler (1980) proposed an age of AD 524 – 562 using tephra layers, whereas fission track dating by Bigiazzi *et al.* (2003) proposed an age of 1.4 ±0.4 ka. The widely accepted age for the lava flow using archaeomagnetic dating, yielded an age of AD 1220 (Tanguy *et al.* 2003).

1.3.3 Salina

The volcanic complex of Salina is the second largest island in the Aeolian archipelago with a subaerial area of ~27 km^2, and maximum elevation 982 metres above sea-level. Subaerial volcanism on Salina occurred from c. 244 ka until 15.6 ka (Lucchi *et al.* 2013b). Volcanic deposits are characterised by lava flows, scoriaceous deposits, breccias, and conglomerates separated by palaeosols and marine terraces (Lucchi *et al.* 2013b). Two cycles of volcanism were identified on Salina (Keller 1980b; Gertisser & Keller 2000). The older cycle is related to the eruption of high-alumia basalts from the Pizzo Corvo, Serro del Capo, and Monte Rivi stratocones, and late andesites and dacites from the 982-metre-high Fossa delle Felci stratocone (Keller 1980b; Gertisser & Keller 2000). The younger volcanic cycle is associated with the eruption of the andesitic Monte dei Porri stratocone and Pollara activity (Keller 1980b; Calanchi *et al.* 1987).

Volcanism on Salina was later refined by Lucchi *et al.* (2013b) into six eruptive epochs (synthems) by Lucchi *et al.* (2013b); Paleo-Salina informal unit (Pizzo Capo volcano), Vallone Martello Synthem (Pizzo Capo volcano), Scoglio della Fortuna Synthem (Vallone del Castagno Subsynthem; Monte Rivi and Monte Fossa delle Felci stratovolcanoes), Scoglio della Fortuna Synthem (Vallone d'Agliastro Subsynthem; Monte Fossa del Felci stratovolcano), Valdichiesa Synthem (Monte dei Porri stratocone) and Serra di Pollara Synthem (Pollara tuff ring) (Fig. 1.7; Lucchi *et al.* 2013b). Each eruptive epoch is characterised by different active centres separated by extended periods of dormancy, erosion and volcano-tectonic collapses and shifts of the eruptive vents and changes in magma compositions of eruptive products (Lucchi *et al* 2013b).

Eruptive epochs 1-4 (Paleo-Salina, c. 244 – 226 ka, Vallone Martello Synthem, c. 240 ka, Scoglio della Fortuna Synthem, c. 160 – 121 ka) are associated with effusive strombolian activity and eruptions of basaltic to dacitic scoria and lava flows of the Pizzo Capo, Monte Rivi, and Monte Fossa delle Felci stratocones (Lucchi *et al.* 2013b). Eruptive Epoch 5 (Valdichiesa Synthem, c. 70 – 57 ka) is associated with pyroclastic deposits and lava flows of the Monte dei Porri succession, truncated by a NW dipping collapse structure (Lucchi *et al.* 2013b) followed by a long period of quiescence and deposition of the so-called Brown Tuffs from Vulcano (Lucchi *et al.* 2008). Deposits from Eruptive Epoch 6 (Serra di Pollara Synthem, c. 30 – 15.6 ka) are observed in NW Salina and the eruption of the Punta di Perciato lava flows and Pollara tuff ring (Lower Pollara and Upper Pollara eruptions; Keller 1980b; Calanchi *et al.* 1993; Sulpizio *et al.* 2008). These eruptive epochs are separated by erosional unconformities associated with quiescent periods, volcano-tectonic collapses and sea-level fluctuations (Lucchi *et al.* 2013b).

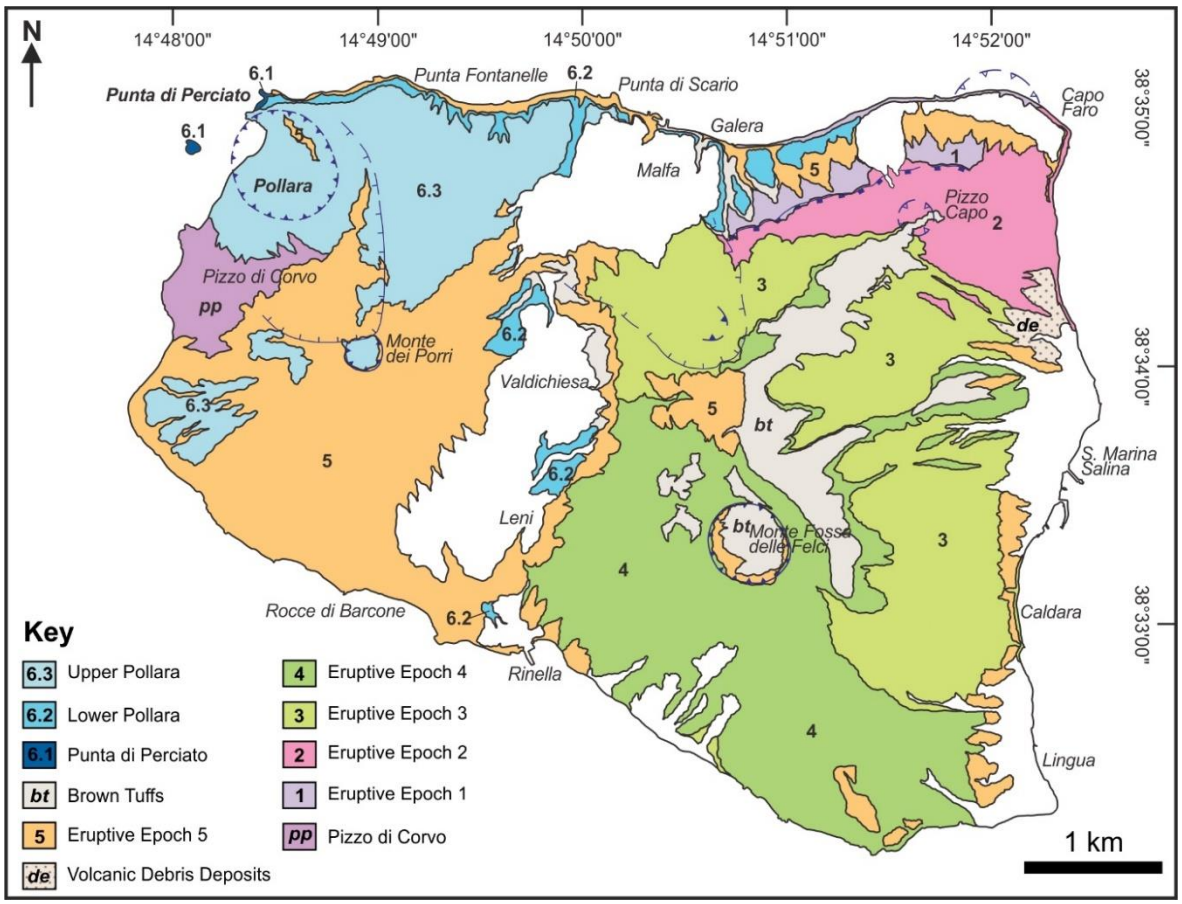

Fig. 1.7: Simplified geological map of the island of Salina, identifying all major eruptive epochs. Eruptive Epoch 6 is divided into 3 main eruptions: Punta di Perciato, Lower Pollara and Upper Pollara. (After: Lucchi *et al.* 2013b).

Eruptive products from Salina display the widest compositional range in SiO_2 in the entire Aeolian archipelago, belonging to the calc-alkaline magmatic series ranging in composition from basalts to rhyolites (Fig. 1.8; Keller 1980b; Gertisser & Keller 2000; Lucchi *et al.* 2013b), dominated by basaltic andesites, andesites and dacites (Gertisser & Keller 2000). Magma compositions varied through time due to the contamination of primary magmas from the Calabro-Peloritano basement, followed by later magma mixing and mingling processes (Keller 1980b; Lucchi *et al.* 2013b). The earliest erupted products on Salina are dominated by basalts from a deep magma reservoir located at or close to the crust-mantle boundary with later erupted andesites and dacites formed by assimilation and fractional crystallisation in magma reservoirs located in the middle and upper crust (Lucchi *et al.* 2013b). Rhyolites are only found in the most recent eruption of the Pollara tuff ring

(Keller 1980b; Sulpizio *et al.* 2008; Lucchi *et al.* 2013b). Deposits from Eruptive Epoch 6 represent the most recent volcanism on the island. This epoch consists of thick lava flows and voluminous pumiceous pyroclastic deposits, ranging from basalts to rhyolites. Three distinct eruptions have been identified; Eruption 6.1: Punta di Perciato (Punta di Perciato Subsynthem; Lucchi *et al.* 2013b), Eruption 6.2: Lower Pollara (Timpone Mona Subsynthem; Lucchi *et al.* 2013b) and Eruption 6.3: Upper Pollara (Semaforo di Pollara Subsynthem; Lucchi *et al.* 2013b).

The Punta di Perciato eruption (c. 30 ka; K-Ar age (Gillot 1987)) forms thick andesitic lava flows up to 10 metres thick creating the Punta di Perciato arch and Scoglio Faraglione islet. The vent location is thought to be within the present-day Pollara crater (Fig. 1.7). This eruption was subsequently unconformably overlain by the explosive eruption producing the widespread Lower Pollara pyroclastic succession (c.f. Keller 1980b; Morche 1988; Calanchi *et al.* 1993; Lucchi *et al.* 2013b).

The Lower Pollara eruption has been radiocarbon dated at 27.5 ka using charcoal fragments in the Intermediate Brown Tuffs (from Vulcano) at the base and top of the unit (Lucchi *et al.* 2013d). Three distinct strombolian to subplinian eruption units are identified; (1) dense, highly porphyritic, poorly vesiculated dark scoriae, (2) vesiculated grey pumices with banded pumices and (3) subaphyric to aphyric white pumices (Lucchi *et al.* 2013b) with abundant basement and conduit wall lithic fragments throughout the succession (Lucchi *et al.* 2013b). The Lower Pollara activity formed from a compositionally inversely zoned magmatic system (Keller 1980b; Calanchi *et al.* 1993).

The Lower Pollara pyroclastic succession was succeeded by a period of quiescence on Salina and the formation of a palaeosol, deposition of Brown Tuffs (from Vulcano), and the Monte Guardia activity (Lipari). The Upper Pollara eruption formed a widespread, massive to stratified pyroclastic succession (c.f. Keller 1980b; Sulpizio *et al.* 2008),

comprising white amphibole-bearing pumices with minor andesitic and banded pumices. Calibrated ^{14}C dating yielded an age of 15.6 ka (Keller 1980b).

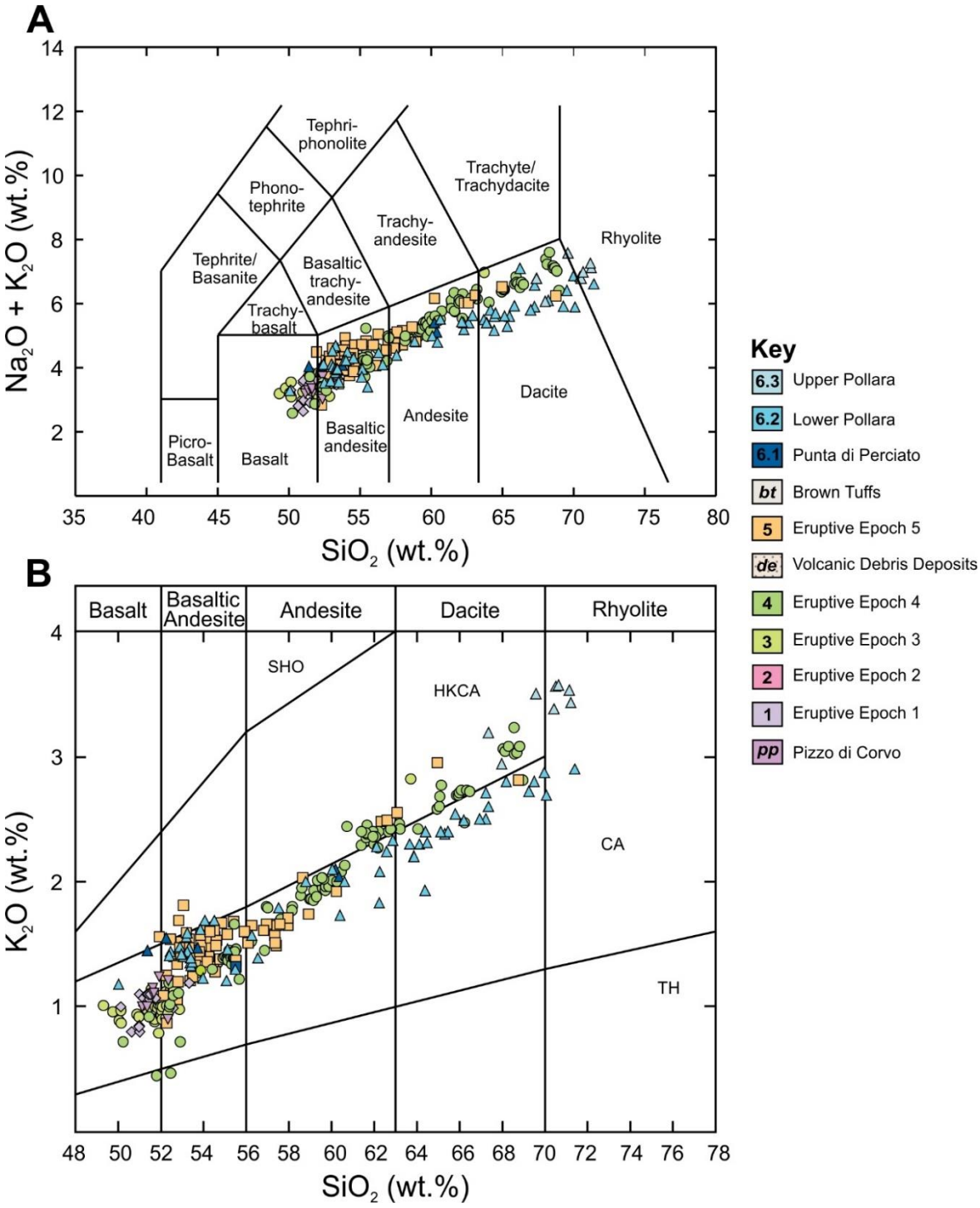

Fig. 1.8: (A) Total Alkali versus silica (SiO_2) diagram (Le Bas *et al.* 1986) and (B) K_2O versus silica (SiO_2) diagram (Peccerillo & Taylor 1976) for lavas and pyroclastic rocks covering the entire eruptive history of Salina. Analyses are normalised to 100 wt.% and are volatile free. TH: Tholeiitic, CA: calc-alkaline; HKCA: High-K calc-alkaline, SHO: Shoshonitic. (Data from: Keller 1980b; Ellam *et al.* 1988; 1989; Calanchi *et al.* 1993; Gertisser & Keller 2000; De Rosa *et al.*2003; Peccerillo 2005; Lucchi *et al.* 2013b).

The initial eruption was characterised by a short-lived, sustained eruption column forming coarse-grained lithic-rich fallout deposits at the base of the succession, followed by dilute PDCs, depositing most of the pyroclastics attributed to the eruption. The Upper Pollara activity formed due to intermittent Vulcanian explosive eruptions driven by magmatic fragmentation (Sulpizio *et al.* 2008; Lucchi *et al.* 2013b).

1.4 Aims and Objectives

This thesis investigates magma storage and differentiation at volcanic arcs, and the implications these processes have on the magmatic system, which can then be applied to other volcanic arcs worldwide. This work has been subdivided into three overarching aims to quantify magmatic processes in the central Aeolian arc, at La Fossa di Vulcano and during the 1888-90 eruption.

Aim 1: To constrain the evolution of the La Fossa di Vulcano magmatic system geochemically and isotopically over the last 5.5 ky.

Objective 1.1 Determine the depth of clinopyroxene crystallisation in the La Fossa di Vulcano magmatic system using clinopyroxene crystal structure and chemistry.

Objective 1.2 To use whole-rock, and mineral geochemistry to quantify the La Fossa di Vulcano magmatic system.

Objective 1.3 Assess the role of crustal contamination at La Fossa di Vulcano using Oxygen isotopes.

Objective 1.4 Evaluate the depth and extent of crustal contamination during the distinct stages of magma evolution at La Fossa di Vulcano.

Aim 2: To determine the shallow conduit processes and origins of the different bomb types during the 1888 – 90 Vulcanian eruption of La Fossa di Vulcano.

Objective 3.1 Catalogue the different bomb types erupted during the 1888 – 90 eruption using detailed field studies.

Objective 2.2 Characterise variations in mineral chemistry in feldspars erupted in the different bomb types.

Objective 2.2 Utilise textural analysis, including measuring the crystal size distributions to evaluate shallow conduit processes.

Objective 3.3 Determine the origins of breadcrust bombs during the 1888 – 90 eruption.

Aim 3: To quantitatively assess the role of crustal contamination in the generation of intermediate and silicic magmas in the central Aeolian arc.

Objective 3.1 Analyse Oxygen and Strontium isotopic data from mineral separates and glass from key eruptions of the most recent and active centres of Salina, Lipari and Vulcano.

Objective 3.2 Determine the source and extent of crustal assimilation within the different magmas using; whole-rock geochemical, O and Sr isotopic characterisation of potential bulk crustal contaminants.

Objective 3.3 Evaluate the significance of magma-crust interactions in influencing the different eruptions observed in the Central Aeolian Arc.

1.5 Thesis Outline

CHAPTER 1 – Introduction

This chapter provides a general overview of volcanic arcs, the Aeolian arc and the geology of the Central Aeolian arc, specifically the islands of Vulcano, Lipari and Salina. The study rationale, aims, objectives and thesis outline are also included.

CHAPTER 2 – Magma storage and magmatic processes at La Fossa di Vulcano

This chapter comprises a detailed O isotope and clinopyroxene crystal structure and chemistry study covering the entire stratigraphy of La Fossa di Vulcano, using whole-rock geochemistry, detailed petrography and mineral chemistry, X-Ray diffraction, O isotope data and thermobarometry. The observations and results presented in this chapter have been used to provide an updated model and more detailed understanding of the evolution of La Fossa di Vulcano over the last 5.5 ky.

CHAPTER 3 – Shallow conduit processes leading up to the 1888 – 90 Vulcanian eruption of La Fossa di Vulcano

Chapter 3 identifies the different bomb types erupted during the 1888 – 90 Vulcanian eruption. This chapter comprises detailed quantitative textural analysis of feldspar microlites, and petrological and geochemical data from all bomb types identified. The aim of this chapter is to determine timescales of magma ascent and evaluate conduit processes occurring during the eruption, thus providing detailed insights into the shallow conduit at La Fossa di Vulcano.

CHAPTER 4 – Source versus crustal contamination: An O and Sr isotope study of the central Aeolian arc, Italy

Chapter 4 comprises a detailed, large-scale O and Sr isotope study to quantitatively assess the influence of source and crustal contamination during the generation of intermediate and silicic magmas in the Central Aeolian Arc. This chapter presents new O and Sr isotopic data combined with geochemical and petrological data from key eruptions on Salina, Lipari and Vulcano, along with new whole-rock O and Sr isotope analysis of representative lithologies from the Calabro-Peloritano basement. This data has been used to evaluate the degree of source- and crustal- contamination in intermediate to silicic magmas in the Central Aeolian arc, specifically the effects and sources of contamination in

the different magmas erupted.

CHAPTER 5 – Petrogenesis of arc magmas

This chapter presents the synthesis and discussion of all the data presented in this thesis, linking the key findings from the previous chapters and discussing them in a broader context to other eruptions in the Aeolian arc in addition to the wider implications for other arc volcanoes. The main conclusions from all the work contained within this thesis is summarised at the end of this chapter.

This thesis concludes with appendices and geochemical data contained within this thesis.

CHAPTER 2 – Magma storage and magmatic processes at La Fossa di Vulcano

2.1 Introduction

To decipher the magma storage conditions of the Fossa di Vulcano this study examines intensive parameters (temperature and pressure), chemical changes that occurred during magma storage, magmatic processes (e.g. mush remobilisation) and processes that may trigger eruptions. Through the utilisation of clinopyroxene crystal structure and chemistry, stable oxygen isotope geochemistry, detailed petrological studies, major- and trace-element geochemistry, and clinopyroxene and feldspar compositions, this chapter aims to determine the depth of clinopyroxene crystallisation, clinopyroxene and plagioclase crystallisation temperatures and the depth and extent of crustal contamination linked to distinct stages of the magma evolution. Clinopyroxene is used in this study to geobarometrically constrain conditions of crystallisation in the volcanic system, as clinopyroxene cell parameters (unit cell volume, VCell and volume of the M1 site, VM1) are dependent upon crystallisation pressures, hence crystallisation depths (Dal Negro *et al.* 1982; 1984; 1989; Manoli & Molin 1988; Nazzareni *et al.* 2001). These pressures are then be combined with oxygen isotope data to determine where crustal contamination occurs in the magmatic system.

This chapter presents a new detailed stratigraphically controlled oxygen isotope, mineral chemical compositions, and a clinopyroxene crystal chemistry data set covering the entire eruptive history of La Fossa di Vulcano, crystallisation conditions of clinopyroxene and present an updated model of the evolution of the magmatic system.

2.2 La Fossa di Vulcano

The currently active La Fossa di Vulcano (Fig. 2.1A) is widely considered the most hazardous volcano in the Aeolian Islands and is characterised by alternating periods of explosive Vulcanian-subplinian events and lava flow effusion (Fig. 2.1B) last erupting in 1888-90 (Keller 1970; 1980a; Frazzetta *et al.* 1982; Dellino & La Volpe 1997; De Rosa *et al.* 2004; De Astis *et al.* 2007). It has long been known that processes of fractional crystallisation, magma mixing, mingling and replenishment dominate at La Fossa di Vulcano (De Astis *et al.* 2013). The magmatic system of Vulcano has been widely studied in recent years, utilising a combination of geophysical, petrological and geochemical studies (e.g. Clocchiatti *et al.* 1994; Zanon *et al.* 2003; Peccerillo *et al.* 2006; De Astis *et al.* 2003; 2013).

These studies indicate the presence of a polybaric magma plumbing system beneath La Fossa di Vulcano, consisting of several magma storage zones located above the mantle-crust boundary up to very shallow crustal depths (Clocchiatti *et al.* 1994; Nuccio *et al* 1999; Zanon *et al.* 2003; Peccerillo *et al.* 2006; De Astis *et al.* 2013; Paonita *et al* 2002; 2013; Fusillo *et al.* 2015; Mandarano *et al.* 2016; Nicotra *et al.* 2018; Bullock *et al.* 2019; Costa *et al.* 2020). Magma mixing at La Fossa has previously been examined in detail by various authors (e.g. Perugini *et al.* 2007; 2015; Piochi *et al.* 2009; De Astis *et al.* 1997; 2013; Vetere *et al.* 2015; Rossi *et al.* 2017; Nicotra *et al.* 2018; Bullock *et al.* 2019; Costa *et al.* 2020).

The 391-metre high stratocone formed over the past 5.5 kyr and the eruptive units are subdivided into eight eruptive units (formations, Fig. 2.1B): Punte Nere (pn), Grotta dei Palizzi 1 (gp1), 2 (gp2) & 3 (gp3), Caruggi (ca), Pietre Cotte (pc) and Gran Cratere 1 (gc1) & 2 (gc2) (Keller 1970; 1980a; De Astis *et al.* 1997; 2013).

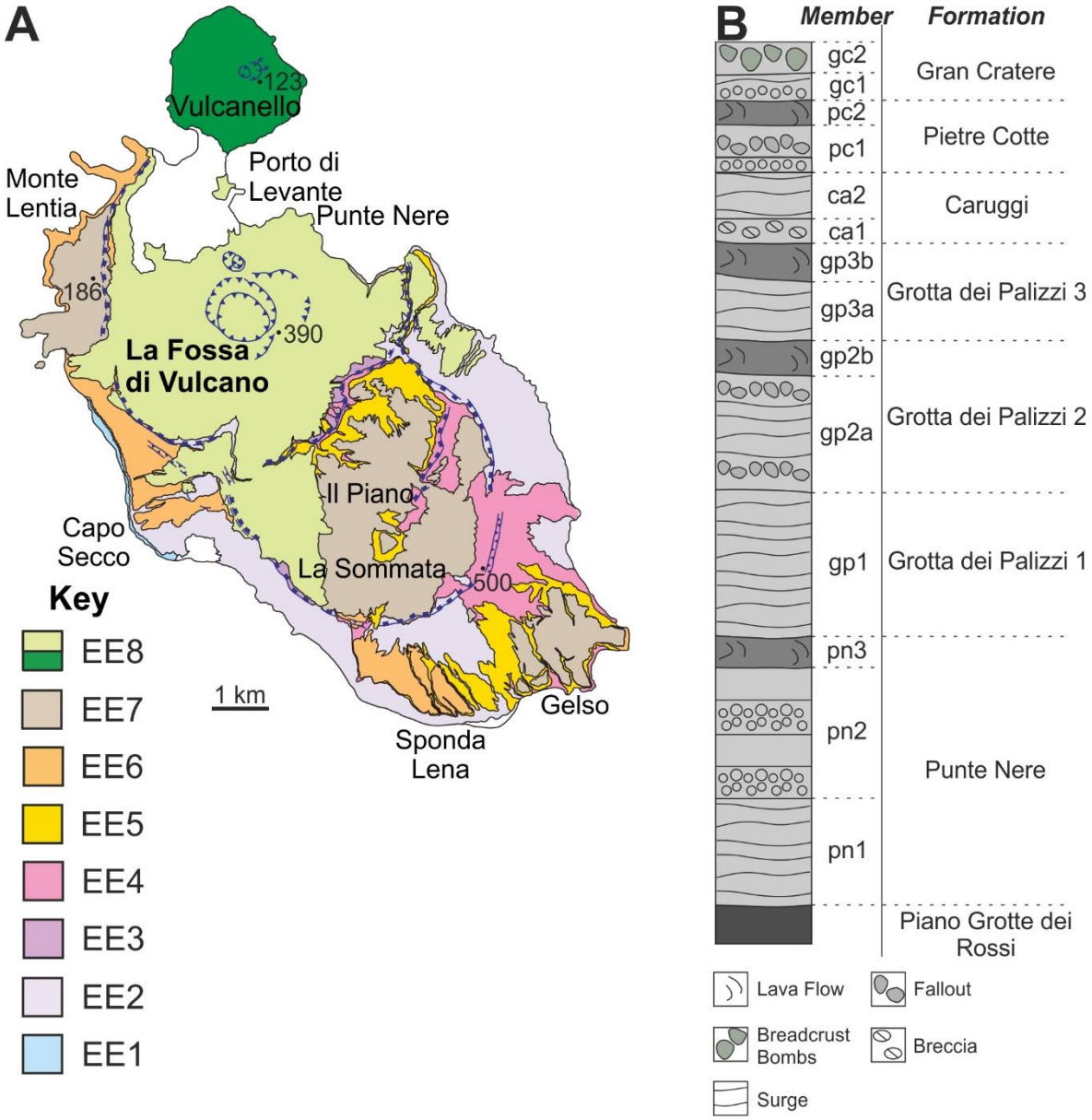

Fig. 2.1: (A) Simplified sketch geological map of the island of Vulcano (from De Astis *et al.* 2013), divided into eruptive epochs (EE). (B) Summary stratigraphic section of eruptions of La Fossa di Vulcano (from Dellino & La Volpe 1997; *In:* De Astis *et al.* 2013).

The Punta Nere activity commenced at 5.5 ka, after the widespread Piano Grotte dei Rossi tuffs (Upper Brown Tuffs) from alternating dilute pyroclastic density currents (PDCs) and periodic fallout (latite – trachyte) with late-stage effusive activity forming an A'a lava flow on the northern flanks of La Fossa (Frazzetta *et al.* 1983; 1985; Gillot 1987; Soligo *et al.* 2000; De Astis *et al.* 2013). Grotta dei Palilzzi 1 is dated at 2.9 ka (Voltaggio *et al.* 1995) and comprises a pyroclastic succession of PDCs, with abundant scoriaceous bombs at the

base, $Ø_{max}$ 1 metre (De Astis 1995; De Astis *et al.* 2013). This was followed by early explosive phases forming PDCs of latitic to rhyolitic composition attributed to Grotta dei Palizzi 2 (2.2 – 2.1 ka; Frazzetta *et al.* 1985; Voltaggio *et al.* 1995). These were proceeded by a late-stage rhyolitic lava flow on the southern flanks with abundant magmatic enclaves (De Astis *et al.* 2013). Similarly, Grotta dei Palizzi 3 commenced with initial explosive PDCs and ended with late-stage trachytic lava flow dated at 1.6 - 1.5 ka (Frazzetta *et al.* 1985; Voltaggio *et al.* 1995). Renewed volcanism after a quiescent period of a few hundred years formed the Caruggi formation, comprising a reworked tuff breccia and explosive latitic PDC deposits (Dellino & La Volpe 1997). This was followed by the activity of Pietre Cotte, commencing with early explosive phases of PDCs and subordinate fallout from a discontinuous eruption column and a rhyolitic obsidian lava flow (AD 1739; Keller 1970) on the northern flanks. Lava flow effusion was then followed by intermittent explosive eruptive phases of alternating PDCs and fallout, forming the Gran Cratere 1 formation. The most recent eruption of La Fossa di Vulcano (Gran Cratere 2) was the 1888 - 1890 'type' Vulcanian eruption documented by Mercali & Silvestri (1891). Gran Cratere 2 formed dense lapilli tuffs with abundant bombs and breadcrust bombs from intermittent fallout pulses (De Astis *et al.* 2013).

Several different models have previously been proposed for La Fossa di Vulcano based upon geophysical, geochemical, and petrological observations (Clocchiatti *et al* 1994; De Astis *et al.* 1997; 2013; Zanon *et al* 2003; Peccerillo *et al.* 2006; Perugini *et al.* 2007; Piochi *et al.* 2009; Vetere *et al.* 2015; Nicotra *et al.* 2018; Bullock *et al.* 2019). However, there is no agreed model, and none covers the entire evolution of La Fossa di Vulcano. La Fossa magmas are stored in reservoirs throughout the crust, with the most primitive magmas stored at mid to lower crustal depths, and evolved magmas stored at shallower depths in the upper crust. Studies on the 1888-1890 eruption identified two distinct magma systems at La Fossa which evolved by a combination of wall-rock assimilation and

fractional crystallisation (Clocchiatti *et al.* 1994). Clocchiatti *et al.* (1994) also proposed the trachyte formed by mixing of rhyolite and latite magma which resided at intermediate crustal depths and was contaminated with gneiss and quartz crustal lithologies inferred from the occurrence of xenoliths and Pb isotopic trends in the shallow magmatic system.

Conversely, De Astis *et al.* (1997) suggested magma in the shallowest storage region evolved to trachytic and rhyolitic compositions assimilating upper crustal material and mixing. More recent studies on CO_2 inclusions in quartz xenoliths on Vulcano from 4 lava flows (Sponda Lena, Monte Lentia, Mastro Minico and Vulcanello) during the last 120 kyr, concluded ponding of mantle-derived magmas in at least two distinct reservoirs located at lower crustal depths (close to the mantle boundary) and shallow crustal levels (Zanon *et al.* 2003).

Combined petrological data from this study indicated deep reservoirs (18 - 21 km) were the sites of extensive fractional crystallisation, mixing with mantle source derived magmas and various degrees of crustal contamination (Zanon *et al.* 2003). These evolutionary processes also occurred in the shallow magma chambers located at ~ 5 km. A further model based upon petrological, geophysical and fluid-inclusion data by Peccerillo *et al.* (2006) identified two major storage zones located at 8 - 13 km and 17 - 21 km depth and a minor magma storage zone located between 1 and 5 km. They concluded continuous fractional crystallisation, crustal contamination and mixing with mantle melts dominated in the deepest storage zone. These magmas then rise into the intermediate storage zone and pond. Peccerillo *et al.* (2006) suggested magmas only reside in the shallowest storage regions for a short time prior to eruption, where degassing dominates. Piochi *et al.* (2009) modelled processes of magma evolution for the Pietre Cotte lava flow where mingling of an uprising rhyolitic magmas and a shallower latitic-trachytic plug, is followed by the formation of the latitic to trachytic enclaves within the rhyolite. Piochi *et al.* (2009) proposal for enclave

formation was based upon the dominantly subcircular morphology of enclaves and the presence of enclave-type veins within the host rhyolite with the sharp contact between enclaves and the rhyolitic host explained by elemental diffusion with physical mingling of the magmas. Conversely, Perugini *et al.* (2007) and Vetere *et al.* (2015) both proposed the enclaves within the Pietre Cotte rhyolitic lava formed due to the injection of a latitic to trachytic enclave forming magma into the rhyolitic host magma using enclave morphologies and size distributions and thermodynamic and rheological modelling.

A detailed geochemical and petrological study on plagioclase crystals from lavas < 1000 years constrained plagioclase crystallisation depths proposing three main magma levels beneath La Fossa (Nicotra *et al.* 2018). In agreement with previous studies the deep basaltic to shoshonitic magma storage region was interpreted to be located between 21 and 18.5 km. The presence of an intermediate, zoned shoshonitic to latitic magma reservoir was proposed at a depth of 16.8 to 12.5 km, and a further small shallow latitic to trachytic magma reservoir between 3.5 and 3 km, dominated by magma mixing forming sieve textured plagioclase (Nicotra *et al.* 2018). The authors concluded that the shallowest rhyolitic magma storage region is at the same depths as proposed by Clocchiatti *et al.* (1994). A more recent study by Bullock *et al.* (2019) on the magmatic evolution of La Fossa prior to extrusion of the AD 1739 Pietre Cotte lava flow proposed the mobilisation of a mafic crystal mush at a depth of 28 km. Fractional crystallisation of a shoshonitic to latitic magma to a trachytic magma occurred between ~ 24 and 16 km. Similarly, to other authors, Bullock *et al.* (2019) proposed a rhyolitic storage reservoir located at < 5 km depth.

2.3 Methods

Twenty-one samples comprising lavas and pyroclastic deposits (ash, pumice lapilli and scoria lapilli) covering the entire stratigraphy of La Fossa di Vulcano were analysed in this study. For whole-rock major element compositions, samples were washed in deionised water for 48 hours and all weathered and altered surfaces were removed. Samples were then crushed in a jaw crusher and reduced to a fine powder in an agate mill for 2 – 6 minutes and dried overnight at 130°C. Major elements were analysed using Inductively Coupled Plasma – Atomic Emission Spectroscopy (ICP-AES) at Bureau Veritas Minerals laboratories, Canada, using the lithium metaborate (LiB_2) flux fusion, followed by dilution using dilute nitric acid. Andesite and rhyolite standards were used to calibrate the ICP-AES. Detection limits for the major elements were 0.01 wt.% with the exception of Fe_2O_3 for which the detection limit was 0.04 wt.%. For trace elements the detection limits were 1 ppm for Sc, 2 ppm for Sr, 3 ppm for Y, 5 ppm for Ba, Nb, Zr and 20 ppm for Cr and Ni. Precision was better than 5%.

Mineral and glass chemistry were determined using a Cameca SX100 electron microprobe at the Natural History Museum, London, UK. Major elements were measured in minerals and glass, with Sr and Ba also measured in feldspar. Volatiles (Cl and S) were measured in glass with a defocused beam and extended peak counting times of 30 seconds. Pyroxene (1 µm beam diameter), feldspar (5 µm beam diameter), oxides (1 µm beam diameter) and glass (20 µm beam diameter) were measured using a 20 kV accelerating voltage and 20 nA beam current. Na and K were measured first to minimise the effects of alkali migration. Na was measured first using short peak counting times (10 seconds).

Clinopyroxene crystallography (structure) for 19 phenocrysts were determined. The phenocrysts selected did not show evidence of disequilibrium (e.g. compositional zoning, embayed) and are euhedral, ranging in size from 125-300 µm. Single-crystal X-ray

diffraction data were obtained using an Oxford single-crystal diffractometer with Mo radiation at Keele University, UK. Samples were run at room temperature. The resolution was set to 0.7, with a scan width of 1.6 and frame width of 1.0. The unit cell volume (VCell, $Å^3$) and pairs of ± hkl and ± hkl reflections were measured over the range of $3° < 2\Theta < 60°$ using Ω scans. Cell parameters and site partitioning data were calculated using the least-squares minimisation of structural data refinement method in SHELX (Sheldrick 1976). Structural refinements were performed using SHELX and xtaldraw software (Downs & Bartelmehs 1997), using the methods of Faraone *et al.* (1988), Malgrotto *et al.* (1993) and Nazzareni *et al.* (1998; 2001). Structural refinements were carried out using the c2/c space group in the monoclinic crystal system without chemical constraints, starting with diopside coordinates (Clarke *et al.* 1969) to determine the polyhedral volume of the M1 site occupancy using xtaldraw (Downs & Bartelmehs 1997). Repeat measurements on different clinopyroxenes from the same sample yielded reproducible values (VCell and VM1) within 2σ. Pressures were converted to depths using a crustal density of 2.83 g/cm^3.

For oxygen isotope analyses, rock samples were briefly crushed and sieved. Feldspar and pyroxene minerals were then selected from the 250 – 125 μm sieve fractions using a binocular microscope. Stable isotope analyses on mineral separates (1 – 4 mg) of pyroxene, feldspar and obsidian glass were run at Scottish Universities Environmental Research Centre, East Kilbride, UK. Oxygen isotope analyses were carried out using the laser fluorination method of Sharp (1990). For pyroxene and obsidian glass, overnight pre-fluorination was undertaken to remove any adsorbed environmental water from the line and sample chamber. Feldspar, which is inherently more reactive with ClF_3, underwent a short (90 second) pre-fluorination stage prior to each analysis. Oxygen isotopes are reported using the standard δ-notation relative to Standard Mean Ocean Water (SMOW). Two garnet standards (UWG-2 (+5.8‰ ± 0.1‰); GP147 (+7.3‰ ± 0.1‰)) and a quartz standard (YP2 (+16.4‰)) were run at the beginning, middle and end of each run, and are

better than ± 0.2 ‰. All measured values for standards were close to the accepted values, therefore no corrections were made. Repeat measurements of unknown samples are all less than ± 0.3‰.

2.4 Results

2.4.1 Petrography, rock classification and mineral compositions

Eruptive products from La Fossa range from shoshonite to latite, trachyte and rhyolite (Fig. 2.2A, B) and define a high-K calc-alkaline and shoshonitic series in the K_2O versus SiO_2 diagram (Peccerillo & Taylor 1976) with most rocks having a shoshonitic affinity. The main mineral phases in lavas and pyroclastics of La Fossa are clinopyroxene, plagioclase, alkali feldspar and magnetite, occurring as phenocrysts and in the groundmass, with less abundant olivine and biotite and accessory apatite (De Astis *et al.* 2013). Glomerocrysts consisting of plagioclase, clinopyroxene, olivine and magnetite are common in the pyroclastic deposits, lavas and magmatic enclaves. Lavas, scoria and pumice have a glassy to microcrystalline groundmass. Deposits from La Fossa have complex mineral assemblages, evidenced by abundant disequilibrium textures including embayed clinopyroxene as well as compositional zoning in clinopyroxene, plagioclase and alkali feldspar (Fig. 2.3). Mafic magmatic enclaves are abundant in the Pietre Cotte and Grotta dei Palizzi 2 lavas, indicating magma mingling processes dominate.

Feldspar is the most abundant mineral phase across the entire compositional range of La Fossa (Appendix A). Plagioclase range in composition from $An_{42\text{-}70}Ab_{25\text{-}50}Or_{3\text{-}10}$ in latite, $An_{26\text{-}59}Ab_{36\text{-}65}Or_{2\text{-}10}$ in trachyte, $An_{36\text{-}54}Ab_{38\text{-}55}Or_{1\text{-}10}$ in rhyolite, and $An_{45\text{-}66}Ab_{30\text{-}46}Or_{3\text{-}10}$ in latitic-trachytic enclaves (Fig. 2.4A). Plagioclase phenocrysts commonly exhibit twinning, compositional zoning, oscillatory zoning, sieve textures and patchy cores (Fig. 2.4A).

Alkali feldspars range from $An_{2\text{-}7}Ab_{29\text{-}52}Or_{43\text{-}67}$ in latite, $An_{1\text{-}7}Ab_{30\text{-}58}Or_{35\text{-}69}$ in trachyte and $An_{4\text{-}10}Ab_{35\text{-}44}Or_{45\text{-}59}$ in latitic-trachytic enclaves.

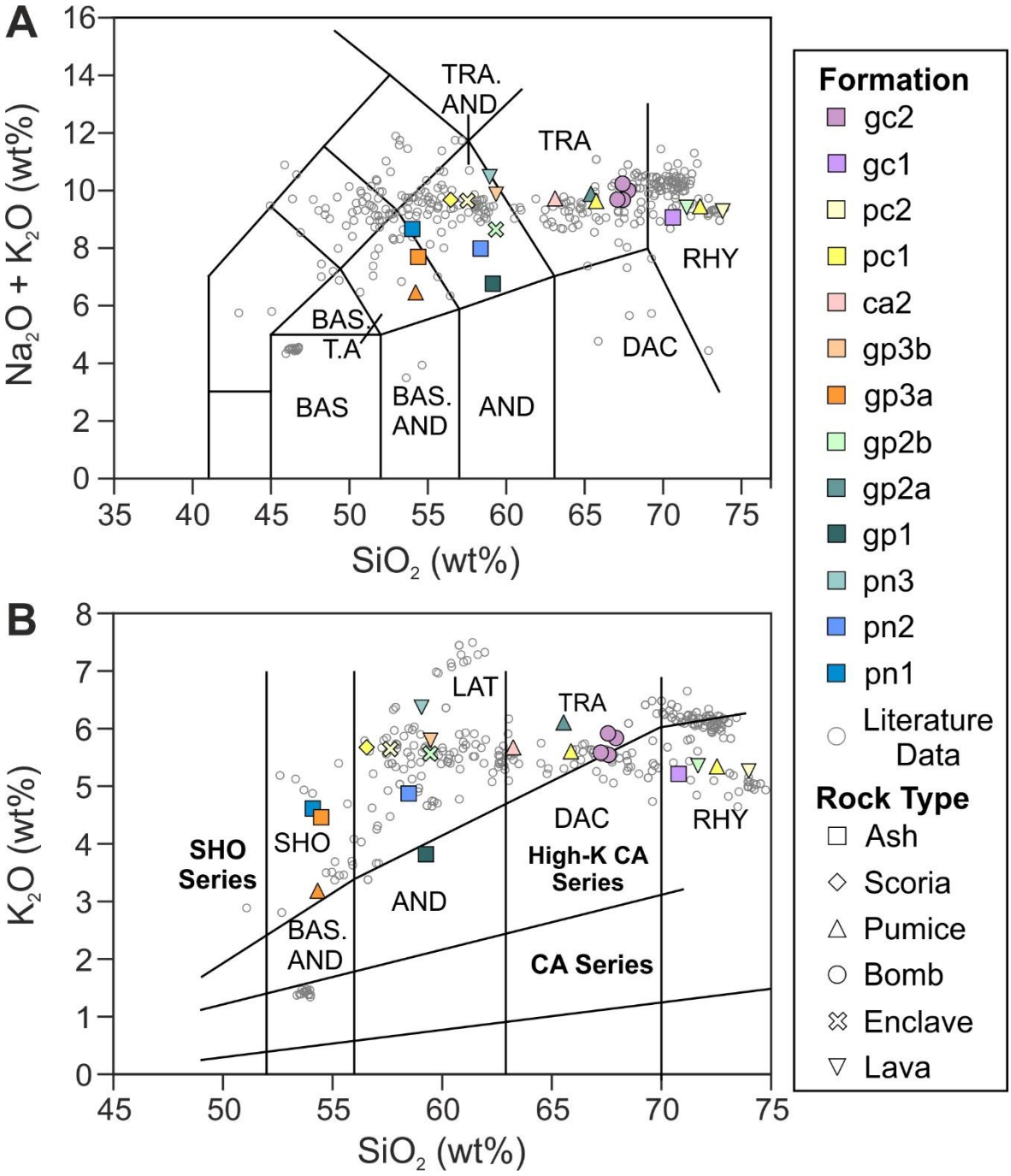

Fig. 2.2: (A) Total Alkali versus SiO_2 (Le Bas *et al.* 1986) and (B) K_2O versus SiO_2 classification diagrams (Peccerillo & Taylor 1976) from La Fossa di Vulcano. Oxides are expressed in weight percent (wt.%), and compositions are all normalised and LOI-free. Existing literature data (light grey circles) from De Astis *et al.* (2013) and references therein.

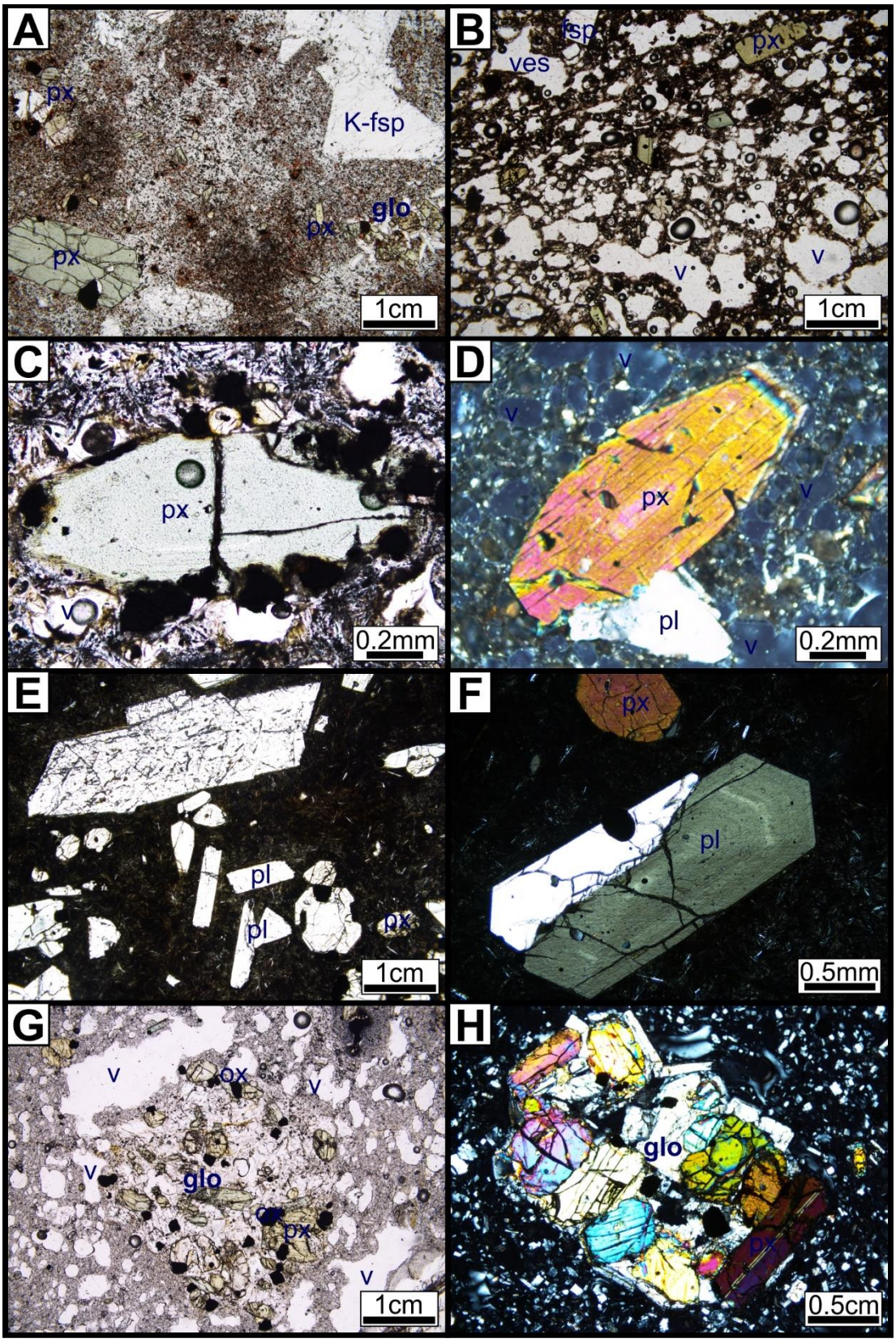

Fig. 2.3: Photomicrographs showing a selection of disequilibrium textures from La Fossa deposits. Overview section of (A) gp3b trachytic lava. (B) pc1 scoria. Clinopyroxene phenocryst in (C) pn3 lava. (D) pc1 scoria. (E - F) Feldspar textures in gp3a. eruption. (G-H) Common glomerocrysts found in most La Fossa deposits. (G – gc2 H - ca2). px: clinopyroxene, pl: plagioclase K-fsp: alkali feldspar, v: vesicle, ox: Fe-Ti oxide, glo: Glomerocrysts.

Clinopyroxene occurs across the entire compositional range of La Fossa di Vulcano. Clinopyroxenes are dominantly diopside, rarely extending into the augite field (Fig. 2.4B; Appendix A; Morimoto 1988). Clinopyroxene phenocrysts range in size from 0.5 up to 7 mm diameter with Mg# 71-85 ($Wo_{34-49}En_{29-48}Fs_{6-28}$). Clinopyroxene crystals have euhedral to subhedral habits (Fig. 2.3), with concentric- and oscillatory-zoning, with abundant Fe-Ti oxide, apatite and melt inclusions.

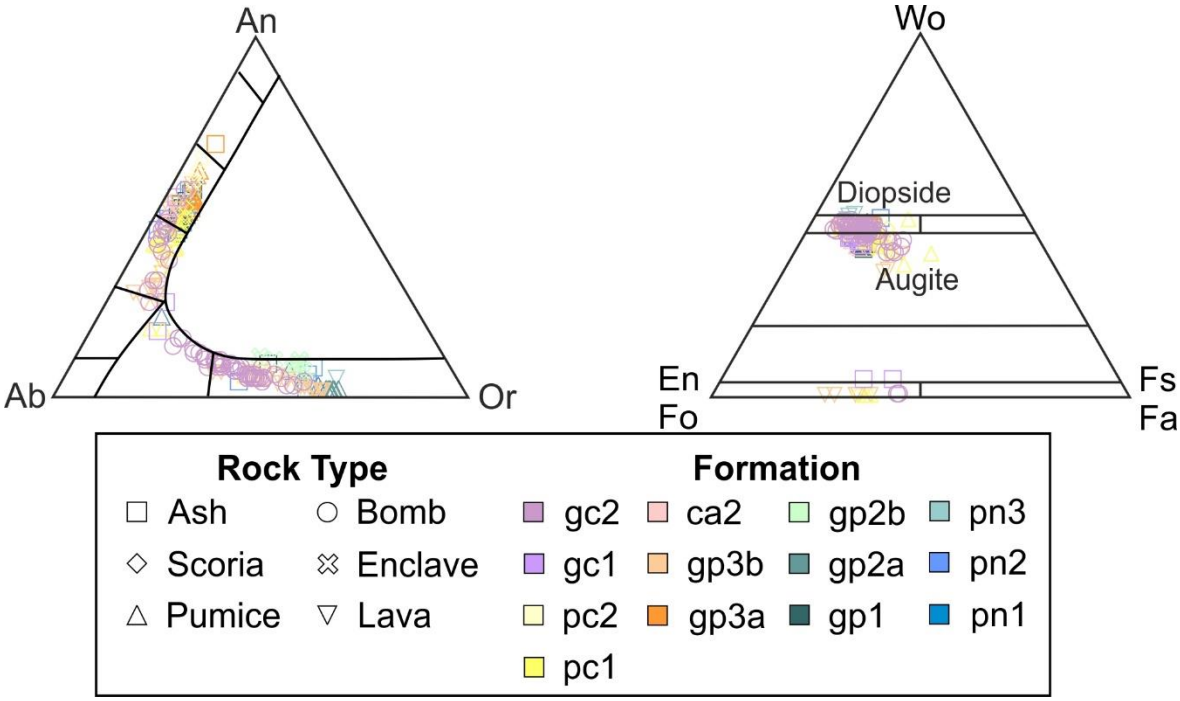

Fig. 2.4: Mineral chemistry of La Fossa di Vulcano eruptive products. (A) Feldspar ternary classification diagram for feldspar phenocrysts and groundmass. (B) Pyroxene ternary classification diagram, with olivine compositions plotted along the bottom axis (Fo = Forsterite, Fa = Fayalite) (Morimoto 1988).

Olivine occurs in the less evolved shoshonites from La Fossa di Vulcano. Olivine phenocrysts (0.5 to 2 mm) frequently have euhedral to subhedral habits and are heavily fractured and sometimes display embayment textures with abundant Fe-Ti oxide and melt inclusions. Olivine compositions range from Fo_{55-73} (Fig. 2.4B; Appendix A). Fe-Ti oxides occur across the entire compositional range of La Fossa di Vulcano. Fe-Ti oxides occur as phenocrysts (0.5 to 4 mm), microlites within the groundmass and inclusions in other minerals. Apatite is an accessory mineral commonly occurring in clinopyroxene and

olivine. Biotite and dark brown amphibole occur sporadically in La Fossa di Vulcano deposits, specifically in Punte Nere (pn) and Grotta dei Palizzi 3 (gp3).

2.4.2 Clinopyroxene crystal structure

The crystal structures of clinopyroxenes were determined from each stratigraphically constrained formation of La Fossa. The structural parameters (VCell and VM1 site occupancies; Table 2.1) vary with stratigraphy, covering and exceeding the entire range of Vulcano lavas proposed by Nazzareni *et al.* (2001) (Fig. 2.5). VCell ranges from 436.932 - 441.546 $Å^3$ in pyroclastic deposits, from 439.727 - 440.255 $Å^3$ in lavas and from 439.407 - 441.070 $Å^3$ in magmatic enclaves. VM1 ranges from 11.733 - 11.925 $Å^3$ in pyroclastic deposits, from 11.810 - 11.877 $Å^3$ in lavas and from 11.866 - 11.869 $Å^3$ in magmatic enclaves.

Generally, the largest variations in VCell and VM1 are observed in deposits from explosive eruptions. Clinopyroxenes from La Fossa lavas, crystallised at a pressure (~3 and 4 kbar, c. 11 and 14 km depth, Fig. 2.5), whereas in the pyroclastic deposits the clinopyroxenes crystallised at a range of pressures (~2 – 6 kbar; c. 7 – 21 km, Fig. 2.5). Clinopyroxenes found in the obsidians from pc2 and gp2 were not measured as they are thought to be disrupted enclaves and not from the host lava. There is no evidence supporting clinopyroxene crystallisation at very shallow depths (< 5 km) in the more evolved magmas or at depths above 21 km.

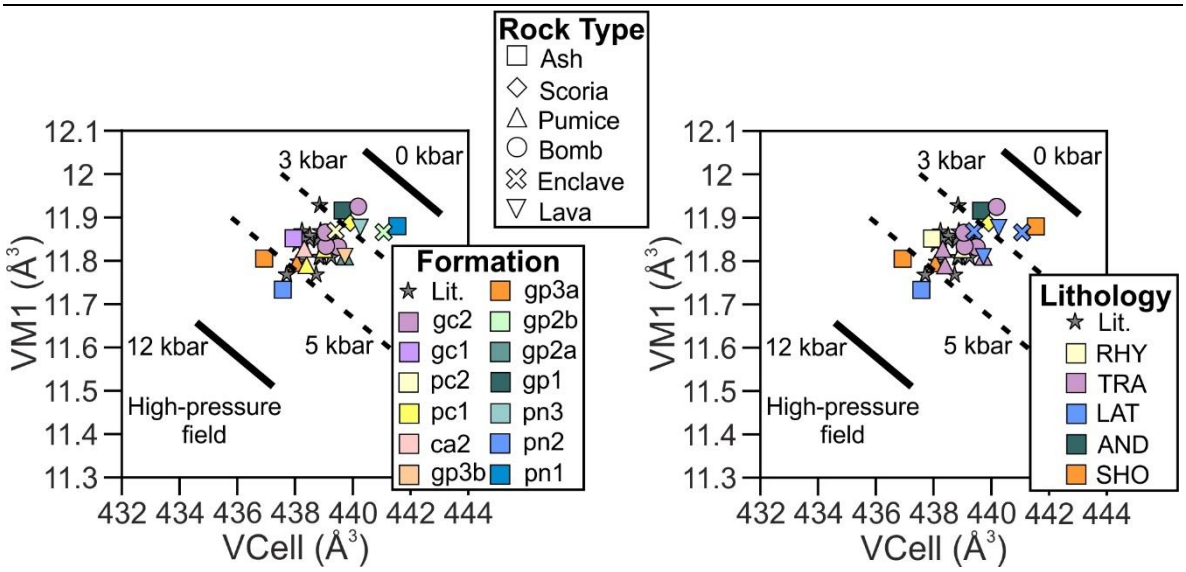

Fig. 2.5: (A) VCell (Å) versus VM1 (Å) site volumes for clinopyroxene phenocrysts from La Fossa di Vulcano using symbols corresponding to stratigraphy. (B) VCell (Å) versus VM1 (Å) site occupancies for clinopyroxene phenocrysts from La Fossa di Vulcano using symbols corresponding to whole-rock composition. Additional data from Vulcano lavas from Nazzareni *et al.* (2001). The high-pressure field (12 kbar) is identified using Manoli & Molin (1988). Pressure lines are taken from Nazzareni *et al.* (2001).

Table 2.1: Clinopyroxene crystal unit cell volumes (VCell) and volume of the M1 site (VM1) for rock samples covering the entire stratigraphy of La Fossa di Vulcano arranged in stratigraphical order from oldest to youngest. n.a. not analysed.

	pn1	pn2	pn3	gp1	gp2a	gp2b	gp2b
Sample	AI-17-041	AI-18-058	AI-17-006	AI-17-073	AI-17-049	AI-17-117	AI-17-056
	Ash	Ash	Lava	Ash	Pumice	Lava	Enclave
VCell (Å^3)	441.546	437.578	440.256	439.652	439.727	n.a.	441.07
VM1 (Å^3)	11.88	11.733	11.877	11.916	11.81	n.a.	11.866

	gp3a	gp3a	gp3b	ca2	pc1	pc1	pc1
Sample	AI-18-056	AI-18-057	AI-17-045	AI-17-034	AI-17-019	AI-17-021	AI-17-025
‰	Ash	Pumice	Lava	Pumice	Scoria	Pumice	Pumice
VCell (Å^3)	438.059	436.932	439.727	438.319	439.913	439.012	438.402
VM1 (Å^3)	11.795	11.805	11.81	11.828	11.887	11.827	11.79

	pc2	pc2	gc1	gc2	gc2	gc2	gc2
Sample	AI-17-009	AI-17-028	AI-17-070	AI-17-120	AI-18-072	AI-18-074	AI-18-076
‰	Lava	Enclave	Ash	Bomb	Bomb	Bomb	Bomb
VCell (Å^3)	n.a.	439.407	437.947	440.189	439.493	439.078	439.056
VM1 (Å^3)	n.a.	11.869	11.852	11.925	11.832	11.834	11.865

2.4.3 Whole-rock, groundmass glass and melt inclusion geochemistry

Major and trace element compositions for ash, pumice, scoriae, breadcrust bombs, lavas and enclaves covering the entire stratigraphy of La Fossa di Vulcano are summarised in Table 2.2. SiO_2 values range from 51.74 - 73.34 wt.% and K_2O ranges from 3.02 - 6.12 wt.% (Fig. 2.2B).

Table 2.2: Major-, and Trace-element geochemistry for rock samples covering the entire stratigraphy of La Fossa di Vulcano arranged in stratigraphical order from oldest to youngest. b.d. below detection limit.

	pn1	pn2	pn3	gp1	gp2a	gp2b	gp2b
Sample	AI-17-041	AI-18-058	AI-17-006	AI-17-073	AI-17-049	AI-17-117	AI-17-056
wt.%	Ash	Ash	Lava	Ash	Pumice	Lava	Enclave
SiO_2	52.26	55.77	57	57.02	62.99	70.92	57.21
TiO_2	0.68	0.55	0.6	0.5	0.35	0.18	0.62
Al_2O_3	16.47	14.9	18.75	14.25	14.93	13.57	15.76
Fe_2O_3	8.17	7.07	6.39	7.24	4.53	2.88	5.74
MnO	0.16	0.1	0.08	0.12	0.1	0.08	0.09
MgO	3.79	3.26	1.14	4.43	1.3	0.65	2.92
CaO	7.13	6.59	2.75	6.73	2.78	1.7	5.81
Na_2O	3.92	2.98	3.98	2.84	3.65	4.03	2.97
K_2O	4.44	4.63	6.12	3.66	5.85	5.28	5.34
P_2O_5	0.46	0.31	0.43	0.24	0.18	0.08	0.42
LOI	2.1	3.4	2.2	2.6	3.1	0.5	2.7
Total	99.58	99.56	99.44	99.63	99.76	99.87	99.58
ppm							
Ba	1054	794	2281	522	427	185	951
Sr	1290	964	1589	826	375	182	1087
Zr	160	185	192	130	297	207	174
Nb	19	19	23	17	31	32	22
Y	21	22	13	27	31	38	33
Ni	b.d.	21	b.d.	20	b.d.	b.d.	b.d.
Cr	117	88	b.d.	248	29	b.d.	88
Sc	17	19	7	21	7	4	18
Mg#	55	56	33	63	46	40	14

Table 2.2 cont'd: Major-, and Trace-element geochemistry for rock samples covering the entire stratigraphy of La Fossa di Vulcano arranged in stratigraphical order from oldest to youngest. b.d. below detection limit.

	gp3a	gp3a	gp3b	ca2	pc1	pc1	pc1
Sample	AI-18-056	AI-18-057	AI-17-045	AI-17-034	AI-17-019	AI-17-021	AI-17-025
wt.%	Ash	Pumice	Lava	Pumice	Scoria	Pumice	Pumice
SiO_2	51.78	51.74	58.65	62.22	55.46	71.17	64.5
TiO_2	0.65	0.7	0.5	0.39	0.57	0.14	0.3
Al_2O_3	18.04	17.43	16.16	15.15	16.33	13.47	15.02
Fe_2O_3	8.13	8.57	6.5	5.26	7.31	2.55	4.31
MnO	0.16	0.14	0.11	0.11	0.14	0.08	0.1
MgO	3.67	3.26	2.41	2.05	3.23	0.41	1.41
CaO	7.21	6.3	4.99	4.01	5.94	1.35	3.2
Na_2O	3.13	3.08	4.02	4	3.94	4.04	3.96
K_2O	3.02	4.22	5.7	5.56	5.54	5.23	5.47
P_2O_5	0.4	0.45	0.32	0.25	0.4	0.06	0.18
LOI	3.3	3.7	0.3	0.7	0.7	1.4	1.3
Total	99.49	99.59	99.66	99.7	99.56	99.9	99.75
ppm							
Ba	1033	959	761	584	948	104	408
Sr	1542	1138	845	609	1057	113	498
Zr	151	155	257	240	205	214	233
Nb	17	18	25	30	19	33	30
Y	24	24	28	30	26	39	32
Ni	b.d.	b.d.	b.d.	b.d.	b.d.	b.d.	b.d.
Cr	73	58	58	73	88	b.d.	58
Sc	17	15	12	10	14	3	7
Mg#	55	50	51	54	55	32	49

La Fossa rocks display almost continuous trends of major and trace elements versus SiO_2. With increasing SiO_2, TiO_2, $Fe_2O_3^*$, MnO, MgO, CaO and P_2O_5, Ba, Sr, Cr, and Sc all decrease, whereas Zr, Nb and Y increase (Fig. 2.6; 2.7). A slight kink at 61 wt.% SiO_2 is observed in Al_2O_3 in an overall decreasing trend with SiO_2 (Fig. 2.6). Zr displays a peaked trend decreasing at > 66 wt. SiO_2 thereafter (Fig. 2.7). Sc and to some extent Cr decrease with increasing SiO_2 (Fig. 2.7). Na_2O and K_2O have a slight increase with increasing SiO_2 (Fig. 2.6).

Table 2.2 cont'd: Major-, and Trace-element geochemistry for rock samples covering the entire stratigraphy of La Fossa di Vulcano arranged in stratigraphical order from oldest to youngest. b.d. below detection limit.

	pc2	pc2	gc1	gc2	gc2	gc2	gc2
Sample	AI-17-009	AI-17-028	AI-17-070	AI-17-120	AI-18-072	AI-18-074	AI-18-076
wt.%	Lava	Enclave	Ash	Bomb	Bomb	Bomb	Bomb
SiO_2	73.34	56.86	68.73	67.2	66.68	66.68	66.18
TiO_2	0.11	0.54	0.19	0.27	0.28	0.28	0.28
Al_2O_3	13.39	16.5	13.62	14.88	14.83	14.8	14.93
Fe_2O_3	2.16	6.88	3.01	3.78	3.86	3.97	4.03
MnO	0.07	0.13	0.07	0.09	0.09	0.09	0.09
MgO	0.2	2.92	0.95	0.91	0.93	1.11	1.14
CaO	0.99	5.7	2.08	2.26	2.32	2.55	2.61
Na_2O	4	3.96	3.75	4.14	4.28	4.09	4.05
K_2O	5.2	5.55	5.05	5.75	5.82	5.45	5.48
P_2O_5	0.03	0.38	0.07	0.14	0.1	0.15	0.16
LOI	0.4	0.2	2.4	0.4	0.6	0.6	0.8
Total	99.89	99.62	99.92	99.82	99.79	99.77	99.75
ppm							
Ba	62	918	173	374	376	368	389
Sr	59	1047	234	366	376	373	410
Zr	208	203	178	254	250	240	240
Nb	32	23	29	35	32	29	31
Y	39	24	34	32	32	32	31
Ni	b.d.	b.d.	b.d.	b.d.	b.d.	b.d.	b.d.
Cr	b.d.	73	58	29		44	b.d.
Sc	2	13	5	5	5	6	6
Mg#	22	54	48	42	42	45	46

Scattering is observed in K_2O in mafic-intermediate eruptive products (Fig. 2.2B). The pyroclastic deposits from La Fossa di Vulcano span a wide compositional range (51.78 - 52.26 wt.% SiO_2 in shoshonites, 55.46 – 55.77 wt.% SiO_2 in latites, 62.22 to 67.2 wt.% SiO_2 in trachytes and 68.73 – 71.17 wt.% SiO_2 in rhyolites), whereas the lavas (70.9 - 73.3 wt.% SiO_2 for rhyolites and 57.0 - 58.7 wt.% SiO_2 for trachytes) and enclaves (56.9 – 57.2 wt.% SiO_2) span a much smaller compositional range.

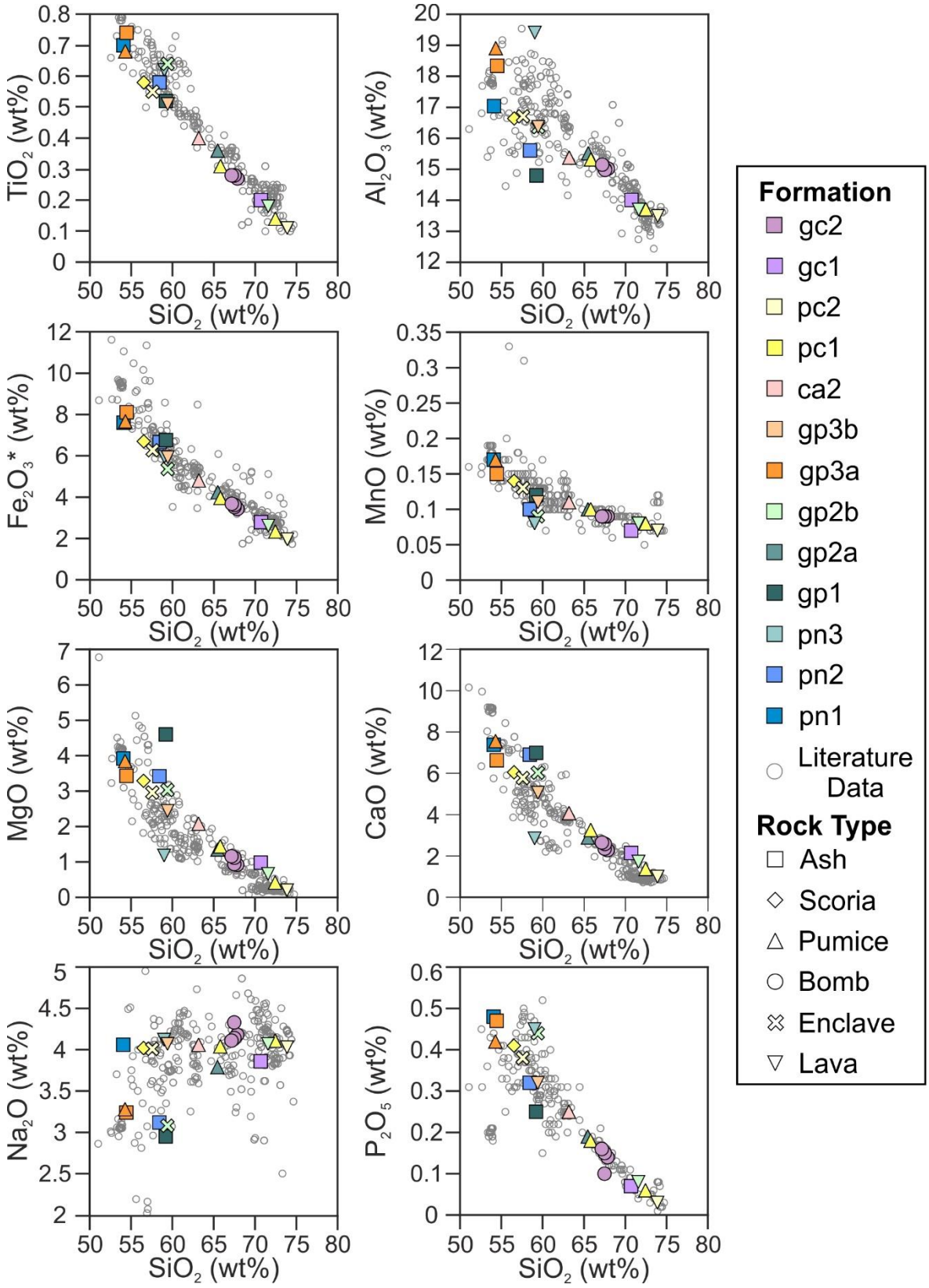

Fig. 2.6: Major element variation diagrams versus SiO_2 covering the entire eruptive history of La Fossa di Vulcano, plotted with existing literature data (De Astis *et al.* 2013 and references therein). All rock compositions are reported in wt.%, normalised and LOI-free.

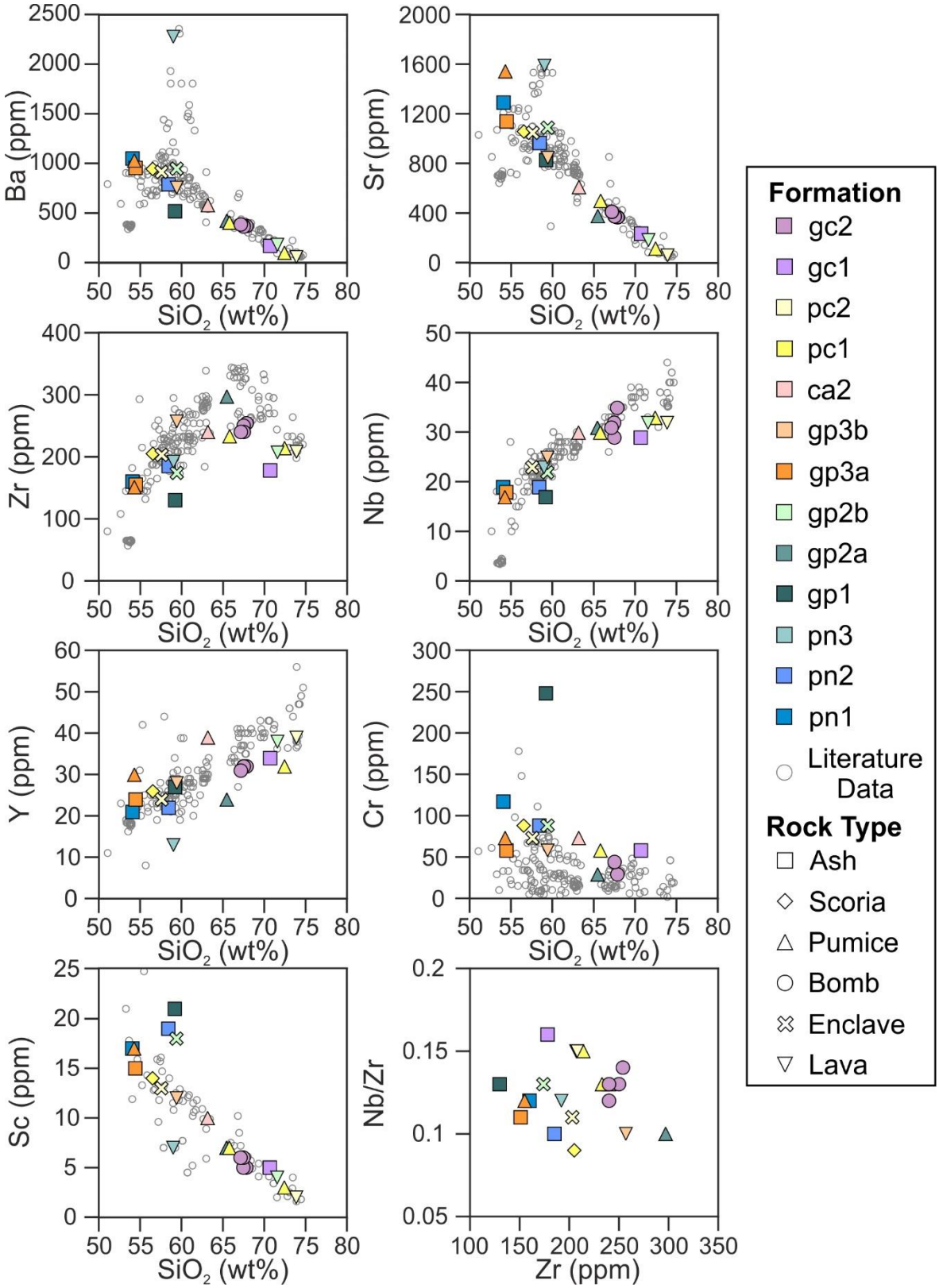

Fig. 2.7: Trace element variation diagrams versus SiO_2 covering the entire eruptive history of La Fossa di Vulcano, plotted with existing literature data (De Astis *et al.* 2013 and references therein). All rock compositions are reported in wt.%, normalised and LOI-free.

La Fossa di Vulcano comprises shoshonites, latites, trachytes and rhyolites. Shoshonites are found in the oldest deposits of Punte Nere 1, and intermediate Grotta dei Palizzi 3 formation dated at 1.6 – 1.5 ka (Frazzetta *et al.* 1985; Voltaggio *et al.* 1995). Through time eruptive products evolved to more silicic compositions, namely trachytes and rhyolites of Pietre Cotte 1 and 2 and Gran Cratere 1 and 2 formations. Furthermore, at La Fossa di Vulcano the eruptive products evolve during a single eruptive period, e.g., Pietre Cotte 1 and 2 formations, where the initial pyroclastic deposits were latites evolving to trachytes and finally the effusive rhyolitic lava flow with latitic enclaves.

Major element compositions of groundmass glass (Table 2.3) are similar to the whole-rock compositions in the samples. SiO_2 contents range from 53.10 to 73.54 wt.%, with the highest SiO_2 values in the obsidian lava flow of gp2b. Total alkalis range from 9.08 to 13.12 wt.%, with K_2O ranging from 5.27 to 8.29 wt.% and plot within the shoshonitic series. Groundmass glass analyses yield low S contents between 80 and 200 ppm, and Cl contents ranging from 1200 to 3930 ppm.

Melt inclusions in clinopyroxene phenocrysts yield SiO_2 contents ranging from 53.86 up to 69.02 wt.% (Table 2.4). Total alkalis range from, 8.59 up to 15.44 wt.%, with K_2O ranging from 4.82 to 9.71 wt.%, plotting within the shoshonitic series. Analysed melt inclusions have volatile contents ranging from 80 up to 469 ppm S and 2730 to 6530 ppm Cl.

Table 2.3: Analysed groundmass glass analyses for La Fossa di Vulcano arranged in stratigraphical order. b.d. below detection limit.

	pn1	pn1	pn1	pn2	pn2	pn2	pn2	pn2
Sample	AI-17-042	AI-17-042	AI-17-042	AI-18-058	AI-18-058	AI-18-058	AI-18-058	AI-18-058
wt.%								
SiO_2	56.24	55.11	54.92	58.16	58.21	58.4	57.89	58.4
TiO_2	0.57	0.6	0.55	0.54	0.54	0.52	0.53	0.53
Al_2O_3	17.5	17.35	17.42	17.41	17.44	17.36	17.35	17.36
FeO	5.53	5.96	5.92	5.62	5.47	5.36	5.55	5.38
MnO	0.13	0.11	0.13	0.14	0.13	0.11	0.13	0.12
MgO	1.56	2.29	2.28	1.54	1.28	1.24	1.41	1.27
CaO	3.65	4.58	4.79	3.03	2.98	2.94	3.13	2.89
Na_2O	5.11	4.71	4.62	4.5	4.64	4.67	4.63	4.62
K_2O	7.34	6.87	6.97	7.13	7.13	7.11	7.07	7.06
P_2O_5	0.6	0.6	0.58	0.46	0.4	0.38	0.39	0.37
Total	98.23	98.18	98.18	98.53	98.22	98.09	98.08	98
S	120	b.d.	120	80	80	80	120	b.d.
Cl	2500	2400	2500	2200	2200	2500	3200	2600
	pn2	gp1	gp1	gp1	gp1	gp1	gp1	gp1
Sample	AI-18-058	AI-17-073	AI-17-073	AI-17-073	AI-17-073	AI-17-073	AI-17-073	AI-17-073
wt.%								
SiO_2	58.1	62.43	62.64	62	62.59	62.18	62.45	62.53
TiO_2	0.53	0.5	0.52	0.51	0.51	0.51	0.5	0.52
Al_2O_3	17.36	15.85	16.03	15.86	15.96	16.04	15.93	16.01
FeO	5.41	4.73	4.79	4.75	4.73	4.75	4.78	4.69
MnO	0.12	0.1	0.11	0.09	0.09	0.1	0.1	0.08
MgO	1.31	1.16	1.19	1.28	1.21	1.21	1.11	1.05
CaO	2.91	2.44	2.41	2.73	2.47	2.52	2.46	2.35
Na_2O	4.66	4.12	4.15	4.13	4.17	4.16	3.96	4.19
K_2O	7.24	6.5	6.47	6.46	6.41	6.45	6.59	6.64
P_2O_5	0.39	0.37	0.4	0.38	0.36	0.4	0.39	0.37
Total	98.03	98.2	98.71	98.19	98.5	98.32	98.27	98.43
S	200	b.d.	b.d.	b.d.	b.d.	b.d.	b.d.	b.d.
Cl	2600	1600	1800	1600	1700	1200	1600	1700

Table 2.3 cont'd: Analysed groundmass glass analyses for La Fossa di Vulcano arranged in stratigraphical order. b.d. below detection limit.

	gp1	gp1	gp1	gp1	gp2a	gp2b	gp2b	gp2b
Sample	AI-17-073	AI-17-073	AI-17-073	AI-17-073	AI-17-057	AI-17-117b	AI-17-117b	AI-17-117b
wt.%								
SiO_2	62.34	62.03	62.16	62.12	60.61	72.98	73.14	73.53
TiO_2	0.51	0.52	0.51	0.51	0.4	0.14	0.14	0.15
Al_2O_3	15.79	16.05	16.06	15.77	17.98	13.67	13.61	13.71
FeO	4.78	4.73	4.82	4.77	3.76	2.01	1.94	1.9
MnO	0.1	0.09	0.09	0.1	0.13	0.06	0.06	0.06
MgO	1.16	1.2	1.18	1.13	0.69	0.13	0.12	0.11
CaO	2.46	2.54	2.4	2.44	1.85	0.7	0.8	0.66
Na_2O	3.99	4.08	4.08	4.07	4.83	3.44	3.54	3.37
K_2O	6.83	6.62	6.6	6.74	8.29	5.7	5.79	5.71
P_2O_5	0.37	0.36	0.36	0.38	0.17	n.a.	n.a.	n.a.
Total	98.33	98.22	98.26	98.03	98.71	98.83	99.14	99.19
S	b.d.	80	b.d.	b.d.	b.d.	b.d.	b.d.	b.d.
Cl	1500	1700	1400	1700	3930	3060	2980	3130
	gp2b	gp2b	gp2b	gp2b	gp2b	gp2b	gp2b	gp3a
Sample	AI-17-117b	AI-17-117b	AI-17-117b	AI-17-117b	AI-17-117b	AI-17-117b	AI-17-117b	AI-18-056
wt.%								
SiO_2	73.54	72.58	72.15	72.28	71.71	72.89	72.76	53.45
TiO_2	0.15	0.12	0.12	0.13	0.17	0.12	0.12	0.67
Al_2O_3	13.73	13.58	13.56	13.56	13.9	13.72	13.64	17.58
FeO	1.87	1.99	1.96	1.97	2.18	1.97	1.99	7.24
MnO	0.06	0.08	0.08	0.07	0.07	0.07	0.06	0.15
MgO	0.11	0.12	0.12	0.12	0.25	0.12	0.13	2.36
CaO	0.66	0.77	0.96	0.78	1.05	0.78	0.78	5.32
Na_2O	3.44	4.22	4.22	4.28	4.29	4.39	4.36	4.48
K_2O	5.93	5.93	5.82	5.91	5.96	5.74	5.83	6.21
P_2O_5	n.a.	n.a.	0.16	n.a.	0.07	n.a.	n.a.	0.56
Total	99.47	99.39	99.15	99.1	99.62	99.79	99.68	98.02
S	b.d.	b.d.	b.d.	b.d.	b.d.	b.d.	b.d.	160
Cl	2840	2700	2920	3060	3420	2750	2920	2900

Table 2.3 cont'd: Analysed groundmass glass analyses for La Fossa di Vulcano arranged in stratigraphical order. b.d. below detection limit.

	gp3a	gp3a	gp3a	gp3a	gp3a	gp3a	gp3a
Sample	AI-18-056	AI-18-056	AI-18-056	AI-18-056	AI-18-056	AI-18-057	AI-18-057
wt.%							
SiO_2	53.75	53.29	53.83	53.33	53.19	53.1	53.13
TiO_2	0.68	0.64	0.68	0.67	0.69	0.69	0.69
Al_2O_3	17.44	17.41	17.57	17.41	17.37	17.37	17.43
FeO	7.23	7.93	7.21	7.43	7.46	7.47	7.38
MnO	0.17	0.14	0.14	0.15	0.15	0.17	0.14
MgO	2.23	2.18	2.39	2.59	2.5	2.62	2.61
CaO	5.15	5.28	5.21	5.53	5.55	5.55	5.44
Na_2O	4.45	4.64	4.54	4.37	4.42	4.4	4.49
K_2O	6.33	6.3	6.22	6.05	6.11	6.2	6.29
P_2O_5	0.57	0.55	0.56	0.57	0.56	0.56	0.57
Total	98	98.36	98.35	98.1	98	98.13	98.17
S	120	80	160	80	120	80	160
Cl	3000	2500	2600	2400	2900	2700	3000
	pc1	pc1	pc1	pc1	pc1	pc1	
Sample	AI-17-021	AI-17-021	AI-17-021	AI-17-021	AI-17-025	AI-17-025	
wt.%							
SiO_2	72.1	70.96	67.99	72.46	66.9	67.36	
TiO_2	n.a.	n.a.	n.a.	n.a.	n.a.	n.a.	
Al_2O_3	13.61	15.12	14.26	14.43	17.98	16	
FeO	1.83	1.5	3.46	1.66	1.33	1.82	
MnO	0.07	n.a.	0.07	n.a.	n.a.	0.06	
MgO	0.09	0.07	0.2	0.07	0.11	0.12	
CaO	0.77	0.99	0.85	0.94	2.07	1.82	
Na_2O	4.22	4.57	3.53	4.8	5.96	5.27	
K_2O	5.69	5.54	8.12	5.27	5.37	5.57	
P_2O_5	n.d.	n.d.	0.06	n.d.	0.03	0.28	
Total	98.38	98.74	98.53	99.63	99.74	98.3	
S	b.d.	b.d.	b.d.	b.d.	b.d.	b.d.	
Cl	3520	2550	3500	2800	2040	2690	

Table 2.4: Analysed melt inclusion analyses in clinopyroxene for La Fossa di Vulcano arranged in stratigraphical order. b.d. below detection limit.

	gp2b	gp2b	gp2b	gp2b	gp2b	gp2b	gp2b	gp3a
Sample	AI-17-117b	AI-17-117b	AI-17-117b	AI-17-117b	AI-17-117b	AI-17-117b	AI-17-118c	AI-17-049-2
wt.%								
SiO_2	62.42	60.63	58.68	57.41	57.22	57.88	55.07	53.86
TiO_2	0.27	0.45	0.70	0.62	0.65	0.61	0.18	0.58
Al_2O_3	20.24	19.97	19.14	18.20	16.92	17.74	21.09	16.86
FeO	0.97	2.76	5.73	6.11	6.58	6.82	5.04	6.51
MnO	0.06	0.06	0.10	0.15	0.15	0.14	0.09	0.15
MgO	0.09	0.07	0.26	0.90	1.88	0.85	1.06	2.88
CaO	1.17	1.10	1.21	2.49	4.77	2.30	0.94	5.98
Na_2O	5.60	5.88	5.57	5.53	5.24	5.29	5.25	4.04
K_2O	8.41	8.50	8.07	7.57	6.44	7.63	8.99	6.95
P_2O_5	0.63	0.45	0.34	0.39	0.43	0.45	0.63	0.62
Total	99.86	99.86	99.78	99.36	100.29	99.70	98.33	98.42
S	b.d.	b.d.	b.d.	b.d.	b.d.	b.d.	b.d.	116
Cl	4200	4170	3750	3460	2990	3240	5050	2930
	gp3a	gp3b	gp3b	gp3b	gp3b	gp3b	pc1	pc1
Sample	AI-17-049	AI-17-045b	AI-17-045b	AI-17-045c	AI-17-045c	AI-17-045c	AI-17-011	AI-17-011
wt.%								
SiO_2	56.69	60.69	59.91	61.82	62.59	60.15	55.76	57.17
TiO_2	0.27	n.a.	n.a.	n.a.	n.a.	n.a.	n.a.	n.a.
Al_2O_3	20.66	21.59	21.03	20.35	19.98	21.48	17.36	21.02
FeO	4.97	1.05	0.43	0.72	0.70	0.64	4.58	2.12
MnO	0.09	0.00	0.00	0.00	0.00	0.00	0.07	0.00
MgO	0.31	0.11	0.04	0.06	0.05	0.06	2.48	1.25
CaO	1.70	1.01	0.76	1.04	0.87	0.88	4.27	1.63
Na_2O	4.65	6.31	5.73	6.15	5.86	6.63	7.96	5.67
K_2O	8.78	7.60	9.71	8.65	8.55	8.76	5.78	8.61
P_2O_5	0.68	0.75	0.73	0.45	0.42	0.71	0.28	0.86
Total	98.80	99.11	98.33	99.23	99.02	99.29	98.54	98.33
S	160	b.d.	160	b.d.	b.d..	b.d.	228	172
Cl	4100	4470	3640	4160	3870	4340	2730	3020

Table 2.4 cont'd: Analysed melt inclusion analyses in clinopyroxene for La Fossa di Vulcano arranged in stratigraphical order. b.d. below detection limit.

	pc1	pc1	pc1	pc1	pc1	pc1	pc1	pc1
Sample	AI-17-011	AI-17-011	AI-17-011	AI-17-011	AI-17-011	AI-17-011	AI-17-017	AI-17-017
wt.%								
SiO_2	56.93	58.77	58.96	57.07	58.91	56.63	54.45	56.45
TiO_2	n.a.	n.a.	n.a.	n.a.	n.a.	n.a.	n.a.	n.a.
Al_2O_3	18.08	17.99	17.73	18.28	18.13	14.83	13.25	18.98
FeO	4.22	5.51	5.37	5.50	5.26	6.57	9.74	5.43
MnO	0.10	0.10	0.10	0.11	0.11	0.18	0.21	0.11
MgO	2.08	0.79	0.94	1.24	0.77	3.74	5.19	1.24
CaO	3.98	1.87	2.14	2.50	1.87	6.53	8.14	2.92
Na_2O	5.37	5.62	5.13	5.05	5.18	4.30	3.78	4.99
K_2O	7.10	7.22	7.87	7.92	7.84	5.87	4.82	7.47
P_2O_5	0.58	0.39	0.43	0.40	0.40	0.26	0.17	0.40
Total	98.45	98.25	98.66	98.05	98.46	98.92	99.74	98.00
S	304	276	268	240	292	296	152	268
Cl	4620	4120	3480	3350	3840	2700	2720	3690
	pc1	pc1	pc1	pc1	pc1	pc1	pc1	pc1
Sample	AI-17-017	AI-17-017	AI-17-017	AI-17-017	AI-17-017	AI-17-019	AI-17-019	AI-17-019
wt.%								
SiO_2	56.56	57.93	58.15	58.38	56.11	58.74	58.92	58.21
TiO_2	n.a.	n.a.	n.a.	n.a.	n.a.	n.a.	n.a.	n.a.
Al_2O_3	18.69	17.82	17.57	17.21	17.82	17.63	17.46	17.47
FeO	5.56	5.69	5.57	5.84	6.30	5.65	5.78	5.78
MnO	0.09	0.11	0.13	0.12	0.15	0.15	0.11	0.13
MgO	1.35	1.20	1.36	1.40	1.38	0.97	0.95	1.14
CaO	3.14	2.74	3.02	2.99	2.95	2.21	2.35	2.70
Na_2O	5.02	5.05	4.63	4.66	5.27	5.08	4.94	4.90
K_2O	7.83	7.60	7.43	7.28	7.65	7.83	7.22	7.50
P_2O_5	0.43	0.35	0.33	0.41	0.48	0.38	0.44	0.43
Total	98.68	98.48	98.16	98.28	98.10	98.65	98.17	98.25
S	208	268	264	296	469	200	272	252
Cl	2980	3360	3240	3230	3180	3400	3610	3470

Table 2.4 cont'd: Analysed melt inclusion analyses in clinopyroxene for La Fossa di Vulcano arranged in stratigraphical order. b.d. below detection limit.

	pc1	pc1	pc1	pc1	pc1	pc1	pc1	pc1
Sample	AI-17-019	AI-17-019	AI-17-019	AI-17-019	AI-17-019	AI-17-019	AI-17-019	AI-17-021
wt.%								
SiO_2	58.32	57.84	60.03	58.36	58.70	58.15	59.06	59.21
TiO_2	n.a.	n.a.	n.a.	n.a.	n.a.	n.a.	n.a.	n.a.
Al_2O_3	17.56	17.80	18.80	17.46	17.57	17.60	17.13	20.15
FeO	5.38	5.55	3.31	5.59	5.57	5.73	5.74	3.05
MnO	0.13	0.13	0.07	0.13	0.13	0.12	0.14	0.07
MgO	0.98	1.06	0.69	0.99	0.94	1.02	1.01	0.27
CaO	2.36	2.54	1.86	2.49	2.58	2.49	2.37	1.24
Na_2O	5.26	5.05	5.46	5.30	5.26	5.05	4.78	5.63
K_2O	7.71	7.71	8.36	7.54	7.56	7.64	7.59	8.41
P_2O_5	0.33	0.39	0.41	0.38	0.34	0.40	0.40	0.25
Total	98.04	98.07	98.98	98.23	98.64	98.21	98.22	98.28
S	192	304	b.d.	268	208	280	224	124
Cl	3430	3130	3600	3210	3380	3070	3620	4390
	pc1	pc1	pc1	pc1	gc2	gc2	gc2	gc2
Sample	AI-17-021	AI-17-021	AI-17-025	AI-17-025	AI-18-074B	AI-18-074B	AI-18-074B	AI-18-074B
wt.%								
SiO_2	54.40	57.83	60.27	60.65	69.02	67.23	60.74	61.46
TiO_2	n.a.	n.a.	n.a.	n.a.	0.24	0.28	0.27	0.30
Al_2O_3	17.92	20.64	19.48	19.03	16.19	17.00	20.51	20.32
FeO	4.05	3.25	2.81	2.94	1.43	2.41	1.84	1.54
MnO	0.11	0.08	0.06	0.00	0.05	0.07	0.09	0.07
MgO	3.40	0.15	0.39	0.35	0.08	0.23	0.27	0.28
CaO	6.37	1.27	1.34	1.27	1.30	1.10	1.48	1.15
Na_2O	4.68	5.81	5.63	5.67	5.43	4.56	5.53	5.60
K_2O	7.06	8.88	8.35	8.36	6.35	6.70	8.41	8.46
P_2O_5	0.75	0.70	0.14	0.13	0.07	0.19	0.55	0.15
Total	98.72	98.60	98.46	98.40	100.16	99.77	99.69	99.33
S	144	132	b.d.	b.d.	b.d.	b.d.	160	280
Cl	6530	4940	3880	3660	2900	5700	3400	3500

Table 2.4 cont'd: Analysed melt inclusion analyses in clinopyroxene for La Fossa di Vulcano arranged in stratigraphical order. b.d. below detection limit.

	gc2	gc2	gc2	gc2	gc2	gc2
Sample	AI-18-074B	AI-18-074B	AI-18-074B	AI-18-074B	AI-18-078A	AI-18-078C
wt.%						
SiO_2	61.85	64.81	65.42	64.60	58.83	59.02
TiO_2	0.36	0.29	0.25	0.20	0.51	0.52
Al_2O_3	19.51	19.33	18.43	19.05	17.78	17.60
FeO	1.83	1.72	2.07	1.36	5.61	5.35
MnO	0.06	0.05	0.05	0.03	0.14	0.14
MgO	0.27	0.35	0.25	0.09	1.08	0.93
CaO	1.33	1.37	1.48	0.92	2.63	1.89
Na_2O	5.11	5.39	5.04	5.10	4.91	4.73
K_2O	8.64	6.78	6.71	8.07	7.22	7.75
P_2O_5	0.49	0.10	0.15	0.09	0.36	0.43
Total	99.45	100.19	99.85	99.51	99.07	98.36
S	240	240	80	240	320	200
Cl	3700	3400	4700	4100	3900	3400

2.4.4 Oxygen isotope data

New oxygen isotope data from mineral separates (clinopyroxene and feldspar) and volcanic glass from 21 samples of pumice, scoriae, breadcrust bombs, lavas and mafic magmatic enclaves are listed in Table 2.5. $\delta^{18}O$ values range from +6.0 ‰ to +6.7 ‰ (relative to SMOW) for clinopyroxene (n=19; Fig. 2.8), +7.0 ‰ to +8.1 ‰ for plagioclase feldspar (n=15; Fig. 2.8) and +8.3 ‰ to +8.7 ‰ for obsidian glass (n=2; Fig. 2.8).

$\delta^{18}O_{px}$ values are lower than $\delta^{18}O_{fsp}$ in all measured samples (Fig. 2.9A) where mineral pairs are available. To determine the $\delta^{18}O_{melt}$ it is assumed $\Delta_{fsp\text{-}melt}$ = +0.2 ‰ and $\Delta_{px\text{-}melt}$ = -0.3‰ (Kyser *et al.* 1981; Chiba *et al.* 1989). $\delta^{18}O_{fsp(melt)}$ = +6.8 ‰ to +7.9 ‰ and $\delta^{18}O_{px(melt)}$ = +6.3 ‰ to +7.0 ‰.

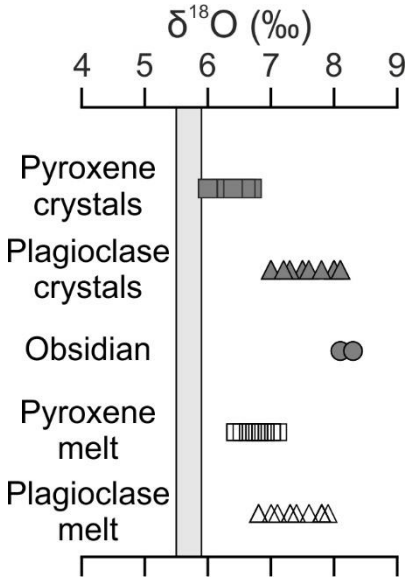

Fig. 2.8: Chart showing oxygen isotope variations in obsidians, mineral separates (pyroxene and feldspar), and their calculated melt compositions in La Fossa di Vulcano lavas and pyroclastics. The light grey shaded area is the $\delta^{18}O$ range for the mantle values (Bindemann 2008). To calculate $\delta^{18}O_{melt}$ it is assumed $\Delta_{fsp\text{-}melt}$ = +0.2‰ and $\Delta_{px\text{-}melt}$ = -0.3‰ (Kyser *et al.* 1981; Chiba *et al.* 1989). The calculated pyroxene melt values correspond to mantle ranges, however, plagioclase $\delta^{18}O$ crystal and melt values are elevated to the mantle range indicating the involvement of the crust during magmatic differentiation.

Oxygen isotope data from mineral separates are similar to previously reported whole-rock O isotope data (+6.3 ‰ to +8.4 ‰ from eruptive epoch 8; Ellam & Harmon (1990) and +6.1 ‰ to +6.3 ‰ for clinopyroxene from an enclave in the Pietre Cotte lava, De Astis *et al.* (2013)). $\delta^{18}O_{px}$ values overlap or are higher than values of mafic arc melts (+5.2 ‰ to +6.2‰; Eiler *et al.* 2000). Where available, mineral pairs (feldspar-clinopyroxene) have been used to identify whether they are in O-isotopic equilibrium. $\delta^{18}O$ values for clinopyroxene do not vary systematically with the degree of differentiation of the host rock (Fig. 2.9A). By contrast, $\delta^{18}O$ values for feldspar increase with the degree of differentiation of the host rocks (Fig. 2.9A). Feldspar-pyroxene isotherms have been calculated for temperatures of 600, 800, 1000, and 1200°C (Fig. 2.9B), using the calibration of Chiba *et al.* (1989). The range in $\Delta^{18}O_{fsp\text{-}px}$ for La Fossa is +0.4 ‰ to +2.0 ‰ (Fig. 2.9C). With increasing $\Delta_{fsp\text{-}px}$, $\delta^{18}O_{fsp}$ increases, however this increase is not entirely systematic (Fig. 2.9D). Conversely, no systematic variations are observed in $\delta^{18}O_{px}$ with increasing $\Delta_{fsp\text{-}px}$.

The highest values of $\Delta^{18}O_{fsp\text{-}px}$ and $\delta^{18}O_{fsp}$ are found in the most explosive eruptions from La Fossa (subplinian pumice and breadcrust bombs).

Table 2.5: Oxygen (O) isotope geochemistry for rock samples covering the entire stratigraphy of La Fossa di Vulcano arranged in stratigraphical order from oldest to youngest. To determine the $\delta^{18}O_{melt}$ it is assumed $\Delta_{fsp\text{-}melt}$ = +0.2‰ and $\Delta_{px\text{-}melt}$ = -0.3‰ (Kyser *et al.* 1981; Chiba *et al.* 1989). b.d. below detection limit n.a. not analysed.

	pn1	pn2	pn3	gp1	gp2a	gp2b	gp2b
Sample	AI-17-041	AI-18-058	AI-17-006	AI-17-073	AI-17-049	AI-17-117	AI-17-056
‰	Ash	Ash	Lava	Ash	Pumice	Lava	Enclave
$\delta^{18}O_{cpx}$	6	6.3	6	6.4	6.5	n.a.	6.4
$\delta^{18}O_{fsp}$	7.3	n.a.	8	n.a.	8.1	n.a.	8
$\delta^{18}O_{gl}$	n.a.	n.a.	n.a.	n.a.	n.a.	8.3	n.a.
$\Delta^{18}O_{fsp\text{-}cpx}$	1.3		2		1.6		1.6
$\delta^{18}O_{fsp\ (melt)}$	7.5		8.2		8.3		8.2
$\delta^{18}O_{cpx\ (melt)}$	5.7	6	5.7	6.1	6.2		6.1

	gp3a	gp3a	gp3b	ca2	pc1	pc1	pc1
Sample	AI-18-056	AI-18-057	AI-17-045	AI-17-034	AI-17-019	AI-17-021	AI-17-025
‰	Ash	Pumice	Lava	Pumice	Scoria	Pumice	Pumice
$\delta^{18}O_{cpx}$	6.4	6.2	6.6	n.a.	6.7	6.7	6.2
$\delta^{18}O_{fsp}$	7.5	7	7.5	7.3	7.2	n.a.	8
$\delta^{18}O_{gl}$	n.a.	n.a.	n.a.	n.a.	n.a.	n.a.	n.a.
$\Delta^{18}O_{fsp\text{-}cpx}$	1.1	0.8	0.9		0.5		1.8
$\delta^{18}O_{fsp\ (melt)}$	7.7	7.2	7.7	7.5	7.4		8.2
$\delta^{18}O_{cpx\ (melt)}$	6.1	5.9	6.3		6.4	6.4	5.9

	pc2	pc2	gc1	gc2	gc2	gc2	gc2
Sample	AI-17-009	AI-17-028	AI-17-070	AI-17-120	AI-18-072	AI-18-074	AI-18-076
‰	Lava	Enclave	Ash	Bomb	Bomb	Bomb	Bomb
$\delta^{18}O_{cpx}$	n.a.	6.3	6.3	6.6	6.4	6	6.3
$\delta^{18}O_{fsp}$	n.a.	7	7.2	7.7	n.a.	7.8	8.1
$\delta^{18}O_{gl}$	8.1	n.a.	n.a.	n.a.	n.a.	n.a.	n.a.
$\Delta^{18}O_{fsp\text{-}cpx}$		0.7	0.9	1.1		1.8	1.8
$\delta^{18}O_{fsp\ (melt)}$		7.2	7.4	7.9		8	8.3
$\delta^{18}O_{cpx\ (melt)}$		6	6	6.3	6.1	5.7	6

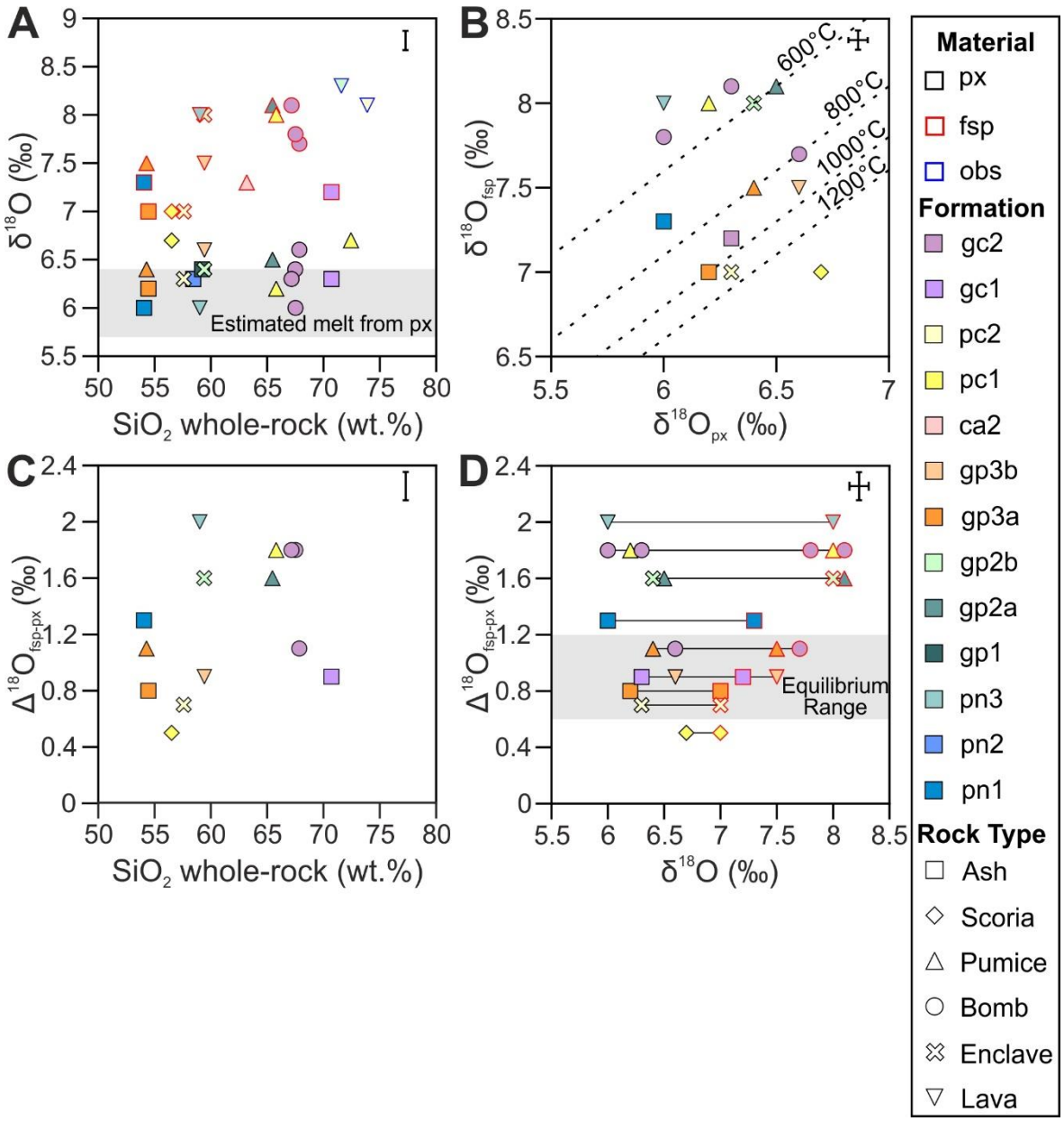

Fig. 2.9: (A) Plot of $\delta^{18}O$ (‰) versus SiO_2 (wt.%) from lavas, enclaves, pumice, scoria and breadcrust bombs with estimated clinopyroxene melt values identified. (B) Plot of $\delta^{18}O_{feldspar}$ (‰) versus $\delta^{18}O_{clinopyroxene}$ (‰) for La Fossa di Vulcano samples, where mineral pairs were available. Feldspar-pyroxene isotherms for 1200, 1000, 800 and 600 °C are shown. Isotherms were calibrated using Chiba *et al.* (1989), based upon an An_{55} component. (C) Plot of $\Delta_{feldspar\text{-}clinopyroxene}$ versus whole-rock SiO_2 (wt.%) for La Fossa di Vulcano. (D) $\Delta_{feldspar\text{-}clinopyroxene}$ versus mineral $\delta^{18}O$. All mineral pairs are connected by lines. Assuming an overall feldspar composition of $An_{50}Ab_{50}$, the equilibrium range for $\Delta^{18}O_{fsp\text{-}cpx}$ is 0.68 – 1.12 at temperatures between 800 and 1100°C. All O isotopes are reported relative to SMOW (Standard Mean Ocean Water).

2.5 Discussion

The wide range of rock compositions, textural variations and mineral disequilibrium observed in eruptive products from La Fossa di Vulcano, illustrate the complex evolution of the Fossa magma system. To constrain the evolution of the magmatic system of La Fossa di Vulcano, this study uses a combination of stable O isotopes and new pressure data from clinopyroxene crystal structure and chemistry to constrain the crystallisation conditions of clinopyroxene and feldspar to determine where and when contamination occurs in the magmatic system.

2.5.1 Intensive variables

2.5.1.1 Temperature

Magmatic temperatures are calculated for mineral phases in the same sample (clinopyroxene and feldspar) to deduce constrain crystallisation conditions and the order of crystallisation at La Fossa di Vulcano. Temperature calculations for clinopyroxene phenocrysts have been calculated using a clinopyroxene composition thermometer (equation 32d; Putirka 2008). The thermometer based solely upon clinopyroxene compositions is selected as the clinopyroxene phenocrysts are antecrystic in the more evolved products of La Fossa and not in equilibrium (Fig. 2.10) with their host melt in the more evolved products (latites, trachytes and rhyolites), therefore a thermometer independent of melt compositions was used. Calculated temperatures are 1153°C ± 8°C in shoshonite (n=18), 1130°C ± 37°C in latite (n=18), 1177 ± 7°C in andesite (n=12), 1124°C ± 23°C in trachyte (n=64) and 1117°C ± 19°C (n=24) in rhyolite, indicating clinopyroxene in rhyolites are antecrysts. The temperature range in all La Fossa deposits is ~200°C across all rock types, and the averages between the different rock types vary by ~60°C, indicating

there is significant overlap between rock compositions, which may indicate the clinopyroxene phenocrysts all crystallised from a primary shoshonitic/basaltic melt but not necessarily the same melt at the same pressure or depths, however crystallisation temperatures for clinopyroxene are still very high, suggesting clinopyroxenes are antecrysts.

Temperature calculations for plagioclase phenocrysts have been performed using a plagioclase-liquid thermometer (RiMG equation 26; Putirka 2005). Calculated temperatures are 1045°C ± 6°C in shoshonite, 1015°C ± 1°C in latite, 1003°C ± 1°C in trachyte and 964°C ± 1°C in rhyolite. Average crystallisation temperatures for plagioclase are always lower than clinopyroxene crystallisation temperatures in the same rock type. Feldspar temperatures systematically decrease in the more evolved rock types. However, in the more evolved rocks (trachytes and rhyolites) there is a larger temperature difference between feldspar and clinopyroxene, further suggesting clinopyroxene is antecrystic in the more evolved rocks and did not crystallise in equilibrium with feldspar in these rocks.

2.5.1.2 Pressure: Insights from clinopyroxene chemistry and structure

Variations in crystal structures (VCell and VM1) of clinopyroxene phenocrysts (Fig. 2.5) record differences in crystallisation pressures (depth), showing clinopyroxene nucleates at different depths in the magmatic system, with some eruptions, specifically the 1888-1890 eruption (gc2) spanning a wide range of pressures ~2 – 4 kbar, hence crystallisation depths (c. 7-14 km), indicating clinopyroxene crystallises throughout the system. The shoshonitic ash samples (pn1 and gp3a) yield the highest crystallisation pressures of all analysed samples (c. 6 kbar, c. 21 km, Fig. 2.5). There is no evidence in this study for clinopyroxene phenocrysts crystallisation at very shallow depths (< 5 km) or depths above 21 km. Therefore, clinopyroxene no longer crystallises in the more evolved magmas (rhyolites) at

shallow depths at La Fossa, indicating it is an antecrystic phase in the more evolved magmas. Maximum clinopyroxene crystallisation depths (c. 21 km) from shoshonitic ash samples are in agreement with previous works which propose a maximum depth of ~21 km in the mantle (Zanon *et al.* 2003; Peccerillo *et al.* 2006; Nicotra *et al*. 2018).

This detailed study of erupted products from La Fossa indicates clinopyroxenes in the different rock types crystallise at different pressures within the magmatic system within a single eruptive formation. For example, clinopyroxene phenocrysts in the ash, pumice, and lava from Grotta dei Palizzi 3 (gp3) all crystallised at different pressures. All analysed clinopyroxenes lie above the high-pressure field (12 kbar) defined by Manoli & Molin 1988). Our results show all analysed clinopyroxenes crystallised between c. 2 – 6 kbar (c. 7 – 21 km: Fig. 2.5). The error related to the calibration of the pressure lines is estimated to be 1-2 kbar. Our results show clinopyroxene from lavas crystallised between 3 and 4 kbar (11 – 14 km), whereas clinopyroxene from pyroclastic rocks crystallised over a range of pressures between 2 and 6 kbar (c. 7 – 21 km; Fig. 2.5). La Fossa lavas are situated within the range of Vulcano lavas proposed by Nazzareni *et al.* (2001), however pyroclastic deposits were not analysed in this study. The large pressure (hence depth) variation observed in pyroclastic deposits from La Fossa exceeds the range proposed by Nazzareni *et al.* (2001) for Vulcano lavas. The largest depth variations are observed in La Fossa pyroclastic deposits, indicating clinopyroxene in pyroclastic deposits crystallised over a relatively large range of pressure covering a large portion of the magmatic system. Conversely, clinopyroxene in the magmatic enclaves from gp2b and pc2 crystallised at a more restricted and shallower depth (< c. 14 km), suggesting that they originated from the same magma storage region which is also the source of clinopyroxene for the lavas and enclaves.

Furthermore, the magma which formed one of the oldest ash from La Fossa (pn2) contains clinopyroxene that crystallised at the greatest depth (c. 6 kbar, 21 km), and the magma forming the associated pumice comprises clinopyroxene that crystallised at shallower crustal levels (c. 5 kbar, 18 km). The magma forming the lava flow marking the end of this period of activity contains clinopyroxene that crystallised at a pressure of c. 4 kbar and depth of c. 14 km. This indicates a dynamic magma plumbing system beneath La Fossa, where there is a series of interconnected magma storage regions where magma recharge occurs into the more differentiated storage regions from deeper before the eruption. This is supported by the presence of glomerocrysts in many of the eruptive products from La Fossa di Vulcano. Therefore, eruptive products from a single eruption have different degrees of magmatic evolution e.g. from shoshonite to latite during Punte Nere activity and record different storage pressures and depths. This trend is also observed between the Pietre Cotte pyroclastic succession and lava flow. Clinopyroxene in shoshonites from La Fossa mainly crystallised at the greatest depths (up to 21 km), whereas in trachytes clinopyroxenes crystallised between 11 km and 18 km, and between 7 and 14 km in most latites (Fig. 2.5B).

Petrological and geochemical data from this study on clinopyroxenes from La Fossa show some are not in equilibrium with their host melt lying outside of the calculated equilibrium values (Fig. 2.10). The equivalent Mg# melt values for clinopyroxene phenocrysts have been calculated using whole-rock compositions, and clinopyroxene and liquid Mg# are plotted in the Rhodes diagram modified for clinopyroxene (Fig. 2.10).

Clinopyroxene equilibrium tests of Putirka (2008) based upon Fe-Mg exchange ($K_D(Fe\text{-}Mg)^{cpx\text{-}liq}$) show disequilibrium as analysed samples lie away from the 1:1 fully equilibrated line (Fig. 2.11). The $K_D(Fe\text{-}Mg)^{cpx\text{-}liq} = 0.28\pm0.08$ is based upon 1,245 experimental results (Putirka 2008). These results indicate clinopyroxene at La Fossa are in

disequilibrium with the host magmas they are located within, crystallising in primitive melts (e.g. shoshonites) further supporting our conclusion clinopyroxene are antecrysts in the more evolved products (trachytes) from La Fossa. The Rhodes diagram indicates clinopyroxene is in equilibrium with the more primitive melts from La Fossa (shoshonites – latites), however clinopyroxene equilibrium tests using observed and predicted clinopyroxene compositions suggest all rocks are in disequilibrium.

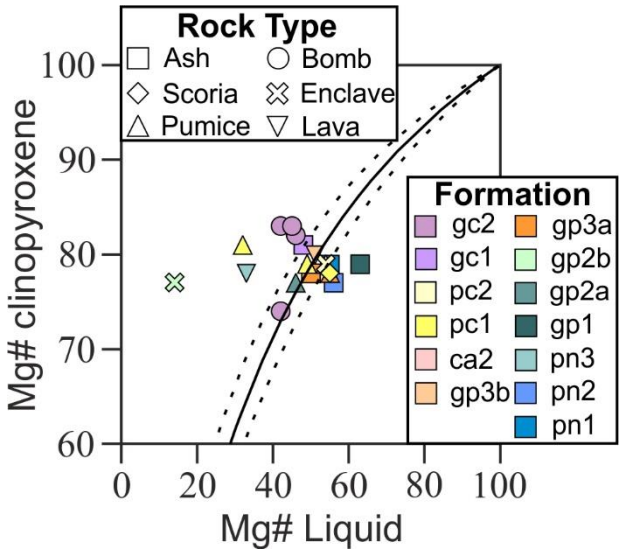

Fig. 2.10: Rhodes diagram. The $Mg\#_{clinopyroxene}$ values were calculated using an average of individual analyses for each sample (minimum 4 analyses). The $Mg\#_{liquid}$ is calculated from the Whole-rock liquid values. The solid line is the equilibrium line calculated using a $K_D(Fe\text{-}Mg)^{cpx\text{-}liq} = 0.28$ (Sisson & Grove 1993), and dashed lines are equilibrium ± 1σ.

It is proposed clinopyroxene crystallised from a shoshonitic crystal mush originating from the Vulcano shoshonite source located at the crust-mantle boundary which was remobilised and transported into the trachytic magma storage region, shown by well constrained $\delta^{18}O_{px}$ and contaminated $\delta^{18}O_{fsp}$ (~+8.0‰) at mid-crustal depths. This study concludes clinopyroxenes found in the trachyte crystallised at depths of c.14 km and were incorporated into the magma by magma mixing and mostly occur as antecrysts in the trachytes at La Fossa, whereas previous pressure estimates from Bullock *et al.* (2019) suggested the trachytic magma crystallised at depths of up to c. 23 km.

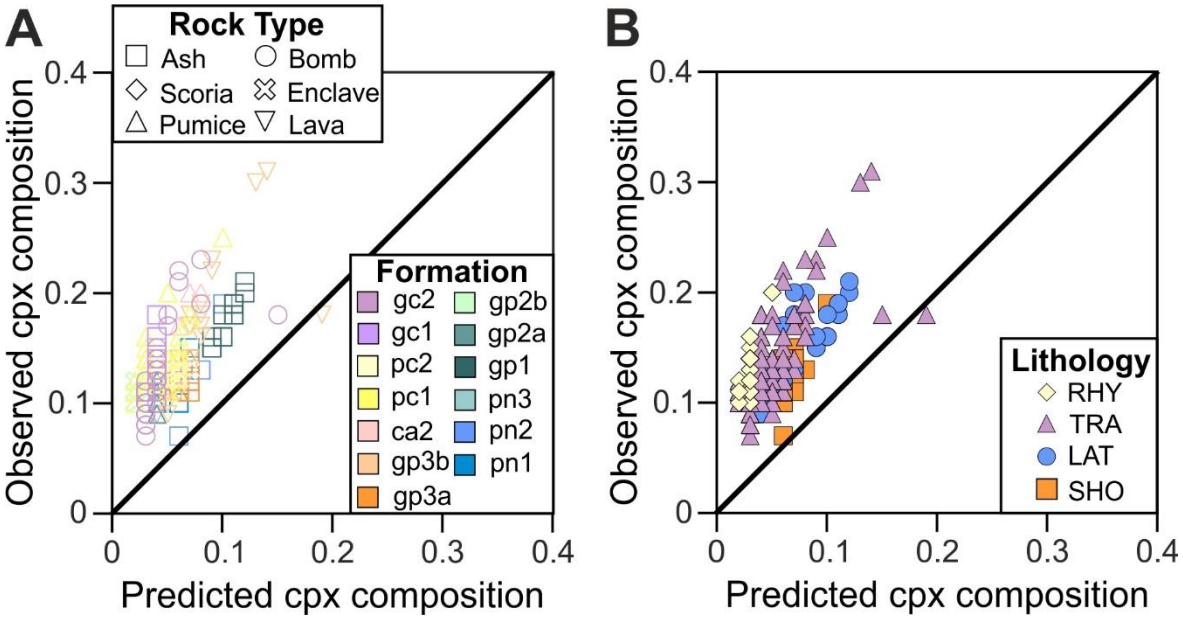

Fig. 2.11: Clinopyroxene equilibrium test based upon observed and predicted clinopyroxene compositions (KD(Fe-Mg) clinopyroxene-liquid) Data is identified based upon composition. The 1:1 line represents a fully equilibrated system between clinopyroxene and melt.

2.5.2 Magmatic processes at La Fossa di Vulcano

The interplay of complex dynamics and evolutionary processes during varying stages of magma ascent and evolution at La Fossa di Vulcano, results in the diversity of eruptive products observed. The plumbing system beneath La Fossa consists of multiple storage levels with several different independently evolving magma batches at variable depths from similar parental magmas (e.g. Clocchiatti *et al.* 1994; Zanon *et al.* 2003; Peccerillo *et al.* 2006; Piochi *et al.* 2009; De Astis *et al.* 2013; Paonita *et al.* 2013; Vetere *et al.* 2015; Mandarano *et al.* 2016; Nicotra *et al.* 2018; Bullock *et al.* 2019; Costa *et al.* 2020).

Eruptive products from La Fossa span a large compositional range (shoshonite to rhyolite) with abundant mixing and mingling textures and interactions with the underlying crust. Trends in major elements and Ba, Ni and Sr variation diagrams with increasing SiO_2 (Fig. 2.6) are indicative of fractional crystallisation processes, notably the fractionation of olivine, clinopyroxene and plagioclase, resulting in the increase in Al_2O_3 and incompatible

trace elements with the degree of differentiation. A positive correlation is also observed Zr with Nb indicative of fractional crystallisation in the La Fossa system.

To model fractional crystallisation, a simple mass balance fractionation model was produced using Olive (Cortés 2016). Olive (Cortés 2016) is a platform which produces simple mass balance fractionation models, by calculating changes in melt compositions using mass balance using weight proportions of known fractionated minerals in a melt. The input parameters for the model are summarised in Appendix A4. For the model, the starting composition has been recalculated as a 'dry' magma as the H_2O content is unknown and are based on fractionating 90% of the melt. The model results for Al_2O_3 and CaO are shifted to the left of the La Fossa di Vulcano data trends (Fig. 2.12), which indicates solely fractional crystallisation processes cannot be responsible for all of the observed trends in the data. A decrease in Al_2O_3, MgO, FeO and CaO with increasing SiO_2 are indicative of fractional crystallisation of plagioclase, olivine and clinopyroxene. The progressive decrease in CaO with SiO_2, is initially due to the crystallisation of clinopyroxene followed by the crystallisation of calcic plagioclase, resulting in the removal of both aliminium and calcium from the melt. The mass balance fractionation models using Olive, indicate fractional crystallisation alone does not account for the observed geochemical variations in the La Fossa di Vulcano suite. Instead, fractional crystallisation combined with other processes such as crustal contamination, partial melting and magma mixing are responsible for the observed trends in the suite.

Magma mingling is well-documented at La Fossa and is observed at macroscopic (enclaves) and microscopic (chemical zoning in minerals, particularly clinopyroxene and plagioclase) scales (De Astis *et al.* 1997; 2013; Nicotra *et al.* 2018; Bullock *et al.* 2019). Macroscale evidence for magma mingling is also observed in banded pumices, particularly in the pc1 pyroclastic succession. Microscale observations in this study show

compositional zoning and resorption textures of plagioclase and clinopyroxene phenocrysts, reflecting changes in the compositions of the melts the mineral phases crystallised from. Compositional zoning, resorption and dissolution and sieve textures in plagioclase have previously been studied in detail by Nicotra *et al.* (2018). Furthermore, oscillatory zoning in plagioclase reflects equilibrium crystallisation (Anderson 1984) at La Fossa. Conversely, plagioclase phenocrysts exhibit patchy cores and sieve textures in most deposits, with the exception of gc2, providing further evidence of disequilibrium, probably due to magma recharge events or decompression melting.

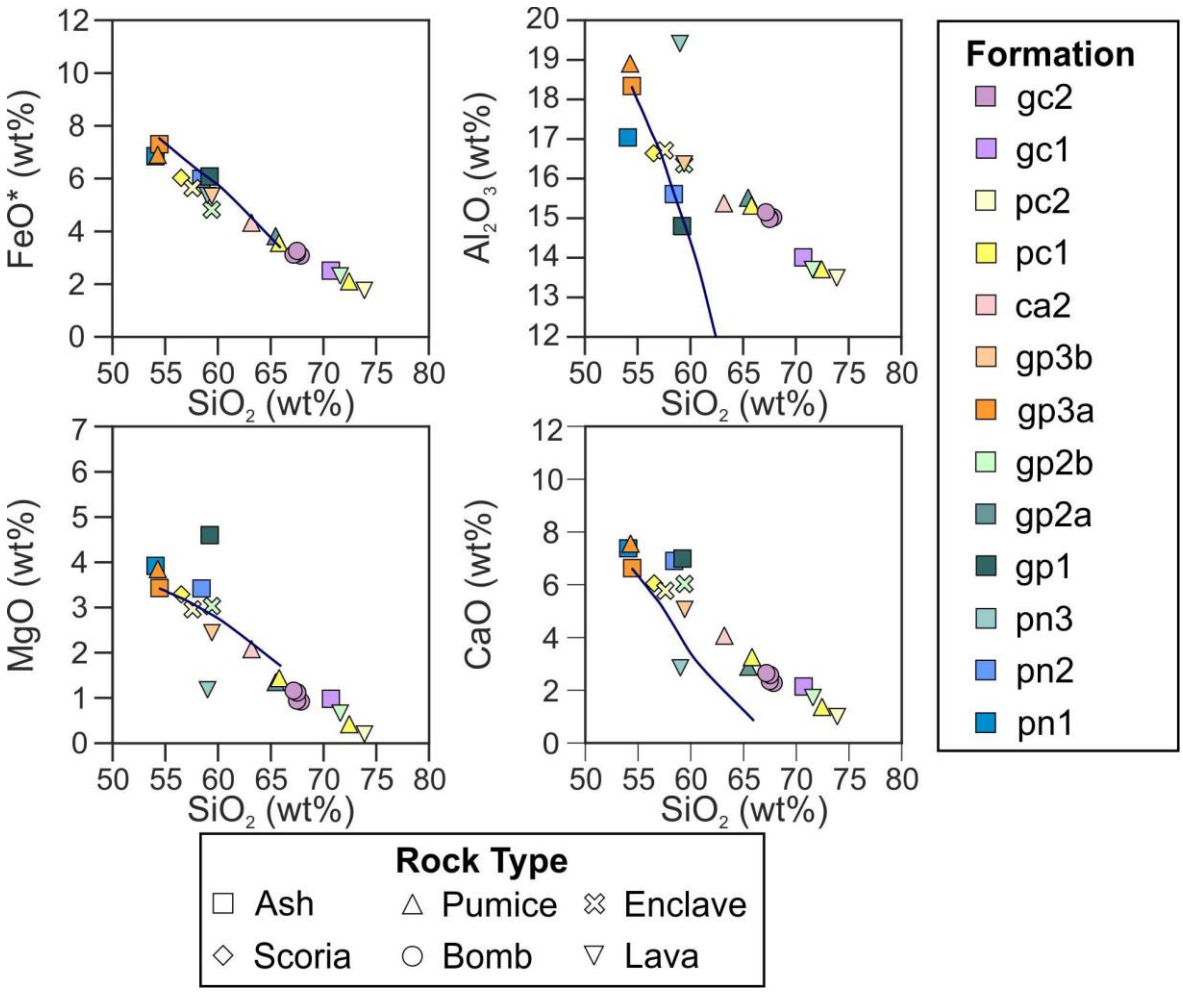

Fig. 2.12: Fractionation Model with major element variation diagrams versus SiO_2 covering the entire eruptive history of La Fossa di Vulcano. Model results are the solid dark blue lines. All rock compositions are reported in wt.%, normalised and LOI-free.

This study shows magmatic enclaves found within the gp2b and pc2 obsidian lava flows are more primitive (57.21 and 56.86 wt.% SiO_2 respectively; Fig. 2.2) than their host (70.92 and 73.34 wt. % SiO_2 respectively; Fig. 2.2). Furthermore, enclaves have abundant glomerocrysts and mineral disequilibrium textures (e.g. sieve textures and zoning), thus representing the influx of a mafic to intermediate magma from depth into a shallower magma storage region during mixing, replenishment, and mush remobilisation, not the physical mingling between two chemically distinct magmas.

Glomerocrysts are abundant in magmatic enclaves and their rhyolitic hosts from La Fossa (Bullock *et al.* 2019), however, they are also found in pyroclastic deposits and lava flows. Glomerocrysts are characterised by dominant mineralogy of plagioclase, clinopyroxene, olivine and magnetite. Textures observed throughout La Fossa eruptive products include mineral zonation in clinopyroxene, alkali feldspar and plagioclase, sieve textures in plagioclase and alkali feldspar and glomerocrysts indicate the presence of a series of interconnected, independently evolving magma batches at different depths, replenished by a deeper shoshonitic magma reservoir (Clocchiatti *et al.* 1994; De Astis *et al.* 1997; 2013; Del Moro *et al.* 1998; Zanon *et al.* 2003; Piochi *et al.* 2009; Nicotra *et al.* 2018). The presence of glomerocrysts across the entire compositional range of rocks erupted at La Fossa suggests the presence of dynamic crystal mush regions at varying depths in the plumbing system forming as a result of magma stagnation in a crystal mush zone, entraining the xenocrystic and antecrystic mineral phases during magma replenishment and remobilisation into the shallower storage regions.

2.5.3 Crustal contamination at La Fossa di Vulcano

This study is the first detailed mineral specific O isotope study of La Fossa di Vulcano magmatic system. Oxygen isotopes used in conjunction with petrological, textural, and geochemical data fit a model for crustal contamination at La Fossa. Oxygen isotopes from mineral separates and glass in this study are lower than those previously obtained whole-rock O isotopes from Ellam & Harmon (1990). This is due to the overestimation of $\delta^{18}O$ in whole-rock analyses in comparison to phenocrysts, as the groundmass is susceptible to alteration (Eiler *et al.* 2000). A general increasing trend is observed in $\delta^{18}O_{fsp}$ with increasing SiO_2 (Fig. 2.9A), indicative of the incorporation of crustal material into magma (Grunder 1987; Eiler *et al.* 2000). Previous isotopic studies conducted by Ellam & Harmon (1990) on lavas from Vulcano and the data from this study have steeper trends in $\delta^{18}O$ versus SiO_2 than that of closed system fractional crystallisation.

$\delta^{18}O$ values from all La Fossa samples of feldspar and clinopyroxene crystals are all higher or overlap with the field for mantle-derived crystals (+5.7‰ ± 0.2‰ (Bindemann 2008) indicating these mineral phases do not crystallise in the mantle, confirming crustal contamination is significant in the production of La Fossa magmas, specifically in the more evolved magmas. New data in this study suggest contamination dominates in the upper part of the system above 11 km (Fig. 2.5), the plagioclase nucleation depth proposed by Nicotra *et al.* (2018). This is also reflected in clinopyroxene antecysts, particularly in the more evolved products.

Clinopyroxene from the most primitive shoshonitic magmas from pn1 and gp3a at La Fossa yield $\delta^{18}O_{px}$ of +6.0 ‰ and +6.2 ‰ respectively and are in equilibrium with their host magma whole-rock compositions (Fig. 2.9), indicating clinopyroxene occurs as antecrysts in the magma. Higher $\delta^{18}O_{px}$ values (>6.5‰) occur in samples crystallising at shallower levels (~3 – 4 kbar; c. 12 – 16 km; Fig. 2.5; 2.13). This indicates contamination

of clinopyroxene dominates at mid-crustal levels. These $\delta^{18}O_{px}$ and $\delta^{18}O_{fsp}$ data in equilibrium have been used as a baseline for contamination at La Fossa and all $\delta^{18}O$ above this indicate a higher degree of contamination (Fig. 2.9D).

Ash erupted during pn2, gp3a and gc1 show the least contamination (lowest $\delta^{18}O_{fsp}$ +7.0 to +7.3‰) and pn2 and gp3a are among the most primitive products from La Fossa (shoshonites). Grotta dei Palizzi 1 to 3 ranges from $\delta^{18}O_{fsp}$ +7.0 to +8.1 ‰, the highest difference observed in all eruptions. Here, the latitic enclave of Grotta dei Palizzi 2b is the most contaminated, with a $\delta^{18}O_{fsp}$ value of +8.0‰ close that of the host glass (+8.3‰). Conversely, the latitic enclave from pc2 has a much lower $\delta^{18}O_{fsp}$ of +7.0‰, suggesting it is less contaminated. The latitic enclave has the same $\delta^{18}O_{fsp}$ and composition as the scoria from pc1, indicating they have the same degree of crustal contamination and crystallised from the same magma. It is proposed the latites from Grotta dei Palizzi and Pietre Cotte crystallised from storage zones with different degrees of crustal contamination. The largest variation in $\delta^{18}O_{px}$ and degree of differentiation (latite to rhyolite) is observed in Pietre Cotte from +6.2 to +6.7 ‰, with the highest values from the scoria. The most recent phase of eruptive activity from La Fossa shows a large variation in the extent of contamination, with the gc1 eruption ($\delta^{18}O_{fsp}$ +7.2‰) being far less contaminated than the 1888-90 (+7.6 to +8.0 ‰) eruption (gc2).

Further evidence for contamination and fractional crystallisation at La Fossa is observed in radiogenic isotopes which suggest contamination is a ubiquitous process in the most evolved magmas of La Fossa (Ellam *et al.* 1988; De Astis *et al.* 2013). An overall increasing trend is observed in $\delta^{18}O_{fsp}$ with the degree of evolution of the magma except for the Gran Cratere 1 (gc1) ash (Fig. 2.9A). $\delta^{18}O_{melt}$ values for feldspar range from +7.2 to +8.3‰ suggesting that this variation cannot be caused by fractionation of mineral phases alone. This suggests the more evolved products of La Fossa have a higher degree of crustal

contamination. The maximum $\delta^{18}O_{fsp}$ is the highest value (+8.1‰) of all magmatic crystals at La Fossa. The observed high $\delta^{18}O_{fsp}$ cannot be explained by closed system Rayleigh-style fractionation, which would only account for an increase < 1‰ (Sheppard & Harris 1985; Bindemann 2008).

2.5.4 Oxygen isotope equilibria

The difference in $\delta^{18}O$ values for feldspar and clinopyroxene show clinopyroxenes are in isotopic disequilibrium in the latites and trachytes (Fig. 2.9C), further providing evidence that clinopyroxene are antecrysts in these rocks and crystallised in different portions of the plumbing system undergoing varying degrees of crustal contamination. Variations in O isotopes from this study and previous petrological and geochemical studies (e.g. Clocchiatti *et al.* 1994; Zanon *et al.* 2003; Piochi *et al.* 2009; De Astis *et al.* 2013; Nicotra *et al.* 2018; Bullock *et al.* 2019; Costa *et al.* 2020) indicate a series of open system processes e.g. magma mixing, replenishment, fractional crystallisation (and AFC), operating within La Fossa magmatic system. Ellam & Harmon (1990) analysed two crustal contaminants yielding O isotope values of +10.7‰ and +7.9‰ respectively. The large variation observed in $\Delta_{fsp\text{-}px}$ indicates feldspar and clinopyroxene exhibit a large degree of disequilibrium.

Feldspar-pyroxene isotherms (Fig. 2.9B) corroborate isotopic disequilibrium between the two mineral phases as some of the mineral pairs plot below the 800°C isotherms and a limited number at temperatures above the 1200°C, which is unrealistic at La Fossa based upon calculated crystallisation temperatures from this study and others (e.g. Nicotra *et al.* 2018; Bullock *et al.* 2019; Costa *et al.* 2020). No systematic trends are observed in $\delta^{18}O$ in clinopyroxene, feldspar and obsidian with stratigraphy at La Fossa, however systematic

trends are observed between $\delta^{18}O$ in clinopyroxene, feldspar and obsidian n with the degree of differentiation and eruptive products.

Mineral pairs (clinopyroxene-feldspar) from gp3a gp3b, pc2 enclave, gc1, and one breadcrust bomb from gc2 show they are in isotopic equilibrium, whereas all other available mineral pairs are in isotopic disequilibrium. Samples exhibiting isotopic disequilibrium between plagioclase and clinopyroxene (Fig. 2.9D; pn1, pn3, gp1, gp2b enclave, pc1, and gc2) crystallised at pressures < 3 kbar (< 11 km depth), which is consistent with the remobilisation of a clinopyroxene-rich crystal mush prior to eruption. Unit Cell Volume (VCell) and the volume of the M1 site occupancy (VM1) both generally increase with increasing $\delta^{18}O_{cpx}$ (Fig. 2.13), above +6.1‰. As the cell parameters are a proxy to depth the progressive increase in $\delta^{18}O_{cpx}$ with increasing VCell and VM1 suggest crustal contamination increases with decreasing pressure (depth) in the system. The three samples with $\delta^{18}O_{cpx}$ +6.0‰ (from Punte Nere1, Punte Nere 3 and Gran Cratere 2) yielded the lowest pressure estimates, less than < 3 kbar, indicating they crystallised shallower in the magmatic system.

To further assess which samples are in chemical equilibrium, this study used $\Delta^{18}O_{fsp\text{-}cpx}$ and $\Delta Mg\#_{clinopyroxene\text{-}liquid}$ (Fig. 2.14). Assuming an overall feldspar composition of $An_{50}Ab_{50}$, the equilibrium range for $\Delta^{18}O_{fsp\text{-}cpx}$ is 0.68 – 1.12 at temperatures between 800 and 1100°C. The calculated equilibrium range for $Mg\#_{clinopyroxene\text{-}liquid}$ is between 24 and 33, assuming Mg# is 80 for clinopyroxene. The results show samples that are in O isotopic equilibrium are also in Mg# equilibrium, however the reverse is not always true as some samples in Mg# chemical equilibrium are not in O isotopic equilibrium e.g. pumices from gp2a and pc2. Therefore, the Rhodes diagram modified for clinopyoxene based upon chemical equilibrium tests using Mg# of clinopyroxene and liquids is more applicable at La Fossa where some clinopyroxenes are in equilibrium with their host melt.

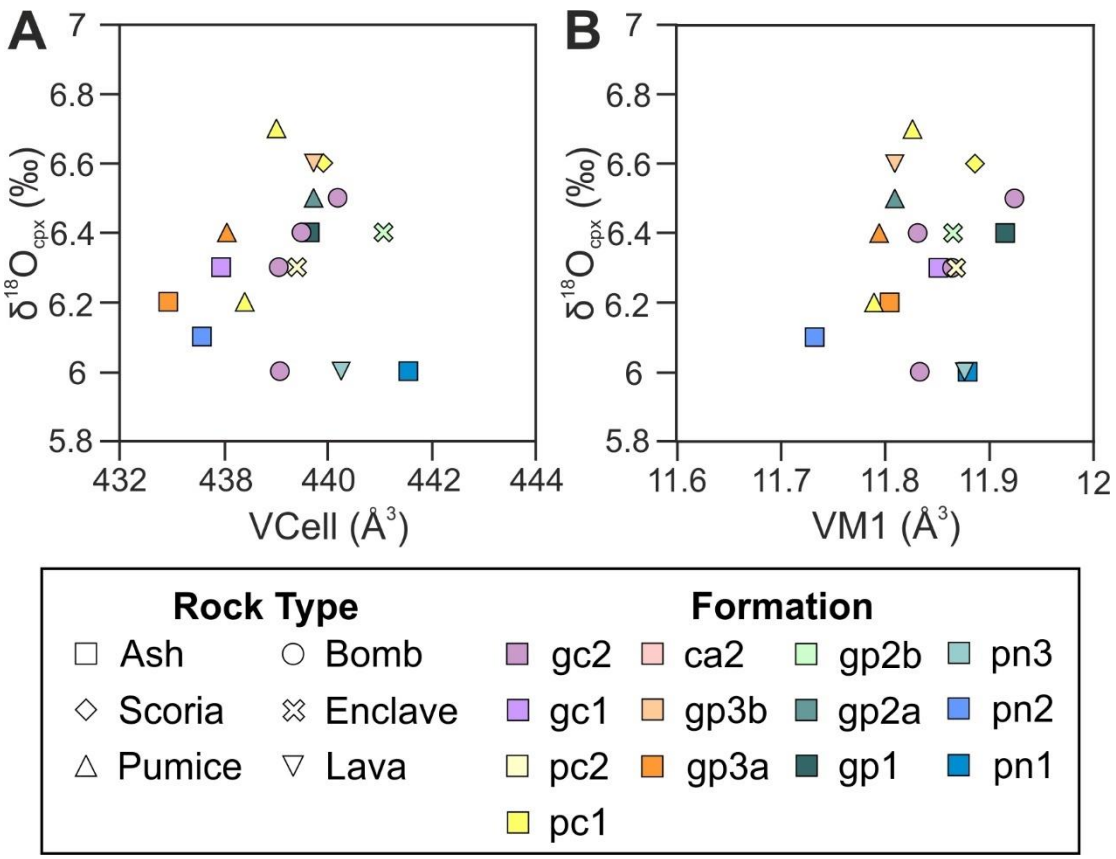

Fig. 2.13: (A) Plot of VCell (Å) versus $\delta^{18}O_{cpx}$ (‰). (B) Plot of VM1 (Å) versus $\delta^{18}O_{cpx}$ (‰).

Using all mineral pairs available, this study shows samples from gp3a, gp3b, pc2, gc1 and one sample from gc2 lie within the calculated field for O isotopic and Mg# chemical equilibrium (Fig. 2.14). However, it can be assumed the other sample from gp3a, along with pn1 and pc1 scoria are also in equilibrium as they lie within the calculated error range. Some samples display large degrees of O isotopic and Mg# chemical disequilibrium (e.g. pn3 lava, gp2b enclave and two gc2 breadcrust bomb samples) however, the trend in the degree of disequilibrium is not systematic. Conversely, 2 pumice samples from gp2a and pc1 both lie within the Mg# equilibrium range, however exhibit O isotope disequilibrium. The feldspars analysed from these samples have more sodic compositions, resulting in an increase in $\Delta^{18}O_{fsp\text{-}cpx}$ therefore explaining the observed isotopic disequilibrium.

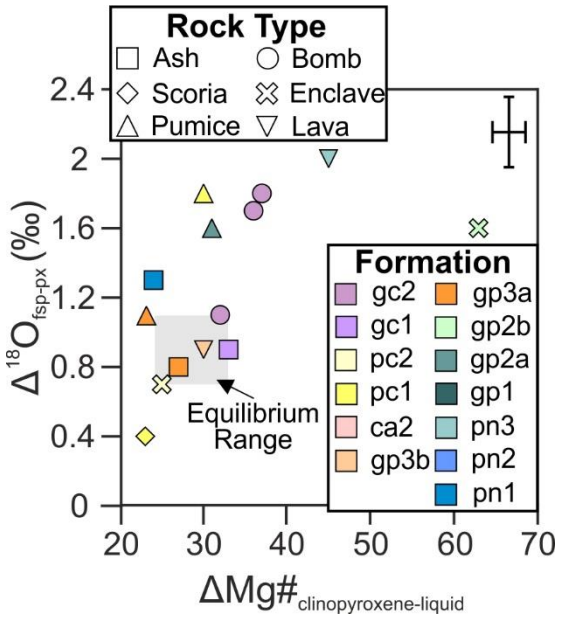

Fig. 2.14: Equilibrium plot of $\Delta_{feldspar\text{-}clinopyroxene}$ versus $\Delta Mg\#_{clinopyroxene\text{-}liquid}$. The calculated equilibrium range is highlighted in light grey. The calculated equilibrium range for $Mg\#_{clinopyroxene\text{-}liquid}$, assuming Mg# is 80 for clinopyroxene, is between 24 and 33.

2.5.5 La Fossa magma plumbing system

It has long been accepted a shoshonitic magma resides in the lower crust (Gioncada *et al.* 1998; Zanon *et al.* 2003; De Astis *et al.* 2013; Fusillo *et al.* 2015; Nictora *et al.* 2018; Bullock *et al.* 2019) at a depth of 18 - 21 km (Nicotra *et al.* 2018). This 'parental' shoshonitic magma feeds all other magma storage zones beneath La Fossa and is the source of clinopyroxene phenocrysts. Previous textural, geochemical and geobarometric investigations identified mid-crustal storage region located between 12.5 and 16.8 km (De Astis *et al.* 2013; Fusillo *et al.* 2015), a latitic reservoir at 3 km and a rhyolite reservoir at 1-2 km depth (Pecerrillo *et al.* 2006; Paonita *et al.* 2013). Micro-textural and geochemical studies on plagioclase crystals recorded magma ascent, recharge, and mixing processes in the Fossa magmatic system in the last 1000 years identified three magma storage zones located between 2 and 17 km (Nicotra *et al.* 2018). More recent studies focusing on the Pietre Cotte lava (pc2) proposed shoshonitic – trachytic storage regions located in the crust (~15 - 20 km, ~7 km and ~5 km depth) and a disturbed crystal mush resulting from magma

recharge and/or partial melting located at 20 km responsible for glomerocryst formation (Bullock *et al.* 2019). Glomerocrysts are common in all La Fossa products and originate from mush zones which are remobilised by mafic magma injection (Bullock *et al.* 2019) into a shallower crystal mush zone representing the leftover material from this process.

Through the utilisation of new, geochemical, thermobarometrical, isotopic data and a synthesis of current literature data an updated model for the evolution of La Fossa di Vulcano magmatic system is proposed, identifying the different magmatic processes which dominate at different magma storage levels within the subvolcanic basement and the role of the magma plumbing system in the different eruptions of La Fossa, including magma mingling, AFC processes, and mush remobilisation. This study suggests magma mingling between latitic and rhyolitic end members and remobilisation of the crystal mush dominate at intermediate crustal levels and AFC processes dominate in the shallower rhyolitic magmas.

The presence of several interconnected magma reservoirs beneath La Fossa di Vulcano is widely accepted (Clocchiatti *et al.* 1994; Paonita *et al.* 2002; 2013; Zanon *et al.* 2003; Peccerillo *et al.* 2006; Piochi *et al.* 2009; De Astis *et al.* 2013; Mandarano *et al.* 2016; Nicotra *et al.* 2018; Bullock *et al.* 2019). This study suggests the interconnected reservoirs result in the diversity of erupted deposits observed from one single eruption. For example, erupted products from pc1 range from shoshonite to rhyolite with the highest $\delta^{18}O$ values in the rhyolitic obsidian and pumice, and a range of $\delta^{18}O$ in feldspar (+7.2‰ to +8.0‰) and pyroxene (+6.2 ‰ to +6.7 ‰) from the pc1 eruption, indicating the eruption did not originate from one single reservoir, and instead originated from several reservoirs located beneath La Fossa. This injection of shoshonitic magma into shallower magma storage regions (latites and rhyolites) beneath La Fossa over short timescales may be an eruption trigger. This model is similar to that proposed by Bullock *et al.* (2019) for the succeeding

Pietre Cotte lava flow. Therefore, magma injection from depth triggered the pc1 eruption, due to the eruption of latite at the beginning of the eruption, followed by the eruption of a trachytic pumice then rhyolitic pumice (Fig. 2.15). The injection of mafic magma and consequent mixing into more evolved storage regions (e.g. trachytic reservoir) resulted in chemical disequilibrium in the trachytic portion of the system, through the incorporation of clinopyroxene from the primitive magmas in rhyolites. Magma influx from deeper parts of the system incorporates antecrystic clinopyroxene (Fig. 2.15), and large plagioclase xenocrysts in chemical disequilibrium with the surrounding magma, evidenced by resorbed cores and dissolution textures, described by Nicotra *et al.* (2018).

This study concludes clinopyroxenes in the trachytes of La Fossa are antecrystic with limited variation in $\delta^{18}O_{px}$, and highest $\delta^{18}O_{fsp}$ representing the storage region where the largest amount of interaction with crustal lithologies occurs. Conversely, the shoshonites have limited ranges in $\delta^{18}O_{px}$ and $\delta^{18}O_{fsp}$ and are closer to that of mantle-derived values suggesting they are less contaminated. This study indicates the latites and trachytes of La Fossa are the most contaminated products, indicating contamination dominates at mid-crustal levels. Consequently, clinopyroxene crystals found in La Fossa deposits crystallised in the shoshonitic magmas, located at different depths within the magmatic system. At least two distinctive cumulate mushes are present beneath La Fossa di Vulcano, the deepest mush zone located at depths of up to 6 kbar (c. 21 km) which is directly fed by the shoshonitic magma. This mush zone feeds a smaller mush region located in the upper crust (c. 3 – 4 kbar; 11 – 14 km; Fig. 2.5; 2.14). However, Bullock *et al.* (2019) suggest a deeper mush zone is located at depths of 28 km). Glomerocrysts and antecrysts originating from the cumulate mush regions are incorporated into the shallower magma storage regions. Clinopyroxene is incorporated into erupted products originating from the shallower sections of La Fossa's magmatic system during magma recharge events and the remobilisation of a dynamic cumulate mush (< 3 kbar, c. 11 km) into the trachytic and

latitic magmas, possibly as a result of magma recharge events transporting it into shallower magma storage regions, entraining and incorporating antecrystic clinopyroxene and glomerocrysts in erupted products.

The largest depth variations in clinopyroxene are observed in the explosive volcanic eruptions (Fig. 2.5), namely gc2 blocks and bombs. Compositionally, using major element geochemistry, the erupted products from the 1888-90 eruption are almost identical, however their $\delta^{18}O_{px}$ and $\delta^{18}O_{fsp}$ vary considerably from +6.0 to +6.5‰ and +7.6 to +8.0‰ respectively. Elevated values of $\delta^{18}O_{fsp}$ coupled with a large range in clinopyroxene pressures suggests the 1888-90 eruption occurred as a result of the influx of magma from a deeper magma storage zone in the interconnected system. The influx of shoshonite from depth remobilised mineral phases, namely clinopyroxene in the crystal mush entraining it with the magma into shallower parts of the system (trachyte). This suggests the most explosive eruptions of La Fossa may be triggered by the influx of magma from depth for example, during the Pietre Cotte (pc) eruption where initial erupted products are scoria (55.46 wt. SiO_2) evolving to rhyolite (73.34 wt. SiO_2). La Fossa eruptions were triggered by the influx of the shoshonitic magma and subsequent mingling between the two chemically distinct magmas. This is observed in erupted products and rock compositions observed for example mingled pumice at the top of the pyroclastic pc1 succession, highlighting the importance of magma influx and mingling as eruption triggers.

Using the results obtained in this study, a model for the magmatic evolution of La Fossa di Vulcano is presented consisting of a ‘parental’ shoshonitic magma, several magma storage zones, and cumulate mush regions, summarised below (Fig. 2.15; 2.16).

1. A ‘parental’ source shoshonitic of all magmas of La Fossa. This is the region of primary clinopyroxene crystallisation, where values of $\delta^{18}O_{px}$ are elevated with respect to mantle-derived values (+5.7‰; Bindemann 2008), resulting from source contamination (Chapter 4) or contamination in the lower crust.
2. Mafic cumulate mush zone located at depth of 21 km, possibly extending up to 28 km (Bullock *et al.* 2019). This region is fed directly by the shoshonitic magma and forms the antecrystic clinopyroxene observed in most La Fossa deposits. This region also forms glomerocrysts of clinopyroxene, olivine, magnetite, and feldspar.
3. Shoshonitic to latitic magma storage region linked to the source region, forming the explosive pumice and ash of pn1, pn2, gp1, gp3 enclaves, gc1 and gc2. In this region, clinopyroxene phenocrysts are in equilibrium with their host shoshonitic melt. These phenocrysts were then incorporated as antecrysts into other La Fossa products through crystal recycling in the magmatic system.
4. A smaller cumulate mush region is located below the latitic-trachytic storage region, with antecrysts of feldspar and clinopyroxene. Antecrysts are incorporated into the replenishing magma into the latitic-trachytic magma located above the mush.
5. Located above this is a secondary latitic-trachytic magma located within a shallow antecryst dominated mush zone incorporating quartz restites into the eruptions of pn3 and gp3b, scoria of pc1, pumices of gp2a, gp3a, gc1 and gc2. This zone also forms many of the enclaves found in the rhyolitic eruptions. The latitic – trachytic storage zone is the region in which the largest degree of contamination, hence interaction with crustal lithologies occurs at La Fossa, with the highest values of $\delta^{18}O_{fsp}$ (up to +8.1‰) and $\delta^{18}O_{px}$ (up to +6.6‰).
6. A Rhyolitic magma storage region located < 5km, associated with the obsidians of gp2b and pc2, and rhyolitic pumices of pc1. The banded white pumices at the top

of the pc1 pyroclastic succession show a mafic magma was injected into the rhyolitic magma just prior to the eruption. The abundant latitic enclaves found throughout both obsidian lava flows indicate mingling of the latite with the host rhyolite prior to eruption.

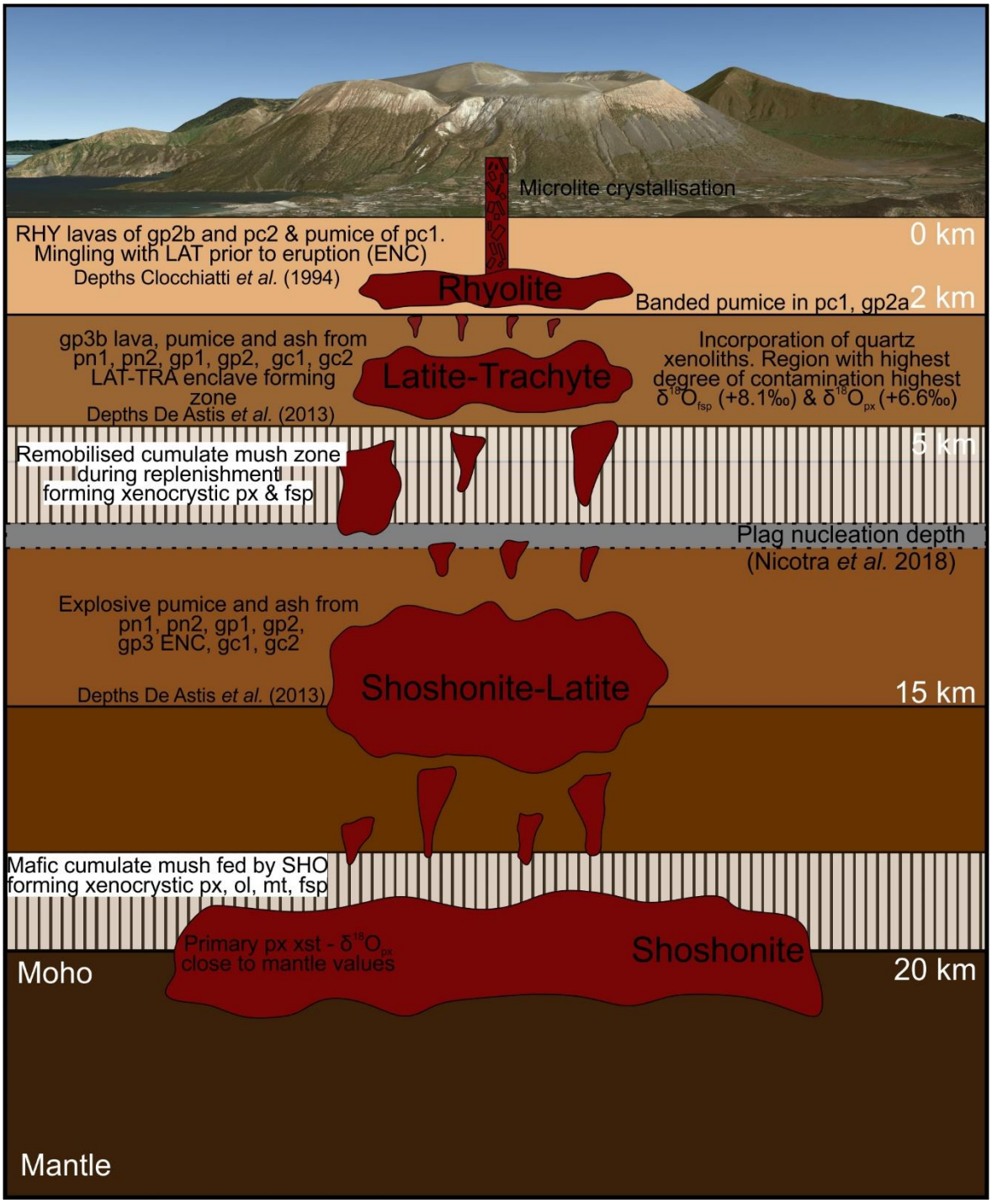

Fig. 2.15: Schematic model showing the geochemical evolution of the magma plumbing system of La Fossa di Vulcano, over the last 5.5 kyr. Modified from Nicotra *et al.* 2018.

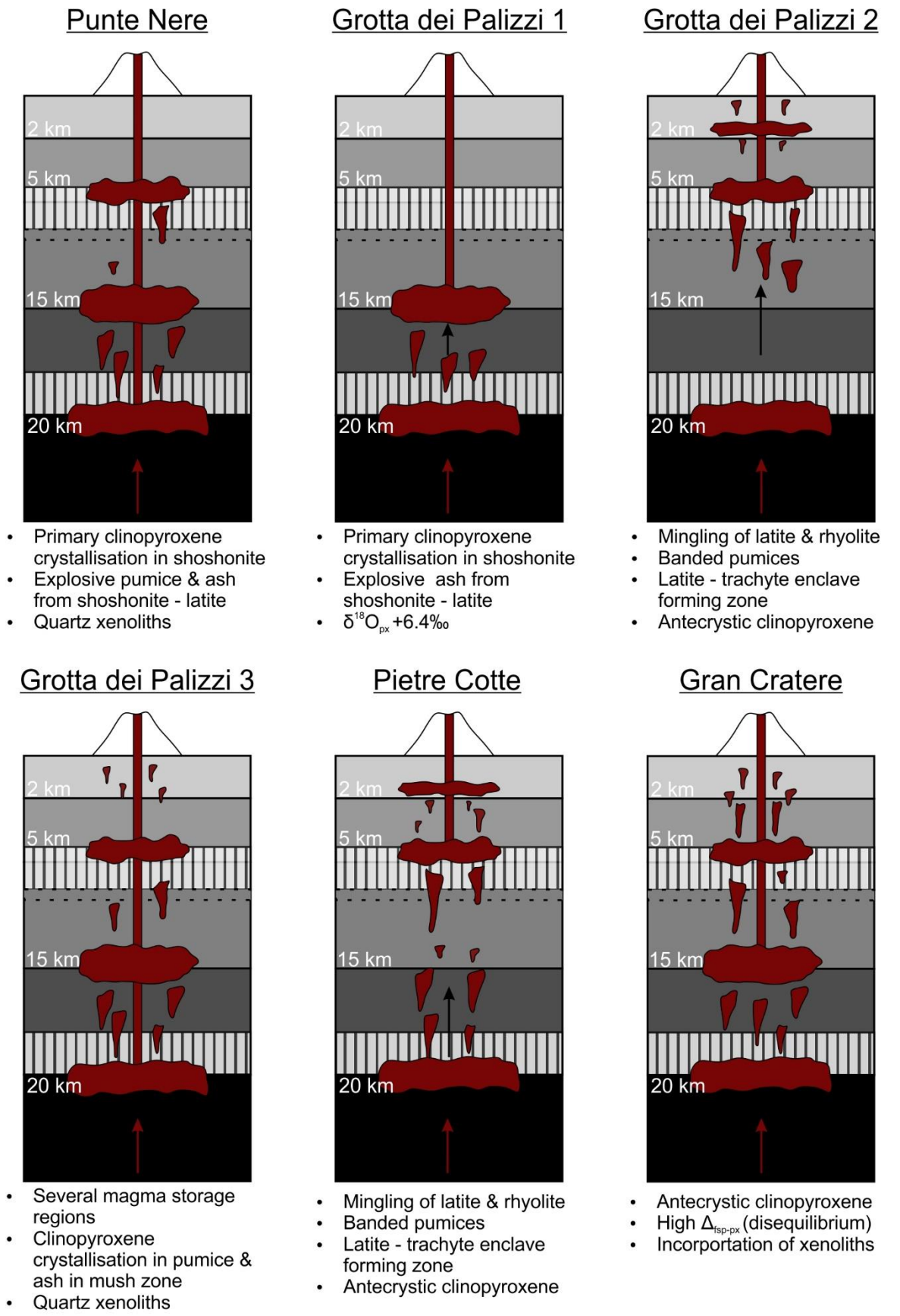

Fig. 2.16: Sketch model showing the evolution of the magma plumbing system of La Fossa di Vulcano, over the last 5.5 kyr.

2.6 Conclusion

This study contributes a stratigraphically controlled mineral and volcanic glass oxygen isotope dataset to help constrain the evolution of La Fossa. Oxygen isotopes, petrological and textural observations, whole-rock major and trace element geochemistry, mineral chemistry and structure, and geochemical modelling indicate crustal contamination is a ubiquitous process in the latitic to trachytic storage region beneath La Fossa. We show that:

- The highest degrees of crustal contamination occur in the intermediate to evolved (latites to rhyolites) products of La Fossa where clinopyroxene occurs as an antecrystic phase.
- Clinopyroxene crystallises over a range of depths from c. 7 – 21 km, within a series of dynamic crystal mush zones which are remobilised during recharge events and incorporated into the intermediate to evolved (latitic to rhyolitic) magma storage regions.
- The highest degree of isotopic disequilibrium between mineral pairs is observed in intermediate to evolved erupted products (e.g. pn3, pc2, gp2a, gc2), corresponding to clinopyroxene crystallisation depths of 7 to 11 km, consistent with the remobilisation of a clinopyroxene dominated crystal mush.

This study proposes an updated plumbing system model which identifies a series of interconnected magma storage regions and remobilised crystal mush zones responsible for the evolution of dynamic, constantly evolving La Fossa di Vulcano magmatic system.

CHAPTER 3 - Shallow conduit processes leading up to the 1888-1890 Vulcanian eruption of La Fossa di Vulcano

3.1 Introduction

Vulcanian eruptions are characterised by discreet, short-lived explosions (seconds to minutes), erupting relatively small magma volumes (<1 km^3; Clarke *et al.* 2015). They are typically associated with the eruption of breadcrust bombs and blocks close to the vent, pyroclastic density currents (PDCs) and thin ash fall (Walker 1969), frequently associated with the destruction of lava domes. Large-magnitude Vulcanian explosions are frequently accompanied by large SO_2 gas fluxes (>30 kg/s; Edmonds & Herd 2007) and more importantly, they are associated with the injection of volatile-rich magmas into a low permeable volcanic plug (e.g. Clarke *et al.* 2007; Williamson *et al.* 2010; Wright *et al.* 2012). These eruptions are renowned for being extremely hazardous, particularly because they are unpredictable, and it is therefore imperative to understand the emplacement and evolution of magma plugs that are typically fractured during more violent Vulcanian explosions (Sparks 1997; Voight *et al* 1998; Wright *et al.* 2007; Clarke *et al.* 2007; Burgisser *et al.* 2010; 2011). The driving factors of Vulcanian eruptions have been the subject of extensive research in recent years through detailed geochemical and textural studies focused upon conduit processes leading up to and during eruptions (e.g. Clarke *et al.* 2007; Wright *et al.* 2007; Burgisser *et al.* 2010; 2011; Cassidy *et al.* 2015; Bain *et al.* 2019). Variable mechanisms and parameters control these eruptions, such as differing magma ascent rates, interaction with conduit walls, magma permeability and degassing-induced crystallisation (e.g. Clarke *et al.* 2007; Wright *et al.* 2007; Burgisser *et al.* 2010; 2011; Morrisey & Mastin 2010; Cassidy *et al.* 2015; Bain *et al.* 2019) during the evolution of a single volcano.

Breadcrust bombs are recurrent eruptive products associated with Vulcanian eruptions and are interpreted to reflect either quenching of magma due to external water influx or the delayed vesiculation of partially degassed magmas (Hoblitt & Harmon 1993). A previous study focusing upon deciphering the formation of bombs, such as measuring H_2O contents in glassy rinds in breadcrust bombs from the Mt St Helens 1980 eruption, concluded pre-eruptive magma degassing resulted in a syn-eruptive bubble nucleation delay forming glassy rinds (Hoblitt & Harmon 1993). Breadcrust bombs have been used to decipher pre-eruptive magma processes including magma degassing and the role of volatiles during volcanic eruptions at various locations including Mt St Helens, USA (Hoblitt & Harmon 1993), Tokachidake volcano, Japan (Yamagishi & Feebrey 1994), Mt Pinatubo, Philippines (Polacci *et al.* 2001), Novarupta, Alaska (Adams *et al.* 2006; Isgett *et al.* 2017), Guagua Pichincha, Ecuador (Wright *et al.* 2007), Soufrière Hills, Montserrat (Burgisser *et al.* 2010; 2011), Volcán de Colima, Mexico (Cassidy *et al.* 2015) and Galeras, Colombia (Bain *et al.* 2019). As such, breadcrusts bombs can be used to constrain the pre-eruptive history of magma storage and ascent to provide insights into timescales of pre-eruptive processes at active volcanoes.

La Fossa di Vulcano (Aeolian Islands, Italy) is the site of the 'type' Vulcanian eruption, the 1888-90 eruption first described by Mercalli & Silvestri (1891) and is often characterised by eruption columns with unconfined PDCs and fallout of ballistics, blocks and breadcrust bombs. Early studies on volcanic bombs from Vulcano by Walker (1969) identified 3 principal block and bomb types: 1) Dense blocks which did not expand on impact, 2) Blocks with thick, quenched rims and limited expansion and 3) Highly expanded blocks with thin glassy crusts and shallow cracks ('typical' breadcrust bomb).

This chapter presents new feldspar phenocryst and microlite compositions, detailed textural analyses of feldspar microlites and timescales obtained from crystal size distributions on feldspar microlites from breadcrust bombs from the 1888-90 eruption of La Fossa di Vulcano to assess conduit evolution and timescales of magma ascent during the eruption and the origin of four different bomb types identified. This study shows changes from closed- to open-system degassing, varying magma ascent rates, magma recharge and switches between growth- and nucleation-dominated crystallisation result in the variety of bomb types erupted from La Fossa di Vulcano. These are identified as the key processes governing the occurrence and magnitude of Vulcanian eruptions which can be applied to the 1888-90 eruption and to other arc volcanoes. Understanding theses eruption triggering processes can be used in hazard mitigation and management on Vulcano and elsewhere.

3.2 The 1888-1890 eruption

The most recent eruption of la Fossa di Vulcano was the 1888-1890 'type' Vulcanian eruption documented by Mercalli & Silvestri (1891). The 1888-90 eruption formed a large widespread block and bomb field at the summit of La Fossa di Vulcano originating from the vent 'Gran Cratere' (Fig. 3.1A, C, D).

The eruption succession has previously been described in depth by Clocchiatti *et al.* (1994). The eruption was proceeded by minor explosive events in 1886. The main eruptive period commenced on the 3 August 1888, ending in March 1890. The eruptive sequence has been divided into at least 12 units by Clocchiatti *et al.* (1994) (Fig. 3.1B), which represent the most explosive phases of the eruption described by Silvestri *et al.* (1891). Units 1 and 2 (3^{rd} – 4^{th} August 1888; Silvestri *et al.* 1891) consist of phreatomagmatic breccias of rhyolitic composition with latitic magmatic enclaves. Units 3 – 6 (5^{th} August

1888 – February 1889; Silvestri *et al.* 1891) form the main explosive phases identified by pyroclastic surges and fall products. The deposits from these units span a compositional range from trachyte to latite with abundant magmatic enclaves. Units 7 – 12 (February – December 1889; Silvestri *et al.* 1891) form rhyolitic tephras similar to those of units 1 and 2. It has previously been suggested the range in compositions from trachyte to rhyolites in the magmatic system of the 1888-90 eruption, resulted from mixing processes between different magmas (De Fino *et al.* 1991). De Fino *et al.* (1991) suggest breadcrust bombs were erupted at the start and during the middle to late stages of the eruption.

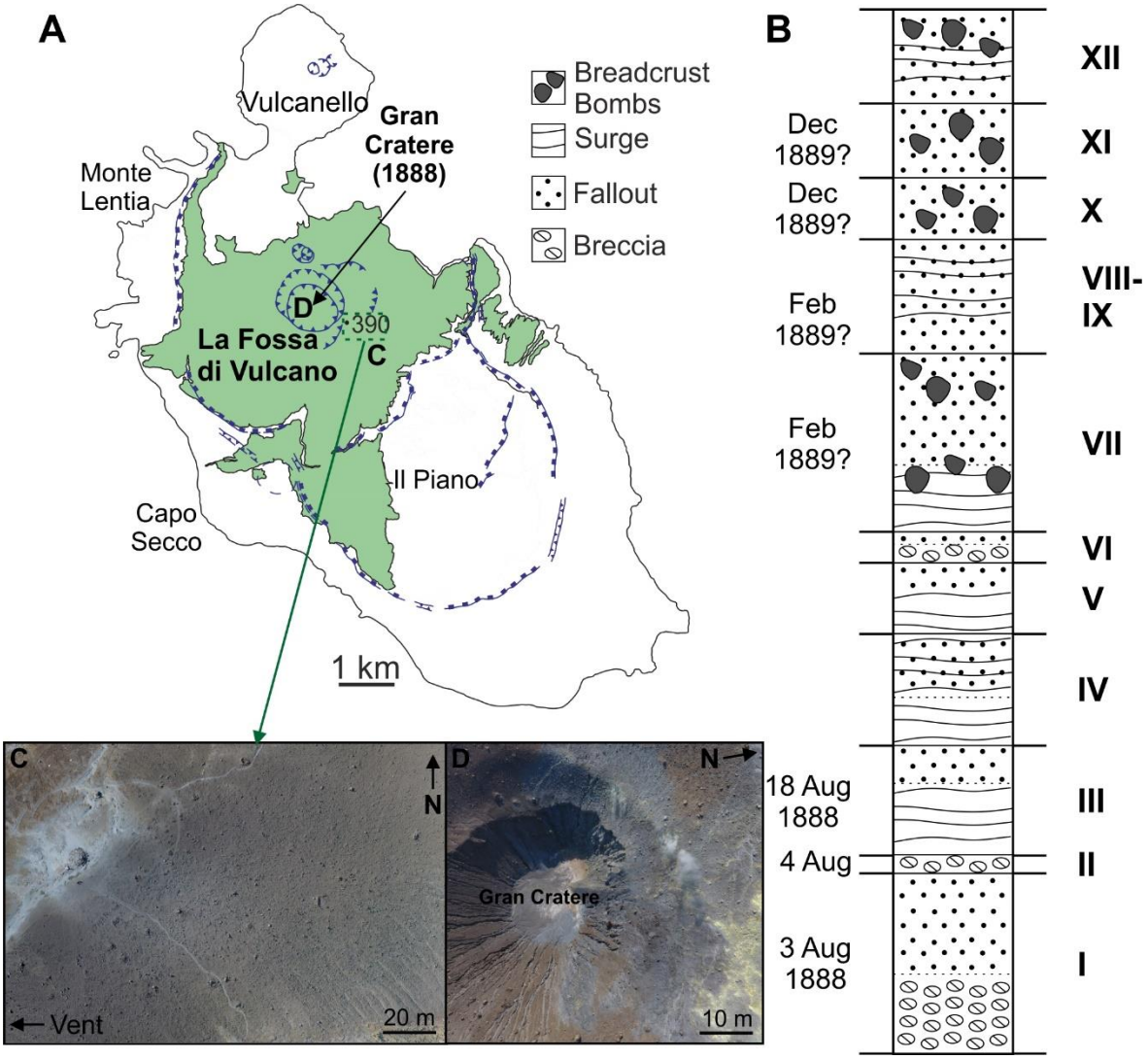

Fig. 3.1: (A) Simplified map of the island of Vulcano and the location of inset E (After: De Astis et al. 2013). (B) Stratigraphic sequence of the 1888-90 eruption, divide into eruptive units (After: Clocchiatti *et al.* 1994). Aerial images of (C) The bomb field at the summit and (D) Gran Cratere, the site of the 1888-90 eruption.

The study by Clocchiatti *et al.* (1994) focused upon constraining the chemical and physical conditions of the magma chamber at the time of the 1888-90 eruption. Major, trace and radiogenic isotope geochemistry on erupted rhyolites indicate they originated from fractional crystallisation of a latitic magma and assimilation of crustal material, whereas trachytes are interpreted to result from mixing of latitic and rhyolitic magmas subsequently contaminated in the shallow magmatic system (Clocchiatti *et al.* 1994). Thermobarometric calculations indicate crystallisation temperatures in latites and trachytes are 1050 - 1100°C, and ~1000°C in rhyolites, with 1 – 1.5 wt.% H_2O dissolved in magmas (Clocchiatti *et al.* 1994). Secondary fluid inclusions in metamorphic xenoliths yielded low equilibration pressures (30 – 60 MPa), suggesting the upper magma chamber is located at depths of only 1500 – 2000 metres (Clocchiatti *et al.* 1994). They concluded individual eruptive units from the eruption are compositionally zoned (rhyolites – latites) and heterogeneous due to syn-eruptive mingling processes.

3.3 Sampling and analytical techniques

Eight breadcrust bombs and fragments and one magmatic enclave from the 1888-90 eruption of La Fossa di Vulcano were examined. Samples selected for analyses are all fresh and unaltered, representing the range of different types of breadcrust bombs recognized in the field (2 for type 1 bombs, 2 for type 2 bombs, 3 for type 3 bombs, 1 for type 4 bomb; see below for bomb types).

Samples for whole-rock major and selected trace element compositions were washed in deionised water for 48 hours and all weathered and altered surfaces were removed. Samples were then crushed in a jaw crusher and reduced to a fine powder in an agate mill for 2 – 6 minutes and dried overnight at 130°C. Major elements were analysed using Inductively Coupled Plasma – Atomic Emission Spectroscopy (ICP-AES) at Bureau

Veritas Minerals laboratories, Canada, using the lithium metaborate (LiB_2) flux fusion followed by dilution using dilute nitric acid. Andesite and rhyolite internal laboratory standards were analysed for quality control. Detection limits for the major elements were 0.01 wt.% with the exception of Fe_2O_3 for which the detection limit was 0.04 wt.%. For trace elements the detection limits were 1 ppm for Sc, 2 ppm for Sr, 3 ppm for Y, 5 ppm for Ba, Nb, Zr and 20 ppm for Cr and Ni. Precision was better than 5%.

Major and minor element compositions for feldspars were analysed using a Cameca SX-100 electron microprobe at the Natural History Museum, London, UK. Feldspars (5 µm beam diameter) were measured using a 20 kV accelerating voltage and 20 nA beam current. Na and K were measured first to minimise the effects of alkali migration.

Eight samples were selected for a detailed textural study of feldspar microlites, following the method described in Preece *et al.* (2013). High-magnification (1200x) back-scattered electron (BSE) images were taken of representative groundmass areas from samples using a Hitachi TM3000 desktop SEM at Keele University. The total area of groundmass selected was based upon imaging enough microlites for statistical significance (n > 700 microlites). Images were stitched using Image Composite Editor software to produce one single continuous image area per sample. Feldspar microlite images were identified using the images and outlined manually using CorelDraw X7. ImageJ was used to outline the area of interest and polygons on the traced images (Schneider *et al.* 2012). Microlites not completely within the area of interest were omitted. All other microlites were then measured in ImageJ (Schneider *et al.* 2012) using the best-fit ellipse tool. CSDSlice (Morgan & Jerram 2006) was used to convert the crystal length and width measurements into 3-dimensional crystal shapes gaining the short (S), intermediate (I) and long (L) axes for every sample. CSDCorrections (version 1.6; Higgins 2000) was utilised for stereological conversions using 2-dimensional crystal intersections and convert them to 3-

dimensional crystal size distributions (CSDs). Vesicularity was corrected for, and the data were separated into 5 size bins per decade, with all bins containing less than 5 crystals removed (Higgins 2000).

3.4 Results

3.4.1 Breadcrust bomb classification

A Previous study by Walker (1969) identified 3 types: dense, vesiculated with limited expansion and thick quenched rims and highly vesiculated with thick glassy rims. This study has further subdivided bombs based upon textural variations into 4 distinct types (Fig. 3.2); vesiculated bombs with red-brown interiors, dense bombs, vesiculated bombs with glassy rinds, and scoriaceous bombs. The scoriaceous bombs is an additional bomb type not described by Walker (1969); however, they have previously been noted by De Fino *et al.* (1991). The bombs analysed in this study represent different depths and processes operating within the volcanic plug.

3.4.1.1 Type 1 – Vesiculated bombs with red-brown interior

Type 1 bombs were previously interpreted as the first erupted bombs representing the pre-existing volcanic plug prior to eruption by Keller (1980). Type 1 bombs are identified in the field by their classic red-brown colour (Fig. 3.2A). Type 1 bombs are heavily fractured with the classic ‘breadcrust’ texture with expansion cracks (Fig. 3.2A).

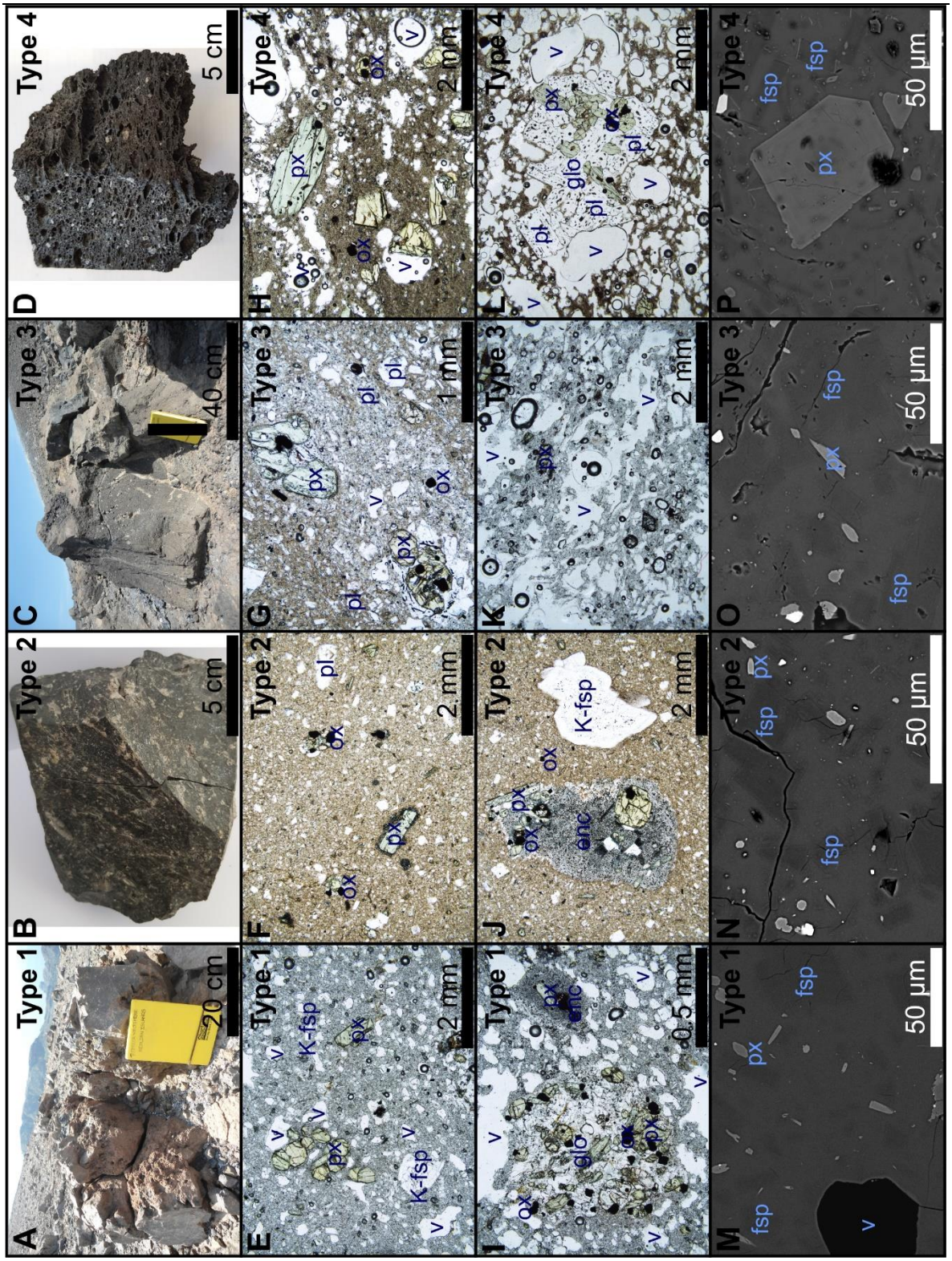

Fig. 3.2: Representative field-, thin section- and Backscattered Electron (BSE) images of all bomb types. (A) Type 1 vesiculated bomb with a red-brown interior. (B) Dense bomb. (C) Vesiculated bomb. (D) Scoriaceous bomb. (E-L) Photomicrographs in plane-polarised light thin section images of all bomb types, with Glomerocrysts (I, L) and fine-grained magmatic enclaves (J). (M-P) BSE images showing feldspar and pyroxene microlites in the groundmass of all bomb types. Note: Black areas are voids in the section, dark grey outlines are feldspar microlites, light grey are pyroxene microlites and white microlites are Fe-Ti oxides in BSE images.

They have large, rounded vesicles less than 5 mm diameter, which are sometimes infilled with secondary minerals. Glomerocrysts commonly occur in the rind and interior of these bombs (Fig. 3.2I). Type 1 bombs have a thin dense rind, typically less than a few centimetres thick. These bombs have abundant crustal xenoliths.

3.4.1.2 Type 2 – Dense bombs

Dense bombs are characterised by a uniform texture from rim to core in hand specimen. The surface morphology is slightly fractured to non-fractured (Fig. 3.2B; N). They are entirely void of vesicles in hand specimen with occasional elongate vesicles observed in thin section (<0.5 mm; Fig. 3.2F; J). Dense bombs are the smallest bombs erupted from la Fossa di Vulcano and are typically smaller than 20 cm in diameter (Fig. 3.2B). These bombs contain crustal xenoliths and magmatic enclaves.

3.4.1.3 Type 3 – Vesiculated bombs with glassy rinds

Type 3 vesiculated bombs form the characteristic ‘breadcrust bombs’ (Fig. 3.2C). They are distinct from type 1 by the presence of a grey interior instead of the typical red brown of type 1. They have glassy rinds ranging from a few millimetres up to some centimetres thick (~3 cm). They also have a gradational boundary between core and rim. These bombs are moderately vesicular and pumiceous in some cases, with light-grey interiors (Fig. 3.2C, G, K). Some bombs have non-vesiculated veins running through with similar textural characteristics to type 2 bombs. Similar to type 1 bombs, vesicles are typically less than 5 mm diameter, varying in morphology from rounded to irregular in both hand specimen and thin section and are coalesced in places.

Expansion cracks are abundant on the surface of type 3 bombs (Fig. 3.2C). The surfaces of the bombs also have cognate inclusions of other bomb types and lithic rhyolitic fragments with phenocrysts of plagioclase and clinopyroxene, probably representing the remaining volcanic plug, incorporated during ascent and subsequent interaction with the conduit walls. Some of these inclusions are post-eruptive whilst the bombs were still hot after they were erupted. Additionally, magmatic enclaves are also common.

3.4.1.4 Type 4 – Scoriaceous bombs

Scoriaceous bombs are uncommonly erupted products from the 1888-90 eruption. These bombs are highly irregular in shape up to 40 cm diameter (Fig. 3.2D). Scoriaceous bombs are typically characterised by a dense, dark grey, glassy rind up to 20 mm with small vesicles and a highly vesicular dark interior (Fig. 3.2D, H, L). The boundary between the rim and interior of the bombs are gradational over ~10 mm. The large vesicles (>1 mm) in scoriaceous bombs are elongate, interconnected and branching throughout. Large vesicles can range up to 15 mm. Small vesicles (<1 mm) are elliptical to sub-elliptical in shape and are coalesced in places.

3.4.2 Petrography

All analysed breadcrust bomb samples are porphyritic with complex mineral assemblages, zoning, and mineral disequilibrium textures. All bomb types are characterised by phenocrysts and micro-phenocrysts of alkali-feldspar, plagioclase, clinopyroxene, Fe-Ti oxides, minor biotite with rare olivine glomerocrysts occurring only in type 4 bombs within a microlite-bearing (predominantly plagioclase and alkali feldspar with some clinopyroxene and minor Fe-Ti oxides) glassy groundmass (Fig. 3.2E - L). Fe-Ti oxide and melt inclusions commonly occur in clinopyroxene phenocrysts. Clinopyroxene phenocrysts are typically less than 2 mm in all bombs, however they are characteristically much larger,

up to 5 mm diameter, in type 4 scoriaceous bombs. Some clinopyroxene phenocrysts and microlites also exhibit single-band zoning. Magmatic enclaves have phenocrysts of clinopyroxene, plagioclase, alkali feldspar, Fe-Ti oxides set in a microcrystalline groundmass consisting largely of plagioclase.

Groundmass mineral phases (microlites) are dominated by alkali feldspar, plagioclase feldspar, clinopyroxene and Fe-Ti oxides set in a glassy groundmass. Glomerocrysts (up to 10 mm) consisting of the main mineral phases are found in all bomb types (Fig. 3.2I, L) in addition to magmatic enclaves (Fig. 3.2J) of variable size, crustal xenoliths (quartz-bearing restites) and lithic fragments.

3.4.3 Whole-rock geochemistry

Analysed breadcrust bombs are characterised by a uniform composition in major and trace elements except for the scoriaceous bomb sample that is geochemically distinct (Table 3.1). Major and trace element data for all analysed bomb samples are summarised in Table 3.1 and Figures 3.4 and 3.5. Type 1, 2 and 3 bombs are all trachytic (66.13 – 67.20 wt. % SiO_2, 5.45 – 5.78 wt.% K_2O) whereas the type 4 bomb is latitic (58.42 wt.% SiO_2; 5.33 wt.% K_2O), with all samples defining a shoshonitic affinity and following the general trends of La Fossa di Vulcano (Fig. 3.3). Al_2O_3, TiO_2, $Fe_2O_3^*$, MnO, MgO, CaO and P_2O_5 (Fig. 3.4), Ba, Sr, Cr and Sc (Fig. 3.5) all decrease with increasing SiO_2. Conversely, K_2O, Nb, Y and Zr (Fig. 3.5) all increase with increasing SiO_2.

Table 3.1: Major- and Trace-element geochemistry of representative breadcrust bomb samples from the 1888-90 eruption.

Sample	AI-18-076	AI-18-072	AI-17-120	AI-18-074	AI-18-070	AI-18-078
Bomb Type	1	1	2	2	3	4
wt.%						
SiO_2	66.18	66.13	67.20	66.68	66.36	58.42
TiO_2	0.28	0.28	0.27	0.28	0.29	0.50
Al_2O_3	14.93	14.93	14.88	14.8	14.72	15.64
Fe_2O_3	4.03	3.86	3.78	3.97	4.01	6.52
MnO	0.09	0.09	0.09	0.09	0.09	0.13
MgO	1.14	1.03	0.91	1.11	1.03	3.07
CaO	2.61	2.49	2.26	2.55	2.35	5.51
Na_2O	4.05	4.16	4.14	4.09	4.14	3.88
K_2O	5.48	5.70	5.75	5.45	5.78	5.33
P_2O_5	0.16	0.09	0.14	0.15	0.12	0.33
LOI	0.80	1.00	0.40	0.60	0.90	0.30
Total	99.75	99.76	99.82	99.77	99.79	99.63
ppm						
Cr	b.d.	44	29	44	29	117
Ba	389	386	374	368	385	814
Ni	b.d.	b.d.	b.d.	b.d.	b.d.	b.d.
Sr	410	395	366	373	372	850
Zr	240	251	254	240	254	207
Y	31	31	32	32	31	24
Nb	31	33	35	29	34	22
Sc	6	6	5	6	6	13

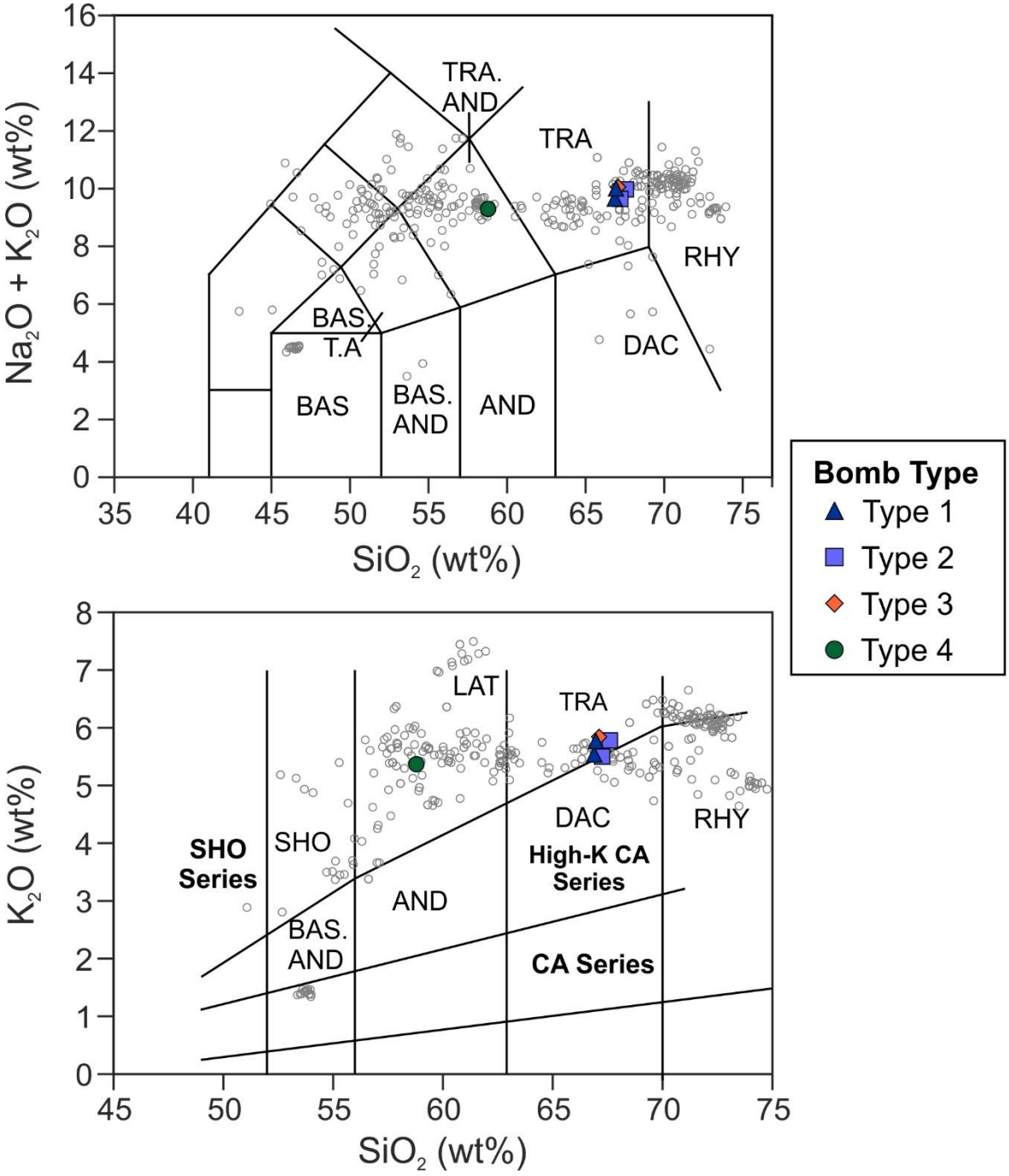

Fig. 3.3: (A) Total Alkali versus SiO_2 (Le Bas *et al.* 1986) and (B) K_2O versus SiO_2 classification diagrams (Peccerillo & Taylor 1976) for bombs from the 1888-90 eruption. Oxides are expressed in weight percent (wt.%), and compositions are all normalised and LOI-free. Existing literature data from Gran Cratere (gc) (light grey circles) from De Astis *et al.* (2013) and references therein.

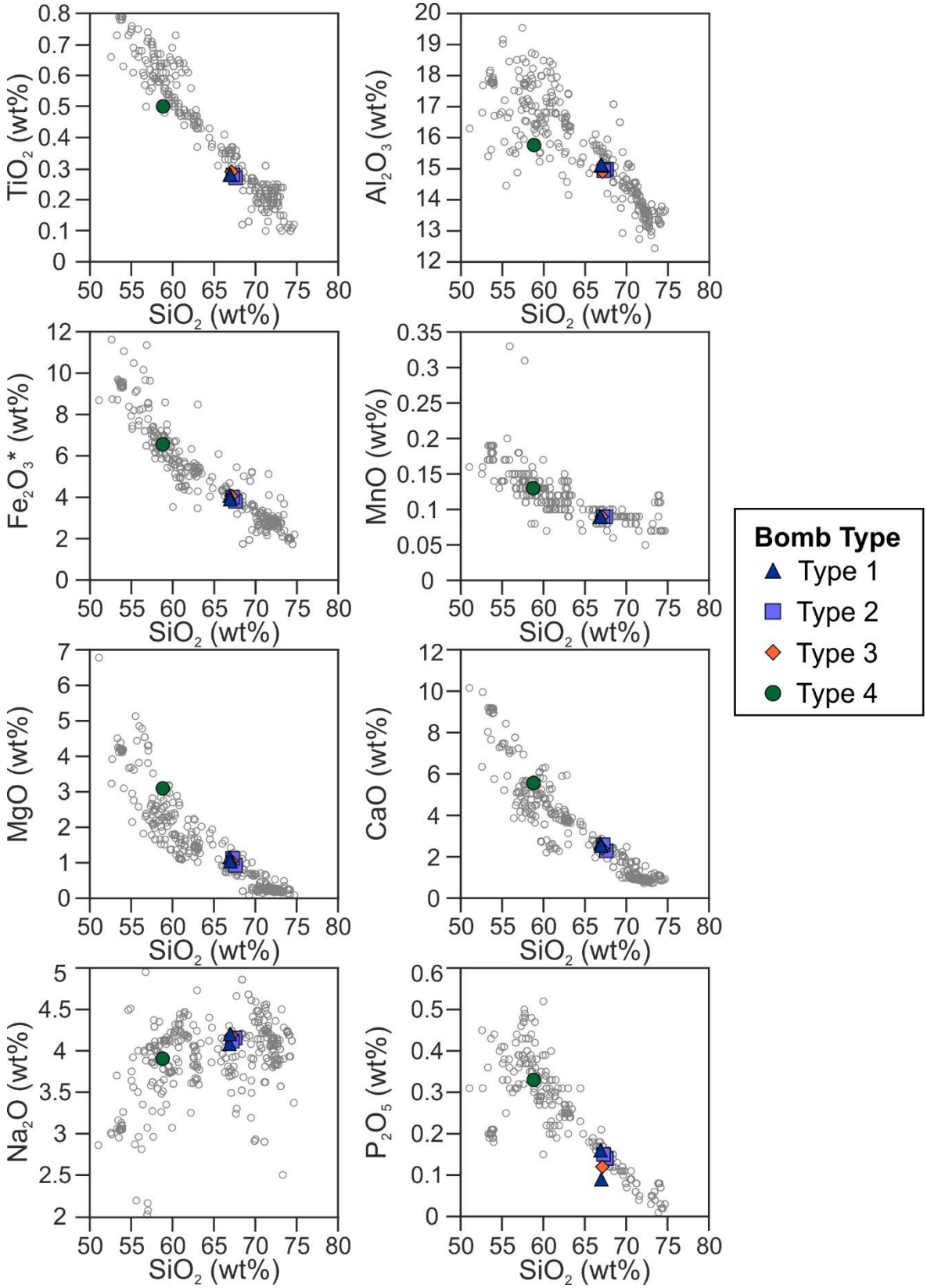

Fig. 3.4: Major element variation diagrams versus SiO_2 for bombs from the 1888-90 eruption, plotted with existing literature data covering the eruptive history of La Fossa di Vulcano (Chapter 2; De Astis *et al.* 2013 and references therein). All rock compositions are reported in wt.%, normalised and LOI-free.

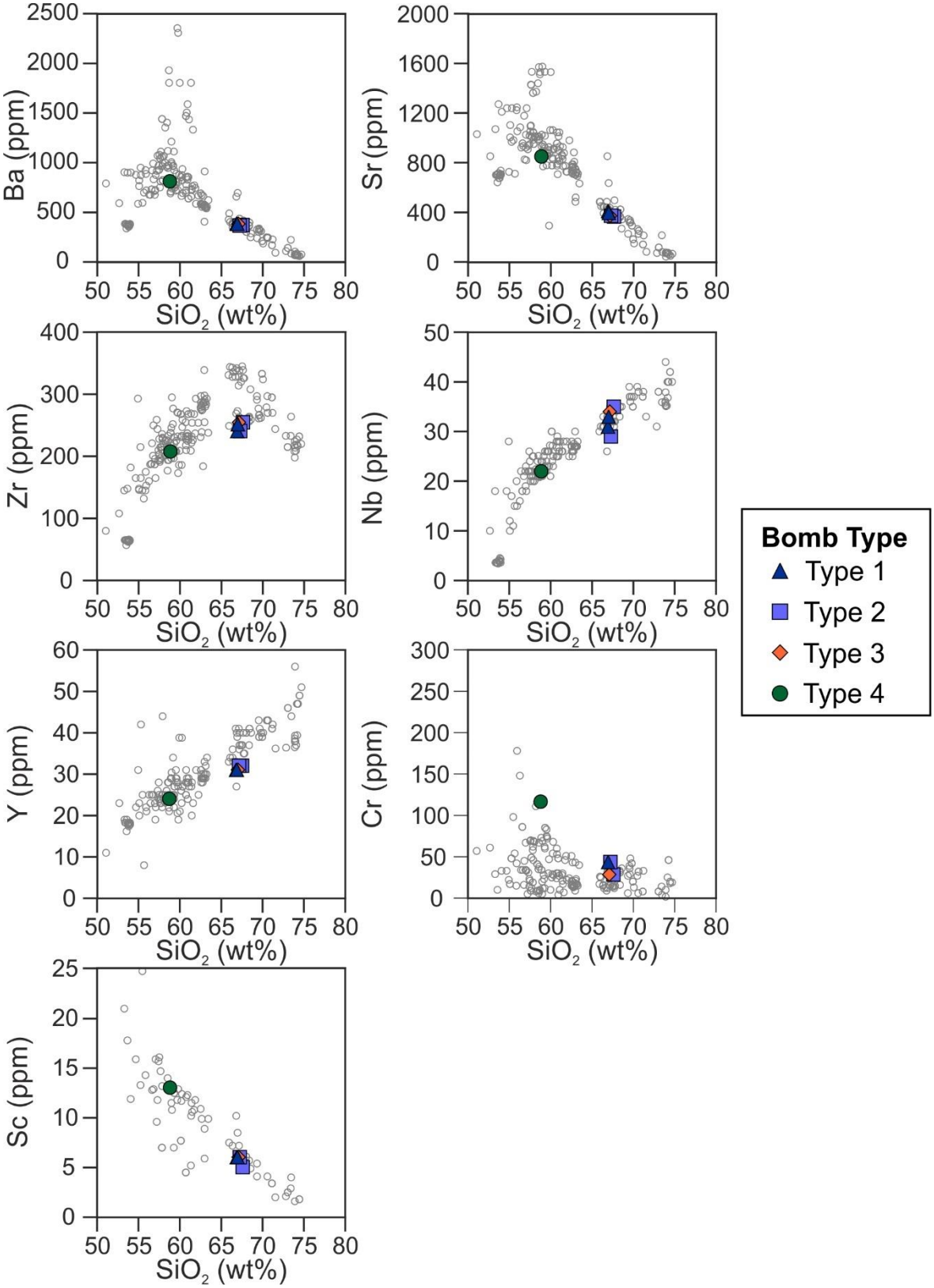

Fig. 3.5: Trace element variation diagrams versus SiO2 for bombs from the 1888-90 eruption, plotted with existing literature data covering the eruptive history of La Fossa di Vulcano (Chapter 2; De Astis et al. 2013 and references therein). All rock compositions are reported in wt.%, normalised and LOI-free.

3.4.4 Feldspar compositions

Plagioclase and alkali feldspar both occur as phenocrysts and microlites in the 1888-90 bomb samples, with the exception of the type 4, scoriaceous bomb that has plagioclase phenocrysts and alkali feldspar microlites. Phenocrysts commonly exhibit sieve-textured zoning, compositional zoning, and multiple twinning. Plagioclase phenocrysts span a range of compositions (Fig. 3.6), with variations in the different breadcrust bomb types: $An_{42-57}Ab_{39-53}Or_{4-10}$ in type 1 bombs, $An_{26-51}Ab_{44-63}Or_{4-11}$ in type 2 bombs, $An_{42-60}Ab_{33-53}Or_{4-9}$ in type 3 bombs and $An_{43-68}Ab_{29-49}Or_{3-11}$ in type 4 bombs. Alkali feldspar phenocrysts span a limited range in compositions from $An_{3-11}Ab_{40-54}Or_{35-57}$ in type 1 bombs, to $An_{3-16}Ab_{37-61}Or_{23-59}$ in type 2 bombs, and $An_{3-17}Ab_{43-62}Or_{22-54}$ in type 3 bombs. Phenocrysts in type 1, 2 and 3 bombs therefore evolved to more sodic compositions, consistent with the more evolved bulk rock geochemical character.

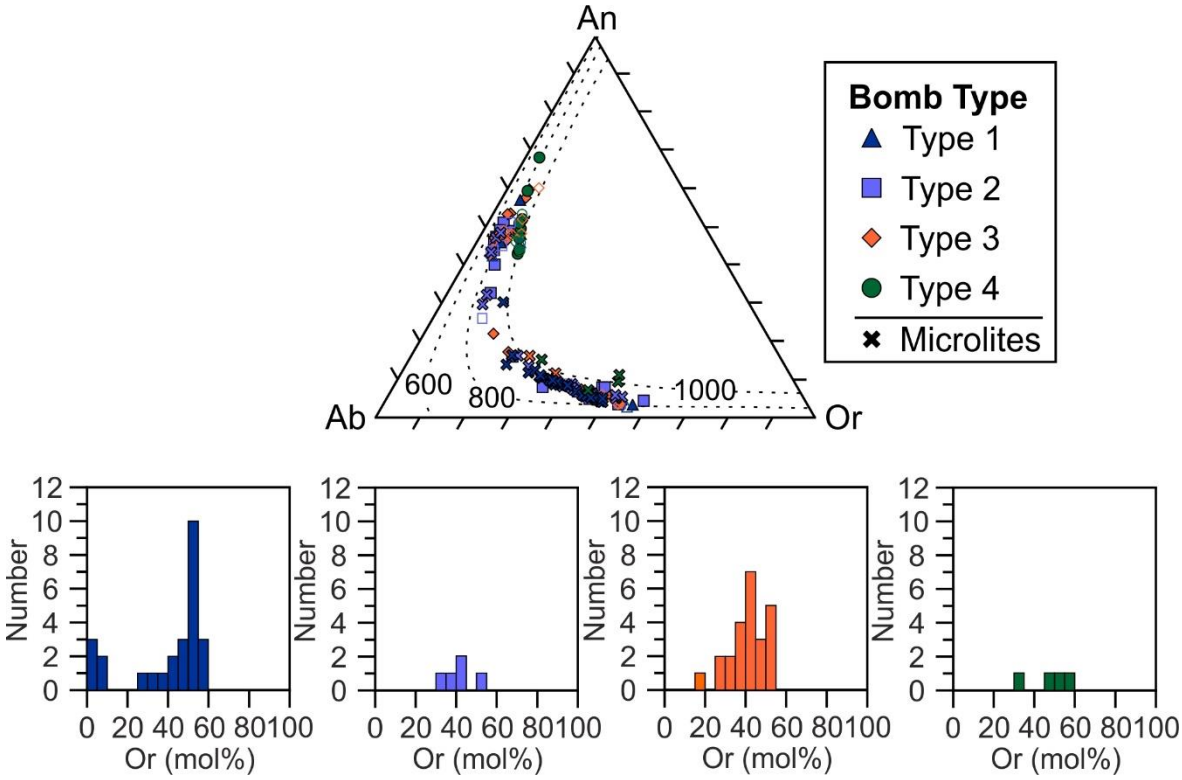

Fig. 3.6: (Top) Feldspar compositions of phenocrysts and microlites from all bomb types of the 1888-90 eruption. (Bottom) Frequency distributions for feldspar microlites using Or contents from each bomb type. Note: Every analysis is of a different microlite. Dry ternary solvus lines (dashed lines) for 600, 800 and 1000 °C, over a range of 1-10 MPa using SOLVCALC (Wen and Nekvasil, 1994).

Feldspar microlites analysed in this study are dominantly alkali feldspar ($An_{7-15}Ab_{47-61}Or_{23-49}$ in type 1 bombs, $An_{6-16}Ab_{49-57}Or_{27-45}$ in type 2 bombs, $An_{4-16}Ab_{46-64}Or_{23-49}$ in type 3 bombs and $An_{7-15}Ab_{39-55}Or_{30-50}$ in type 4 bombs) with the exception of five microlites ($An_{29-48}Ab_{48-61}Or_{4-9}$) in the type 2 bombs and one microlite ($An_{30}Ab_{56}Or_{14}$) in a type 3 bomb. For feldspar microlites, Or content across all bomb types is in the range Or_{4-50}, with type 1, 2 and 3 bombs exhibiting a bi-modal distribution with a range of Or_{35-55} and a dominant peak at Or_{45-50} (Fig. 3.6). The range in Or content in type 1, 3 and 4 bombs are more constrained to Or_{30-50}, with the exception of one analysis from a type 3 bomb with Or_{14}. Feldspar microlite compositions in type 2 bombs have higher Or (Or_{4-45}) content than other bombs. The ranges observed in feldspar compositions in microlites across all bomb types largely overlap, with a limited compositional range in plagioclase and alkali feldspar.

3.4.5 Textural characteristics of feldspar microlites

The abundance of feldspar microlites are described as the number of crystals per unit area (mm^2), expressed as the microlite number density (N_A). The areal feldspar number density (N_A) ranges from 1,179 to 5,582 mm^{-2}. The highest number densities are found in type 2 dense and type 4 scoriaceous bomb samples. Type 1 vesiculated bombs with red-brown interiors have the lowest number densities of all samples analysed (1179 and 1360 mm^{-2} respectively). Groundmass crystallinity (Ø) is expressed as the quantity of the analysed groundmass area occupied by feldspar microlites and is a function of microlite size and abundance. Crystallinity has been calculated on a vesicle- phenocryst- and oxide-free area using calculations of Hammer *et al.* (2000). Groundmass crystallinity ranges from 0.215 to 0.274. Mean crystal areas for analysed microlites range from 38 to 185 μm^2, with the largest microlites found in type 1 vesiculated bombs with red-brown interiors.

Crystal aspect ratios obtained from CSDSlice best fit shape parameters (Morgan & Jerram 2006), have been calculated to determine crystal shapes. The shortest axis (S) is 1.00 in all samples, the intermediate axis (I) ranges from 1.50 to 2.0 and the long axis (L) ranges from 2.40 to 10.00. S/L ranges from 0.1 to 0.42 across all bomb types (Table 3.2; Fig. 3.7). The lowest S/L ratios are found in acicular crystals (AI-18-078). All textural parameters are summarised in Table 3.2. Using CSDSlice (Morgan & Jerram 2006), the morphology of microlites are mostly rectangular prisms with the exception of one type 2 bomb (AI-17-120) and the type 4 bomb sample (AI-18-078) which are acicular. An inverse relationship is observed between N_A and mean crystal area (MCA) (Fig. 3.7A); therefore, these samples have a lower number of large microlites, or large numbers of small microlites. The Type 4 bomb sample (scoriaceous bomb) has a higher N_A and lower Ø than all of the other bomb samples (Fig. 3.7B). An increasing relationship between N_A and Ø is observed with the exception of the Type 4 bombs (Fig. 3.7B).

A positive correlation is observed between N_A and S/L (Fig. 3.7C), therefore samples with higher N_A have more tabular microlites. The acicular microlites in Type 4 bombs have a high N_A and low S/L. The vesiculated bombs (Type 1 and 3) have lower N_A and higher Ø than Type 2 dense bombs. N_A and mean crystal areas are two-dimensional results and therefore must be considered with caution as they are affected by the intersection probability effect and size cut-offs of the analysed crystals (Royet 1991; Higgins 2006). Therefore, two-dimensional data will be combined with three-dimensional crystal size distributions (CSDs) to assess their validity in assessing textural parameters of feldspar microlites in analysed samples. Samples with higher crystal number densities (N_A) are more crystalline than the other samples, and vice versa.

Table 3.2: Textural results and calculated nucleation rates and crystallisation times using growth rates of 10^{-6}, 10^{-8}, and 10^{-10} mms^{-1} for all bomb types examined in this study. All parameters are described in the text.

Sample	Bomb Type	Number of Crystals	Area Analysed (mm^2)	N_A (mm^{-2})	Crystallinity (Ø)	Mean Crystal Area (μm^2)	S:I:L (R^2)[a]	S/L
AI-18-072	1	724	0.848	1179	0.225	185	1:1.6:2.9 (0.72)	0.34
AI-18-076	1	714	0.787	1360	0.248	179	1:1.5:3 (0.76)	0.33
AI-17-120	2	717	0.179	4006	0.240	59	1:1.5:3 (0.42)	0.33
AI-18-074	2	969	0.344	3047	0.239	76	1:1.5:2.4 (0.58)	0.42
AI-18-068	3	904	0.419	2450	0.229	87	1:1.5:3(0.57)	0.33
AI-18-070	3	819	0.721	2167	0.233	107	1:1.5:2.4 (0.62)	0.42
AI-17-122	3	829	0.265	4737	0.274	58	1:1.5:2.4 (0.5)	0.42
AI-18-078	4	988	0.198	5580	0.215	38	1:2:10 (0.37)	0.10

Sample	Ln (n_0 (mm^{-4}))	CSD slope, α (mm^{-1})	$1x10^{-6}$ τ (hours)	$1x10^{-8}$ τ (days)	$1x10^{-10}$ τ (days)	$1x10^{-6}$ J ($mm^{-3}s^{-1}$)	$1x10^{-8}$ J ($mm^{-3}s^{-1}$)	$1x10^{-10}$ J ($mm^{-3}s^{-1}$)	N_v (mm^3)	Lc (μm)
AI-18-072	15.57	-64.31	4.3	18	1800	5.76	0.06	0.0006	89551	16
AI-18-076	15.43	-58.33	4.8	20	1984	5.03	0.05	0.0005	86315	17
AI-17-120	18.99	-171.09	1.6	7	676	177.36	1.77	0.0177	1036647	6
AI-18-074	18.31	-160.88	1.7	7	719	89.47	0.89	0.0089	556137	6
AI-18-068	17.69	-124.14	2.2	9	932	48.05	0.48	0.0048	387054	8
AI-18-070	17.79	-158.15	1.8	10	1019	53.32	0.53	0.0053	337178	6
AI-17-122	19.34	-205.99	1.3	10	1003	249.64	2.50	0.0250	1211945	5
AI-18-078	16.70	-42.86	6.5	17	1683	18.58	0.19	0.0019	433522	23

[a] R^2 value and S:I:L ratios are from CSDSlice (Morgan & Jerram 2006).

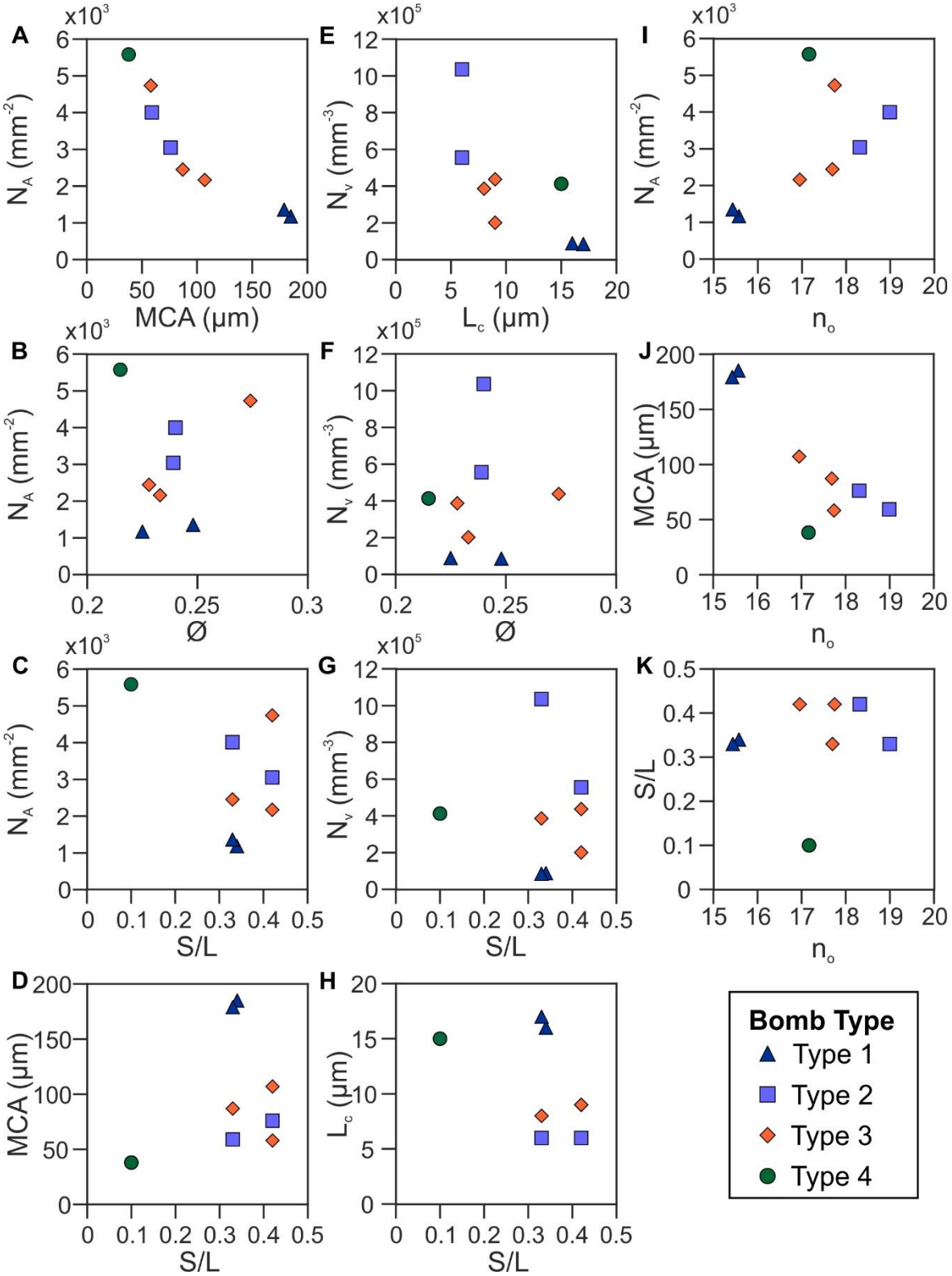

Fig. 3.7: (A-D) Batch textural results for feldspar microlites. (E-H) Three-dimensional textural results calculated using the steepest portion of the CSD slope of each sample at the smallest bin sizes (see dashed lines on Fig. 3.8). (I-K) Combined batch and three-dimensional textural results.

To combine two-dimensional textural parameters with three-dimensional textural parameters, a volumetric feldspar number density (N_v) and the characteristic crystal size (L_c) are calculated where $N_v = n_0 \times \frac{-1}{\alpha}$ and $L_c = \frac{-1}{\alpha}$ (Blundy & Cashman 2008). With increasing N_v, L_c decreases (Fig. 3.7E) and a general decreasing trend is observed in L_c with increasing S/L (Fig. 3.7H), thus samples with higher L_c have larger crystal sizes and more tabular microlite morphology. However, no trends are observed between N_v and Ø or S/L (Fig. 3.7F, G). Overall, S/L exhibits an increasing trend with Mean Crystal Area (Fig. 3.7D), showing larger microlites are more prismatic. Consequently, the two-dimensional textural parameters identified and the three-dimensional CSD data both record significant textural information, even though the three-dimensional stereological conversions introduce intersection probability and cut-section effect errors (Royet 1991; Higgins 2000).

3.4.6 Crystal Size Distributions

Crystal Size Distributions (CSDs) are stereologically corrected, three-dimensional textural analyses which provide textural information independent of the size cut off for the analysed crystals from two-dimensional intersection measurements (Higgins 2006). CSDs describe the number of feldspar crystals per unit volume, in a series of predefined size intervals. CSDs are plotted using the number of crystals per unit volume of the population (population density) versus crystal size.

All CSDs for feldspar microlites in this study are concave upwards in shape (Fig. 3.8), resulting from shape variability in the sample (Castro *et al.* 2003) or progressive changes in crystal growth and nucleation rates as a function of changing ΔT in the system (Preece *et al.* 2016). The slope (α, mm^{-1}) of the straight portion of CSDs immediately after the left-hand downturn, and the y intercept, n_0 are summarised in Table 3.2 and Fig. 3.8. A left-hand downturn is observed in most of the CSDs, resulting from a decrease in the

population density at the smallest crystal sizes. A decrease in the abundance of the smallest crystal sizes has previousl been reported in natural and experimental samples, resulting from insufficient spatial resolution (e.g. Marsh 1998; Hammer *et al.* 1999) and stereological conversions due to intersection probability effects at the smallest crystal sizes (e.g. Cashman 1988; Brugger & Hammer 2010; Higgins 2010).

The shallowest CSD slopes and lowest y-axis intercepts (n_0) are found in type 1 vesiculated bombs and type 4 scoriaceous bombs ranging from 15.43 to 16.70 mm^{-4}. Conversely, the steep CSD slopes occur in the samples with higher y-axis intercepts (16.95 to 18.99 mm^{-4}) in type 2 dense and type 3 vesiculated bombs. One sample, AI-17-122 (type 3 bomb) is close to a straight line CSD slope (Fig. 3.8).

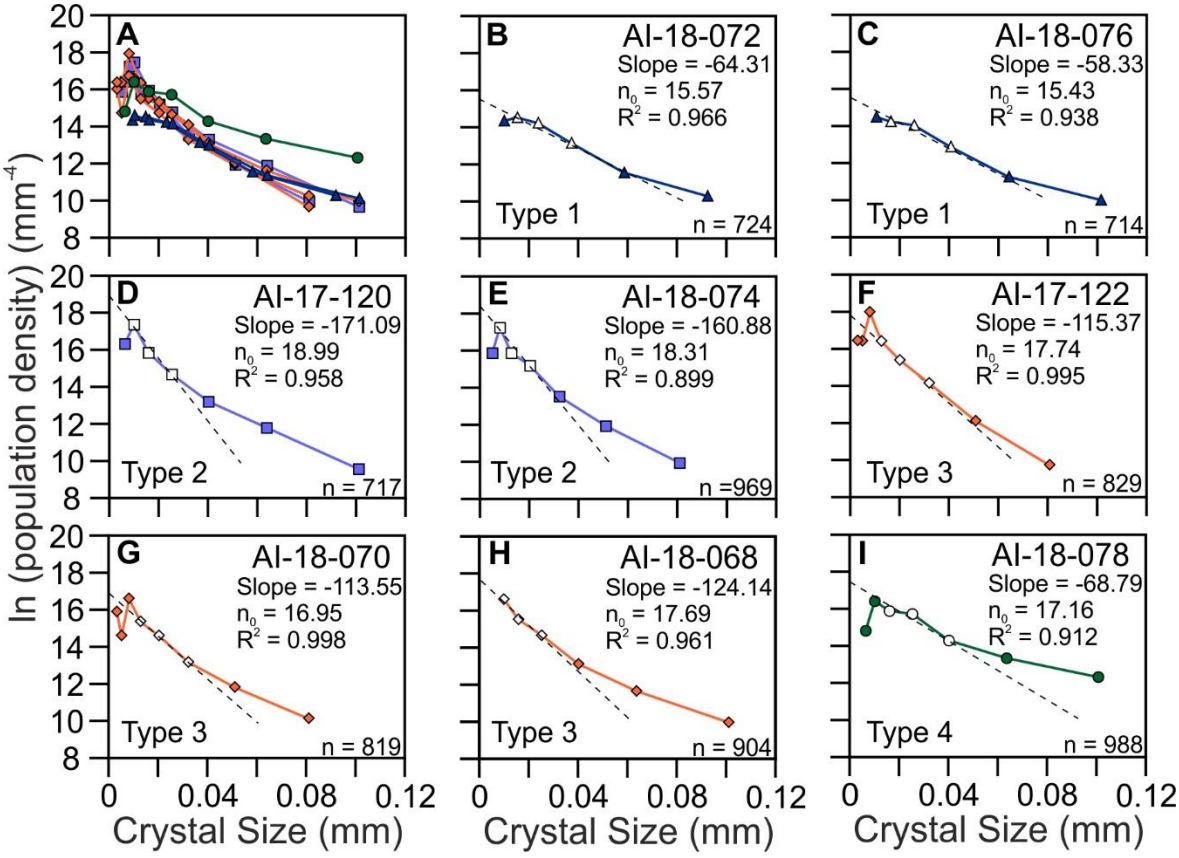

Fig. 3.8: Crystal size distributions (CSD) plots of feldspar microlites from each bomb type from the 1888-90 eruption. (A) All CSDs. (B-C) CSDs from Type 1 bombs. (D-E) CSDs from Type 2 bombs. (F-H) CSDs from Type 3 bombs. (I) CSD from Type 4 bomb. A regression line is shown for the steepest portion of the CSD slope omitting downturns at the smallest crystal sizes, alongside the slope of the regression line, nucleation density (n0) or y-axis intercept, R2 value and the number of crystals (n) analysed in each sample.

As n_0 increases, N_A (Fig. 3.7I) and S/L (Fig. 3.7L) increase, whereas Mean Crystal Areas decreases (Fig. 3.7J). Consequently, the tabularity of crystals increase. Type 1 bombs are characterised by low final nuclei population densities (n_0) and areal feldspar number densities (N_A), and the largest mean crystal areas of all samples analysed. The type 4, scoriaceous bomb sample has a very shallow CSD slope (Fig. 3.8), compared to the other bomb types and a lower S/L (0.1) indicating the microlites are much more acicular in shape.

3.5 Discussion

3.5.1 Feldspar microlite compositions

Feldspar microlite compositions are used in this study as they record melt evolution and degassing prior to eruption. At other arc volcanoes (Merapi and Galeras) feldspar microlites span a large range of An contents (Hammer *et al.* 2000; Preece *et al.* 2016; Bain *et al.* 2018). However, at Vulcano feldspar microlites are dominantly potassic (alkali feldspar) not calcic (anorthite), due to the more alkaline compositions of the crystallising melts, with eruptive products belonging to the shoshonitic series. Alkali feldspar microlites are present in type 1, 3 and 4 bombs, resulting from changing H_2O in the melt phase, enriching the melt in alkalis as a result of degassing and evolution of the residual melt phase (Fig. 3.6; Hammer *et al.* 2000; Preece *et al.* 2016). Type 2, dense bombs and one microlite from a type 3, vesiculated bomb are characterised by feldspar microlites with higher An contents compared to other bomb types. The most An-rich phenocrysts are observed in Type 4 bombs, corresponding to the most primitive samples. However, the analysed microlites are all alkali feldspar in most samples with the exception of type 2 dense bombs where both plagioclase and alkali feldspar microlites occur, suggesting the

crystallisation of alkali feldspar dominated during late stages in the conduit. Therefore, there is no significant relationship observed between microlite and phenocryst compositions and bomb types.

3.5.2 Feldspar microlite textures as indicators of conduit processes

Crystal Size Distributions (CSDs) of feldspar microlites all have concave upwards profiles, representing shape variability of samples (Castro *et al.* 2003) or the progressive change in crystal growth rates and nucleation rates due to changing ΔT in a system (Preece *et al.* 2016). A left-hand downturn is observed in the smallest crystal size bins in type 2 and 3 bombs, as a result of the intersection probability effect on the smallest crystal sizes (Cashman 1988; Brugger & Hammer 2010). These data points are therefore disregarded in calculations (Brugger & Hammer 2010; Preece *et al.* 2016). Variations in microlite size and morphology are attributed to changing magmatic conditions at varying depths (Melnik *et al.* 2011). In addition, microlites from type 1, 2 and 3 bombs have higher S/L ratios of 0.33 to 0.42 suggesting decompression occurred under small degrees of ΔT (Lofgren 1974; Couch *et al.* 2003). Type 2, dense bombs, and type 3, vesiculated bombs are characterised by steep CSD slopes and short residence times. This is interpreted to result from an increase in ΔT (Zieg & Marsh 2002) with slow crystal growth rates.

The more curved CSD slopes of type 1, vesiculated bombs are interpreted to replicate a multi-step ascent accompanying periods of stalling in the upper conduit prior to the onset of the Vulcanian eruption which degasses under higher ΔT conditions (Hammer & Rutherford 2002) as decompression and vesiculation change nucleation rates. Type 1 bombs with a red-brown interior are also characterised by markedly lower N_A (1179 and 1360 mm^{-2}) and low crystallinity, Ø (0.225 and 0.248), high mean crystal areas (MCA) in comparison to the other bomb types (Fig. 3.7A-D), indicating crystallisation is more

nucleation-dominated during this period not growth dominated. This supports the interpretation Type 1 bombs are the first erupted products during the onset of Vulcanian activity, representing the pre-existing magma plug. The high feldspar number density (N_A) and volumetric feldspar number density (N_v), and the lower mean crystal areas and characteristic crystal sizes (L_c) observed in Type 2 dense bombs indicate that these bombs have increased nucleation rates and decreasing microlite growth rates (Fig. 3.7E-H). Type 3, vesiculated bombs are closest to that of straight line concave upwards CSDs (Fig. 3.8F-H), characterised by a high Ø, reflecting a rapid and constant ascent rate resulting in constant crystal growth rates, illustrating the system progressively transitions to a more open-system during the eruption of type 3 vesiculated bombs with short periods of stalling during ascent within the conduit system. The highest nuclei population density occurs in the type 4, scoriaceous bomb closely followed by Type 2, dense bombs.

Microlite nucleation and growth rates are reflected in groundmass textures observed (Williams *et al.* 1954; Hammer & Rutherford 2002) and are a function of changing ΔP and ΔT. Variations observed in N_A, mean crystal area, short/long axis ratios (S/L), final nuclei population density (n_0), volumetric feldspar number density (N_v) and characteristic crystal size (L_c) all reflect changing ΔP conditions. Type 2 dense bombs have high N_A and the highest N_v with smaller mean crystal areas and L_c than those of type 1 and 3 vesiculated bombs, reflecting higher degrees of ΔT in dense bombs. N_A and Ø systematically increase with the exception of the type 4 scoriaceous bomb sample. Variations in the calculated crystallisation times (τ) change based upon bomb types reflecting changing ascent rates in the conduit (Table 3.2).

3.5.3 Timescales of magma ascent

The final nuclei population density, n_0 (mm^{-4}), areal feldspar number density, N_A (mm^{-2}), slope of the CSD, α (mm^{-1}) are all related to the average nucleation rates, J ($mm^{-3}s^{-1}$), crystal growth rates, G ($mm^{-3}s^{-1}$), and the residence time, τ (sec), where $\alpha = \frac{-1}{G\tau}$ and $J = n_oG$ (Cashman 1988; Marsh 1988). Final nuclei population densities, n_0, α and G relate to the degree of effective undercooling in the melt (Williams *et al.* 1954; Hammer & Rutherford 2002; Zieg & Marsh 2002) and can be correlated to the textural parameters (Bain *et al.* 2019). Consequently, effective undercooling is a driving force for crystallisation, resulting in decreasing ΔT.

A constant growth rate for feldspar microlites of 10^{-8} mm s^{-1} is assumed for the eruption, because they yield realistic crystallisation times fitting the eruption chronology described by Clocchiatti *et al.* (1994) which is within the range for silicate systems of 10^{-6} to 10^{-11} mms^{-1} (Hammer *et al.* 2000; Mock & Jerram 2005; Brugger & Hammer 2010). A growth rate of 10^{-6} would result in crystallisation times less than 7 hours which is unrealistic during the 1888-90 eruption. Furthermore, an assumed growth rate of 10^{-10} would increase crystallisation times by 2 orders of magnitude up to 2000 days which are unrealistically long for such small crystals and the duration of the eruption. The final crystallisation time (τ) for the concave upwards CSDs is calculated using a regression line of the three steepest points on the CSD slope immediately succeeding the artificial left-hand downturn at the smallest crystal sizes (Brugger & Hammer 2000; Preece *et al.* 2016).

Calculated crystallisation times, τ, maximum crystallisation times, τ_{max} and minimum crystallisation times, τ_{min} for the smallest microlites, using the steepest portion of the CSD slope and a single growth rate of 10^{-8} vary considerably across bomb types. Crystallisation times, τ, range from τ_{min} 18 days up to τ_{max} 20 days for type 1 bombs, τ_{min} 7 days up to τ_{max} 7 days for type 2 bombs, τ_{min} 9 days up to τ_{max} 10 days for type 3 bombs, and τ_{min} 17 days

up to τ_{max} 17 days for type 4 bomb. Different growth rates yield crystallisation times varying across several orders of magnitude. For example, a growth rate of 10^{-6} yields crystallisation scales in the order of hours from 1.6 up to 6.5 hours, whereas a growth rate of 10^{-10} yields crystallisation scales in the order of years from 1.85 up to 5.44 years. Crystallisation times using a growth rate of 10^{-6} are unrealistically short for the 1888-90 eruption.

The shortest microlite crystallisation times are found in type 2 and 3 bombs where the most calcic feldspar microlites occur and the longer crystallisation times are attributed to the more potassic alkali feldspar microlites. The longest crystallisation times are recorded in type 1 (τ_{max} 18 to 20 days) and 4 (τ_{max} 17 days) bombs. This further confirms previous conclusions that type 1 vesiculated bombs with red-brown interiors represent the first erupted products during the onset of Vulcanian explosions during the 1888-90 eruption and represent the remanence of the conduit plug prior to the eruption, and therefore have the longest calculated τ due to the slow cooling and crystallisation of the magma forming the plug close to the surface. Conversely, type 2 and 3 vesiculated bombs represent juvenile material, crystallising over shorter periods of time (τ_{max} 10 days).

Calculated crystallisation times for the largest microlites, using the shallowest portion of the CSD slope at the largest crystal sizes and the universal growth rate of 10^{-8} are between 16 and 23 days for type 1 bombs, 16 to 19 days for type 2 bombs, 13 to 23 days for type 3 bombs and 19 days for the type 4 bomb, whereas for the smallest crystal sizes they are between 7 and 20 days. The range in τ between small and large microlites are largest in type 2 dense and type 3 vesiculated bombs (up to 13 days) and may therefore record different processes prior to eruption, with larger crystals recording crystallisation conditions during initial ascent in the conduit, whereas small crystals record the final stages of magma ascent in the conduit. Timescales for the largest and smallest microlites in

type 1 bombs overlap, which further supports the conclusion that type 1 bombs represent the initial volcanic plug. The largest differences in crystallisation times are observed in type 2 and 3 bombs.

Nucleation rates, J are calculated using G and n_0 to deduce changing crystallisation conditions in the shallow conduit prior to eruption (Marsh 1988). Using a constant growth rate of 10^{-8}, yields nucleation rates of 0.05 to 0.06 $mm^{-3}s^{-1}$ for type 1 bombs, 0.89 to 1.77 $mm^{-3}s^{-1}$ for type 2 bombs, 0.48 to 2.50 $mm^{-3}s^{-1}$ for type 3 bombs, and 0.19 $mm^{-3}s^{-1}$ in the type 4 bomb. Calculated nucleation rates show changes in the crystallisation conditions in the magmas feeding eruptions for each bomb type prior to eruption. The calculated nucleation rates (Table 3.2) are highest in the type 2 dense bombs, and lowest in type 1 vesiculated bombs. Low nucleation rates in type 3 vesiculated bombs reflects the slow cooling of the magma in the plug, as experimental studies have shown crystal growth and nucleation rates are a function of ΔT (Williams *et al.* 1954; Hammer & Rutherford 2002).

Calculated nucleation rates for the 1888-90 eruption using a growth rate of 10^{-8} mms^{-1} are mostly within the range of breadcrust bombs from Galeras volcano, Colombia (Bain *et al.* 2019). It must be noted that growth rates and nucleation rates vary with the degree of undercooling (Hammer & Rutherford 2002; Couch *et al.* 2003) and may therefore be underestimated if there was a higher degree of undercooling fitting the model of a transcrustal magmatic system at La Fosssa di Vulcano.

3.5.4 Origin of breadcrust bombs during the 1888-90 eruption

Previous studies indicate the top of the magma region is located in the shallow crust (1500 – 2000 m depth; Clocchiatti *et al.* 1994). Due to the intermittent nature of explosions observed by Mercalli & Silvestri (1891) this study suggests the Vulcanian explosions were controlled by volatiles and over pressure in the conduit, as type 1, 2 and 3 bombs have the

same geochemical characteristics but are characterised by different textures resulting from different styles of explosions and decompression. It is proposed the similar geochemistry of type 1, 2 and 3 bombs indicate they are all sourced from the same magma and subsequently modified during ascent in the conduit (Fig. 3.9) at shallow levels (<1500m; Clocchiatti *et al.* 1994).

Type 1 vesiculated bombs with a red-brown interior are texturally distinct from type 3 bombs. These bombs have markedly longer crystallisation times compared to type 2 and 3 bomb types and lower feldspar number densities (N_A) volumetric feldspar number densities, (N_v) and nucleation rates (J), high crystal sizes (L_c) and mean crystal areas, characterised by low degrees of undercooling. Furthermore, the curved shape of the CSD slopes suggest a multi-step magma ascent with stalling in the upper conduit prior to the onset of Vulcanian eruption, with long crystallisation times possibly at the same level in the ascent pathway. Type 1 bombs represent the top of the volcanic plug and formed under closed system degassing conditions due to gas overpressure as a result of the conduit being plugged prior to the onset of the eruption resulting in fewer crystals per unit area and smaller crystals.

Type 2 dense bombs have a uniform texture and morphology throughout, forming some of the smallest bombs erupted during the 1888 -90 eruption. Type 2 bombs are characterised by slow growth rates, high nucleation rates, high feldspar number densities (N_A), and volumetric feldspar number densities (N_v), and low mean crystal areas and crystal sizes (L_c), indicating the magma underwent degassing and high degrees of undercooling prior to eruption. It is postulated dense bombs formed below the type 1 forming region in a dense, crystalline magma with limited gas undergoing rapid magma ascent under relatively closed system degassing conditions. Therefore, type 2 dense bombs are some of the earlier

erupted bombs during the initial onset of Vulcanian explosions following the eruption of type 1 bombs. Dense bombs have slower ascent rates and less fragmentation.

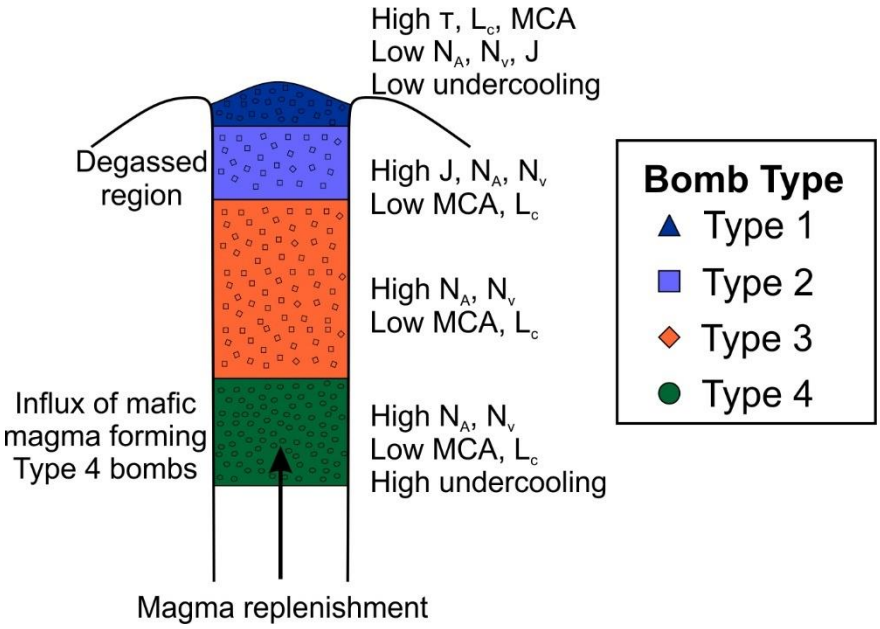

Fig. 3.9: Conceptual model showing the architecture of the conduit during the 1888-90 eruption and the origin of each bomb type.

Type 3 vesiculated bombs are the 'classic' breadcrust bombs with expansion cracks and vesiculated interiors resulting from volatile exsolution erupted from La Fossa di Vulcano. Type 3 bombs are characterised by glassy rinds indicate bubble nucleation, growth and coalescence occurred as a result of magma degassing. A large volume of bombs located on the crater rim are type 3 indicating an almost continuous prolonged eruption of vesiculated bombs, possibly emptying the conduit. Type 3 bombs are characterised by relatively slow crystal growth rates, quite high feldspar number densities (N_A), and volumetric feldspar number densities (N_v), and low crystal sizes (L_c), suggesting the magma was subjected to moderate degrees of undercooling. These bombs are characterised by moderate ascent rates under relatively open system degassing conditions, forming a high number of small crystals.

Type 4 scoriaceous bombs are intermittently identified by their dark grey appearance and large coalesced vesicles. This bomb type is characterised by high feldspar number densities (N_A), high volumetric feldspar number densities (N_v), the smallest mean crystal areas, low crystal sizes (L_c), and high degrees of undercooling. These bombs have long crystallisation times and undergo the highest degree of decompression, similar to type 1 bombs. Type 4 bombs result from mafic recharge and gas over pressurisation driving the Vulcanian eruption. Type 4 bombs represent the most mafic compositions erupted during this period due to magma replenishment during the middle to latter stages of the eruption indicating the presence of a compositionally layered volcanic plug. Conversely, De Fino *et al.* (1991) interpreted these scoriaceous bombs to mark the beginning of the 1888-90 eruption as they rested on a yellow layer above the Pietre Cotte activity. However, in this study type 4 bombs were found sparsely distributed across the bomb field. It must be noted that type 4 bombs are compositionally very similar to the underlying Pietre Cotte latitic enclaves indicating they originate from the same latitic magma as the preceding eruption, not the main 1888 eruption feeding magma (see chapter 2; De Fino *et al.* 1991; Clocchiatti *et al.* 1994).

3.5.5 Comparisons to other Vulcanian eruptions

Previous research on Vulcanian eruptions has assumed the presence of a zoned magma with gradual degassing and outgassing at decreasing depths in the volcanic conduit resulting in textural and density variations (e.g. Druitt *et al.* 2002; Melnik & Sparks 2002; Clarke *et al.* 2007; Wright *et al.* 2007; Burgisser *et al.* 2010; Gianchetti *et al.* 2010; Isgett *et al.* 2017). For Soufrière Hills, Montserrat, Kennedy *et al.* (2005) proposed the observed banded and brecciated clasts derived from the conduit margin whilst pumice clasts are derived from the conduit centre.

More recently, research has focused upon using breadcrust bombs to decipher the pre-eruptive magma processes leading up to Vulcanian eruptions. However, surprisingly very little focus has been given to the first described Vulcanian eruption (Mercalli & Silvestri 1891), the 1888-90 eruption of La Fossa di Vulcano. The results from this study indicate the presence of a layered volcanic plug within the shallow conduit system of the 1888-90 eruption, evidenced by the presence of contrasting textures, the degree of vesicularity and evidence of mingling in eruptive products.

Our results indicate various processes including, changing ΔP and ΔT, varying ascent rates, multi-step ascents, magma replenishment and the switch from nucleation to growth dominated crystallisation in the conduit system resulting in compositional and textural variations in formation and eruption of bombs. The eruption of bombs during the 1888-90 eruption was also accompanied by numerous smaller explosions resulting in PDCs and fallout forming pumice, scoriae, and lapilli (Clocchiatti *et al.* 1994). The results from this study further develop and reinforce our current knowledge of the driving forces of Vulcanian eruptions e.g. switching between open- and closed-system degassing, or growth dominated to nucleation dominated crystallisation, and varying magma ascent rates.

3.6 Conclusion

This study of the 1888-90 Vulcanian eruption of La Fossa di Vulcano presents a new model showing the evolution of the conduit concluding changes from closed to open system degassing, decompression under small degrees of ΔT, and varying magma ascent rates produced type 1, 2, 3 and 4 bombs.

- Type 1 vesiculated bombs represent the volcanic plug blocking the conduit prior to the eruption resulting in nucleation dominated crystallisation under increasing ΔT

under closed-system conditions, reflecting multi-step ascent accompanying periods of stalling in the upper conduit with crystallisation times, τ_{max} up to 20 days.

- Type 2 dense bombs are associated with the highest degree of ΔT of all bomb types accompanying the shortest calculated crystallisation times of all bomb types, τ_{max} 7 days forming from a dense, degassing crystalline magma in the plug.
- Type 3 vesiculated bombs underwent a steadily rapid ascent in the conduit with constant crystal growth rates, high Ø, representing the transition to open-system conditions in the plug with rapid and steady ascent in the conduit with microlite crystallisation times, τ_{max} up to 10 days.
- The most mafic, type 4 scoriaceous bombs formed due to magma recharge from the latitic magma storage region during the eruption, accompanied by fast magma ascent rates and gas over pressurisation driving the Vulcanian eruption with crystallisation times τ_{max} up to 17 days. Microlites in type 4 bombs have the smallest mean crystal areas and low crystal sizes.

This study indicates the key processes in governing Vulcanian eruptions are i) magma ascent rates and ii) gas over pressurisation and microlite crystallisation times are variable during the 1888-90 eruption of La Fossa di Vulcano, resulting in the different micro-textures observed. These results may also be applicable to other Vulcanian eruptions at volcanic arcs.

CHAPTER 4 –Mantle source versus crustal contamination: An O and Sr isotope study of the central Aeolian arc, Italy

4.1 Introduction

The crust plays an important role during petrogenesis at volcanic arcs. Contamination of arc magmas results in large geochemical and isotopic variations of mantle derived melts. Processes of contamination can broadly be divided into two models; 1) source contamination where crustal material is derived from the subducted slab and added to the arc magma mantle source and 2) crustal contamination where mantle derived magmas are contaminated through interaction with crustal material during magma ascent (e.g. James 1981; Hildreth & Moorbath 1988; Vroon *et al.* 1993; Wilson 1997; Patino *et al.* 2000; Turner & Foden 2001). The role of the subducted lithosphere in the generation of arc magmas is extremely complex, due to the wide variety of potential island arc magma sources (Plank & Langmuir 1998). Sources of arc magmas can be broadly divided into 1) the mantle wedge consisting of the oceanic or continental lithosphere and the asthenospheric upper mantle, and 2) the oceanic crust comprising metamorphosed igneous rocks (basalt, gabbro) and oceanic sediments (e.g. pelagic clays, carbonates, and terrigenous clastic sediments). Source contamination results in the altering of the chemical composition of the mantle wedge during subduction by fluids and melts derived from subducting sediments and oceanic crust (e.g. Ryan & Langmuir 1993; Elliot *et al.* 1997; Johnson & Plank 1999; Eiler *et al.* 2005; Hermann & Rubatto 2009; Martin *et al.* 2014; Gazel *et al.* 2015). Crustal signatures from volcanic arcs are dependent upon compositions of source components, namely, the subducting oceanic crust, overlying sediments and the mantle, and the thermal regime of the system (e.g., Hermann *et al.* 2006; Klimm *et al.*

2005; 2008; Hermann and Rubatto 2009; Skora & Blundy 2010; Avanzinelli *et al*. 2012; Martindale *et al.* 2013; Skora *et al.* 2015).

Oxygen (O) and Strontium (Sr) isotopes are extremely useful tracers to constrain source contamination and the interaction with crustal material during magma ascent due to large variations in isotopic ratios between the crustal and mantle derived magmas (James 1981; Davidson 1985; 1986) such as those associated with subduction zone volcanoes situated on continental crust (Eiler *et al.* 2000; Sharp 2006). Variations in oxygen and strontium isotope signatures occur when mantle-derived magmas stall in complex magma plumbing systems and undergo extensive interaction with continental crustal material during magma ascent via wall-rock assimilation or combined assimilation and fractional crystallisation (AFC) processes (James 1981; Davidson 1985; Altherr *et al.* 1988; Ellam *et al.* 1988; 1989; Ellam & Harmon 1990; Eiler *et al.* 2000). Small scale variations in evolved products, less than 1‰, in $\delta^{18}O$ (James 1981) may also result from closed-system fractional crystallisation (Eiler *et al.* 2000).

Previous studies highlighted that both source and crustal contamination occur in continental arcs, however it is frequently difficult to distinguish between the two processes. Examples include the Andes, South America (e.g. Hildreth & Moorbath 1988; Davidson *et al.* 1990), the Lesser Antilles arc, Caribbean (e.g. Davidson 1987; Van Soest *et al.* 2002), the Sunda arc, Indonesia (e.g. Gasparon *et al.* 1994; Turner & Foden 2001; Gertisser & Keller 2003; Troll *et al.* 2013; Handley *et al.* 2014) and the Aeolian Islands (Ellam 1986; Ellam *et al.* 1988; 1989; Ellam & Harmon 1990; Gertisser & Keller, 2000). Significant aspects of crustal contamination in magmatic systems, particularly in geodynamically complex volcanic arcs, such as the active Aeolian arc, remain poorly constrained.

The Aeolian arc is characterised by some of the largest within arc geochemical variations in the world, which cannot be explained solely by crustal interactions (Peccerillo *et al.*

2013). The large geochemical variability observed in the Aeolian arc have previously been attributed to variations in melt sources to regional variations in the degree of partial melting (e.g. Ellam *et al.* 1988; Francalanci *et al.* 1993; De Astis *et al.* 2000; Peccerillo 2005; Peccerillo *et al.* 2013). This study of the central Aeolian arc provides a comprehensive picture of crustal contamination processes and their influence magma genesis across the central Aeolian arc. These aspects include (1) the extent of crustal assimilation and the distinct crustal contaminant(s) at different crustal levels in the subvolcanic plumbing systems of Salina, Vulcano and Lipari, (2) the degree of crustal assimilation at various stages of magma differentiation, and (3) the role of crustal assimilation in influencing magma composition.

We present a detailed O-Sr isotope study of minerals (pyroxene, plagioclase, and olivine) and glass (obsidian and pumice glass) of rock samples from key eruptions of the young (< 42 ka; Forni *et al.* 2013) and active volcanic centres of Vulcano, Lipari and Salina after the switch from mafic to felsic volcanism in the central sector of the Aeolian arc. This is the first detailed, large-scale study to quantitatively assess the influence of crustal assimilation on the generation of intermediate and felsic (evolved) magmas in the Aeolian arc using mineral separates (clinopyroxene, plagioclase and olivine), obsidian and volcanic glass. This study builds upon previous whole-rock O and Sr data for the central Aeolian arc (Ellam 1986; Ellam & Harmon 1990; Gertisser & Keller 2000). The O-Sr isotopic data and associated whole-rock geochemical data are combined with new geochemical and O-Sr isotope data of the characteristic crustal xenoliths from the Calabro-Peloritano sub-volcanic basement to quantitatively assess the role of source- and crustal contamination at the most hazardous volcanoes in the Aeolian arc.

We show that whilst source contamination of primary magmas in the central Aeolian arc is dominated by altered oceanic crust (AOC) fluids, however, subducted sediments also

contaminate these magmas at deep levels in the subvolcanic system overprinting mantle signatures. Subsequent crustal contamination is dominated in the mid- and upper-crustal levels by meta-sediments and gneisses on Vulcano and Lipari and carbonate lithologies on Salina.

4.2 Study System

Intermediate to felsic volcanism characterises and dominates the most recent eruption stages on Vulcano, Lipari and Salina after a distinct switch to (and the first occurrence of rhyolitic volcanism in the Aeolian archipelago) that occurred at 27.5 ka on Salina, at 42 ka on Lipari and at 28 ka on Vulcano (De Astis *et al.* 2013; Forni *et al*. 2013; Lucchi *et al.* 2013b). This study focuses on key eruptions and volcanic centres after this switch occurred namely: (1) La Fossa di Vulcano, Vulcano (5.5 ka – present; Keller 1970; 1980a; De Astis *et al.* 1997; 2013), widely regarded as the most hazardous volcano in the Aeolian arc, which produced explosive and lava eruptions of latitic to rhyolitic throughout its history and last erupted in 1888-90 (type Vulcanian eruption); (2) the Lentia domes, Vulcano (15 – 13 ka; Keller 1980a; De Astis *et al.* 1997; 2013); (3) the rhyolitic southern lava domes and associated explosive eruptions, Lipari (c. 43 – 20 ka; Gillot 1987; Crisci *et al.* 1991; Forni *et al.* 2013); (4) the northern rhyolitic centres, Lipari, which produced both pumice deposits and obsidian lavas during two eruptive episodes (8.7 ka – 1220 AD; Keller 2002; Tanguy *et al.* 2003; Zanchetta *et al.* 2011; Forni *et al.* 2013); (5) the ~ 30 ka andesite lava and subsequent andesitic to rhyolitic and rhyolitic eruptions of the Pollara crater, Salina, that occurred at 27.5 ka and 15.6 ka and terminated volcanism on Salina (Keller 1980b; Gillot 1987; Morche 1988; Calanchi *et al.* 1993; Sulpizio *et al.* 2008; Lucchi *et al.* 2013b).

Geochemical studies in the southern Tyrrhenian Sea define an upper mantle with a Mid-Ocean Ridge Basalt (MORB-) to Ocean Island Basalt (OIB-) type composition (Trua *et al.*

2004; 2011). Previous studies on the Aeolian archipelago to the source compositions of magmas have identified a minimum of three distinct end members for contamination; the pre-metasomatic mantle, subducted Ionian crust, and subducted Ionian sediments (Peccerillo *et al.* 2013). In the Aeolian archipelago mantle wedge heterogeneity, resulted in the observed variations in radiogenic isotopes in the mafic rocks (e.g. Ellam 1986; Ellam *et al.* 1988; Ellam & Harmon 1990; Francalanci *et al.* 1993; De Astis *et al.* 2000; Peccerillo *et al.* 2004; 2013), however, the considerable influence of magma-crust interactions raises many questions as to the respective contributions of source heterogeneity and magma contamination during differentiation particularly in the central sector. Large variations in both source contamination and crustal contamination are observed across the three sectors in the Aeolian arc (western, central, and eastern). A general increase is observed in $^{87}Sr/^{86}Sr$ and decrease in $^{143}Nd/^{144}Nd$ from West to East, indicating the degree of source contamination increases by subducted sediments increases to the East (e.g. Ellam 1986; Ellam *et al.* 1988; 1989; Ellam & Harmon 1990; Francalanci *et al.* 1993; 2004; 2007; De Astis *et al.* 2000; Peccerillo 2005).

The Calabro-Peloritano basement comprises a volcanic and sedimentary/metasedimentary cover (0 - 5 km) above a continental crust (5 - 20 km) composed predominantly of gneisses, metabasites and granitoids (Peccerillo *et al.* 2006; De Astis *et al.* 2013; Forni *et al.* 2013; Lucchi *et al.* 2013b). This is evidenced by the occurrence of abundant crustal xenoliths in the eruptive products of the Aeolian arc volcanoes (Bergeat 1910; Honnorez & Keller 1968; Keller 1980a, b; Pichler 1980; Ellam 1986; Barker 1987; Ellam *et al.* 1989; Ellam & Harmon 1990; Esperança *et al.* 1992; Del Moro *et al* 1998; Gioncada *et al.* 1998; 2003; 2005; Zanon *et al.* 2003; Frezzotti *et al.* 2004; Zanon & Nikogosian 2004; De Astis *et al.* 2013; Forni *et al.* 2013; Lucchi *et al.* 2013b), with metapelites, quartzites, granitoids, gneisses and metabasites (Ellam 1986; Ellam & Harmon 1990; Gertisser & Keller 2000).

Important regional variations in the central Aeolian arc include the occurrence of abundant marls, marbles, and calc-silicate xenoliths in eruptive products of the highly explosive Pollara eruptions on Salina, which suggest a significant role of magma-carbonate interaction in at least this part of the arc, even though rare calc-silicate xenoliths were also reported from the western Aeolian Islands (Filicudi, Alicudi) as well as in older rocks from Vulcano (Honnorez & Keller 1968). Despite the abundance and lithological variations present in crustal xenoliths from the Aeolian arc, only two xenolith samples, a granodiorite and a leucogneiss from the Upper Pollara eruption, Salina have previously been analysed with $^{87}Sr/^{86}Sr$ ratios of 0.70548 and 0.71424 and $\delta^{18}O$ ratios of +7.9 ‰ and +10.7 ‰, respectively (Ellam 1986; Ellam *et al.* 1988; Ellam & Harmon 1990). Two ultramafic xenoliths from Alicudi yielded $^{87}Sr/^{86}Sr$ ratios between 0.703692 and 0.703827, with $\delta^{18}O$ in clinopyroxene and olivine ranging from +5.08 ‰ and +5.14 ‰ (Peccerillo *et al.* 2004).

4.3 Methods

Forty-three samples covering lavas, enclaves, pumice, scoria, ash, breadcrust bombs and twelve crustal xenoliths were analysed from the central Aeolian arc, comprising the recent eruptions since the onset of rhyolitic volcanism in the central sector (Appendix C). For whole-rock major element compositions, samples were washed in deionised water for 48 hours and all weathered and altered surfaces were removed. Samples were then crushed in a jaw crusher and reduced to a fine powder in an agate mill for 2 – 6 minutes and dried overnight at 130°C. Major elements were analysed using Inductively Coupled Plasma – Atomic Emission Spectroscopy (ICP-AES) at Bureau Veritas Minerals laboratories, Canada, using the lithium metaborate (LiB_2) flux fusion, followed by dilution using dilute nitric acid. Andesite and rhyolite standards were used for calibration. Detection limits for the major elements were 0.01 wt.% with the exception of Fe_2O_3 which was 0.04 wt.%. For

trace elements the detection limits were 1 ppm for Sc, 2 ppm for Sr, 3 ppm for Y, 5 ppm for Ba, Nb, Zr and 20 ppm for Cr and Ni. Precision was better than 5%.

For O and Sr isotopes, samples were washed and cut to remove weathered and altered material in the laboratory, and then briefly crushed in a jaw crusher and sieved. Feldspar, pyroxene, and olivine were had picked from the 250 – 125 µm sieve fractions using a binocular microscope, making sure crystals were free of inclusions and prismatic.

Stable O isotope analysis on mineral separates (1 – 4 mg) of pyroxene (n = 25), feldspar (n = 30), olivine (n = 3), obsidian glass (n = 8) and pumice glass (n = 13) were performed at Scottish Universities Environmental Research Centre, East Kilbride, UK. Mineral separates were selected over whole-rock $\delta^{18}O$, as whole-rock analyses are highly susceptible to post-eruptive hydrothermal and deuteric alteration and weathering processes (Eiler et al. 1995). Furthermore, it is generally accepted that whole-rock analyses may mask some of the detailed information that can only be extracted from rock components, such as fresh magmatic minerals and volcanic glass (Eiler et al.1995). Oxygen isotope analyses were carried out using the laser fluorination method of Sharp (1990). Pyroxene and obsidian glass underwent overnight pre-fluorinations in a block of 12 (9 samples and 3 standards), feldspar underwent a 90 second pre-fluorination in a block of 12, whereas pumice glass samples were run one at a time with a standard and underwent a 90 second pre-fluorination with a standard analysed after each analysis. Two garnet standards (UWG-2 (5.8‰ ± 0.1‰); GP147 (7.3‰ ± 0.1‰)) and a quartz standard (YP2 (16.4‰)) were run at the beginning, middle and end of each run, and precision is better than ± 0.2 ‰. All measured values for standards were close to the accepted values, therefore no corrections were made. Repeat measurements of unknown samples are all better than ± 0.3‰ for pyroxene, feldspar, olivine, and obsidian glass, and ± 0.5‰ for pumice glass.

Whole-rock O isotopes of the xenoliths were measured at Scottish Universities Environmental Research Centre, East Kilbride, UK. The samples were washed and cut to remove weathered and altered material in the laboratory and crushed to a fine powder in an agate mill. Xenolith powders underwent a 90 second pre-fluorination. Bulk whole-rock O isotopes for the carbonate xenoliths were analysed using conventional procedures at Scottish Universities Environmental Research Centre, East Kilbride, UK. CO_2 gas was extracted from the sample by the reaction with 103% H_3PO_4 at 70°C, and the resultant CO_2 gas was dried, purified and measured using an Analytical Precision AP 2003 Mass Spectrometer and all samples were corrected as calcite. $\delta^{18}O$ values for the carbonate xenoliths are reported relative to Vienna Standard Mean Ocean Water (V-SMOW), with analytical accuracy typically better than ± 0.2‰.

Strontium isotope compositions on 12 rock samples (6 feldspars, 4 pyroxenes, and 2 obsidians) and 7 whole-rock xenolith samples were measured from 40 – 80 mg of sample. Samples were leached and digested following the methods of Smet *et al.* (2010) and Cassidy *et al.* (2012), using Sr spec™ resin. Samples were dissolved in a HF-HNO_3 solution for 24 hours at 130°C on a hotplate. The solutions were then evaporated (until dry), and concentrated HCl was added to the samples for a further 12 hours, followed by a further dry down. The samples were then run through Sr columns using Sr spec™ resin following the method of Smet *et al*. (2010). Sr isotopes were measured on a ThermoFisher TRITON Plus (7 collectors) mass spectrometer at the National Oceanography Centre, Southampton, UK. $^{87}Sr/^{86}Sr$ ratios were normalized for mass fractionation to $^{86}Sr/^{88}Sr$ = 0.1194. The measured standard, NBS-987 yielded an average $^{87}Sr/^{86}Sr$ of 0.710249±0.0000132 (2SE, n=3) and were not corrected for any offset as the obtained values were in agreement with the reference value.

4.4 Results

4.4.1 Petrography and geochemistry of erupted products and xenoliths

4.4.1.1 Eruptive products

Recent erupted products from the central Aeolian arc span a large range from lavas, which in some case contain mafic co-magmatic enclaves, to pyroclastic (ash, pumice, scoriae) deposits. Eruptive products from the Pollara eruptions on Salina belong to the calc-alkaline magma series (Fig. 4.1), with a large compositional range from basalt to rhyolite (50.80 to 69.16 wt.% SiO_2, Table 4.1). On Salina, rhyolites are only found in the most recent eruption of the Pollara tuff ring (Keller 1980b; Sulpizio *et al.* 2008; Lucchi *et al.* 2013b). Recent eruptive activity on Lipari (<42 ka; Crisci *et al.* 1991; Di Martino *et al.* 2010) is dominated by high-K calc-alkaline, rhyolitic volcanism (67.33 to 75.57 wt.% SiO_2, Table 4.1), dominated by the eruption of rhyolites. A small high-K dacitic dome sample (66.96 wt.% SiO_2, Table 4.1) and enclave (59.08 wt.% SiO_2, Table 4.1) within the dome from the Falcone dome, located at Punta della Crapazza are the only two samples analysed from Lipari which are not rhyolitic. Eruptive products from Vulcano range from shoshonites to latites, trachytes and rhyolites (51.74 to 73.34 wt.% SiO_2, Table 4.1), defining a high-K calc-alkaline to shoshonitic series, with most samples having a shoshonitic affinity (Fig. 4.1).

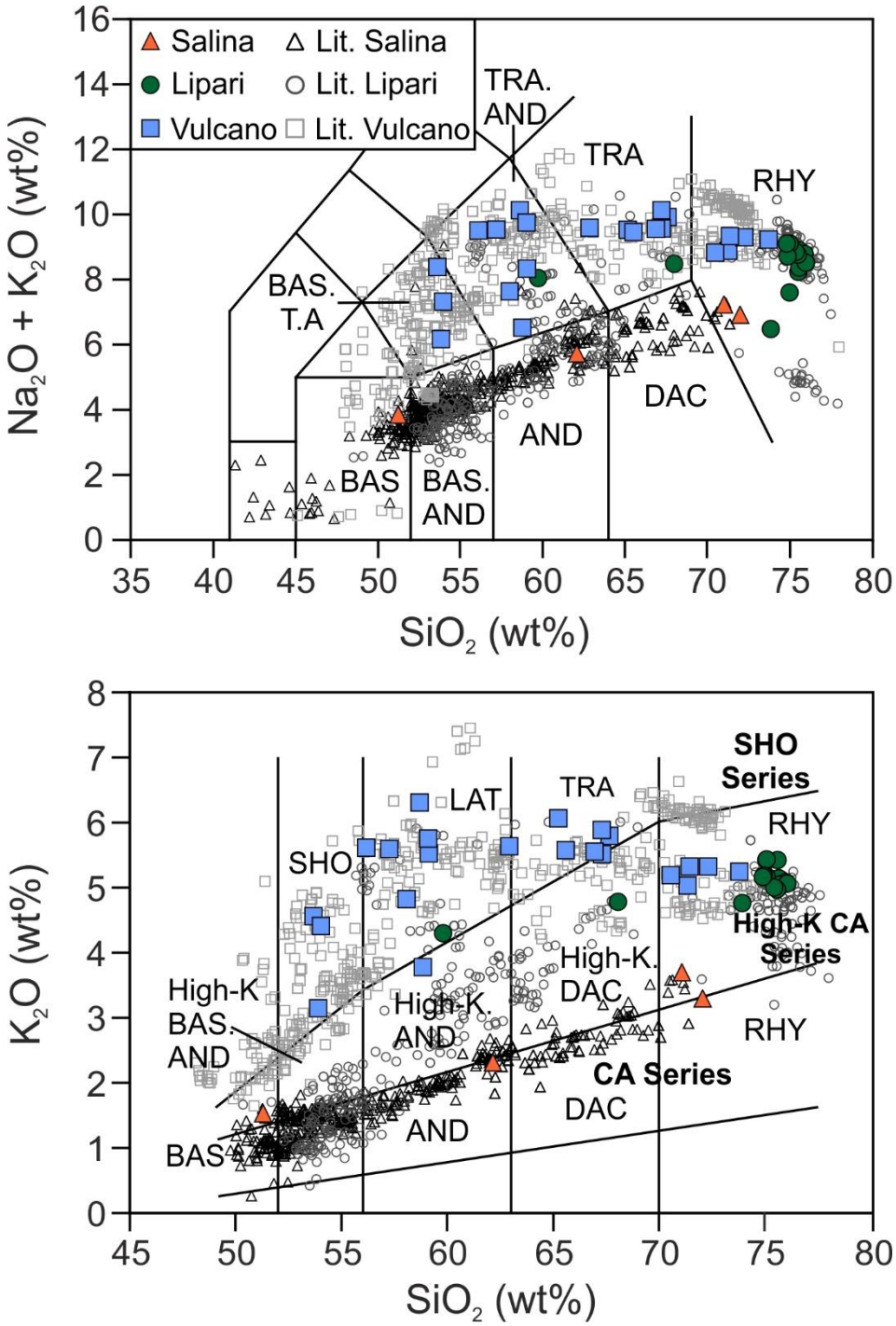

Fig. 4.1: (A) Total Alkali versus SiO_2 (Le Bas *et al.* 1986) and (B) K_2O versus SiO_2 classification diagrams (Peccerillo & Taylor 1976) from the central sector of the Aeolian archipelago (Triangles: Salina; Circles: Lipari; Squares: Vulcano). Oxides are expressed in weight percent (wt.%), and compositions are all normalised and LOI-free. Existing literature data (light grey) from De Astis *et al.* (2013); Forni *et al.* (2013) and Lucchi *et al.* (2013b) and references therein.

Table 4.1: Selected major- and trace-element compositions for all analysed rock samples from recent eruptions in the central sector of the Aeolian Archipelago. b.d. below detection limit n.a. not analysed.

Island	Salina				Lipari		
Volcanic Centre	Pollara				Southern Dome Field		
	Punta di Perciato	Lower Pollara		Upper Pollara	Punta del Perciato		Falcone
Sample	SAL13/19	SAL16-2	SAL16-5	UP	AI-17-080	AI-17-141	AI-17-138
	Lava	Scoria	Pumice	Pumice	Lava	Pumice	Pumice
SiO_2	61.71	50.80	69.16	67.93	75.17	70.16	71.34
TiO_2	0.48	0.78	0.23	0.26	0.08	0.08	0.07
Al_2O_3	16.84	19.11	14.01	14.33	12.91	12.92	12.38
Fe_2O_3	5.47	9.30	2.28	2.35	1.55	1.57	1.51
MnO	0.13	0.16	0.10	0.10	0.05	0.05	0.05
MgO	2.69	4.46	0.79	0.80	0.11	0.36	0.10
CaO	6.23	10.52	2.55	2.60	0.70	0.82	0.77
Na_2O	3.41	2.32	3.74	3.68	3.77	2.52	3.10
K_2O	2.30	1.52	3.16	3.53	5.10	5.06	5.11
P_2O_5	0.14	0.19	0.05	0.08	b.d.	0.01	0.02
LOI	0.40	0.50	3.70	4.10	0.50	6.40	5.50
Total	99.80	99.66	99.77	99.76	99.94	99.95	99.95
Ba	664	432	881	1158	b.d.	11	8
Sr	580	804	346	365	13	26	16
Zr	104	59	135	145	159	135	137
Nb	10	7	10	14	27	25	30
Y	16	17	11	14	35	34	6
Ni	b.d.	b.d.	b.d.	b.d.	b.d.	b.d.	b.d.
Cr	29	b.d.	b.d.	b.d.	b.d.	b.d.	b.d.
Sc	15	28	4	4	1	1	1

4.4.1.1.1 Salina

The Punta di Perciato lava marks the start of the Pollara activity on Salina. The lava is a calc-alkaline andesite with phenocrysts of plagioclase ($An_{42-95}Ab_{5-55}Or_{0-10}$), clinopyroxene ($Wo_{40-47}En_{38-46}Fs_{9-16}$), olivine, orthopyroxene, amphibole and Fe-Ti oxides set in a microcrystalline groundmass dominated by plagioclase (Fig. 4.2 A-E). The Lower Pollara pyroclastic succession comprises basalts to rhyolites (Fig. 4.1), with two end-member pumices analysed in detail in this study, a basalt, and a rhyolite.

Table 4.1 cont'd: Selected major- and trace-element compositions for all analysed rock samples from recent eruptions in the central sector of the Aeolian Archipelago. b.d. below detection limit n.a. not analysed.

Island	Lipari						
Volcanic Centre	Southern Dome Field						
	Falcone				Monte Guardia		
Sample	AI-17-138	AI-17-086	AI-18-065	AI-18-063	AI-17-100	AI-17-129	AI-18-066
	Obsidian	Lava	Dome	Enclave	Pumice	Pumice	Lava
SiO_2	74.68	75.57	66.96	59.08	72.40	67.33	74.09
TiO_2	0.07	0.07	0.25	0.46	0.08	0.07	0.07
Al_2O_3	12.81	12.89	15.13	16.98	12.37	13.85	12.68
Fe_2O_3	1.51	1.52	3.53	5.92	1.57	1.56	1.43
MnO	0.05	0.05	0.09	0.12	0.05	0.05	0.05
MgO	0.03	0.05	0.87	2.18	0.11	0.95	0.02
CaO	0.71	0.63	3.02	5.81	0.85	0.89	0.67
Na_2O	3.70	3.71	3.76	3.78	3.52	2.13	3.57
K_2O	4.98	5.05	4.70	4.24	4.82	4.33	4.92
P_2O_5	0.01	0.01	0.18	0.35	0.02	b.d.	b.d.
LOI	1.40	0.40	1.20	0.70	4.10	8.80	2.50
Total	99.95	99.95	99.69	99.62	99.89	99.96	100.00
Ba	b.d.	b.d.	373	713	12	8	b.d.
Sr	8	10	573	1111	24	39	7
Zr	132	149	136	124	128	135	133
Nb	27	30	22	14	30	31	30
Y	38	31	34	27	37	35	38
Ni	b.d.	b.d.	b.d.	b.d.	b.d.	b.d.	b.d.
Cr	b.d.	b.d.	b.d.	88	b.d.	b.d.	b.d.
Sc	1	1	4	10	1	2	1

The basalt has a mineral assemblage consisting of plagioclase ($An_{58-95}Ab_{5-33}Or_{0-10}$), clinopyroxene ($Wo_{42-47}En_{40-44}Fs_{10-15}$), olivine and Fe-Ti oxides with a microcrystalline to glassy groundmass of plagioclase, and minor olivine, clinopyroxene and Fe-Ti oxides. The rhyolites from the Lower and Upper Pollara eruptions comprise a mineral assemblage of plagioclase ($An_{29-94}Ab_{5-67}Or_{0-7}$), clinopyroxene ($Wo_{39-46}En_{36-46}Fs_{13-21}$), orthopyroxene, Fe-Ti oxides and biotite set within a glassy groundmass (Fig. 4.2).

Table 4.1 cont'd: Selected major- and trace-element compositions for all analysed rock samples from recent eruptions in the central sector of the Aeolian Archipelago. b.d. below detection limit n.a. not analysed.

Island	Lipari						Vulcano
Volcanic Centre	Northern Lipari						Lentia
	Gabellotto			Pomiciazzo	Pilato	Rocche Rosse	Lentia Dome
Sample	FBG	FBG-12	FBG-72	L10-016	Pilato	RR	V10-005
	Pumice	Obsidian	Obsidian	Obsidian	Pumice	Obsidian	Lava
SiO_2	72.50	74.10	74.22	74.57	71.59	74.28	70.97
TiO_2	0.07	0.07	0.07	0.07	0.07	0.07	0.18
Al_2O_3	12.79	12.78	12.90	13.17	12.67	13.24	13.76
Fe_2O_3	1.65	1.66	1.63	1.69	1.70	1.75	2.95
MnO	0.06	0.06	0.06	0.06	0.06	0.06	0.07
MgO	0.05	0.04	0.04	0.04	0.09	0.04	0.85
CaO	0.74	0.70	0.72	0.73	0.72	0.75	1.86
Na_2O	3.82	3.87	3.91	3.69	3.75	3.97	3.86
K_2O	4.99	4.87	4.91	5.39	4.94	5.11	5.00
P_2O_5	b.d.	b.d.	0.02	b.d.	0.01	b.d.	0.06
LOI	3.30	1.80	1.50	0.50	4.30	0.60	0.30
Total	99.97	99.95	99.98	99.91	99.90	99.87	99.86
Ba	13	10	11	12	14	14	163
Sr	17	12	13	13	14	14	209
Zr	171	168	169	173	175	185	179
Nb	33	30	30	30	30	31	27
Y	38	38	38	39	38	39	28
Ni	b.d.	b.d.	b.d.	b.d.	b.d.	b.d.	b.d.
Cr	b.d.	b.d.	b.d.	b.d.	b.d.	b.d.	44
Sc	b.d.	b.d.	b.d.	b.d.	1	b.d.	4

4.4.1.1.2 Vulcano

The pyroclastic rocks span a wide compositional range from shoshonites to rhyolites comprising pumice, scoria, and lithic fragments (Fig. 4.2F-J), whereas the lavas are latitic to rhyolitic in composition. Co-magmatic mafic enclaves in the lavas from Vulcano are porphyritic and latitic in composition. The mafic magmatic enclaves are mostly dark red in colour (Fig. 4.2 G), with the phenocryst assemblage dominated by plagioclase ($An_{41-66}Ab_{30-48}Or_{4-10}$), clinopyroxene ($Wo_{44-47}En_{38-46}Fs_{10-15}$), olivine ($Fo_{55-73}$) and Fe-Ti oxides set in a microcrystalline groundmass.

Table 4.1 cont'd: Selected major- and trace-element compositions for all analysed rock samples from recent eruptions in the central sector of the Aeolian Archipelago. b.d. below detection limit n.a. not analysed.

Island	Vulcano						
Volcanic Centre	La Fossa di Vulcano						
	Punte Nere			Grotta dei Palizzi			
Sample	AI-17-041	AI-18-058	AI-17-006	AI-17-073	AI-17-049	AI-17-117	AI-17-056
	Ash	Ash	Lava	Ash	Pumice	Obsidian	Enclave
SiO_2	52.26	55.77	57.00	57.02	62.99	70.92	57.21
TiO_2	0.68	0.55	0.60	0.50	0.35	0.18	0.62
Al_2O_3	16.47	14.90	18.75	14.25	14.93	13.57	15.76
Fe_2O_3	8.17	7.07	6.39	7.24	4.53	2.88	5.74
MnO	0.16	0.10	0.08	0.12	0.10	0.08	0.09
MgO	3.79	3.26	1.14	4.43	1.30	0.65	2.92
CaO	7.13	6.59	2.75	6.73	2.78	1.70	5.81
Na_2O	3.92	2.98	3.98	2.84	3.65	4.03	2.97
K_2O	4.44	4.63	6.12	3.66	5.85	5.28	5.34
P_2O_5	0.46	0.31	0.43	0.24	0.18	0.08	0.42
LOI	2.10	3.40	2.20	2.60	3.10	0.50	2.70
Total	99.58	99.56	99.44	99.63	99.76	99.87	99.58
Ba	1054	794	2281	522	427	185	951
Sr	1290	964	1589	826	375	182	1087
Zr	160	185	192	130	297	207	174
Nb	19	19	23	17	31	32	22
Y	21	22	13	27	31	38	33
Ni	b.d.	21	b.d.	20	b.d.	b.d.	b.d.
Cr	117	88	b.d.	248	29	b.d.	88
Sc	17	19	7	21	7	4	18

The porphyritic lavas (Fig. 4.2F) and pyroclastic deposits (Fig. 4.2 H-I) comprise a mineral assemblage consisting of plagioclase ($An_{36-70}Ab_{25-55}Or_{1-10}$), alkali feldspar ($An_{2-10}Ab_{29-58}Or_{35-69}$), clinopyroxene ($Wo_{34-49}En_{29-48}Fs_{6-28}$), and Fe-Ti oxides with minor apatite, biotite and amphibole phenocrysts set in a microcrystalline to glassy groundmass (Fig. 4.2F). The two obsidian lava flows from Grotta dei Palizzi 2 and Pietre Cotte are aphyric to subaphyric with glassy textures (Fig. 4.2J) and have abundant spherulites and mafic magmatic enclaves throughout the flows.

Table 4.1 cont'd: Selected major- and trace-element compositions for all analysed rock samples from recent eruptions in the central sector of the Aeolian Archipelago. b.d. below detection limit n.a. not analysed.

Island	Vulcano						
Volcanic Centre	La Fossa di Vulcano						
	Grotta dei Palizzi			Caruggi	Pietre Cotte		
Sample	AI-18-056	AI-18-057	AI-17-045	AI-17-034	AI-17-019	AI-17-021	AI-17-025
	Ash	Pumice	Lava	Pumice	Scoria	Pumice	Pumice
SiO_2	51.78	51.74	58.65	62.22	55.46	71.17	64.50
TiO_2	0.65	0.70	0.50	0.39	0.57	0.14	0.30
Al_2O_3	18.04	17.43	16.16	15.15	16.33	13.47	15.02
Fe_2O_3	8.13	8.57	6.50	5.26	7.31	2.55	4.31
MnO	0.16	0.14	0.11	0.11	0.14	0.08	0.10
MgO	3.67	3.26	2.41	2.05	3.23	0.41	1.41
CaO	7.21	6.30	4.99	4.01	5.94	1.35	3.20
Na_2O	3.13	3.08	4.02	4.00	3.94	4.04	3.96
K_2O	3.02	4.22	5.70	5.56	5.54	5.23	5.47
P_2O_5	0.40	0.45	0.32	0.25	0.40	0.06	0.18
LOI	3.30	3.70	0.30	0.70	0.70	1.40	1.30
Total	99.49	99.59	99.66	99.70	99.56	99.90	99.75
Ba	1033	959	761	584	948	104	408
Sr	1542	1138	845	609	1057	113	498
Zr	151	155	257	240	205	214	233
Nb	17	18	25	30	19	33	30
Y	24	24	28	30	26	39	32
Ni	b.d.	b.d.	b.d.	b.d.	b.d.	b.d.	b.d.
Cr	73	58	58	73	88	b.d.	58
Sc	17	15	12	10	14	3	7

4.4.1.1.3 Lipari

The rhyolitic lavas located in the northern dome field are fine grained to glassy (Fig. 4.2K). Conversely, the rhyolites from the northern dome field are aphyric to subaphyric obsidians (Fig. 4.2O) with abundant spherulites and mafic magmatic enclaves (Fig. 4.2L). Mafic magmatic enclaves (Fig. 4.2L) are common in the rhyolites from both the northern and southern dome fields with a mineral assemblage dominated by plagioclase, clinopyroxene, olivine and minor biotite.

Table 4.1 cont'd: Selected major- and trace-element compositions for all analysed rock samples from recent eruptions in the central sector of the Aeolian Archipelago. b.d. below detection limit n.a. not analysed.

Island	Vulcano						
Volcanic Centre	La Fossa di Vulcano						
	Pietre Cotte		Gran Cratere				
Sample	AI-17-009	AI-17-028	AI-17-070	AI-17-120	AI-18-072	AI-18-074	AI-18-076
	Obsidian	Enclave	Ash	Bomb	Bomb	Bomb	Bomb
SiO_2	73.34	56.86	68.73	67.20	66.68	66.68	66.18
TiO_2	0.11	0.54	0.19	0.27	0.28	0.28	0.28
Al_2O_3	13.39	16.50	13.62	14.88	14.83	14.80	14.93
Fe_2O_3	2.16	6.88	3.01	3.78	3.86	3.97	4.03
MnO	0.07	0.13	0.07	0.09	0.09	0.09	0.09
MgO	0.20	2.92	0.95	0.91	0.93	1.11	1.14
CaO	0.99	5.70	2.08	2.26	2.32	2.55	2.61
Na_2O	4.00	3.96	3.75	4.14	4.28	4.09	4.05
K_2O	5.20	5.55	5.05	5.75	5.82	5.45	5.48
P_2O_5	0.03	0.38	0.07	0.14	0.10	0.15	0.16
LOI	0.40	0.20	2.40	0.40	0.60	0.60	0.80
Total	99.89	99.62	99.92	99.82	99.79	99.77	99.75
Ba	62	918	173	374	376	368	389
Sr	59	1047	234	366	376	373	410
Zr	208	203	178	254	250	240	240
Nb	32	23	29	35	32	29	31
Y	39	24	34	32	32	32	31
Ni	b.d.	b.d.	b.d.	b.d.	b.d.	b.d.	b.d.
Cr	b.d.	73	58	29		44	b.d.
Sc	2	13	5	5	5	6	6

Pyroclastic deposits found on Lipari consist of pumice (Fig. 4.2M), lithic fragments and ash with obsidian fragments found throughout the Monte Guardia and Vallone del Gabellotto pyroclastic successions. The Vallone del Gabellotto and Monte Pilato pumices, are largely aphyric. The lavas and pyroclastic deposits (Fig. 4.2M-N) comprise a mineral assemblage consisting of plagioclase ($An_{18-76}Ab_{22-75}Or_{2-8}$), alkali feldspar ($An_{1-10}Ab_{25-60}Or_{30-69}$), clinopyroxene ($Wo_{36-49}En_{31-48}Fs_{6-27}$), and Fe-Ti oxides and amphibole phenocrysts set in a microcrystalline to glassy groundmass consisting of predominantly alkali feldspar, Fe-Ti oxides and minor clinopyroxene.

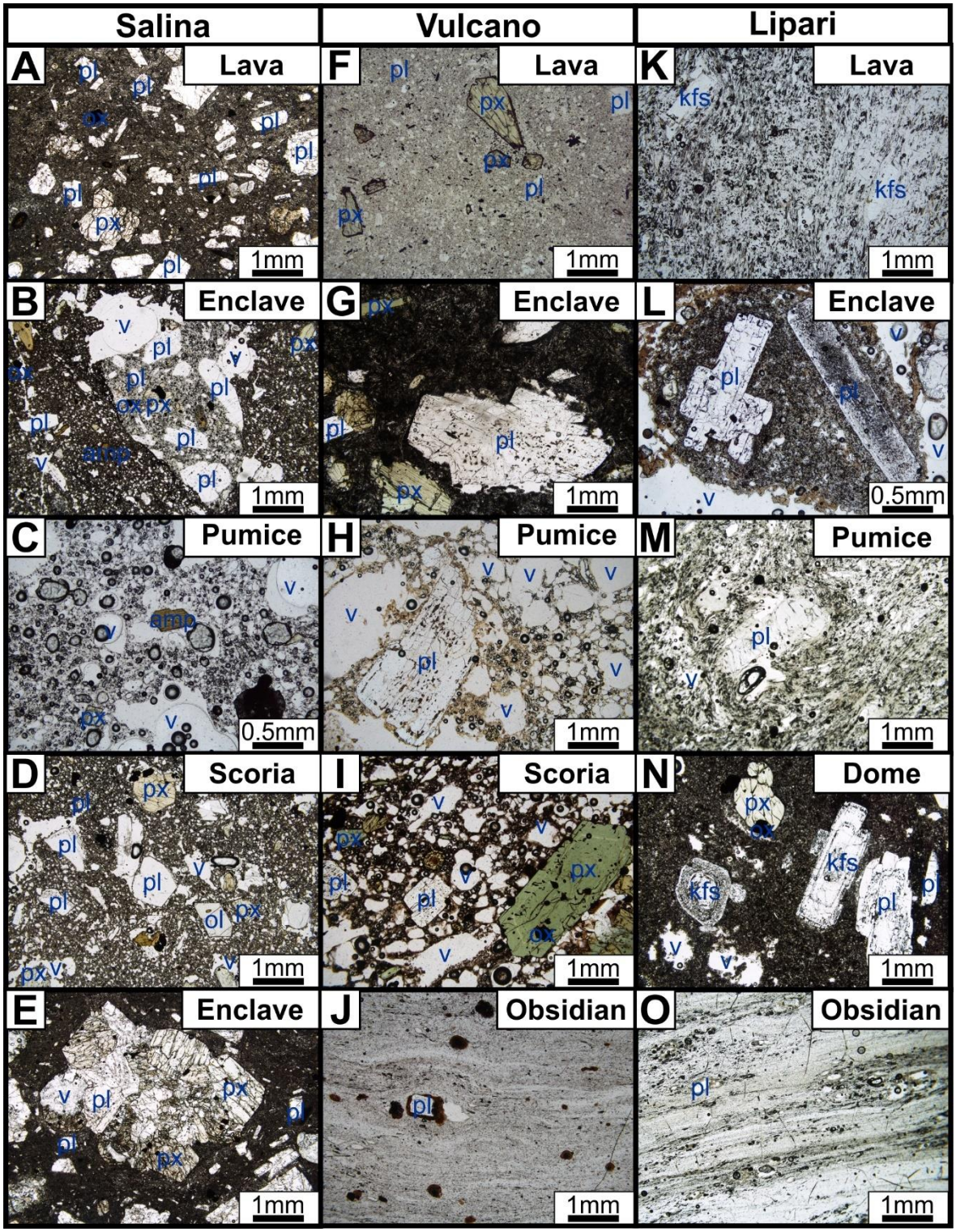

Fig. 4.2: Representative photomicrographs in from studied eruptions on Salina (A-E), Vulcano (F-J) and Lipari (K-O). (A) Punta del Perciato lava flow. (B) Enclave within the Lower Pollara scoria. (C) Lower Pollara pumice. (D) Lower Pollara scoria. (E) Enclave within Punta del Perciato lava. (F) Monte Lentia lava dome. (G) Grotta dei Palizzi 2 pumice. (I) Pietre Cotte scoria. (J) Pietre Cotte obsidian. (K) Punta di Perciato lava. (L) Enclave in Falcone dacitic dome. (M) Monte Guardia pumice. (N) Falcone dacitic dome. (O) Monte Guardia obsidian. Abbreviations: pl: plagioclase feldspar, px: pyroxene, amp: amphibole, v: vesicle.

4.4.1.2 Crustal xenoliths

Abundant xenoliths from the Calabro-Peloritano basement are found within deposits across the central Aeolian arc (Bergeat 1910; Honnorez & Keller 1968; Keller 1980a, b; Pichler 1980; Ellam 1986; Barker 1987; Ellam *et al.* 1989; Ellam & Harmon 1990; Esperança *et al.* 1992; Del Moro *et al* 1998; Gioncada *et al.* 1998; 2003; 2005; Zanon *et al.* 2003; Frezzotti *et al.* 2004; Peccerillo *et al.* 2004; Zanon & Nikogosian 2004; De Astis *et al.* 2013; Forni *et al.* 2013; Lucchi *et al.* 2013b). Twelve representative crustal xenoliths, ranging in size from 2 centimetres up to 20 centimetres, covering the range of xenoliths found in the central Aeolian arc were analysed in detail for whole-rock geochemistry and oxygen isotopes and seven of these were also analysed for Sr isotopes. The crustal xenoliths analysed in this study cover the range of xenoliths found in the Aeolian islands from carbonates, calc-silicates, metapelites, quartzites, granitoids, and gneiss (Bergeat 1910; Honnorez & Keller 1968; Keller 1980a, b; Pichler 1980; Ellam 1986; Barker 1987; Ellam *et al.* 1989; Ellam & Harmon 1990; Esperança *et al.* 1992; Del Moro *et al* 1998; Gioncada *et al.* 1998; 2003; 2005; Zanon *et al.* 2003; Frezzotti *et al.* 2004; Peccerillo *et al.* 2004; Zanon & Nikogosian 2004; De Astis *et al.* 2013; Forni *et al.* 2013; Lucchi *et al.* 2013b).

4.4.1.2.1 Carbonate and calc-silicate xenoliths

Carbonate xenoliths appear to occur only on Salina throughout the Lower and Upper Pollara pyroclastic successions, suggesting localised carbonate crustal lithologies in this part of the arc. Four carbonate xenoliths were analysed in this study (Table 4.2 and Fig. 4.3A-D), two limestones and two marbles. Two xenoliths (SAL17-3-3 and SAL17-3-6, Fig. 4.3A-B) have high CaO contents (>50 wt.%) and abundant trace fossils, representing localised limestone lithologies on Salina. Two further carbonate xenoliths (SAL17-3-4 and

Pollara 026) have large, recrystallised calcite comprising >95 vol.% (Fig, 4.4 C-D) and minor amounts of quartz and Fe-Ti oxide minerals, interpreted to represent marble xenoliths.

One xenolith from the Lower Pollara pyroclastic succession (Fig. 4.3E-F), Salina consists of plagioclase, clinopyroxene, olivine, garnet, amphibole, and quartz and is interpreted to represent calc-silicates.

4.4.1.2.2 Low-grade metasedimentary xenoliths

Metasedimentary xenoliths are found on all islands in the central Aeolian arc. Two low-grade metasedimentary xenoliths from Salina were analysed in this study. The lower SiO_2 metasedimentary xenolith (SAL17-6-5; Table 4.2, Fig. 4.3 G-H) has low SiO_2 and K_2O and high Al_2O_3 and CaO contents with detrital grains (Fig. 4.3 G-H), representing a metamorphosed volcaniclastic siltstone-sandstone. The higher SiO_2 (47.90 wt.% SiO_2) metasedimentary xenolith (SAL17-6-6; Table 4.2, Fig. 4.3 I-J) is a fine-grained sandstone, with quartz, plagioclase, and muscovite, representing a low-grade metasandstone.

4.4.1.2.3 Gneissic xenoliths

Higher-grade metasedimentary xenoliths namely, fine grained gneissic xenoliths with a gneissose texture are also present (Fig. 4.3 K-L). A fine to medium grained xenolith composed of quartz, plagioclase, muscovite, and alkali feldspar (SAL17-8-6 and SAL17-8-7; Fig. 4.3 K-L) classified as a muscovite gneiss, presumably representing a metamorphosed sandstone from the Calabro-Peloritano basement. A high SiO_2 xenolith (SA3A; 70.85 wt.% SiO_2) was analysed in this study containing quartz, garnet and

sillimanite with minor biotite and chlorite (Fig. 4.3M), representing a garnet-sillimanite gneiss.

Table 4.2: Selected major- and trace-element compositions for analysed whole-rock crustal xenoliths from the central sector. b.d. below detection limit n.a. not analysed.

Group	Carbonate & Calc-silicate	Carbonate & Calc-silicate	Carbonate & Calc-silicate	Carbonate & Calc-silicate	Carbonate & Calc-silicate	Meta-sedimentary
Rock Type	Limestone	Limestone	Marble	Marble	Calc-silicate	Meta-pelite
Sample	SAL17-3-3	SAL17-3-6	SAL17-3-4	Pollara 026	AI-18-051F	SAL17-6-5
SiO_2	0.12	2.26	7.29	11.42	38.29	47.90
TiO_2	b.d.	0.06	0.10	0.02	0.33	0.73
Al_2O_3	b.d.	0.53	2.04	0.67	19.56	23.43
Fe_2O_3	b.d.	0.29	0.48	0.24	4.55	7.75
MnO	b.d.	b.d.	0.05	0.07	0.09	0.06
MgO	0.36	1.14	0.41	0.25	2.63	4.78
CaO	55.99	52.56	49.17	48.24	29.53	7.66
Na_2O	0.02	0.08	0.26	0.12	0.02	2.68
K_2O	0.01	0.10	0.46	0.14	b.d.	0.61
P_2O_5	0.07	0.09	0.02	0.02	b.d.	0.15
LOI	43.4	42.8	39.1	38.5	4.9	4
Total	99.97	99.91	99.38	99.69	99.90	99.75
Ba	b.d.	14	119	67	13	166
Sr	160	795	5031	2465	264	533
Zr	b.d.	10	9	b.d.	95	79
Nb	b.d.	b.d.	b.d.	b.d.	b.d.	10
Y	b.d.	5	6	5	10	15
Ni	b.d.	b.d.	b.d.	b.d.	b.d.	b.d.
Cr	b.d.	b.d.	29	b.d.	b.d.	b.d.
Sc	b.d.	b.d.	2	b.d.	b.d.	21

A white quartzite (quartz restite) forms large xenoliths (up to 10 centimetres) in many eruptive products in the central sector representing the residue from partial melting of quartz-feldspathic gneisses and or mica-schists in the crust (e.g. Zanon *et al.* 2003; Frezzotti *et al.* 2004; Zanon & Nikogosian 2004). White coloured quartz-rich xenoliths are abundant throughout the western and central sectors of the Aeolian arc (Peccerillo & Wu 1992; Peccerillo *et al.* 1993; 2004; Frezzotti *et al.* 2003; 2004; Zanon *et al.* 2003; Frezzotti

& Peccerillo 2004; Zanon & Nikogosian 2004; Peccerillo *et al.* 2006; Di Martino *et al.* 2010; 2011; De Astis *et al*. 2013; Forni *et al.* 2013; Lucchi *et al.* 2013b).

Table 4.2 cont'd: Selected major- and trace-element compositions for analysed whole-rock crustal xenoliths from the central sector. b.d. below detection limit n.a. not analysed.

Group	Meta-sedimentary	Gneissic	Gneissic	Gneissic	Gneissic	Granitoid
Type	Psamite	Quartzite	Gneiss	Gneiss	Gneiss	Granite
Sample	SAL17-6-6	SAL17-3-7	SAL17-8-6	SAL17-8-7	SA3A	SA3C
SiO_2	84.81	99.72	70.14	68.85	70.85	67.13
TiO_2	0.37	b.d.	0.46	0.49	0.22	0.43
Al_2O_3	7.08	b.d.	15.86	16.34	17.35	15.77
Fe_2O_3	2.65	b.d.	2.02	2.59	2.13	4.17
MnO	0.06	b.d.	0.02	0.05	0.02	0.06
MgO	0.91	b.d.	0.97	1.29	0.83	1.36
CaO	0.30	0.05	1.45	2.06	2.89	4.22
Na_2O	2.17	b.d.	3.30	3.64	3.08	3.55
K_2O	0.57	b.d.	4.24	2.96	1.62	2.62
P_2O_5	0.08	b.d.	0.23	0.24	0.31	0.16
LOI	0.9	0.3	1.2	1.4	0.6	0.3
Total	99.90	100.07	99.89	99.91	99.90	99.77
Ba	99	38	272	262	289	703
Sr	59	b.d.	145	165	262	569
Zr	210	b.d.	141	164	64	118
Nb	7	b.d.	13	13	b.d.	9
Y	25	b.d.	14	16	13	16
Ni	b.d.	b.d.	b.d.	b.d.	b.d.	b.d.
Cr	44	b.d.	58	44	b.d.	b.d.
Sc	4	b.d.	7	8	11	8

4.4.1.2.4 Granitoid xenoliths

One coarse grained xenolith, with 67.13 wt.% SiO_2, consisting of quartz, plagioclase, K-feldspar, biotite, with minor amounts of chlorite (Fig. 4.3N-O) and are the granitic xenoliths.

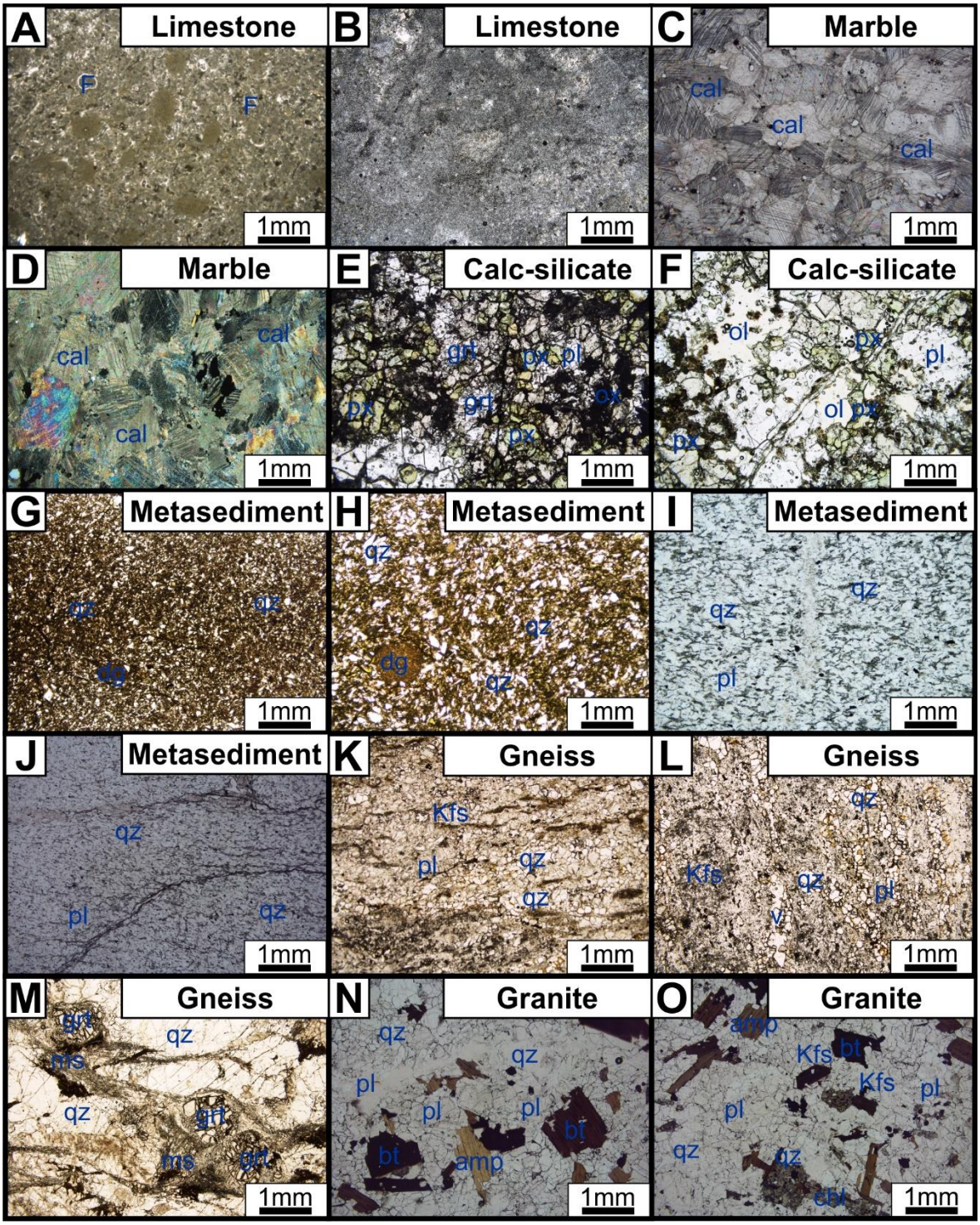

Fig. 4.3: Representative photomicrographs in from studied crustal xenoliths from the central sector. Abbreviations: F: microfossil, cal: calcite, pl: plagioclase feldspar, px: pyroxene, grt: garnet, ol: olivine, dg: detrital grain, Kfs: K-feldspar, ms: muscovite, bt: biotite, amp: amphibole, v: vesicle.

4.4.2 Whole-rock geochemistry of eruptive products

Whole-rock major and trace element compositions of all analysed eruptive products from Vulcano, Lipari and Salina are summarised in Table 4.1 and Figs. 4.5; 4.6. Eruptive products from the Lower Pollara eruption, Salina belong to the calc-alkaline series to high-K calc-alkaline series (Fig. 4.1) and are basalt, andesites and rhyolites. Whole-rock geochemical trends for the Lower Pollara eruption follow the overall geochemical trend for Salina (Figs. 4.2; 4.5; 4.6). Eruptive products from Lipari belong to the high-K calc-alkaline series and are rhyolitic with the exception of the dacitic dome and magmatic enclave from the dacitic dome (Fig. 4.1). Conversely, eruptive products from Vulcano are highly potassic, belonging to the shoshonitic magma series, with some samples plotting in the high-K calc-alkaline series (Fig. 4.1).

Major and trace element trends versus SiO_2 for all analysed samples are almost continuous across the three islands indicating the dominance of fractional crystallisation in the magmatic systems. With increasing SiO_2, TiO_2, Al_2O_3, $Fe_2O_3^*$, MnO, MgO, CaO, P_2O_5, Ba, Sr, Cr, and Sc all decrease, whereas Zr and Nb increase (Figs. 4.5; 4.6). A slight kink at 61 wt.% SiO_2 is observed in Al_2O_3 on Vulcano in an overall decreasing trend with SiO_2 (Fig. 4.4).

Samples from Salina have markedly lower P_2O_5 (<0.2 wt.%) compared to Vulcano and Lipari (<0.5 wt.%) and therefore display a less steep trend with the degree of differentiation compared to the other two islands (Fig. 4.4). Some scattering is observed with increasing SiO_2 in Ba. Zr displays a peaked trend for Vulcano decreasing from 66 wt.% SiO_2, whereas the other islands only exhibit an increasing trend (Fig. 4.5). Y displays an increasing trend with SiO_2 for the islands of Vulcano and Lipari, however, on Salina, Y decreases with increasing SiO_2 following the trend for the island (Fig. 4.5). Furthermore, on Salina the increase in Nb (<10 ppm) with the degree of evolution is far less than on

Vulcano and Lipari (up to 21 ppm). The ferromagnesian elements namely Sc and to some extent Cr decrease with increasing SiO_2 on all islands (Fig. 4.5).

4.4.3 Whole-rock geochemistry of xenoliths

Whole-rock major and trace element compositions for the crustal xenolith analysed in this study are summarised in Table 4.2. The crustal xenoliths span a large range of SiO_2 contents from 0.12 up to 99.72 wt.%, with variable amounts of major elements. The four carbonate xenoliths (limestones and marbles) comprise ~50 wt.% CaO, in addition to minor amounts of the other major elements. The calc-silicate xenolith contains 48.24 wt.% CaO, 11.42 wt.% SiO_2 and minor amounts of Al_2O_3, FeO, K_2O, MnO, MgO, Na_2O, P_2O_5 and TiO_2. The carbonate and calc-silicate xenoliths have high Loss on Ignition (LOI) from 38.5% up to 43.4%. The metasedimentary xenoliths have variable amounts of SiO_2 (47.90 up to 84.81 wt.% SiO_2), The lowest SiO_2 value (47.90 wt.%) is found in the metamorphosed volcanic siltstone-sandstone which also has high Al_2O_3 (23.43 wt.%), CaO (7.66 wt.%) and Sr (533 ppm) and low K_2O (0.57 wt.%). The gneissic xenoliths are leucocratic with SiO_2 contents above 68 wt.%., with high Al_2O_3 (15.86 and 16.34 wt.%), K_2O (2.96 and 4.24 wt.%) and Ba (262 and 272 ppm) and low CaO (1.45 and 2.06 wt.%). The quartz restite is composed almost entirely of SiO_2 (99.72 wt.%) with minor amounts of CaO (0.05 wt.%) and 38 ppm Ba.

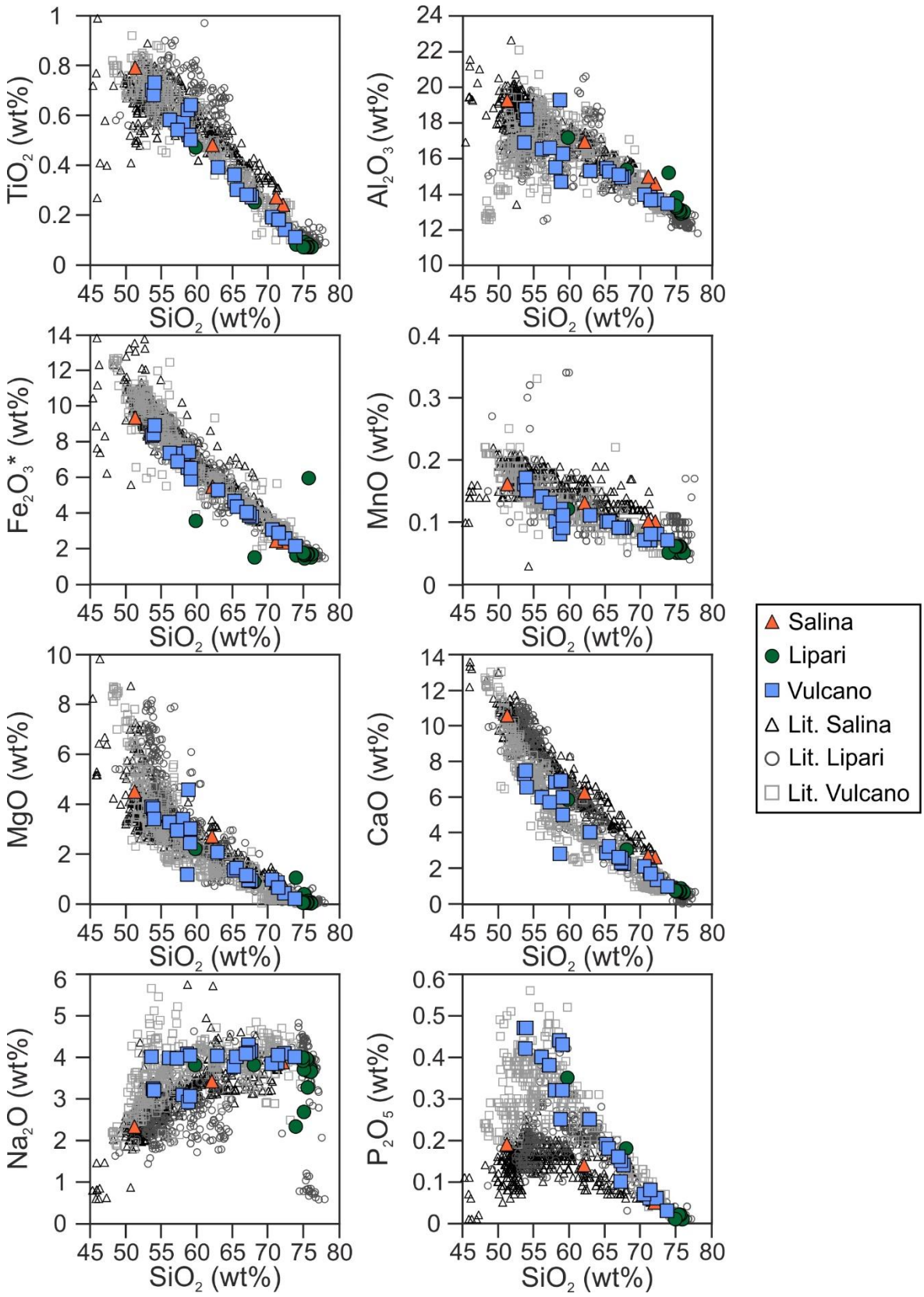

Fig. 4.4: Major element variation diagrams versus SiO_2 covering the eruptive history of the islands of Salina, Lipari and Vulcano, plotted using existing literature data (De Astis *et al.* 2013; Forni *et al.* (2013) and Lucchi *et al.* (2013b) and references therein). All major element analyses are reported in wt.%, recalculated to 100 wt.%, free of volatiles (LOI).

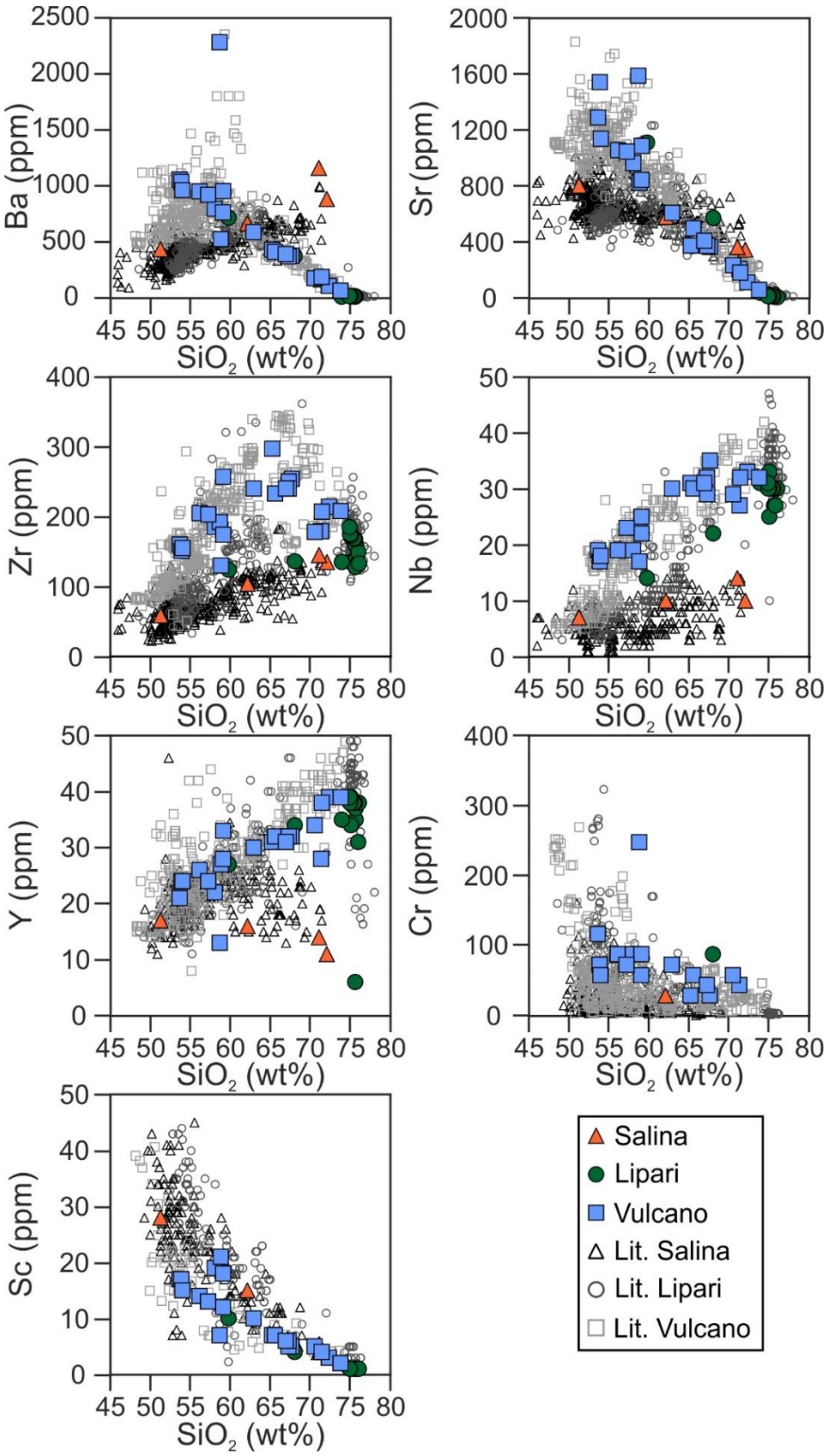

Fig. 4.5: Trace element variation diagrams versus SiO_2 covering the entire eruptive history of La Fossa di Vulcano, plotted with existing literature data (De Astis *et al.* 2013; Forni *et al.* (2013) and Lucchi *et al.* (2013b) and references therein). All major element analyses are recalculated to 100 wt.%, free of volatiles (LOI).

4.4.4 Oxygen isotope geochemistry

Oxygen isotope ratios from mineral separates (clinopyroxene and feldspar) and volcanic glass (obsidian and pumice) from pumice, scoriae, breadcrust bombs, lavas and mafic magmatic enclaves on Salina, Lipari and Vulcano are listed in Table 4.3 and Fig. 4.6; 4.7, with whole-rock oxygen isotope values for crustal lithologies listed in Table 4.4. $\delta^{18}O$ values on Salina are closest to mantle values and do not vary considerably with the degree of differentiation. $\delta^{18}O_{cpx}$ values range from +5.5‰ to +5.8‰ (n=3) on Salina, +6.1‰ to +7.1‰ (n=3) on Lipari and +6.0‰ to +6.7‰ (n=19) on Vulcano and are highest in rhyolites (Fig. 4.7A). Mantle $\delta^{18}O$ values range from +5.5‰ to +5.9‰ for pyroxene (Bindemann 2008). Olivine has only been measured in samples from Salina with $\delta^{18}O_{ol}$ values ranging from +5.0‰ to +5.4‰ (n=3), similar to mantle $\delta^{18}O$ values ranging from +5.0‰ to +5.4‰ (Gurenko *et al.* 2011). $\delta^{18}O_{fsp}$ values range from +6.1‰ to +6.3‰ (n=4) on Salina, +7.7‰ to +8.4‰ (n=10) on Lipari and +7.0‰ to +8.1‰ (n=16) on Vulcano. $\delta^{18}O_{obs}$ values from lavas and pyroclastic deposits range from +8.1‰ to +8.5‰ (n=6) on Lipari and +8.1‰ to +8.3‰ (n=2) on Vulcano. $\delta^{18}O_{gl}$ values significantly higher on Lipari varying from +9.0‰ to +12.6‰ (n=6), corresponding to the highest SiO_2 samples (Fig. 4.7A) compared to Vulcano and Salina which range from +6.1‰ to +10.4‰ (n=4) and +5.5‰ to +7.7‰ (n=3), respectively.

$\delta^{18}O$ values of mineral separates (clinopyroxene and feldspar) from Salina are significantly lower than published whole-rock $\delta^{18}O$ values (+6.4‰ to +8.5‰; Ellam & Harmon 1990; Gertisser & Keller 2000), whereas $\delta^{18}O_{cpx}$ for Lipari lies within the range of previously analysed clinopyroxene separates (+6.3‰ to +7.9‰; Forni *et al.* 2015). $\delta^{18}O$ values for Vulcano are similar to previously reported whole-rock O isotope data (+6.3 to +8.4‰; Ellam & Harmon (1990) and +6.1 to +6.3 for clinopyroxene; De Astis *et al.* (2013)).

Table 4.3: Selected Oxygen (O) isotope compositions for all analysed rock samples from recent eruptions in the central sector of the Aeolian Archipelago. To calculate $\delta^{18}O_{melt}$ it is assumed $\Delta_{fsp\text{-}melt}$ = +0.2‰ and $\Delta_{px\text{-}melt}$ = -0.3‰ (Kyser *et al.* 1981; Chiba *et al.* 1989). b.d. below detection limit n.a. not analysed.

Island	Salina				Lipari		
Volcanic Centre	Pollara				Southern Dome Field		
	Punta di Perciato	Lower Pollara		Upper Pollara	Punta del Perciato		Falcone
Sample	SAL13/19	SAL16-2	SAL16-5	UP	AI-17-080	AI-17-141	AI-17-138
	Lava	Scoria	Pumice	Pumice	Lava	Pumice	Pumice
$\delta^{18}O_{cpx}$ (‰)	5.5	5.7	5.8	n.d.	n.d.	n.d.	n.d.
$\delta^{18}O_{fsp}$ (‰)	6.3	6.2	6.1	6.3	8.4	8.1	7.9
$\delta^{18}O_{ol}$ (‰)	5.4	5.0	5.2	n.d.	n.d.	n.d.	n.d.
$\delta^{18}O_{obs}$ (‰)	n.d.	n.d.	n.d.	n.d.	n.d.	n.d.	n.d.
$\delta^{18}O_{gl}$ (‰)	n.d.	5.7	6.9	7.7	n.d.	12.6	12.0
$\Delta^{18}O_{fsp\text{-}cpx}$	0.8	0.5	0.3	N/A	N/A	N/A	N/A
$\delta^{18}O_{fsp\ (melt)}$	6.1	6.0	5.9	6.1	8.2	7.9	7.7
$\delta^{18}O_{cpx\ (melt)}$	5.8	6.0	6.1	N/A	N/A	N/A	N/A

Island	Lipari						
Volcanic Centre	Southern Dome Field						
	Falcone				Monte Guardia		
Sample	AI-17-138	AI-17-086	AI-18-065	AI-18-063	AI-17-100	AI-17-129	AI-18-066
	Obsidian	Lava	Dome	Enclave	Pumice	Pumice	Lava
$\delta^{18}O_{cpx}$ (‰)	n.d.	n.d.	6.2	6.1	n.d.	7.1	n.d.
$\delta^{18}O_{fsp}$ (‰)	n.d.	8.1	7.9	7.7	8.1	8.2	8.2
$\delta^{18}O_{ol}$ (‰)	n.d.	n.d.	n.d.	n.d.	n.d.	n.d.	n.d.
$\delta^{18}O_{obs}$ (‰)	8.4	n.d.	n.d.	n.d.	n.d.	n.d.	n.d.
$\delta^{18}O_{gl}$ (‰)	n.d.	n.d.	n.d.	n.d.	10.6	12.2	n.d.
$\Delta^{18}O_{fsp\text{-}cpx}$	N/A	N/A	1.7	1.6	N/A	1.1	N/A
$\delta^{18}O_{fsp\ (melt)}$	N/A	7.9	7.7	7.5	7.9	8.0	8.0
$\delta^{18}O_{cpx\ (melt)}$	N/A	N/A	6.5	6.4	N/A	7.4	N/A

Table 4.3 cont'd: Selected Oxygen (O) isotope compositions for all analysed rock samples from recent eruptions in the central sector of the Aeolian Archipelago. To calculate $\delta^{18}O_{melt}$ it is assumed $\Delta_{fsp\text{-}melt}$ = +0.2‰ and $\Delta_{px\text{-}melt}$ = -0.3‰ (Kyser *et al.* 1981; Chiba *et al.* 1989). b.d. below detection limit n.a. not analysed.

Island	Lipari						Vulcano
Volcanic Centre	Northern Lipari						Lentia
	Gabellotto			Pomiciazzo	Pilato	Rocche Rosse	Lentia Dome
Sample	FBG	FBG-12	FBG-72	L10-016	Pilato	RR	V10-005
	Pumice	Obsidian	Obsidian	Obsidian	Pumice	Obsidian	Lava
$\delta^{18}O_{cpx}$ (‰)	n.d.	n.d.	n.d.	n.d.	n.d.	n.d.	6.6
$\delta^{18}O_{fsp}$ (‰)	7.9	n.d.	n.d.	n.d.	n.d.	n.d.	7.6
$\delta^{18}O_{ol}$ (‰)	n.d.	n.d.	n.d.	n.d.	n.d.	n.d.	n.d.
$\delta^{18}O_{obs}$ (‰)	n.d.	8.5	8.5	8.4	n.d.	8.3	n.d.
$\delta^{18}O_{gl}$ (‰)	9.0	n.d.	n.d.	n.d.	9.5	n.d.	n.d.
$\Delta^{18}O_{fsp\text{-}cpx}$	N/A	N/A	N/A	N/A	N/A	N/A	1.0
$\delta^{18}O_{fsp\ (melt)}$	7.7	N/A	N/A	N/A	N/A	N/A	7.4
$\delta^{18}O_{cpx\ (melt)}$	N/A	N/A	N/A	N/A	N/A	N/A	6.9

Island	Vulcano						
Volcanic Centre	La Fossa di Vulcano						
	Punte Nere			Grotta dei Palizzi			
Sample	AI-17-041	AI-18-058	AI-17-006	AI-17-073	AI-17-049	AI-17-117	AI-17-056
	Ash	Ash	Lava	Ash	Pumice	Obsidian	Enclave
$\delta^{18}O_{cpx}$ (‰)	6.0	6.3	6.0	6.4	6.5	n.d.	6.4
$\delta^{18}O_{fsp}$ (‰)	7.3	n.d.	8.0	n.d.	8.1	n.d.	8.0
$\delta^{18}O_{ol}$ (‰)	n.d.	n.d.	n.d.	n.d.	n.d.	n.d.	n.d.
$\delta^{18}O_{obs}$ (‰)	n.d.	n.d.	n.d.	n.d.	n.d.	8.3	n.d.
$\delta^{18}O_{gl}$ (‰)	n.d.	n.d.	n.d.	n.d.	6.8	n.d.	n.d.
$\Delta^{18}O_{fsp\text{-}cpx}$	1.3	N/A	2.0	N/A	1.6	N/A	1.6
$\delta^{18}O_{fsp\ (melt)}$	7.1	N/A	7.8	N/A	7.9	N/A	7.8
$\delta^{18}O_{cpx\ (melt)}$	6.3	6.6	6.3	6.7	6.8	N/A	6.7

$\delta^{18}O_{px}$ values are lower than $\delta^{18}O_{fsp}$ in all measured samples (Fig. 4.7A-B) where mineral pairs are available. To determine the $\delta^{18}O_{melt}$ we have assumed $\Delta_{fsp\text{-}melt}$ = +0.2‰ and $\Delta_{px\text{-}melt}$ = -0.3‰ (Kyser *et al.* 1981; Chiba *et al.* 1989). $\delta^{18}O_{fsp(melt)}$ ranges from +5.9‰ to +6.1‰ on Salina, +7.9‰ to +8.6‰ on Lipari and +7.5‰ to +8.2‰ on Vulcano. $\delta^{18}O_{px(melt)}$ ranges from +5.2‰ to +5.5‰ on Salina, +5.8‰ to +6.1‰ on Lipari and +6.4‰ to +7.4‰ on Vulcano.

Table 4.3 cont'd: Selected Oxygen (O) isotope compositions for all analysed rock samples from recent eruptions in the central sector of the Aeolian Archipelago. To calculate $\delta^{18}O_{melt}$ it is assumed $\Delta_{fsp\text{-}melt}$ = +0.2‰ and $\Delta_{px\text{-}melt}$ = -0.3‰ (Kyser *et al.* 1981; Chiba *et al.* 1989). b.d. below detection limit n.a. not analysed.

Island	Vulcano						
Volcanic Centre	La Fossa di Vulcano						
	Grotta dei Palizzi			Caruggi	Pietre Cotte		
Sample	AI-18-056	AI-18-057	AI-17-045	AI-17-034	AI-17-019	AI-17-021	AI-17-025
	Ash	Pumice	Lava	Pumice	Scoria	Pumice	Pumice
$\delta^{18}O_{cpx}$ (‰)	6.4	6.2	6.6	n.d.	6.7	6.7	6.2
$\delta^{18}O_{fsp}$ (‰)	7.5	7.0	7.5	7.3	7.0	n.d.	8.0
$\delta^{18}O_{ol}$ (‰)	n.d.	n.d.	n.d.	n.d.	n.d.	n.d.	n.d.
$\delta^{18}O_{obs}$ (‰)	n.d.	n.d.	n.d.	n.d.	n.d.	n.d.	n.d.
$\delta^{18}O_{gl}$ (‰)	n.d.	n.d.	n.d.	n.d.	6.2	10.4	6.1
$\Delta^{18}O_{fsp\text{-}cpx}$	1.1	0.8	0.9	N/A	0.3	N/A	1.8
$\delta^{18}O_{fsp\ (melt)}$	7.3	6.8	7.3	7.1	6.8	N/A	7.8
$\delta^{18}O_{cpx\ (melt)}$	6.7	6.5	6.9	N/A	7.0	7.0	6.5

Island	Vulcano						
Volcanic Centre	La Fossa di Vulcano						
	Pietre Cotte		Gran Cratere				
Sample	AI-17-009	AI-17-028	AI-17-070	AI-17-120	AI-18-072	AI-18-074	AI-18-076
	Obsidian	Enclave	Ash	Bomb	Bomb	Bomb	Bomb
$\delta^{18}O_{cpx}$ (‰)	n.d.	6.3	6.3	6.6	6.4	6.0	6.3
$\delta^{18}O_{fsp}$ (‰)	n.d.	7.0	7.2	7.7	n.d.	7.8	8.1
$\delta^{18}O_{ol}$ (‰)	n.d.	n.d.	n.d.	n.d.	n.d.	n.d.	n.d.
$\delta^{18}O_{obs}$ (‰)	8.1	n.d.	n.d.	n.d.	n.d.	n.d.	n.d.
$\delta^{18}O_{gl}$ (‰)	n.d.	n.d.	n.d.	n.d.	n.d.	n.d.	n.d.
$\Delta^{18}O_{fsp\text{-}cpx}$	N/A	0.7	0.9	1.1	N/A	1.8	1.8
$\delta^{18}O_{fsp\ (melt)}$	N/A	6.8	7.0	7.5	N/A	7.6	7.9
$\delta^{18}O_{cpx\ (melt)}$	N/A	6.6	6.6	6.9	6.7	6.3	6.6

$\delta^{18}O_{px}$ values overlap or are higher than values of mafic arc melts (+5.2 to +6.2‰; Eiler *et al.* 2000), with $\delta^{18}O_{px}$ and $\delta^{18}O_{ol}$ values on Salina close to mantle values (+5.5‰ to +5.8‰ and +5.0‰ to +5.4‰, respectively). $\delta^{18}O$ values for clinopyroxene do not show systematic variations with the degree of differentiation of the host rock (Fig. 4.7A). By contrast, $\delta^{18}O$ values for feldspar and pumice glass increase with the degree of differentiation of the host

rocks (Fig. 4.7A). Feldspar-pyroxene isotherms have been calculated for temperatures of 600, 800, 1000, and 1200°C (Fig. 4.7B), using the calibration of Chiba *et al.* (1989). The range in $\Delta^{18}O_{fsp\text{-}px}$ is +0.3‰ to +0.8‰ for Salina, +1.1‰ to +1.7‰ for Lipari and +0.3‰ to +2.0‰ for Vulcano. (Fig. 4.7C). With increasing $\Delta_{fsp\text{-}px}$, $\delta^{18}O_{fsp}$ increases, however this increase is not entirely systematic on Salina and Vulcano (Fig. 4.7D). Conversely, no systematic variations are observed in $\delta^{18}O_{px}$ with increasing $\Delta_{fsp\text{-}px}$ across all three islands.

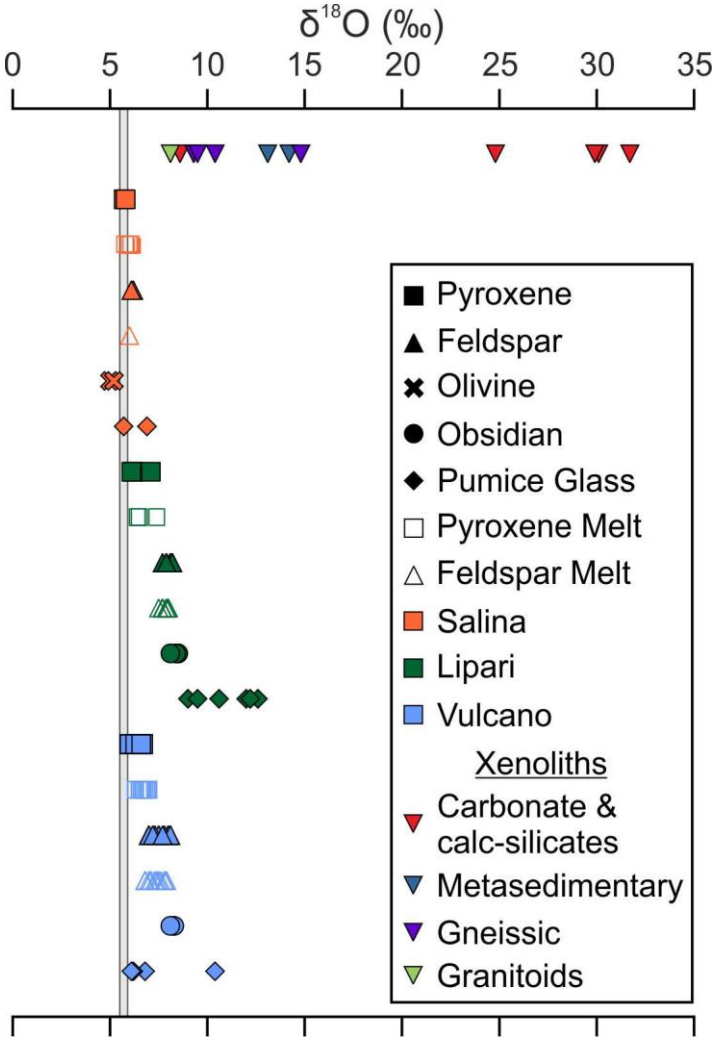

Fig. 4.6: Chart showing oxygen isotope variations in crustal xenoliths and mineral separates (pyroxene and feldspar) and glass (obsidian and pumice), and their calculated melt compositions from the central Aeolian Archipelago. The light grey shaded area is the $\delta^{18}O$ range for the mantle values (Bindemann 2008). To calculate $\delta^{18}O_{melt}$ it is assumed $\Delta_{fsp\text{-}melt}$ = +0.2‰ and $\Delta_{px\text{-}melt}$ = -0.3‰ (Kyser *et al.* 1981; Chiba *et al.* 1989).

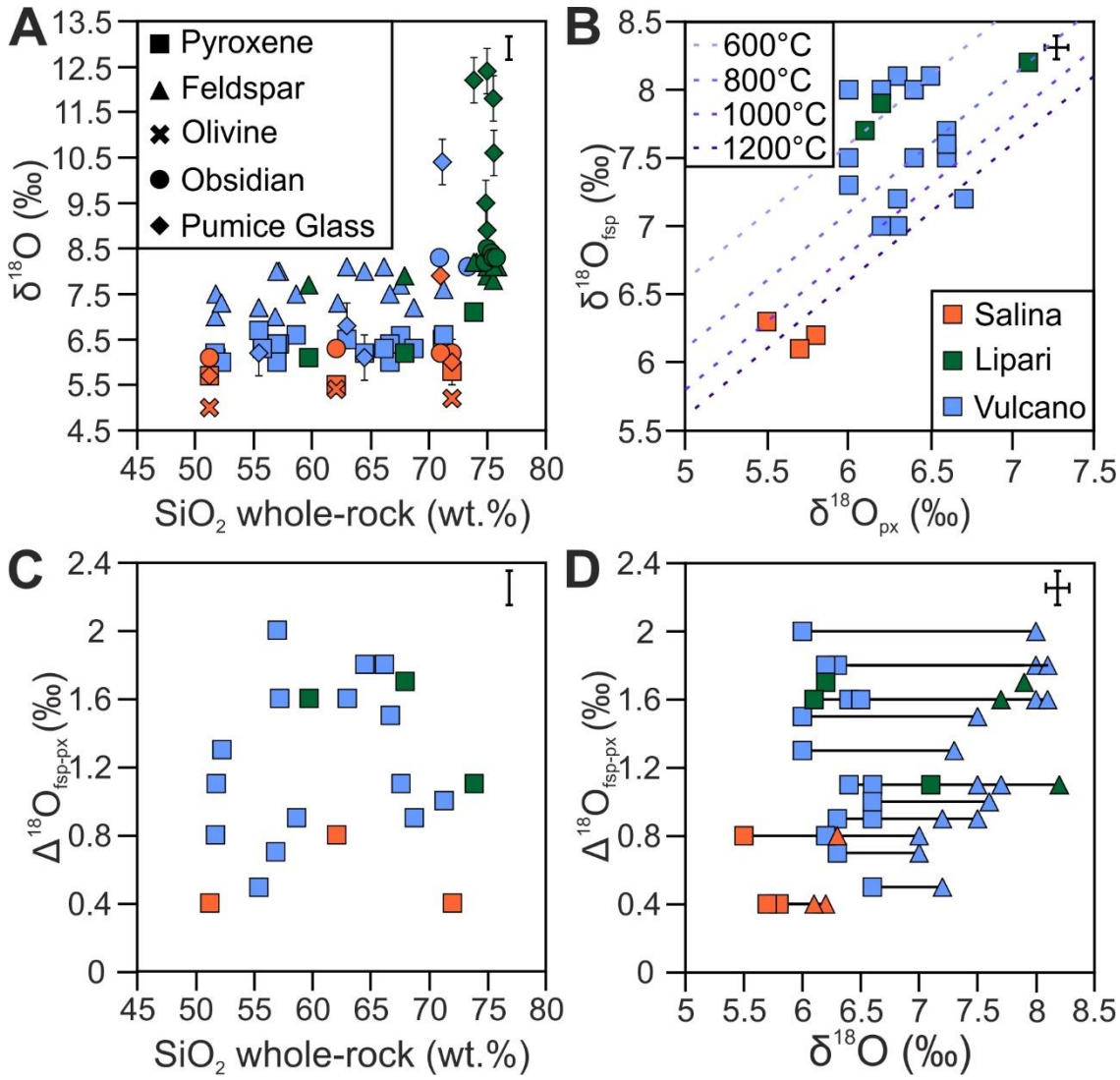

Fig. 4.7: (A) Plot of $\delta^{18}O$ (‰) versus SiO_2 (wt.%) for mineral separates (clinopyroxene, feldspar and olivine) and glass (obsidian and pumice) from Salina, Lipari and Vulcano. (B) Plot of $\delta^{18}O_{feldspar}$ (‰) versus $\delta^{18}O_{clinopyroxene}$ (‰), where mineral pairs were available from Salina, Lipari and Vulcano. Feldspar-pyroxene isotherms for 1200, 1000, 800 and 600 °C are shown. Isotherms were calibrated using Chiba *et al.* (1989), based upon an An_{55} component. (C) Plot of $\Delta_{feldspar\text{-}clinopyroxene}$ versus whole-rock SiO_2 (wt.%) from Salina, Lipari and Vulcano. (D) $\Delta_{feldspar\text{-}clinopyroxene}$ versus mineral $\delta^{18}O$ where mineral pairs were available from Salina, Lipari and Vulcano. All mineral pairs are connected by tie lines. All O isotopes are reported relative to SMOW (Standard Mean Ocean Water).

Representative crustal lithologies from the Calabro-Peloritano basement are summarised in Table 4.4 with whole-rock $\delta^{18}O$ values between +8.1‰ and +31.7‰ (Fig. 4.8), with the highest values observed in carbonate lithologies (+24.8 to +31.7‰, n=4). $\delta^{18}O$ values range from +8.1‰ to +10.4‰ in the gneiss and granitoid xenolith (n=4) and +14.8‰ for the quartz xenolith. The two silicic metasedimentary xenoliths yielded values of +13.1‰

and +14.2‰, respectively. This new range exceeds the range from the two crustal xenoliths (+7.9‰ and +10.7‰) analysed by Ellam & Harmon (1990).

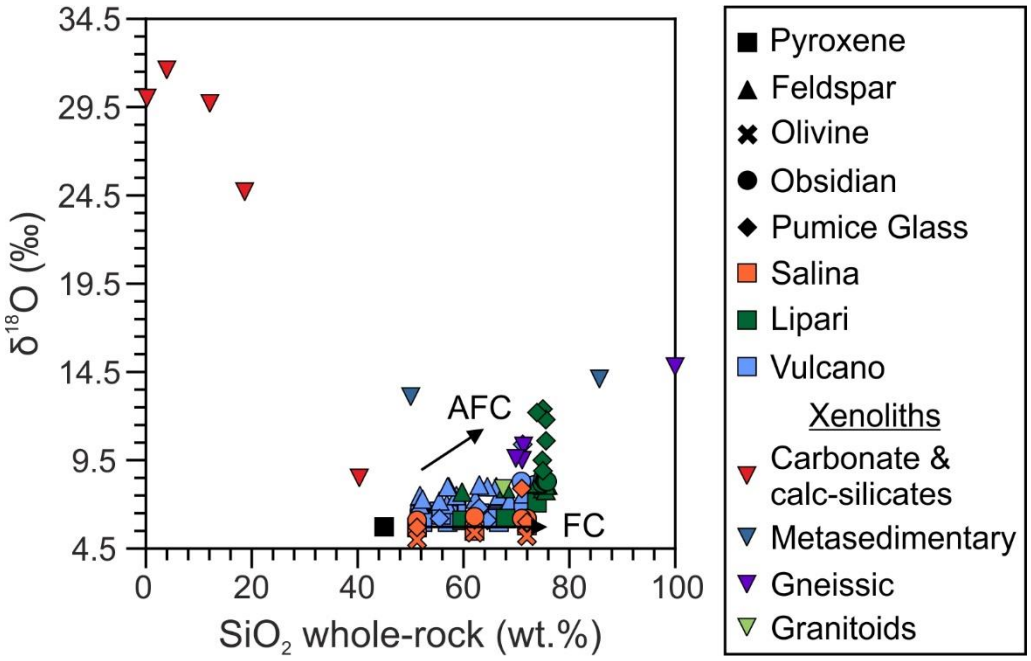

Fig. 4.8: Plot of $\delta^{18}O$ (‰) versus SiO_2 (wt.%) for whole-rock crustal xenoliths and mineral separates (clinopyroxene, feldspar and olivine) and glass (obsidian and pumice glass) from Salina, Lipari and Vulcano. O isotopes are reported relative to SMOW (Standard Mean Ocean Water) except for carbonates which are relative to V-SMOW.

4.4.5 Strontium isotope geochemistry

Strontium isotope ratios from mineral separates (clinopyroxene and feldspar) and obsidian from selected samples on Salina, Lipari and Vulcano and whole rock $^{87}Sr/^{86}Sr$ ratios for representative crustal lithologies (xenoliths) are listed in Table 4.4 Fig. 4.9 and Fig. 4.10 A-B. Strontium isotope ratios of volcanic rocks range from 0.704419 to 0.704582 (n=3) on Salina, 0.704612 to 0.705977 (n=4) on Lipari, and 0.704485 to 0.705603 (n=5) on Vulcano. The lowest $^{87}Sr/^{86}Sr$ ratios are found in clinopyroxenes, ranging from 0.704464 (n=1) on Salina, 0.704612 (n=1) on Lipari and 0.704485 to 0.704607 (n=2) on Vulcano. Conversely, the highest $^{87}Sr/^{86}Sr$ ratios are found in feldspars ranging from 0.704419 to 0.704582 (n=2) on Salina, 0.70465 to 0.705715 (n=2) on Lipari and 0.704630 to 0.705603 (n=2) on Vulcano. $^{87}Sr/^{86}Sr$ ratios for two obsidian samples, from Lipari and Vulcano yield

$^{87}Sr/^{86}Sr$ ratios of 0.705977 and 0.705008, respectively. The lowest $^{87}Sr/^{86}Sr$ ratios for each island are found in clinopyroxene ($^{87}Sr/^{86}Sr$ = 0.704464 to 0.704612, n=4), whilst the highest ratios are found in feldspars ($^{87}Sr/^{86}Sr$ = 0.704419 to 0.705715, n=6) from Lipari and Vulcano and the obsidian ($^{87}Sr/^{86}Sr$ = 0.705008, n=1) from Vulcano.

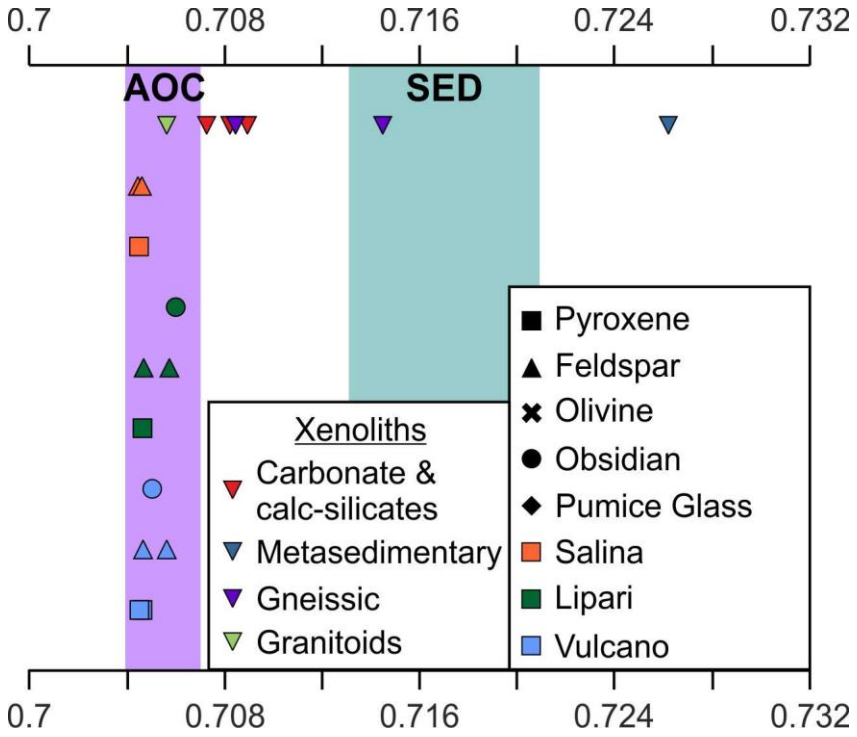

Fig. 4.9: Chart showing strontium isotope variations in crustal xenoliths and mineral separates (pyroxene and feldspar) and glass (obsidian) from the central Aeolian Archipelago. The light pink shaded area is the $^{87}Sr/^{86}Sr$ range for altered oceanic crust (AOC), ranging from 0.70364 to 0.70744 (Staudigel *et al.* 1995). The blue-green shaded area is the $^{87}Sr/^{86}Sr$ range for subducted sediments (SED), ranging from 0.71224 to 0.71958 (Krom *et al.* 1999).

Whole rock $^{87}Sr/^{86}Sr$ ratios for the crustal xenoliths span a large strontium isotopic range from 0.705603 to 0.726233 (Fig. 4.9; 4.10A-B), with the highest values in the meta-sediment ($^{87}Sr/^{86}Sr$ = 0.726233) and gneiss (SAL17-8-7; $^{87}Sr/^{86}Sr$ = 0.714484). The lowest $^{87}Sr/^{86}Sr$ ratios for crustal xenoliths are found in the granite ($^{87}Sr/^{86}Sr$ = 0.705603), calc-silicate ($^{87}Sr/^{86}Sr$ = 0.707247) and gneiss (SA3A; $^{87}Sr/^{86}Sr$ = 0.708433). The carbonate xenoliths (limestone and marble) have moderately high $^{87}Sr/^{86}Sr$ ratios of 0.708201 and 0.708924, respectively.

Table 4.4: Oxygen (O) and Strontium (Sr) isotope compositions for whole-rock crustal xenoliths and selected samples from recent eruptions in the central sector (Salina, Lipari and Vulcano) of the Aeolian Archipelago.

Island	Volcanic Centre	Sample Number	Material Type	$\delta^{18}O$ (‰) ±0.2 ‰	$^{87}Sr/^{86}Sr \pm 2\sigma$	
Crustal Xenoliths		SAL17-3-6	Limestone	+31.7	0.708924	±0.0000118
		SAL17-3-4	Marble	+29.9	0.708201	±0.0000126
		AI-18-051F	Calc-Silicate	+8.6	0.707247	±0.0000112
		SAL17-6-6	Meta-sediment	+14.2	0.726233	±0.0000128
		SAL17-8-7	Gneiss	+9.5	0.714484	±0.0000150
		SA3A	Gneiss	+10.4	0.708433	±0.0000128
		SA3C	Granite	+8.1	0.705603	±0.0000144
Salina	Pollara	SAL16-2	Plagioclase	+6.3	0.704419	±0.0000148
		SAL13/19	Plagioclase	+6.2	0.704582	±0.0000152
		SAL16-2	Clinopyroxene	+5.7	0.704464	±0.0000124
Lipari	Southern Dome Field	AI-18-065	Plagioclase	+7.9	0.704656	±0.0000114
		AI-17-080	Plagioclase	+8.2	0.705715	±0.0000130
		AI-18-065	Clinopyroxene	+6.2	0.704612	±0.0000150
	Northern Dome Field	RR	Obsidian Glass	+8.3	0.705977	±0.0000138
Vulcano	La Fossa di Vulcano	AI-17-049	Plagioclase	+8.1	0.705603	±0.0000136
		AI-17-028	Plagioclase	+7.0	0.704630	±0.0000134
		AI-18-074	Clinopyroxene	+6.0	0.704607	±0.0000124
		AI-17-009	Obsidian Glass	+8.1	0.705008	±0.0000124
	Lentia	V10-005	Clinopyroxene	+6.6	0.704485	±0.0000136

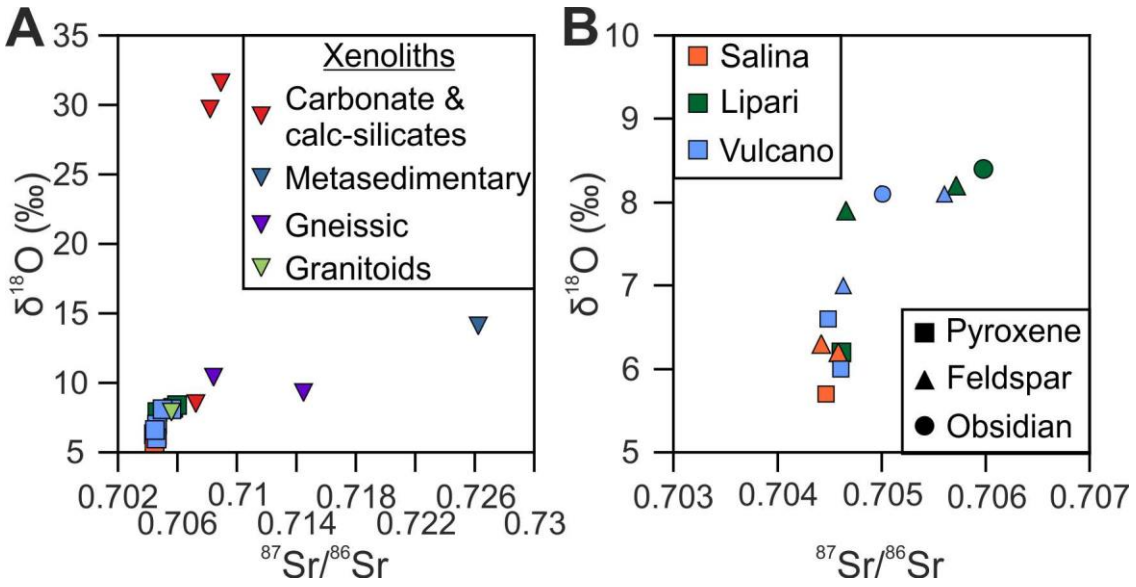

Fig. 4.10: (A) Plot of $\delta^{18}O$ (‰) versus $^{87}Sr/^{86}Sr$ for whole-rock crustal xenoliths, mineral separates (clinopyroxene and feldspar) and glass (obsidian) from Salina, Lipari and Vulcano. (B) Plot of $\delta^{18}O$ (‰) versus $^{87}Sr/^{86}Sr$ for mineral separates (clinopyroxene and feldspar) and glass (obsidian) from Salina, Lipari and Vulcano.

4.5 Discussion

4.5.1 Linking xenoliths to crustal structure

The crustal structure in the central Aeolian arc has previously been constrained using deep seismic sounding experiments by Ventura *et al.* (1999) and P- and S-wave tomography by Neri *et al.* (2002). The crustal xenoliths in this study have been linked to the pre-defined crustal structure and are used to constrain the depths at which contamination occurs in the central Aeolian arc (Fig. 4.11). Gravimetric data (Barberi *et al.* 1994) indicates the uppermost 2 km of the crust consist of unconsolidated sediments and volcaniclastic deposits. We suggest this is the source region for the localised carbonates on Salina, due to the heterogeneous nature of this layer and the preservation of fossils in the limestones. From 2 to 5 km depth there is a layer of low grade metamorphosed silicic metapelites (Fig. 4.11) attributed to the Calabrian arc based upon seismic velocities (Vp = 5 – 5.5 km/s; Continisio *et al* 1997). The deeper crustal layers (5 to 15 km) are marked by Vp = 5.5 km/s and interpreted to represent granitoids and felsic granulites and are hence considered as the source region for the granitic and gneissic xenoliths (dominated by quartz, plagioclase, and alkali feldspar).

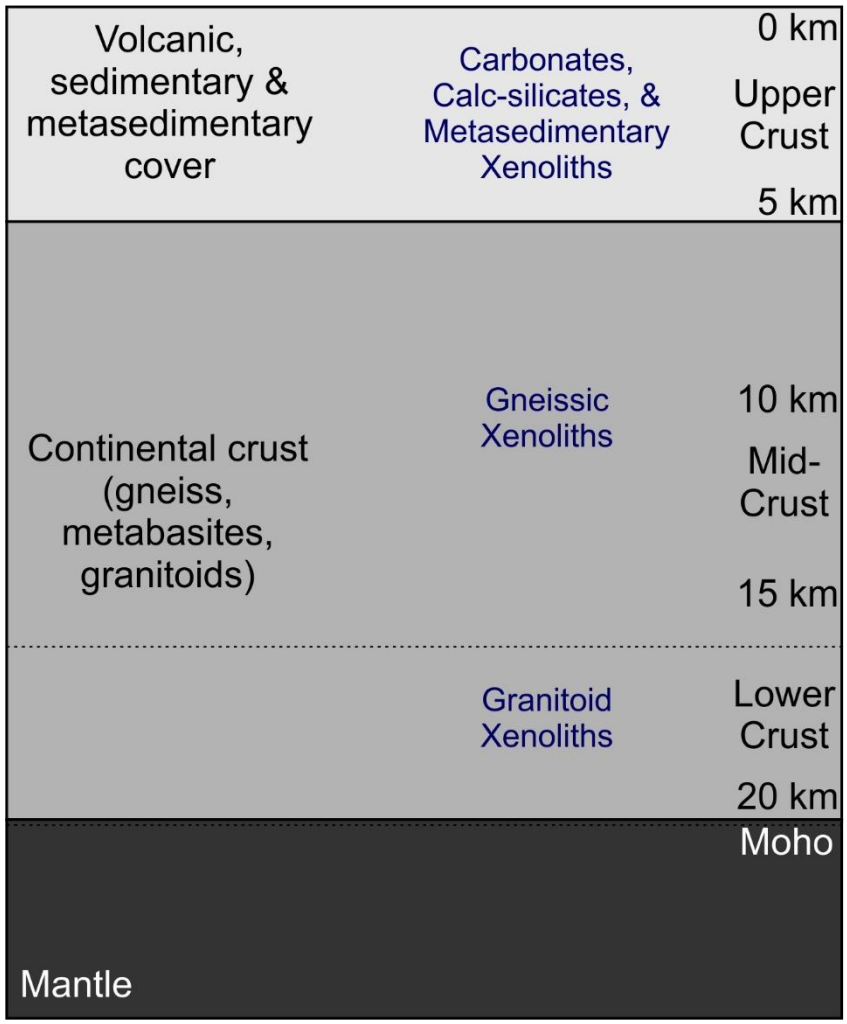

Fig. 4.11: Schematic model showing the origins of crustal xenoliths for Salina, Lipari and Vulcano. Left: Crustal structure of Pecerillo *et al*. 2006. Centre: Xenolith types from this study. Limestone: SAL17-3-3, SAL17-3-6; Marble: SAL17-3-4, Pollara 026; Calc-silicate: AI-18-051F; Metasediment: SAL17-6-5, SAL17-6-6; Quartzite: SAL17-3-7; Gneiss: SAL17-8-6, SAL17-8-7, SA3A; Granite: SA3C. After: Peccerillo *et al*. 2006.

4.5.2 Oxygen isotope equilibria

To assess O isotopic equilibrium between coexisting mineral phases in samples $\delta^{18}O_{fsp}$ is plotted with $\delta^{18}O_{px}$ (Fig. 4.7B) and shows steep positive trends with increasing $\delta^{18}O_{px}$. The large range observed in $\Delta_{fsp\text{-}px}$ (+0.3‰ to +2.0‰) indicates that for some samples, feldspar and clinopyroxene exhibit a large degree of isotopic disequilibrium, particularly in the more evolved rocks with higher SiO_2 contents (e.g. latites and trachytes) as the clinopyroxenes occur antecrysts as they did not crystallise from the host magma in which

they are located and represent less evolved parts of the magmatic system. Therefore, the two mineral phases crystallising from different magmas at different depths in the magmatic system undergoing different degrees of crustal contamination.

Isotopic equilibrium in a rock suite between clinopyroxene and feldspar can be assessed using a line with a constant difference (in $\Delta_{fsp\text{-}px}$) in $\delta^{18}O$ values between the two coexisting minerals (Gregory & Criss 1986; Gregory *et al.* 1989), representing constant temperatures. Feldspar-pyroxene isotherms (Fig. 4.7B) show some of the samples are in isotopic disequilibrium as they plot outside the range of reasonable magmatic temperatures (below 700°C).

Feldspar exhibits the highest $\delta^{18}O$ values of analysed mineral separates, (+6.1‰ to +8.4‰), whereas pyroxene $\delta^{18}O$ values are much lower (+5.5 to +7.1‰), with a high degree of isotopic disequilibrium between the two mineral phases. This isotopic disequilibrium indicates the two mineral phases crystallised under different conditions, with pyroxene representing deeper crystallisation and feldspar shallower. Some $\Delta^{18}O_{fsp\text{-}px}$ values overlap with the equilibrium range for feldspar-pyroxene mineral pairs (Fig. 4.7D), however many of the laititc and trachytic samples exceed this range for equilibrium. These differences suggest many pyroxene and feldspar crystal pairs did not crystallise in the same magma, and instead crystallised from compositionally different magmas in the magma plumbing system of each volcano with different crustal contributions.

The largest range in $\Delta_{fsp\text{-}px}$ are found in latites and trachytes (+0.8‰ to +2.0‰), and therefore exhibit the largest degrees of mineral-mineral disequilibrium. $\delta^{18}O_{fsp}$ values increase with increasing $\Delta_{fsp\text{-}px}$, whereas $\delta^{18}O_{px}$ do not show any systematic variations. This trend may result from either the magmatic evolution of the same magma or the mixing of two geochemically distinct magmas. Assuming an overall feldspar composition of $An_{50}Ab_{50}$, the equilibrium range for $\Delta_{fsp\text{-}px}$ is 0.68 – 1.12 at temperatures between 800 and

1100°C using the calibration of Chiba *et al.* (1989). Variations in O isotopes from this study indicate a series of open system processes and crustal contamination occur across the Central Aeolian arc. Using the three analysed olivine samples from Salina, the equilibrium range for $\Delta_{ol\text{-}px}$ is 0.42 – 0.80 at temperatures between 800 and 1200°C using the calibration of Chiba *et al.* (1989). Two of the samples are in equilibrium, however, the higher $\delta^{18}O_{ol}$ sample (+5.4‰) does not lie within the equilibrium range for magmatic temperatures.

To assess degree of contamination of the melt, the melt values have been calculated for each mineral phase, assuming $\Delta_{fsp\text{-}melt}$ = +0.2‰ and $\Delta_{px\text{-}melt}$ = -0.3‰ (Kyser *et al.* 1981; Chiba *et al.* 1989). $\delta^{18}O_{px(melt)}$ range from +5.8‰ to +7.4‰ and $\delta^{18}O_{fsp(melt)}$ range from +5.9‰ to+8.2‰. Calculated melt values from which the minerals crystallised for pyroxene are lower than that of feldspar (Table 4.3) illustrating feldspar crystallised from more contaminated melts. Therefore, contamination in the upper crust primarily affects feldspar, obsidians, and pumice glass O isotopes, whereas pyroxene is contaminated to a lesser degree at deeper levels. $\delta^{18}O$ values for all mineral separates and glass on Lipari and Vulcano and feldspar and glass on Salina are elevated relative to the mantle. The smallest ranges in $\Delta^{18}O_{fsp\text{-}px}$ is found in the Salina samples from 0.3 to 0.8‰, with these samples in O isotope equilibrium. $\delta^{18}O_{cpx}$ (+5.5‰ to +5.8‰) and $\delta^{18}O_{ol}$ (+5.0‰ to +5.4‰) reflecting mantle values and $\delta^{18}O_{fsp}$ (+6.1‰ to +6.3‰). Therefore, the samples from the Pollara activity, Salina are the most primitive samples found in the central sector with the lava and scoria showing no evidence of contamination in O isotopes and can therefore be used as a baseline to assess the degree of contamination in the central sector. In contrast, $\delta^{18}O_{gl}$ from pumices on Salina are elevated (+6.9‰ and +7.7‰) and therefore reflect a small degree of contamination.

4.5.3 Oxygen and Strontium isotopes as indicators of contamination

Aeolian arc magmas undergo extensive interactions in the crust and upper mantle during petrogenesis. Contamination of Aeolian magmas occurs by (1) source contamination by subducted sediments and altered oceanic crust (AOC) and (2) subsequent crustal contamination during magma ascent in the crust. However, it is difficult to discriminate between the effects of each process.

4.5.3.1 Source Contamination

At volcanic arcs, fluids and melts derived from subducting sediments and the oceanic crust result in modification of the mantle wedge during subduction (e.g. Ryan & Langmuir 1993; Elliot *et al.* 1997; Johnson & Plank 1999; Eiler *et al.* 2005; Hermann & Rubatto 2009; Martin *et al.* 2014; Gazel *et al.* 2015). Contamination of the mantle source ("source contamination") by subducted sediments and altered oceanic crust (AOC) is widely accepted in the Aeolian arc (e.g. Ellam *et al.* 1988; Ellam & Harmon 1990; Peccerillo *et al.* 1993; De Astis *et al.* 2000; Gertisser & Keller 2000; Francalanci *et al.* 2007; Santo & Peccerillo 2008; Peccerillo *et al.* 2013; Zamboni *et al.* 2016). However, the relative contributions from subducted sediments and AOC remains debated in the central Aeolian arc. Petrological and geochemical data such as the high Sr contents and low $^{87}Sr/^{86}Sr$ ratios of mafic calc-alkaline magmas in the Aeolian arc attest to an oceanic nature of the subducting slab (e.g. Finetti 1982; Francalanci *et al.* 1993; Faccenna *et al.* 1997; Catalano *et al.* 2001). Nevertheless, it must be noted that earlier studies by Boccaletti *et al.* (1984) proposed subduction of continental crust under the Calabrian arc. Previous radiogenic isotope studies have argued for the role of subducted sediment in the Aeolian islands, due to the high $^{206}Pb/^{204}Pb$ and $^{208}Pb/^{204}Pb$ ratios with respect to MORB values (Ellam *et al.* 1988; 1989; Ellam & Harmon 1990). However, more recent studies using trace element

geochemistry and by Francalanci *et al.* (2007) and Zamboni *et al.* (2016) argue against the major role of subducted sediment during magma genesis in the central Aeolian arc.

To discriminate between source contamination from subducted sediment and oceanic crust, we have combined O and Sr isotopes. Source contamination is responsible for large variations in Sr isotopes over a limited $\delta^{18}O$ ranges. Sr in the depleted mantle is very low (9.8 ppm; Salters & Stracke 2004), therefore any variations in $^{87}Sr/^{86}Sr$ are due to contamination from subducted sediment or altered oceanic crust with high Sr contents. Low temperature alteration of the uppermost ~ 500 m of oceanic crust are characterised by $\delta^{18}O$ values ranging from +8‰ to +25‰, systematically decreasing with increasing depth, with a weighted average between +8‰ and +10‰ (Muehlenbachs 1986; Staudigel *et al.* 1995; Alt 2003). $^{87}Sr/^{86}Sr$ range from 0.70364 to 0.70744, with an average of 0.70475 and Sr concentration of 130 ppm to 220ppm, with an average of 160 ppm (Staudigel *et al.* 1995). The upper oceanic crust has $\delta^{18}O$ of +9.6 ± 1.3‰ (Simon & Lécuyer 2005). For subducted clastic marine sediments and pelagic clays $\delta^{18}O$ range from +10‰ to +25‰, with most sediments ranging from +15‰ to +20‰ (Land & Lynch 1996).

To calculate the source contributions, we use the mixing equation, $C_L = C_O \times \frac{1}{D\,(1-F)+F}$, where F is the melt fraction, C_O is the Sr concentration (ppm), and D is the bulk distribution coefficient (Winter 2001). To model the contribution from AOC fluids, we used $\delta^{18}O$ values of +8‰ and +10‰, $^{87}Sr/^{86}Sr$ of 0.7074 and Sr concentrations of 130 ppm, 160 ppm and 220 ppm. The partition coefficient for Sr is taken as 0.34 ± 0.17 determined using experimental studies for aqueous fluids at 800°C and 4 GPa (Kessel *et al.* 2005). The composition of the subducting Ionian sediments using Ionian sediment core data from Krom *et al.* (1999). We use the average, high and low $^{87}Sr/^{86}Sr$ ratios of 0.71558, 0.71958 and 0.71224, respectively. Sr concentrations range from 92.3 ppm to 151 ppm, with an average of 126.6 ppm. For the model, $\delta^{18}O$ values used are +20‰ and +25‰

(Land & Lynch 1996). The partition coefficient for Sr used is 2.78 ± 0.08 using experimental studies on clays, with a melt fraction of 29.5% at 800°C (Skora & Blundy 2010). The degree of melting is 20% to 30% for sediments (Hermann & Rubatto 2009).

Source contamination trends from AOC and subducted sediment are shown in Fig. 4.12. The Salina samples are situated between the contamination fields from AOC and subducted sediments in $\delta^{18}O$ versus $^{87}Sr/^{86}Sr$ plots (Fig. 4.12), indicating a small degree of contamination (< 5%) from both components. Alternatively, only AOC-derived fluids may be added and then undergo crustal assimilation affecting all the samples. The melts in which feldspar and pyroxene crystallised from on Salina lie within the region of source contamination, with the basalts and andesites crystallising at depths of c. 18 km (13 – 28 km; n = 16: Putirka 2008, equation 31). The low $\delta^{18}O$ values for minerals from the Pollara eruptions, Salina reflects contamination of the arc crust, by hydrothermally altered oceanic crust (AOC) lowering the $\delta^{18}O$ of clinopyroxene and plagioclase feldspar. In addition, the melts from which clinopyroxene crystallised from on Lipari and Vulcano lie within the region of source contamination from subducted sediment (~3% added), with the Vulcano clinopyroxene crystallising at a depth of c. 14 km (Chapter 2).

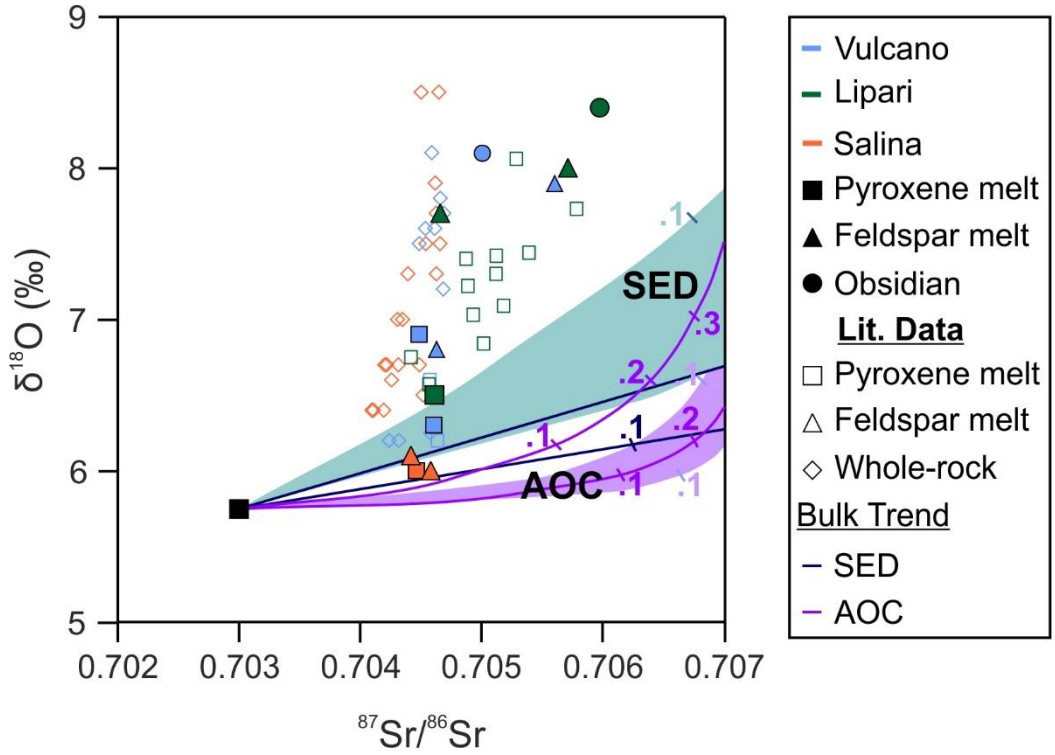

Fig. 4.12: Plot of $\delta^{18}O$ (‰) versus $^{87}Sr/^{86}Sr$ for, and calculated melt values from, mineral separates (clinopyroxene and feldspar) and glass (obsidian) from Salina, Lipari and Vulcano, plotted with existing literature data (Ellam & Harmon 1990; Gertisser & Keller 2000; De Astis *et* al. 2013; Forni *et al*. 2015). Fields for source contamination trends for altered oceanic crust (AOC) and subducted sediment (SED) are shown. Parameters to calculate contamination fields are summarised in the text.

4.5.3.2 Crustal Contamination

Geochemical and petrological data used in conjunction with oxygen and strontium isotope data fit a model of crustal contamination in the central Aeolian arc. Published whole-rock $\delta^{18}O$ values for Aeolian arc volcanic rocks vary systematically with SiO_2, signifying an important role of AFC-type processes in the evolution of Aeolian arc magmas and the generation of intermediate and felsic (rhyolitic) magma compositions (Ellam *et al.* 1990; Gertisser & Keller 2000; De Astis *et al.* 2013; Forni *et al.* 2013; Lucchi *et al.* 2013).

An overall positive correlation is observed between $^{87}Sr/^{86}Sr$ with increasing whole-rock SiO_2. There is a small increase in $^{87}Sr/^{86}Sr$ with the degree of differentiation up to ~ 62 wt.% SiO_2, whereas SiO_2 contents above 62 wt.% exhibit large differences in $^{87}Sr/^{86}Sr$

ratios. Additionally, $^{87}Sr/^{86}Sr$ ratios in clinopyroxene are relatively constant with the increasing whole-rock SiO_2, whereas $^{87}Sr/^{86}Sr$ ratios in feldspar vary considerably with the degree of evolution (increasing SiO_2 in the whole-rock). The large variability in $\delta^{18}O_{fsp}$ and limited range $\delta^{18}O_{cpx}$ with increasing SiO_2, supports the conclusion clinopyroxenes and feldspars are not in O isotope equilibrium in the more evolved rocks (trachytes and rhyolites) in the central sector. Obsidians also exhibit a large degree of variability in $^{87}Sr/^{86}Sr$ ratios over a limited SiO_2 range (< 5 wt.%). The progressive increase in $^{87}Sr/^{86}Sr$ and $\delta^{18}O$ with increasing SiO_2 is indicative of crustal assimilation (AFC processes) in the central Aeolian arc, particularly in the rhyolites from Lipari and Vulcano and trachytes from Vulcano (Fig. 4.13) and Salina (Ellam & Harmon 1990; Gertisser & Keller 2000), suggesting contamination is an important magmatic process in the generation of the more evolved magmas on Lipari, and does not play a major role on Vulcano and Salina.

$\delta^{18}O$ values in feldspars, obsidian and pumice glass from the central Aeolian arc are considerably higher than that of mantle-derived magmas evolving in closed-systems (Sheppard & Harris 1985; Harris *et al.* 2000; Bindemann 2008). $\delta^{18}O_{obsidian}$ values do not vary considerably with a maximum range of 0.4‰. The high $\delta^{18}O$ values observed indicate assimilation is a key process in the central Aeolian arc and is responsible for the O isotopic disequilibrium between mineral pairs. Large variations are observed with the degree of magmatic evolution (e.g. from basalt to rhyolite) feldspar (2.3‰). However, the largest range in $\delta^{18}O$, of 6.9‰, is observed in pumice glass samples.

O and Sr isotopes are combined to determine the composition of the potential crustal contaminant(s) on each island. Due to the variability of the crust beneath the central Aeolian arc, O and Sr isotopes for the dominant crustal lithologies have been characterised to assess the main crustal contaminants on each island. A two-stage process of crustal contamination can be modelled in the central Aeolian arc; (1) source contamination by

subduction, resulting in large Sr isotope variations and small $\delta^{18}O$ variations followed by (2) subsequent crustal contamination and fractional crystallisation processes, giving rise to the steep O – Sr isotope arrays observed (Ellam & Harmon 1990; Gertisser & Keller 2000). The observed trends in O and Sr isotopes further confirm assimilation and fractional crystallisation (AFC) processes and crustal contamination dominate in the intermediate to felsic (rhyolitic) magmas in the central Aeolian arc, with higher $\delta^{18}O$ and $^{87}Sr/^{86}Sr$ values.

Theoretical primary 'parental' magma compositions (O and Sr isotopes) based upon available geochemical data for each island have been calculated to quantify crustal contamination. Sr contents of the 'primary' magmas were estimated using existing literature data from each island separately, assuming a parental SiO_2 content of 48 wt.% and MgO content of 8 wt.% (Appendix C). These data indicate the primary magmas have Sr contents of 800 ppm Sr on Salina, 600 ppm on Lipari and 1100 ppm on Vulcano (Appendix C). The theoretical $^{87}Sr/^{86}Sr$ ratios for each island are calculated using measured $^{87}Sr/^{86}Sr$ ratios from this study and existing literature data. We assume $^{87}Sr/^{86}Sr = 0.7042$ for the primary melts from each island (Ellam *et al.* 1988; Ellam & Harmon 1990; Esperança *et al.* 1992; Gertisser & Keller 2000; De Astis *et al.* 2013). To calculate the $\delta^{18}O$ for the parental magma, we used the corresponding $\delta^{18}O$ values from AOC contamination at a given $^{87}Sr/^{86}Sr$ value. The primary magma $\delta^{18}O$, $^{87}Sr/^{86}Sr$ and Sr contents were then used in the bulk contamination O-Sr mixing models, using a modification of the mixing equation of Langmuir *et al.* (1978), $Ax + Bxy + Cy + D = 0$, where x and y are general variables and A, B, C and D are coefficients of the general variables x and y.

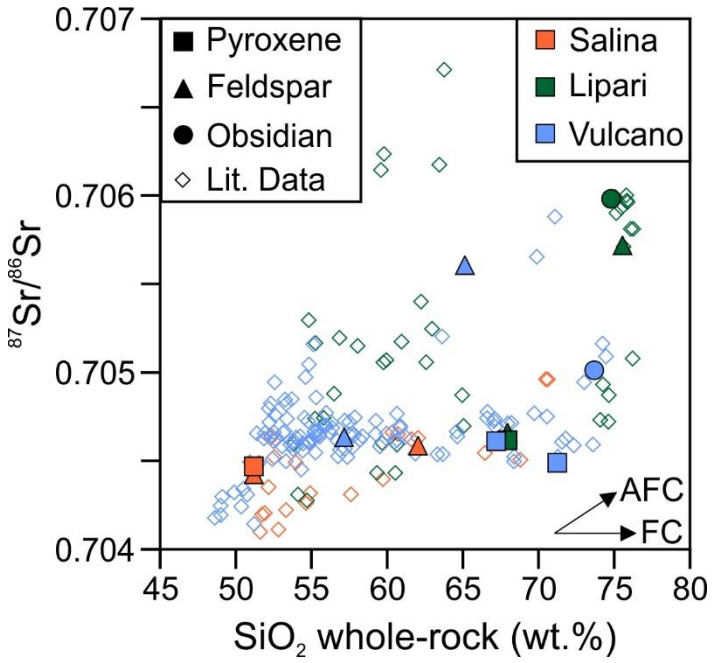

Fig. 4.13: Plot of $^{87}Sr/^{86}Sr$ versus SiO_2 (wt.%) for mineral separates (clinopyroxene and feldspar) and glass (obsidian) from Salina, Lipari and Vulcano. General trends for fractional crystallisation (FC) and assimilation and fractional crystallisation (AFC) are shown. Literature whole-rock data for the central Aeolian arc from: Ellam 1986; Ellam *et al.* 1988; Ellam & Harmon 1990; Esperança *et al.* 1992; Del Moro *et al.* 1998 Gertisser & Keller 2000; Gioncada *et al.* 2003; Peccerillo 2005; De Astis *et al.* 2013; Lucchi *et al.* 2013b.

The island of Salina records the smallest degree of contamination in O isotopes in feldspar and pumice glass. Oxygen isotopes on mineral separates (clinopyroxene ($\delta^{18}O_{cpx}$ +5.5‰ to +5.8‰), feldspar ($\delta^{18}O_{fsp}$ +6.1‰ to +6.3‰) and olivine ($\delta^{18}O_{cpx}$ +5.0‰ to +5.4‰)) and scoria glass ($\delta^{18}O_{gl}$ +5.7‰) from the Pollara activity, Salina show the smallest degrees of contamination of magmas in the arc crust. The highest $\delta^{18}O_{fsp(melt)}$ value for Salina is located close to the crustal contamination array of carbonates (1% - 2% assimilation) and gneisses (8% assimilation). One sample lies slightly above the source contamination trend from AOC and lies along the crustal contamination array of marbles (Fig. 4.14; 4.15). However, all Salina samples lie close to the primary magma composition and therefore distinguishing between the possible different contaminants on Salina is very difficult.

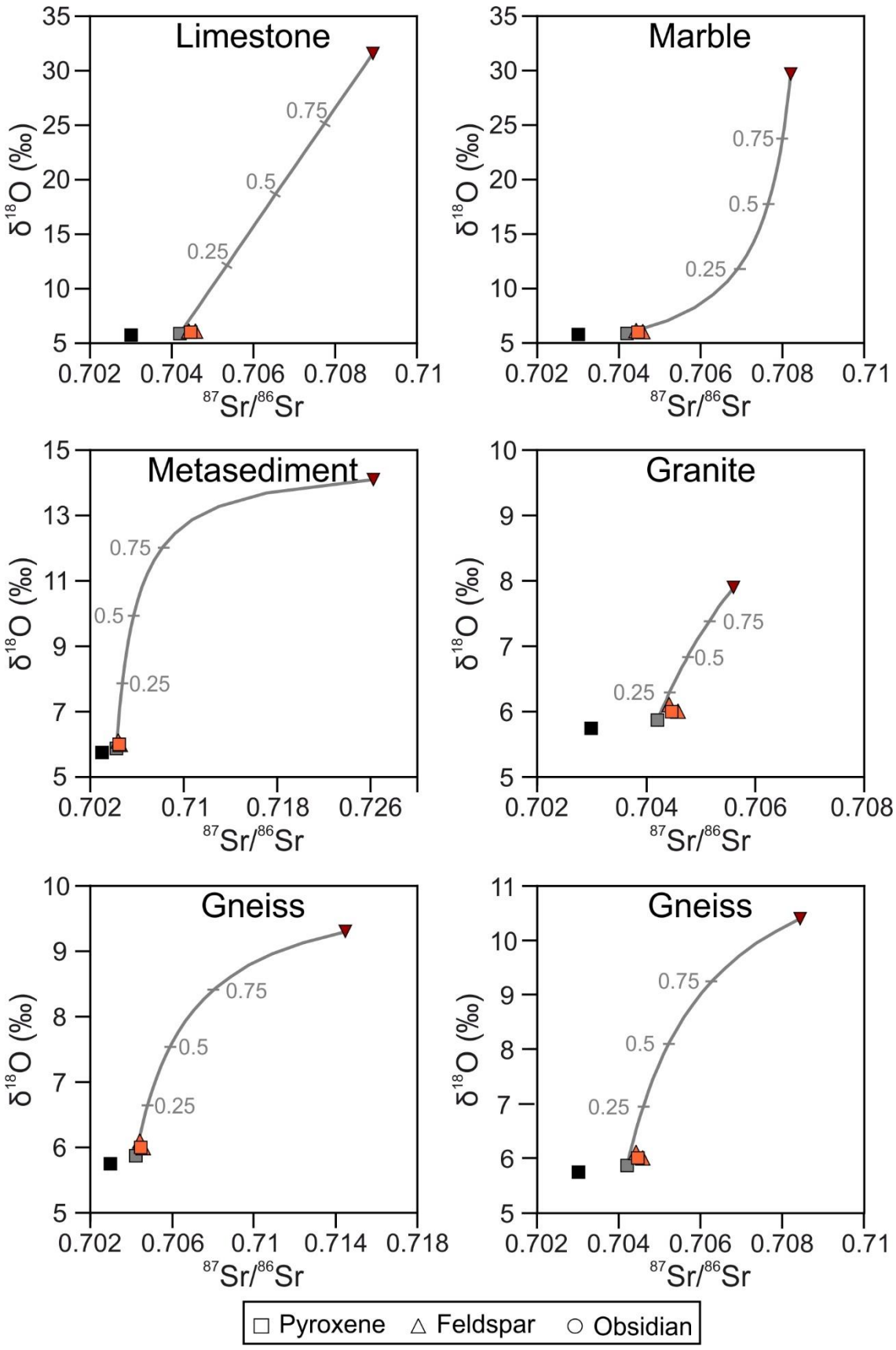

Fig. 4.14: Plot of $\delta^{18}O$ (‰ SMOW) versus $^{87}Sr/^{86}Sr$ for pyroxene and feldspar mineral separates from Salina. The generalised trends for crustal contamination for each contaminant are shown. Black symbol: Mantle, Light grey symbol: Theoretical parental magma for Salina. Ticks show proportion of contaminant.

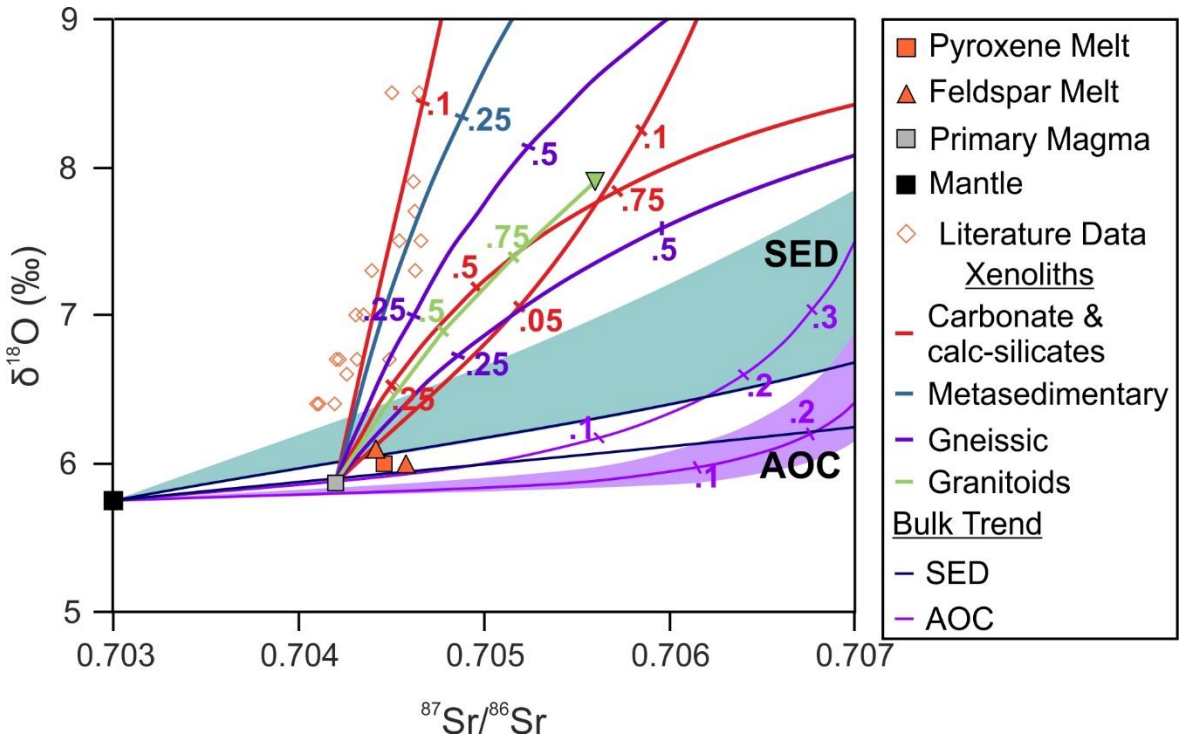

Fig. 4.15: Plot of $\delta^{18}O$ (‰ SMOW) versus $^{87}Sr/^{86}Sr$ for pyroxene and feldspar melt values from Salina. Fields for source contamination trends for altered oceanic crust (AOC) and subducted sediment (SED) and bulk crustal contamination trends for representative crustal lithologies are shown. Black symbol: Mantle, Light grey symbol: Theoretical primary magma for Salina. Whole-rock literature data (diamonds) from Ellam& Harmon 1990; Gertisser & Keller 2000.

On Vulcano, there is strong evidence for crustal contamination in O isotopes, with $\delta^{18}O$ values for feldspar and clinopyroxene crystals higher than or overlapping relative to bulk mantle values (+5.5 ± 0.2‰; Mattey *et al.* 1994; +5.7 ± 0.2‰; Bindemann 2008). Additionally, the peaked trend observed in Zr with increasing SiO_2 suggests crustal contamination occurs at Vulcano, not simple fractionation processes. $\delta^{18}O_{fsp}$ increases with the degree of magmatic evolution. Previous studies indicate clinopyroxene crystals found in latites and trachytes from Vulcano, specifically La Fossa di Vulcano are antecrystic (Chapter 2). $\delta^{18}O_{px}$ reflects source contamination in primitive shoshonitic magmas on Vulcano, lying within estimated melt fields for clinopyroxene. Higher $\delta^{18}O_{px}$ values (> +6.5‰) occur in samples crystallising at shallower levels (c. 12 – 16 km; Chapter 2) and are contaminated by the crust in mid-crustal regions. The variation in $^{87}Sr/^{86}Sr$ in clinopyroxene follows that of FC trends with a small, limited variation observed in

$^{87}Sr/^{86}Sr$ (0.704464 to 0.704612, n=4). $^{87}Sr/^{86}Sr$ versus SiO_2 (Fig. 4.13) indicates feldspars and obsidians from Vulcano follow the trend of AFC processes. By combining $\delta^{18}O$ and $^{87}Sr/^{86}Sr$ (Fig. 4.16; 4.17), this study shows the rhyolite of Lentia (V10-005) and obsidian from Pietre Cotte (AI-17-009) lie on the contamination arrays of gneissic lithology (~20% to 50% assimilation) in the mid-crust at depths of c. 14 km (Chapter 2).

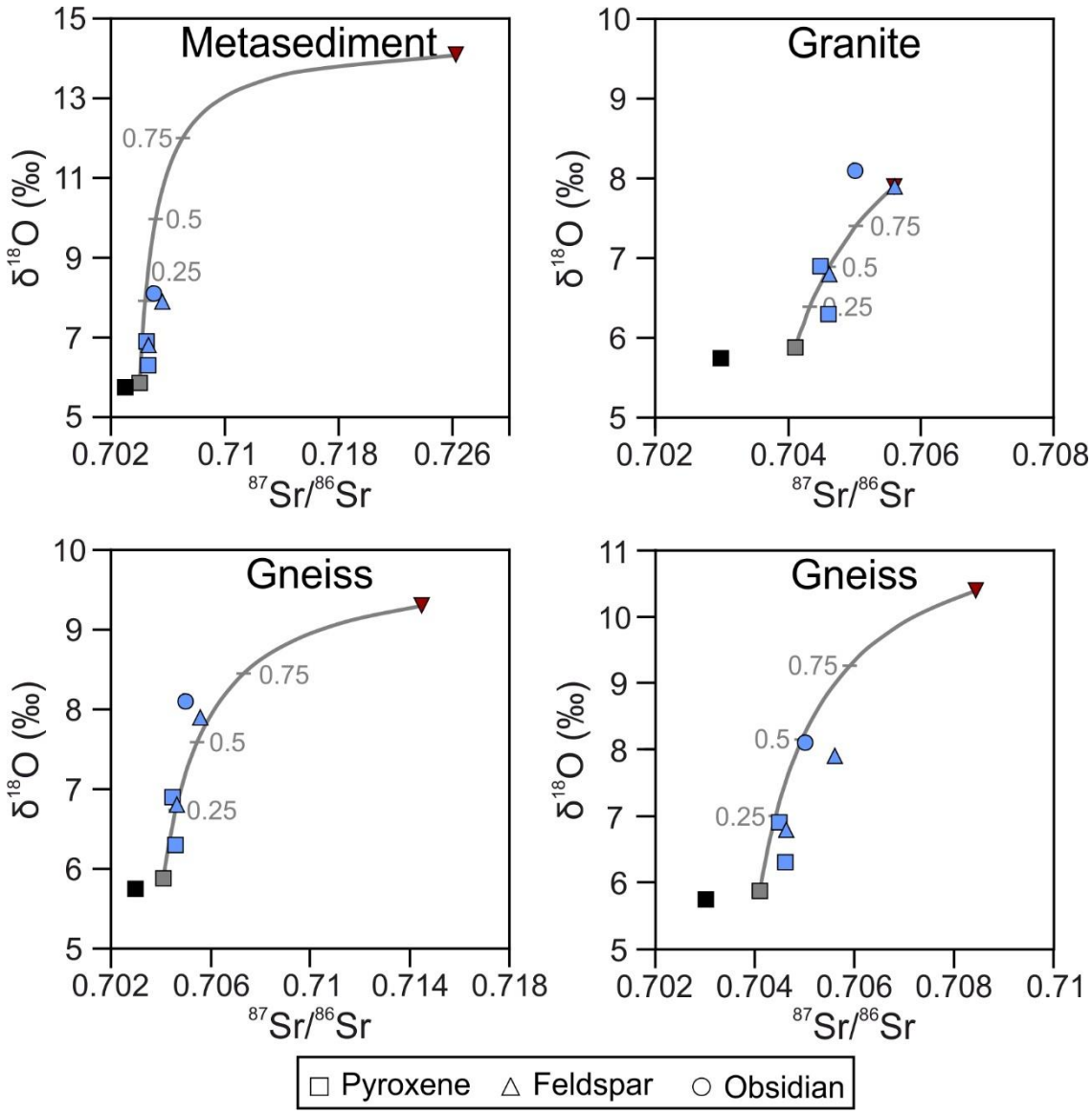

Fig. 4.16: Plot of $\delta^{18}O$ (‰ SMOW) versus $^{87}Sr/^{86}Sr$ for pyroxene and feldspar mineral separates from Vulcano. The generalised trends for crustal contamination for each contaminant are shown. Black symbol: Mantle, Light grey symbol: Theoretical parental magma for Vulcano. Ticks show proportion of contaminant.

The latitic and trachytic melts from which plagioclase crystallised also lie within the contamination array for gneisses and granitoids. However, for granitoids 100% assimilation would be required. Whereas the antecrystic clinopyroxene in the trachytes (Gran Cratere 2; AI-18-074) lie within the source contamination field for subducted sediments with a lower $\delta^{18}O_{px(melt)}$ and $^{87}Sr/^{86}Sr$ ratios.

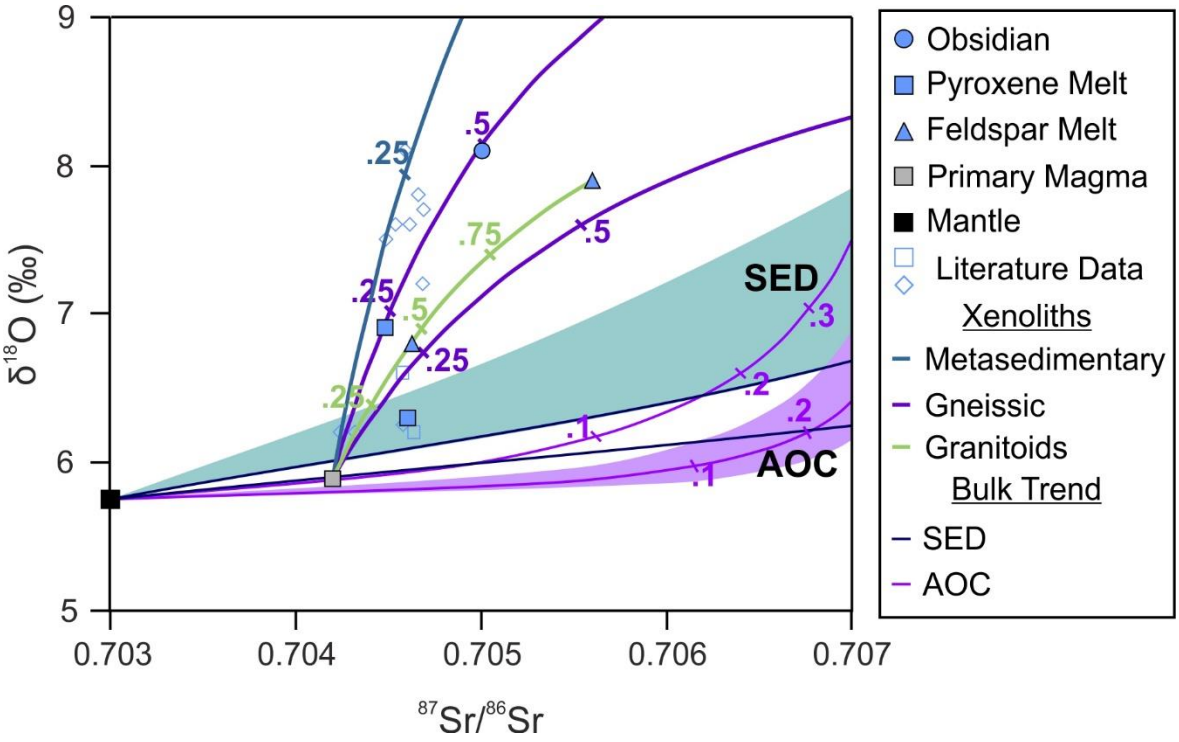

Fig. 4.17: Plot of $\delta^{18}O$ (‰ SMOW) versus $^{87}Sr/^{86}Sr$ for pyroxene and feldspar melt values and obsidian glass from Vulcano. Fields for source contamination trends for altered oceanic crust (AOC) and subducted sediment (SED) and bulk crustal contamination trends for representative crustal lithologies from each island are shown. Black symbol: Mantle, Light grey symbol: Theoretical primary magma for Vulcano. Whole-rock (diamonds) and clinopyroxene literature data from Ellam & Harmon 1990; De Astis *et al.*2013.

Lipari shows strong isotopic evidence for crustal contamination in both O and Sr isotopes (Fig. 4.13). Pumice glass samples from rhyolites on Lipari yield the highest $\delta^{18}O$ values and the largest range in $\delta^{18}O$, (+9.0‰ to +12.6‰ in pumice glass) in the central sector, indicating rhyolitic magma storage regions undergo the highest degree of crustal contamination in the central Aeolian arc. $\delta^{18}O_{fsp}$ values range from +7.9‰ up to +8.4‰, $\delta^{18}O_{obsidian}$ values range from +8.1‰ up to +8.5‰ and a single $\delta^{18}O_{px}$ analysis from a

rhyolite in the Monte Guardia yielded $\delta^{18}O_{px}$ of +7.1‰. The Falcone dacitic dome and latitic enclave within, yielded $\delta^{18}O_{fsp}$ values of +7.9‰ and +7.7‰, and $\delta^{18}O_{px}$ values of +6.2‰ and +6.1‰, respectively. $^{87}Sr/^{86}Sr$ versus SiO_2 (Fig. 4.13) indicates feldspars and obsidians from Lipari follow the trend of AFC processes.

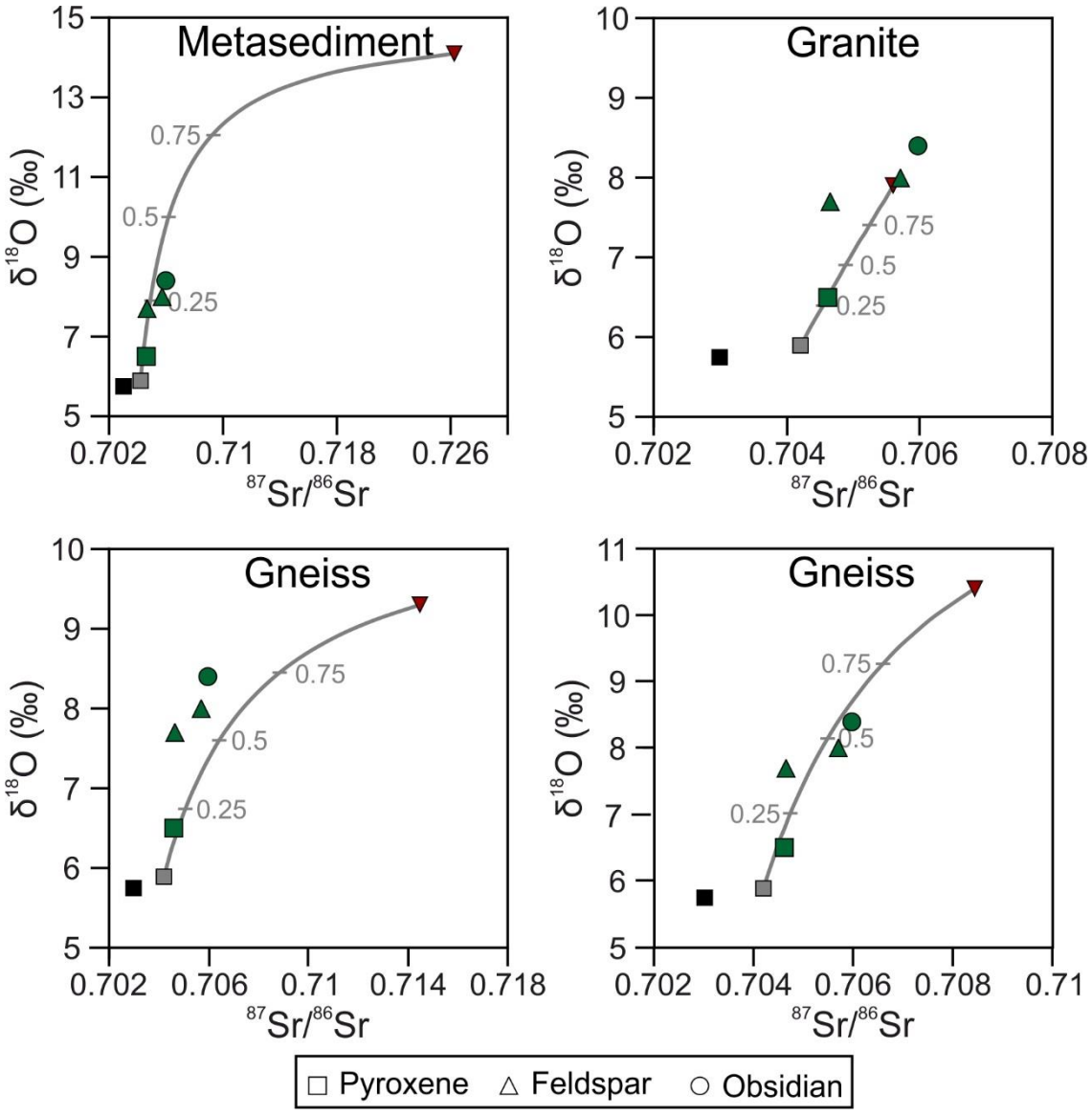

Fig. 4.18: Plot of $\delta^{18}O$ (‰ SMOW) versus $^{87}Sr/^{86}Sr$ for pyroxene and feldspar mineral separates from Lipari. The generalised trends for crustal contamination for each contaminant are shown. Black symbol: Mantle, Light grey symbol: Theoretical parental magma for Lipari. Ticks show proportion of contaminant.

By contrast, the variation in $^{87}Sr/^{86}Sr$ in clinopyroxene follows that of FC trends with a small, limited variation observed in $^{87}Sr/^{86}Sr$ (0.704464 to 0.704612, n=4). Clinopyroxene

and feldspar from the dacitic domes are in O isotopic disequilibrium (Fig. 4.8), indicating they are antecrysts and therefore, similar to Vulcano clinopyroxenes. The melt forming the clinopyroxenes in the Falcone dacitic dome (AI-18-065) is situated upon the contamination array for granitoids, with 25% assimilation, representing lower crustal contamination of these melts (Fig. 4.18; 4.19).

Conversely, the melt from which feldspar crystallised from in the Falcone dacitic dome lies close to the contamination array for meta-sediments (~20% assimilation) indicating late-stage contamination in the upper crust (Fig. 4.19). The rhyolitic melts on Lipari follow the contamination array for meta-sediments, requiring 20% assimilation. Therefore, contamination from meta-sediments in the upper crust may result in the high $\delta^{18}O$ in pumice glass and mineral separates from rhyolites on Lipari.

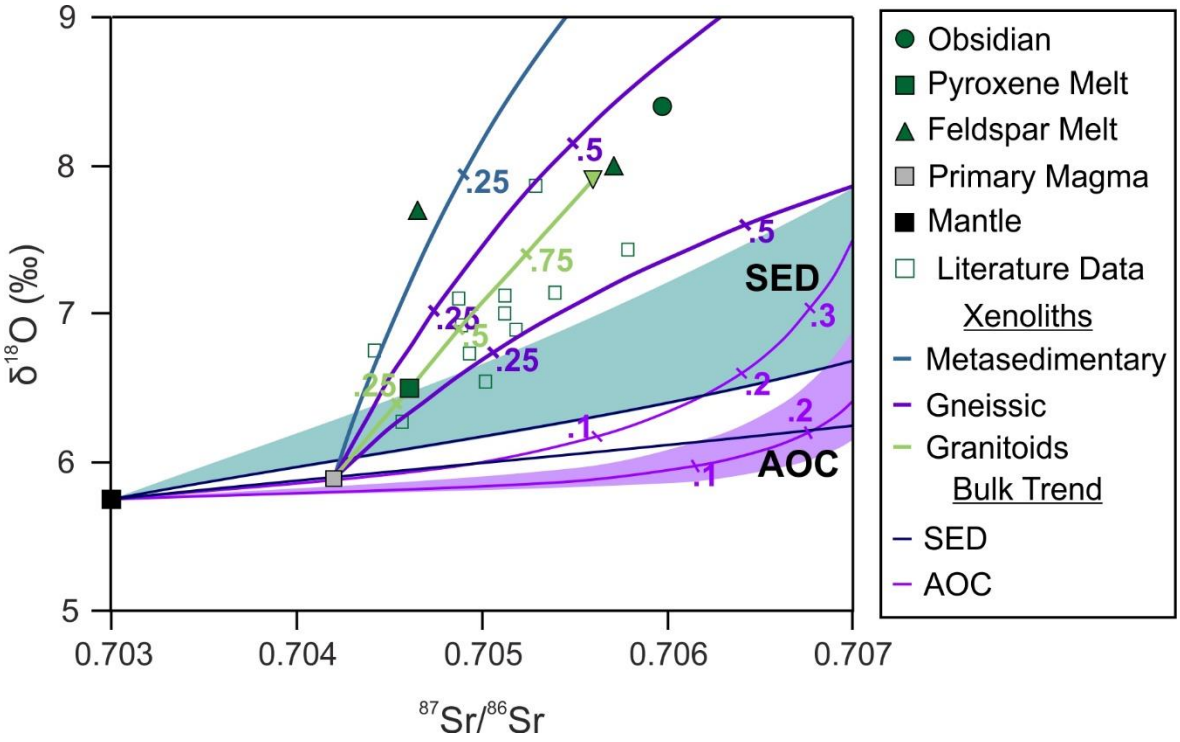

Fig. 4.19: Plot of $\delta^{18}O$ (‰ SMOW) versus $^{87}Sr/^{86}Sr$ for pyroxene and feldspar melt values and obsidian glass from Lipari. Fields for source contamination trends for altered oceanic crust (AOC) and subducted sediment (SED) and bulk crustal contamination trends for representative crustal lithologies from each island are shown. Black symbol: Mantle, Light grey symbol: Theoretical primary magma for Lipari. Clinopyroxene literature data from Forni *et al.* 2015.

This study indicates magmas undergo source contamination and subsequent crustal contamination during ascent and storage in the crust in the central Aeolian arc (Fig. 4.20). Our results show magmas from Salina, Lipari and Vulcano are contaminated by different crustal lithologies. We show that on Salina, the Lower Pollara magmas underwent source contamination by AOC and small amounts of crustal contamination by localised carbonate lithologies (marbles) within the upper crust (uppermost 5 km: Fig. 4.20) resulting in steep mixing trends for carbonate lithologies or crustal contamination by gneisses at mid-crustal depths. Conversely, Vulcano trachytic and rhyolitic magmas underwent source contamination, followed by subsequent contamination from by gneissic lithologies at mid-crustal depths (c. 12 – 16 km: chapter 2).

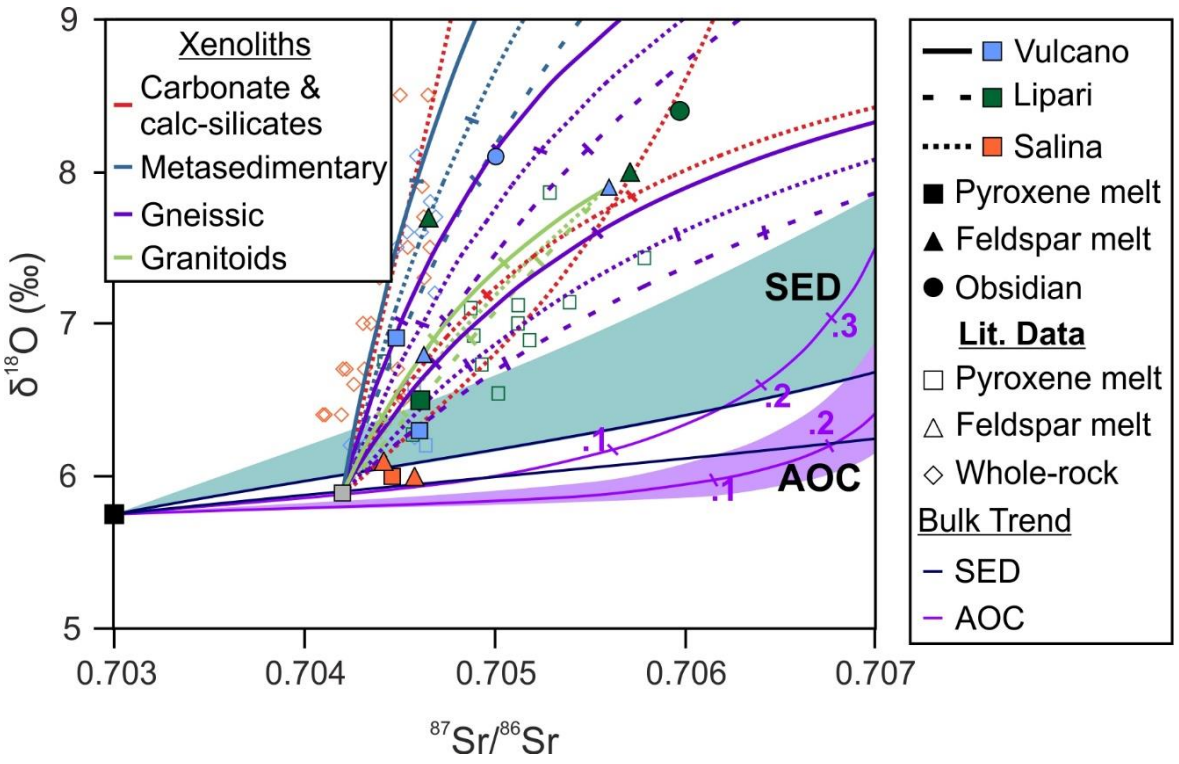

Fig. 4.20: Plot of $\delta^{18}O$ (‰) versus $^{87}Sr/^{86}Sr$ for and calculated melt values from mineral separates (clinopyroxene and feldspar) and glass (obsidian) from Salina, Lipari and Vulcano, plotted with existing literature data (Ellam & Harmon 1990; Gertisser & Keller 2000; De Astis *et* al. 2013; Forni *et al*. 2015). Fields for source contamination trends for altered oceanic crust (AOC) and subducted sediment (SED) are shown. Bulk crustal contamination trends for representative crustal lithologies from each island are shown.

Obsidian glass from Vulcano is situated close to the contamination trends of gneiss. The latitic and trachytic melts from which feldspar crystallised lie upon the contamination array for gneiss and granitoids indicating contamination of their associated melts occurred at mid- to lower-crustal levels. On Lipari, the magma the clinopyroxene in the dacitic dome crystallised from is situated on the source contamination array for subducted sediments or the crustal contamination array from lower crustal granitoids (~ 25% assimilation: Fig. 4.20). In addition, the magmas the feldspar and obsidian glass lie within the contamination array for gneiss and close to the array for meta-sediments. Therefore, theses magmas were contaminated at mid-crustal depths.

4.6 Conclusions

O and Sr data for the central Aeolian arc provides unequivocal evidence for source contamination and subsequent crustal contamination, demonstrating the importance of AFC processes in the generation of intermediate to felsic magmas. Source contamination by altered oceanic crust dominated in the central Aeolian arc, particularly on Salina. However, O and Sr isotopes also indicate contamination of magmas by subducted sediments on Lipari and Vulcano.

This study is the first study to quantify and identify the likely crustal contaminants on each island and to constrain the contaminants which dominate during different stages of magmatic evolution on each island. This study shows crustal contamination dominates in the more evolved magmas, particularly in rhyolites evidenced by O isotope contents in feldspars, obsidians and pumice glasses, and the large variability in Sr isotopes in feldspars and obsidians.

Through the utilisation of O and Sr isotopes, this study has constrained the contaminants on each island:

- Source contamination from AOC fluids and subducted sediment melts affects the primary magmas in the central Aeolian arc.
- On Salina, combined $^{87}Sr/^{86}Sr$ and O isotopes indicate small degrees of contamination (< 5% assimilation) in the basaltic scoria and andesitic lava of Lower Pollara, by either upper crustal carbonates which or mid-crustal gneisses. The new mineral data from this study do not follow the steep whole-rock trends for Salina which appear to follow the contamination arrays of meta-sediments or carbonates. New data from this study are characterised by lower $\delta^{18}O$ and slightly higher $^{87}Sr/^{86}Sr$.
- Most of the analysed mineral pairs on Vulcano are in O isotope disequilibrium, indicating clinopyroxene are antecrysts crystallising from different melts. Crustal contamination dominates in the more evolved melts (trachytes and rhyolites) on Vulcano by mid-crustal gneissic lithologies (20% up to 50% assimilation: c. 11 - 14 km) and/or lower-crustal granitoids requiring 50 % bulk assimilation.
- O isotope disequilibrium in mineral pairs on Lipari, suggests the clinopyroxene are antecrysts and therefore did not crystallise from the same melt. On Lipari, the melt from which clinopyroxene crystallised was contaminated by lower crustal granitoids (requiring 25% assimilation) and the melt from which feldspar crystallised is contaminated by mid-crustal gneisses. Conversely, the rhyolitic melts from Lipari are contaminated by upper-crustal meta-sediments, resulting in the large increase in $\delta^{18}O$.

CHAPTER 5: Petrogenesis of arc magmas

Volcanic arcs are renowned worldwide for the complex magmas erupted, however there is no one universal model that can produce the large spectrum of eruptive products found (basalts to rhyolites). Volcanic arcs are dominated by intermediate magmas which have undergone large degrees of differentiation during magma ascent and stalling at varying crustal levels from the parental mafic magma source (Gill 1981; Hildreth & Moorbath 1988; Carmichael 2002; Zellmer *et al.* 2005; Klaver *et al.* 2017). In contrast to other volcanic arcs, the Aeolian arc is geodynamically complex due to the heterogenous mantle sources and different shallow level processes, resulting in the complexity observed in eruptive products.

Previous work on the Aeolian arc, and more generally volcanic arcs have identified several processes e.g. magma mingling, crustal contamination, and fractional crystallisation, to date it has remained difficult to distinguish between several key processes. The preceding chapters in this thesis have presented a new detailed stratigraphically controlled dataset from La Fossa di Vulcano and the central Aeolian arc to elucidate the processes operating within the subvolcanic system. The new data presented in previous chapters will be combined with previous literature and placed in the wider context of the entire Aeolian arc and more generally volcanic arcs.

5.1 The importance of mantle source compositions in the generation of arc magmas

The composition of arc magmas is strongly influenced by contributions from the slab, mantle, and crustal sources (e.g. Hildreth & Moorbath 1988; Plank & Langmuir 1988; 1993; Miller *et al.* 1994; Lee & Bachmann 2014; Turner & Langmuir 2015). The role of the subducted lithosphere in the generation of arc magmas is extremely complex, due to the wide variety of potential island arc magma sources. Sources of arc magmas can be broadly divided into 1) the mantle wedge consisting of the oceanic lithosphere and the upper mantle, 2) the oceanic crust comprising metamorphosed igneous rocks (basalt, dolerite, gabbro) and oceanic sediments (pelagic clays, carbonates, and terrigenous clastic sediments). The importance of mantle source compositions has been invoked at many other volcanic arcs worldwide including the Andes, South America (Hickey-Vargas *et al.* 1986; Hildreth & Moorbath 1988; Davidson *et al.* 1990; Tormey *et al.* 1991; Hildreth *et al.* 2010; Jacques *et al.* 2013), the Lesser Antilles arc, Caribbean (e.g. Davidson 1987; Van Soest *et al.* 2002), the Sunda arc, Indonesia (e.g. Gasparon *et al.* 1994; Turner & Foden 2001; Gertisser & Keller 2003; Troll *et al.* 2013; Handley *et al.* 2014).

Geochemical studies in the southern Tyrrhenian Sea define an upper mantle with an Ocean Island Basalt (OIB-) to a Mid-Ocean Ridge Basalt (MORB-) type composition (Trua *et al.* 2004; 2011). Previous studies on the Aeolian archipelago to the source compositions of magmas have identified a minimum of three distinct end members; the pre-metasomatic mantle, subducted Ionian crust, and subducted Ionian sediments (Peccerillo *et al.* 2013). In the Aeolian archipelago mantle wedge heterogeneity, results in the observed variations in radiogenic isotopes in the mafic rocks (e.g. Ellam 1986; Ellam *et al.* 1988; Ellam & Harmon 1990; Francalanci *et al.* 1993; De Astis *et al.* 2000; Peccerillo *et al.* 2004; 2013). However, the considerable influence of magma-crust interactions raises many questions as to the respective contributions of source heterogeneity and magma contamination during

differentiation, particularly in the central sector. Large variations in both source contamination and crustal contamination are observed across the three sectors in the Aeolian arc (western, central, and eastern). A general increase is observed in $^{87}Sr/^{86}Sr$ (Fig. 5.1) from West to East with large variations in $\delta^{18}O$ across the entire arc (Fig. 5.1) indicating the degree of source contamination increases by subducted sediments increases to the East (e.g. Ellam 1986; Ellam *et al.* 1988; 1989; Ellam & Harmon 1990; Francalanci *et al.* 1993; 2004; 2007; De Astis *et al.* 2000; Peccerillo 2005), which is also observed in whole-rock trends on Stromboli (Fig. 5.1). To date, the relative contributions of source and crustal contamination have not been differentiated in the central sector. This study shows large variations are observed in $\delta^{18}O$ (+5.0‰ to +12.6‰) across the central sector and smaller variations in $^{87}Sr/^{86}Sr$ (0.704419 to 0.705977), showing source contamination and subsequent crustal contamination in the central Aeolian arc during varying stages of magma differentiation and ascent. Future work should focus upon a more detailed study of the Pollara activity on Salina as current data all plot close together and record little to no contamination. In addition, future work should focus upon quantifying the composition of the subducting components, especially sediments from the Ionian slab, specifically O isotopes which can be used to better constrain the subducted sediment component in the entire arc.

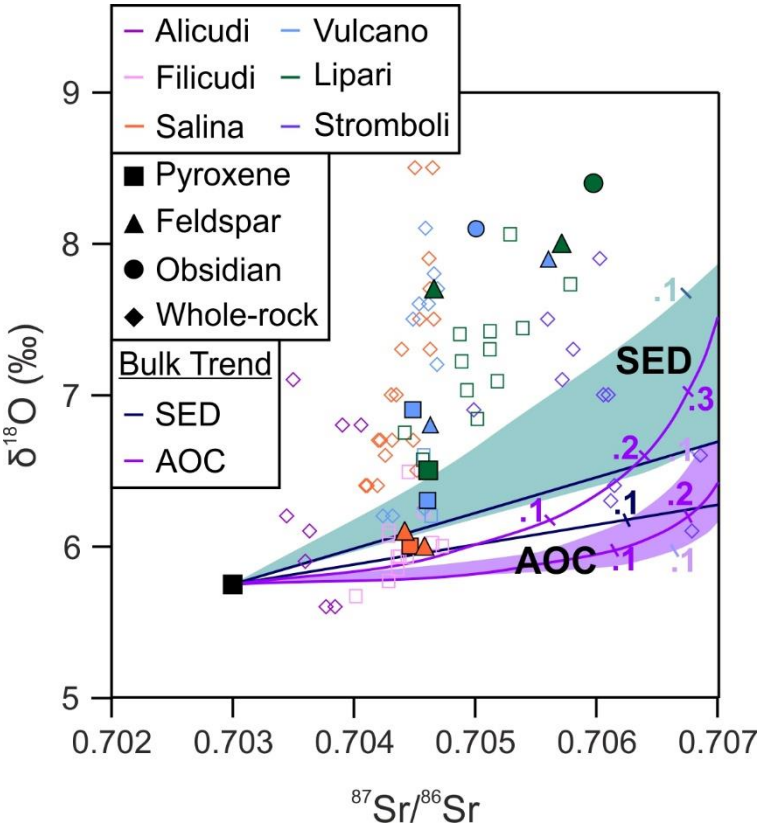

Fig. 5.1: Plot of $\delta^{18}O$ (‰) versus $^{87}Sr/^{86}Sr$ for the western sector (Alicudi and Filicudi), central sector (Salina, Lipari and Vulcano) and the eastern sector (Stromboli) of the Aeolian archipelago. Source contamination trends for altered oceanic crust and subducted sediment are shown. See chapter 4 for calculations. Data from: Ellam & Harmon 1990; Peccerillo & Wu 1992; Peccerillo *et al.* 1993; Gertisser & Keller 2000; Peccerillo *et al.* 2004; Santo & Peccerillo 2008; De Astis *et al.* 2013; Forni *et al.* 2015).

5.2 Magmatic processes at volcanic arcs

The wide range in eruptive compositions erupted at volcanic arcs result from the interplay of a numerous magmatic processes e.g. fractional crystallisation, magma mixing and / or mingling, crustal contamination, and variability in other relevant factors, e.g. magma ascent rates (Hildreth & Moorbath 1988; Davidson *et al*. 1990).

5.2.1 Transcrustal Differentiation

The concept of the 'classic' textbook large magma chamber has shifted to a model where magma differentiation from mafic to silicic compositions occurs throughout the crust (transcrustal differentiation; Fig. 5.2) and the importance of crystal mushes throughout the system (Cashman *et al.* 2017). The concept of transcrustal differentiation centres around the idea that magma chambers are open systems modified by crustal assimilation and replenishment (De Paolo 1981; Anderson 1976), where differentiation occurs at various stages throughout the crust (Fig. 5.2) and not in the 'classic' large aphyric shallow magma reservoir (Cashman *et al.* 2017).

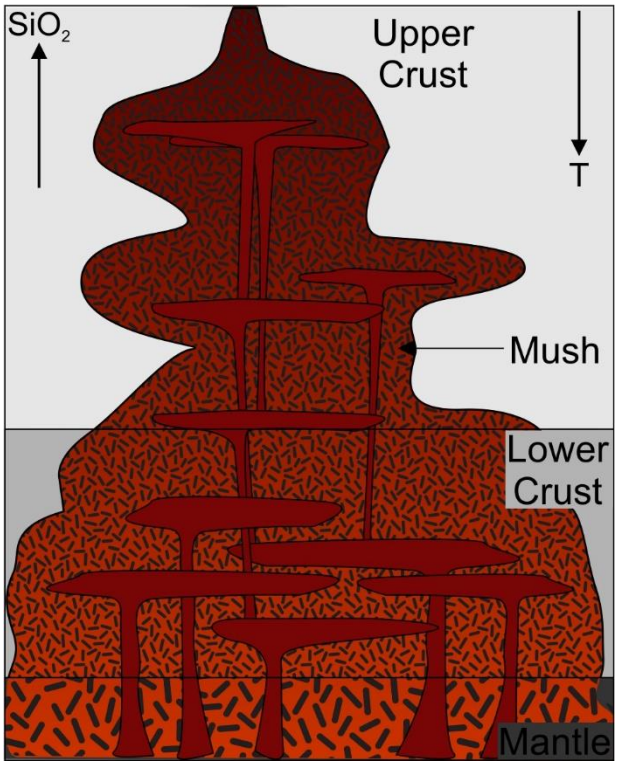

Fig. 5.2: Schematic sketch showing a transcrustal magmatic system, dominated by crystal mush regions within the system. After: Christopher *et al.* 2015; Cashman *et al.* 2017).

Melts located within a transcrustal magma systems are located within large vertically extensive crystal mushes under super solidus conditions (Cashman *et al.* 2017). Melts within the crystal mush regions are extracted and subsequently erupted from the mush and react with different mineral phases to replenish and remobilise parts of the mush crystal system (Marsh 1996; Davidson *et al.*2007; Cooper *et al.* 2016; Bachmann & Huber 2018).

Furthermore, melts within the system also become trapped and crystallise in disequilibrium conditions with the main magmatic system (Bernstein 2006; Krause *et al.* 2007).

In the central Aeolian arc, this work has shown that magmatic differentiation (mafic to silicic) occurs in the mid to upper crustal regions. This work has shown that at La Fossa di Vulcano, Vulcano melts evolve from mafic to silicic compositions at various levels within the magmatic system, interacting with a dynamic crystal mush region. This study has shown glomerocrysts and antecrysts originate from the mush regions and are subsequently incorporated into the shallower magma storage regions during magma recharge events and mush remobilisation into latitic and trachytic magmas. The link between the remobilisation of crystal mushes and eruptions are probably not restricted to La Fossa di Vulcano and are likely to be a common process during silicic eruptions (e.g. Neapolitan Yellow Tuff eruption (Forni *et al.* 2018), Santorini volcano (Fabbro *et al.* 2018).

5.2.2 The role of crystal mushes in magmatic systems

Crystal mushes are multiphase systems where buoyant melts are disseminated within a deformable crystalline matrix (McKenzie 1984; Solano *et al*. 2012; Connolly & Podladchikov 2015; Spiegelman *et al.* 2001). However, crystal mushes cannot be erupted in their entirety (Marsh 1981), but mush fragments are frequently erupted as cumulate nodules, restites and glomerocrysts within erupted products (Cashman *et al.* 2017). Recently, research on Lipari and Vulcano has transitioned to favour a model where crystal mushes dominate during magmatic differentiation (Forni *et al.* 2015; Bullock *et al.* 2019; Costa *et al.* 2020).

Glomerocrysts are not only abundant in magmatic enclaves (Bullock *et al.* 2019) but in all La Fossa di Vulcano eruptive products across the entire compositional range of eruptive products and provide insights into crystal mushes within the magmatic system of La Fossa

di Vulcano. For example, banded pumices were found at the top of the Pietre Cotte 1 formation, which evolved from latite to rhyolite. This study has identified a minimum of two dynamic crystal mushes at intermediate crustal levels in the La Fossa di Vulcano plumbing system. This study has shown crystal mushes are responsible for entraining xenocrystic and antecrystic mineral phases during magma replenishment and remobilisation into the shallower storage regions. Crystal mushes and glomerocrysts formation may also play an important role in the incorporation of xenocrystic and antecrystic mineral phases at other arc volcanoes.

5.2.3 Fractional Crystallisation

It is widely accepted that fractional crystallisation is the dominant process during the genesis of intermediate to felsic magmas at volcanic arcs in general (e.g. Cashman *et al.* 2017) and more specifically the central sector of the Aeolian arc (Peccerillo *et al.* 2013), with basic minerals (e.g. olivine, clinopyroxene, amphibole, biotite, and plagioclase) the main fractionating phases. Fractional crystallisation, however, is not the only magmatic process operating during the evolution of magmas in the central sector of the Aeolian arc, as it is accompanied by magma mixing and wall-rock contamination processes. In the Aeolian arc, fractional crystallisation is also influenced by localised tectonic structures, the Tindari-Letojanni fault (TLF) system, resulting in the formation of large magma reservoirs within a small-scale pull apart basin (Barberi *et al.* 1994).

Combined assimilation and fractional crystallisation dominate the central Aeolian arc evidenced by major and trace element trends (e.g. Al_2O_3, MgO, and Cr versus SiO_2 plots and Sr isotopic trends (Fig. 4.13) and more over the entire arc. Magma mixing in volcanic arcs influences magma compositions across a variety of scales, including during a single eruption, during the evolution of a volcanic centre and at regional scales across volcanic

arcs. Magma mixing and mingling processes dominate in the intermediate to silicic lavas in the Aeolian arc, specifically the islands of Panarea (Calanchi *et al.* 2002; Lucchi *et al.* 2013e), Lipari and Vulcano where mafic magmatic enclaves are abundant (De Rosa & Sheridan 1983; Gioncada *et al.* 2005; Perugini *et al.* 2007; De Astis *et al.* 2013a; Forni *et al.* 2013; Bullock *et al.* 2018). This study has also shown that in addition to magmatic enclaves, there is abundant macroscopic evidence of mingling in the La Fossa di Vulcano magmatic system with banded pumices and abundant microscopic mixing and mingling textures within all La Fossa di Vulcano eruptive products including compositional zoning and resorption textures in plagioclase, alkali feldspar and clinopyroxene.

5.3 The role of the crust in the generation of arc magmas

The genesis of arc magmas can be significantly modified by processes of source contamination from the subducting material and crustal contamination processes (Arculus & Johnson 1981; Davidson 1985; Arculus & Powell 1986). Distinguishing between these two types of contamination has been enigmatic, due to the variability of the end-member compositions. At island arcs source contamination is considered to be very important, however, combined source and crustal contamination processes are becoming more favoured at volcanic arcs (e.g. Arculus & Johnson 1981; Arculus & Powell 1986; Davidson 1995; Plank & Langmuir 1998; Thirwall *et al.* 1996; Chadwick *et al.*2007). A combination of source contamination, followed by crustal contamination is common at many volcanic arcs including the Aeolian arc e.g. the Andes (Thorpe *et al*. 1984), the Lesser Antilles (Davidson 1987), the Taupo Volcanic Zone (Macpherson *et al.* 1998) and the Sunda arc (Handley *et al.* 2014).

In the Aeolian arc, crustal contamination is ubiquitous, particularly in basaltic and andesitic magmas (Peccerillo *et al.* 2013). For example, in the western sector, basaltic magmas on Alicudi show high degrees of crustal contamination, with abundant magmatic

and metamorphic xenoliths (quartzite, quartz – clinopyroxene bearing granofels, rare biotite schists and occasional dunites) and increasing $^{87}Sr/^{86}Sr$ with SiO_2, evidencing the prevalence of magma-wall interactions with variable degrees of melting in the magma reservoir and volcanic conduit (Peccerillo & Wu 1992; Peccerillo *et al.* 1993; 2004; Lucchi *et al.* 2013f). Conversely, Filicudi magmas evolved through fractional crystallisation (FC) processes dominated the differentiation of Filicudi magmas, with variable contributions from magma mixing and wall-rock assimilation (Santo & Peccerillo 2004; Lucchi *et al.* 2013g).

In the eastern sector, metamorphic crustal xenoliths are abundant in eruptive products from Panaraea however, a large degree of scattering is observed in $^{87}Sr/^{86}Sr$ versus SiO_2 variation diagrams (Fig. 5.3) indicating the variability in Sr isotopes is not only due to magma-crust interactions. However, it must be noted within single rock suites a positive correlation between $^{87}Sr/^{86}Sr$ versus SiO_2 is observed indicating AFC processes occur during the evolution of rock suites (Lucchi *et al.* 2013e). Eruptive products from the easternmost island of Stromboli contain abundant xenoliths including subvolcanic, cumulates, thermometamorphic, anatectic and residual crustal xenoliths from partial melting (Honnorez & Keller 1968). At Stromboli, different periods of volcanic activity show different degrees of contamination. The Stromboli magmatic system is dominated by mantle source heterogeneities and magma mixing processes dominate (Francalanci *et al.* 2013).

In the central Aeolian arc, source contamination by subducted sediment and subsequent crustal assimilation and fractional crystallisation (AFC) processes dominates (Ellam *et al.* 1988; Ellam & Harmon 1990; Crisci *et al.* 1991; Esperança *et al.* 1992; Gertisser & Keller 2000; Francalanci *et al.* 2007; De Astis *et al.* 2013a; Lucchi *et al.* 2013b; Forni *et al.* 2013; Peccerillo *et al.* 2013). The central sector is marked by an increase in O and Sr isotope ratios with SiO_2 on Lipari and Vulcano (Fig. 5.3). This study provides the most

comprehensive isotopic study to date on crustal xenoliths where we linked the crustal xenoliths to the known crustal structure from geophysical studies (Peccerillo *et al.* 2006) to discriminate between the different crustal contaminants in different magmas. This study has identified the main crustal contaminants are subducted sediments in the central Aeolian arc orginating from the volcanic and metasedimentary cover. Future work in the Aeolian Islands should focus on further constraining the crustal xenoliths through detailed P-T investigations of the range of xenoliths could be undertaken to further constrain the known crustal structure.

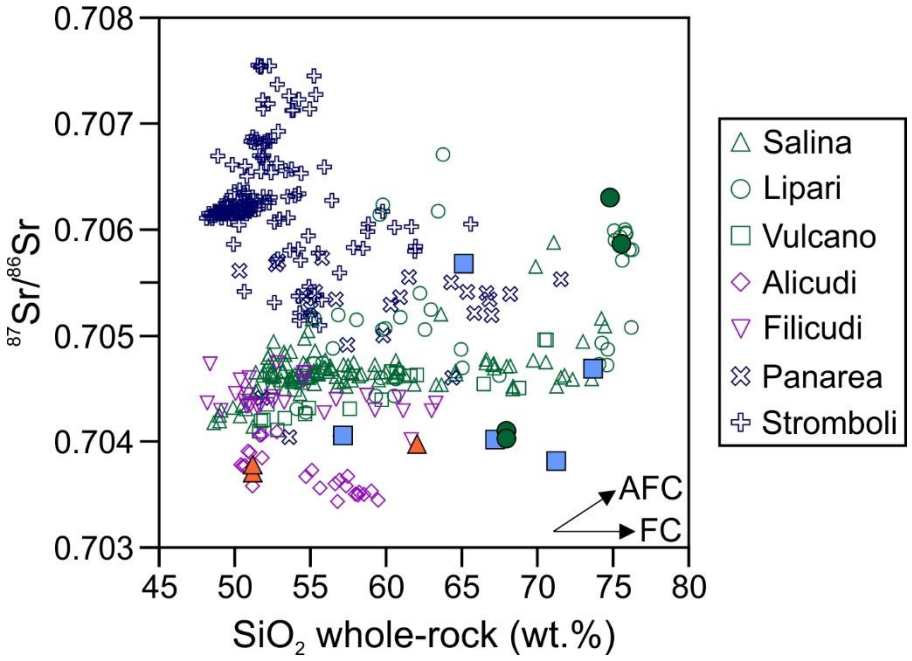

Fig. 5.3: Plot of $^{87}Sr/^{86}Sr$ versus SiO_2 (wt.%) from the entire Aeolian arc. General trends for fractional crystallisation (FC) and assimilation and fractional crystallisation (AFC) are shown. Literature whole-rock data from De Astis *et al.* 2013; Lucchi *et al.* 2013b; c; d; e; f; g; Forni *et al.* 2013; Francalanci *et al.* 2013 and references therein.

5.4 Problems determining magma storage conditions in the central Aeolian arc

Clinopyroxene crystallisation conditions in volcanic systems are constrained using geobarometrical modelling. A large variety of thermometers and barometers using

clinopyroxene compositions or clinopyroxene-melt compositions have been developed for igneous systems (e.g. Nimis 1995; 1999; Nimis & Ulmer 1998; Nimis & Taylor 2000; Putirka *et al.* 1996; 2003; Putirka 2008). These models are all valid for calc-alkaline systems and have been derived from regression of analyses of experimental data and are therefore associated with large inherent uncertainties. To date one clinopyroxene-liquid geobarometer has been developed specific to phonolitic and trachytic systems only (Massotta *et al.* 2013). However, this barometer cannot be applied successfully to La Fossa di Vulcano as the system is alkaline and not only composed of trachytes, therefore this barometer would product high errors in the estimates (Massotta *et al.* 2013). Previous works by Nazzareni *et al.* (1998; 2001) defined the crystallographic parameters of clinopyroxene from lavas across the Aeolian arc, using these parameters to constrain crystallisation pressures (and depths). To estimate clinopyroxene crystallisation conditions at La Fossa di Vulcano, clinopyroxene crystal structures (unit cell volume (VCell) and volume of the M1 site occupancy (VM1)) were determined as they are analogous to pressure variations during crystallisation, hence depths.

The Aeolian arc is characterised by polybaric crystallisation at variable depths, with mafic to intermediate magmas ponding in deep reservoirs at depths of 18 – 21 km (Peccerillo *et al.* 2013). Our results are largely in agreement with previous depth estimates at Vulcano (e.g. Clocchiatti *et al.*1994; De Astis *et al.* 2013; Nicotra *et al.* 2018; Bullock *et al.* 2019; Costa *et al.* 2020). This study has built upon previous works using crystallographic cell parameters, by defining the crystallisation parameters of clinopyroxene phenocrysts from lavas, pyroclastic deposits and enclaves covering the entire eruptive history of La Fossa di Vulcano. This study shows clinopyroxene crystals at La Fossa di Vulcano crystallise over a large range of depths in the subvolcanic system and are often incorporated as antecrysts originating from the crystal mush regions into the interconnected magma storage regions. This work has shown that at La Fossa di Vulcano magmatic differentiation during the

evolution of one volcanic occurs in the upper to mid crust (< 18 km), however there are large variations in one single lithology e.g. latite. Future work at Vulcano should focus upon developing a more accurate geobarometer applicable to alkaline systems which can then be applied to other alkaline systems.

5.5 Magma ascent and crystallisation in the conduit

Variations in magma ascent rates, magma recharge and crystallisation conditions have been linked to differing degrees of explosivity and are therefore crucial in deciphering the often-cyclic transitions from initially explosive to effusive volcanic eruptions. These processes have been observed at many other arc volcanoes including; Guagua Pichincha, Ecuador (Wright *et al.* 2007), Galeras, Colombia (Stix *et al.* 1993; Bain *et al.* 2018), Mt St Helens, USA (Fink *et al.* 1990; Hoblitt & Harmon 1993; Cashman & McConnell 2005), Merapi, Indonesia (Preece *et al.* 2013; 2016), Mt Pelée, Martinique (Villemant & Boudon 1998; Martel 2012), Mt Pinatubo, Philippines (Polacci *et al.* 2001), Novarupta, Alaska (Adams *et al.* 2006; Isgett *et al.* 2017), Mt Taranaki, New Zealand (Platz *et al.* 2006); Soufrière Hills, Montserrat (Young *et al.* 1998; Burgisser *et al.* 2010; 2011), Tokachidake volcano, Japan (Yamagishi & Feebrey 1994), and Volcán de Colima, Mexico (Cassidy *et al.* 2015).

This study has shown closed system degassing and crystallisation resulting in gas overpressure resulting in the explosive 1888-90 eruption on Vulcano has also been linked as dominant mechanism behind driving explosive eruptions at other arc volcanoes e.g. Galeras (Stix *et al.* 1993; Bain *et al.* 2018), Merapi (Preece *et al.* 2013; 2016), Mt Pelee (Villemant & Boudon 1998; Martel 2012) Soufrière Hills (Voight & Elsworth 2000; Clarker *et al.* 2007; Edmonds & Herd 2007; Burgisser *et al.* 2011). Textural analyses of feldspar microlites and timescales of crystallisation using crystal size distributions in this

study, identified the shallow conduit processes during conduit evolution and the eruption of breadcrust bombs. In the days preceding the 1888-90 eruption, the conduit system switched from closed- to open-system degassing. To constrain magma pre-eruptive magma storage conditions; crystal times in the magmatic system can be traced (e.g. Hawkesworth *et al*. 2004; Costa & Dungan 2005; Morgan *et al.* 2004; Druitt *et al.* 2012; Fabbro *et al.* 2017; Petrone *et al.* 2016; 2018). Future research on the 1888-90 eruption will focus on the clinopyroxene population, to deduce deeper processes occurring prior to eruption, yielding information on magma storage, ascent, mixing and clinopyroxene crystal residence times prior to eruption.

5.6 Main Thesis Conclusions

This thesis sought to investigate magma storage and differentiation processes at volcanic arcs, and the implications these processes have on the magmatic system. The previous chapters included in this thesis have examined the role of source contamination and extent of crustal contamination in the generation of intermediate and silicic magmas, the bulk crustal contaminations, the driving forces of explosive and effusive eruptions and the role of shallow conduit processes during single eruptions. This thesis has developed our understanding of the processes operating within the subvolcanic system and insights into the pre-eruptive magmatic system of some of the most hazardous young volcanic centres in the Aeolian arc, specifically those on Lipari and Vulcano.

The evolution of La Fossa di Vulcano magmatic system over the last 5.5 kyr was constrained geochemically and isotopically, using a detailed stratigraphically controlled study, encompassing the range of eruptive products from one single eruptive formation (e.g. ash, pumice, scoria, lava, and enclaves from the Pietre Cotte Formation), whereas previous studies have primarily focused upon lavas (e.g. Nazzareni *et al.* 2001; Piochi *et*

al. 2009; Bullock *et al.* 2019). Through a detailed approach sampling both lavas and pyroclastic products, our results give more insights into magmatic processes during and leading up to each eruption, specifically the depth of clinopyroxene crystallisation in the magmatic sustem, the role of magma recharge, crystal mushes and mingling in the magmatic system. This study concludes several interconnected magma reservoirs are present at La Fossa di Vulcano resulting in the wide variety of erupted products. This stratigraphic approach analysing both explosive and effusive could be applied to other arc volcanoes to decipher the pre-eruptive magmatic system through the evolution of a single volcano.

Oxygen isotopes, petrological and textural studies, whole-rock major and trace element geochemistry, mineral chemistry, and structure indicate crustal contamination is ubiquitous in the latitic to trachytic storage region beneath La Fossa di Vulcano. Clinopyroxene and plagioclase exhibit a large degree of oxygen isotopic disequilibrium in the more evolved eruptive products at La Fossa di Vulcano, coupled with large variations in calculated crystallisation temperatures, indicating that clinopyroxene occurs as an antecrystic phase. Through the quantification of clinopyroxene crystal structures, we show clinopyroxene in lavas from crystallised between 11 and 14 km whereas pyroclastic deposits crystallised over a larger range of depths between 7 and 21 km. These data are interpreted to reflect a series of dynamic crystal mush zones that are remobilised during recharge events and incorporated into the more evolved magma storage regions, resulting in the diversity of eruptive products. Fractional crystallisation, magma mingling, and crustal contamination processes dominate during the evolution of the dynamic, constantly evolving magmatic system of La Fossa di Vulcano.

The shallow conduit processes and origins of four distinct bomb types during the 1888 – 90 Vulcanian eruption of La Fossa di Vulcano. Through a detailed quantitative textural analysis of feldspar microlites, we constrained timescales of magma ascent and the

evolution of the conduit system leading up to and during the eruption. The four distinct bomb types identified indicate changes from closed- to open-system degassing, decompression under small degrees of ΔT, and varying magma ascent rates produced the different bomb types. Through the utilisation of mineral chemistry and detailed textural analysis, this thesis has shown shallow level conduit processes operating immediately prior to eruption (in the order of days) govern eruption style and intensity. This study indicates the key processes in governing Vulcanian eruptions are magma ascent rates and gas over pressurisation during the final stages of magma ascent. These results may also be applicable to other Vulcanian eruptions at volcanic arcs.

The distinct switch to intermediate to silicic volcanism in the central Aeolian arc occurred at 27.5 ka on Salina, at 42 ka on Lipari and at 28 ka on Vulcano (De Astis *et al.* 2013; Forni *et al*. 2013; Lucchi *et al.* 2013b) was accompanied by distinct geochemical and petrological changes in eruptive products. Geochemical and Sr-O isotopic data provides unequivocal evidence for source contamination in the central Aeolian arc. However, it is remains difficult to distinguish between contamination from altered oceanic crust (AOC) fluids and/or subducted sediment (SED) melts and subsequent crustal contamination. This study aimed to and successfully identify the likely crustal contaminants in the central arc and constrain the contaminants which dominate during different stages of magmatic evolution. Our results indicate crustal contamination dominates in the more evolved magmas, particularly in rhyolites evidenced by Oxygen isotope contents in feldspars, obsidians and pumice glasses, and the large variability in Strontium isotopes in feldspars and obsidians. The highest degrees of crustal contamination (up to 50%) by mid crustal gneisses and upper crustal metasediments, occur in intermediate to silicic eruptive products and correspond to the highest $\delta^{18}O$ in volcanic products of the central Aeolian arc.

Reference List

Adams, N.K. Houghton, B.F. Hildreth, W. 2006. Abrupt transitions during sustained explosive eruptions: examples from the 1912 eruption of Novarupta, Alaska. *Bulletin of Volcanology*, **69**, 189-206.

Alt, J.C. 2003. Stable isotope composition of upper oceanic crust formed at a fast spreading ridge, ODP Site 801: *Geochemistry*, *Geophysics*, *Geosystems*, **4**(5).

Altherr, R. Henjes-Kunst, F. Matthews, A. Friedrichsen, H. Hansen, B.T. 1988. O-Sr isotopic variations in Miocene granitoids from the Aegean: evidence for an origin by combined assimilation and fractional crystallization. *Contributions to Mineralogy and Petrology*, **100**(4), 528-541.

Anderson, A.T. 1976. Magma mixing: petrological process and volcanological tool. *Journal of Volcanology and Geothermal Research*, **1**(1), 3-33.

Anderson, H. Jackson, J. 1987. The deep seismicity of the Tyrrhenian Sea. *Geophysical Journal International*, **91**, 613–637.

Arculus, R.J. Johnson, R.W. 1981. Island arcmagma sources: a geochemical assessment of the roles of slab derived components and crustal contamination. *Geochemical Journal*, **15**, 109–133.

Arculus, R.J. Powell, R. 1986. Source component mixing in the regions of arc magma generation. *Journal of Geophysical Research*, **91**, 5913–5926.

Arrighi, S. Tanguy, J. Rosi, M. 2006. Eruptions of the last 2200 years at Vulcano and Vulcanello (Aeolian Islands, Italy) dated by high accuracy archeomagnetism. *Physics of the Earth and Planetary Interiors*, **159**, 225–233.

Bachmann, O. Huber, C. 2018. The inner workings of crustal distillation columns; the physical mechanisms and rates controlling phase separation in silicic magma reservoirs. *Journal of Petrology*, **60**, 3–18.

Bain, AA. Calder, ES. Cortés, JA. Cortés, GP. Loughlin, SC. 2019. Textural and geochemical constraints on andesitic plug emplacement prior to the 2004–2010 vulcanian explosions at Galeras volcano, Colombia, *Bulletin of Volcanology*, **81**:1.

Barberi, F. Gasparini, P. Innocenti, F. Villari, L. 1973. Volcanism of the Southern Tyrrhenian Sea and its geodynamics implications. *Journal of Geophysical Research*, **78**, 5221-5232.

Barberi, F. Innocenti, F. Ferrara, G. Keller, J. Villari, L. 1974. Evolution of Eolian Arc volcanism Southern Tyrrhenian Sea. Earth and Planetary Science Letters, 21, 269-276.

Barberi, F. Gandino, A. Gioncada, A. La Torre, P. Sbrana, A. Zenucchini, C., 1994. The deep structure of the Eolian arc (Filicudi–Panarea–Vulcano sector) in light of gravity, magnetic and volcanological data. *Journal of Volcanology and Geothermal Research*, **61**, 189–206.

Barker, D. S. 1987. Rhyolites contamined with metapelite and gabbro, Lipari, Aeolian Islands, Italy: products of lower crustal fusion or of assimilation plus fractional crystallization? *Contributions of Mineralogy and Petrology*, **97**, 460–472.

Beccaluva, L. Gabbianelli, G. Lucchini, F. Rossi, P. L.Savelli, C. 1985. Petrology and K/Ar ages of volcanics dredged from the Eolian seamounts: implications for geodynamic evolution of the southern Tyrrhenian sea. *Earth and Planetary Science Letters*, **74**, 187-208.

Bergeat, A. 1910. Der Cordieritandesit von Lipari, seine andalusitfu¨hrenden Einschlu¨sse und die genetischen Beziehungen zwischen dem Andalusit, Sillimanit, Biotit, Cordierit, Orthoklas und Spinell in den letzteren. *Neues Jaharbuch fu¨r Mineralogie*, **30**, 575–627.

Bernstein, S. 2006. In situ fractional crystallization of a mafic pluton: Microanalytical study of a Palaeogene gabbronorite plug in East Greenland. *Lithos*, **92**, 222–237.

Bigazzi, G. Coltelli,M. Norelli, P. 2003. Nuove eta` delle ossidiane di Lipari determinate con il metodo delle tracce di fissione. GeoItalia, 4th Forum FIST, Bellaria, 16–18 September, Abstract Volume, 444–446.

Bindeman, I. 2008. Oxygen isotopes in mantle and crustal magmas as revealed by single crystal analysis. *Reviews in Mineralogy and Geochemistry*, **69**(1), 445-478.

Bindeman, I. Gurenko, A. Sigmarsson, O. Chaussidon, M. 2008. Oxygen isotope heteroeneity and disequilibria of olivine crystals in large volume Holocene basalts from Iceland: evidence for magmatic digestion and erosion of Pleistocene hyaloclastites. *Geochimica et Cosmochimica Acta*, **72**, 4397–4420.

Blundy, J. Cashman, K. 2008. Petrologic reconstruction of magmatic system variables and processes. *Reviews in Mineralogy and Geochemistry*, **69**(1),179–239.

Boccaletti, M. Nicolich, R. Tortorici, L. 1984. The Calabrian arc and the Ionian sea in the dynamic evolution of the Central Mediterranean. *Marine Geology*, **55**, 219–245.

Borisova, A. Y. Martel, C. Gouy, S. Pratomo, I. Sumarti, S., Toutain, J. P. Bindeman, I.N. de Parseval, P., Metaxian, J. P. Surano. 2013. Highly explosive 2010 Merapi eruption: Evidence for shallow-level crustal assimilation and hybrid fluid. *Journal of Volcanology and Geothermal Research*, **261**, 193-208.

Bosman, A. Casalbore, D. Chiocci, F. L. Romagnoli, C. 2013. Bathy-morphological map. Central Aeolian Sector. Scale 1:50 000. In: Lucchi, F. Peccerillo, A. Keller, J. Tranne, C. A. Rossi, P. L. (eds) *The Aeolian Islands Volcanoes*. Geological Society, London, Memoirs, 37.

Brugger, C.R. Hammer, J.E. 2010. Crystal size distribution analysis of plagioclase in experimentally decompressed hydrous rhyodacite magma. *Earth and Planetary Science Letters*, **300**(3–4), 246–254.

Bullock L.A. (2015) Structure, emplacement and textural evolution of young obsidian lavas in the Aeolian Islands, Italy. PhD thesis, Keele University, UK.

Bullock, L.A. Gertisser, R. O'Driscoll, B. 2018. Emplacement of the Rocche Rosse rhyolite lava flow (Lipari, Aeolian Islands). *Bulletin of Volcanology*, **80**:48.

Bullock, L.A. Gertisser, R. O'Driscoll, B. Harland, S. 2019. Magmatic evolution and textural development of the 1739 CE Pietre Cotte lava flow, Vulcano, Italy. *Journal of Volcanology and Geothermal Research*, **372**, 1-23.

Burgisser, A. Poussineau, S. Arbaret, L. Druitt, T.H. Giachetti, T. Bourdier, J.L. 2010. Pre-explosive conduit conditions of the 1997 vulcanian explosions at Soufrière Hills volcano, Montserrat: I. Pressure and vesicularity distributions. *Journal of Volcanology and Geothermal Research*, **194** (1–3), 27–41.

Burgisser, A. Arbaret, L. Druitt, T.H. Giachetti, T. 2011. Pre-explosive conduit conditions of the 1997 vulcanian explosions at Soufrière Hills volcano, Montserrat: II. overpressure and depth distributions. *Journal of Volcanology and Geothermal Research*, **199**(3–4), 193–205.

Calanchi, N. De Rosa, R. Mazzuoli, R. Rossi, P. L. Santacroce, R. 1987. L'attivita` esplosiva del centro di Pollara. Bollettino GNV (Gruppo Nazionale per la Vulcanologia), 1, 263–272.

Calanchi, N. De Rosa, R. Mazzuoli, R. Rossi, P. L. Santacroce, R. Ventura, G. 1993. Silicic magma entering a basaltic magma chamber: eruptive dynamics and magma mixing – an example from Salina (Aeolian Islands, southern Tyrrhenian Sea). *Bulletin of Volcanology*, **55**, 504–522.

Calanchi, N. Peccerillo, A. Tranne, C.A. Lucchini, F. Rossi, P.L. Kempton, P. Barbieri, M. Wu, T.W. 2002. Petrology and geochemistry of volcanic rocks from the island of Panarea: implications for mantle evolution beneath the Aeolian island arc (southern Tyrrhenian sea). *Journal of Volcanology and Geothermal Research*, **115**(3-4), 367-395.

Caputo, M. Panza, G. Postpischl, D. 1972. New evidences about the deep structure of the Lipari arc. *Tectonophysics*, **15**, 219-231.

Carmichael, I.S. 2002. The andesite aqueduct: perspectives on the evolution of intermediate magmatism in west-central (105–99 W) Mexico. *Contributions to Mineralogy and Petrology*, **143**, 641–663.

Carminati, E. Wortel, M.J.R. Spakman, W. Sabadini, R. 1998. The role of slab detachment processes in the opening of the Western–Central Mediterranean basins: some geological and geophysical evidence. *Earth and Planetary Science Letter*s, **160**, 651–665.

Cashman, K.V. 1988. Crystallization of Mount St. Helens 1980-1986 dacite: a quantitative textural approach. *Bulletin of Volcanology*, **50**(3),194–209.

Cashman, K.V. McConnell, S.M. 2005. Multiple levels of magma storage during the 1980 summer eruptions of Mount St. Helens, WA. *Bulletin of Volcanology*, **68**(1), 57–75.

Cashman, K.V. Sparks, R.S.J. Blundy, J.D. 2017. Vertically extensive and unstable magmatic systems: a unified view of igneous processes. *Science*, **355** (6331).

Cassidy, M. Taylor, R.N. Palmer, M.R. Cooper, R.J. Stenlake, C. Trofimovs, J. 2012. Tracking the magmatic evolution of island arc volcanism: Insights from a high-precision Pb isotope record of Montserrat, Lesser Antilles. *Geochemistry, Geophysics, Geosystems*, **13**(5).

Cassidy, M. Cole, P.D. Hicks, K.E. Varley, N.R. Peters, N. Lerner, A.H. 2015. Rapid and slow: Varying magma ascent rates as a mechanism for Vulcanian explosions. *Earth and Planetary Science Letters*, **420**, 73– 84.

Catalano, R. Doglioni, C. Merlini, S. 2001. On the Mesozoic Ionian basin. *Geophysical Journal International*, **144**, 49–64.

Chadwick, J.P. Troll, V.R. Ginibre, C. Morgan, D. Gertisser, R. Waight, T.E. Davidson, J.P. 2007. Carbonate assimilation at Merapi Volcano, Java, Indonesia: insights from crystal isotope stratigraphy. *Journal of Petrology*, 48, 1793–1812.

Chiarabba, D. De Gori, P. Speranza, F. 2008. The Southern Tyrrhenian Subduction Zone: deep geometry, magmatism and Plio-Pleistocene evolution. *Earth and Planetary Science Letters*, **268**, 408-423.

Chiba, H. Chacko, T. Clayton, R.N. Goldsmith, J.R. 1989. Oxygen isotope fractionations involving diopside, forsterite, magnetite, and calcite: applications to geothermometry. *Geochimica et Cosmochimica Acta*, **53**, 2985–2995.

Christopher, T.E. Blundy, J. Cashman, K. Cole, P. Edmonds, M. Smith, P.J. Sparks, R.S.J. Stinton, A. 2015. Crustal-scale degassing due to magma system destabilization and magma-gas decoupling at S oufrière Hills Volcano, Montserrat. *Geochemistry, Geophysics, Geosystems*, **16**(9), 2797-2811.

Clark, J.R. Appleman, D.E. Papike, JJ. 1969: Crystal-chemical characterization of clinopyroxenes based on eight new structure refinements, in "Pyroxenes and amphiboles: crystal chemistry and phase petrology", JJ. Papike Ed., *Mineralogical Society of America Special Papers*, **2**, 31-50.

Clarke, A.B. Stephens, S. Teasdale, R. Sparks, R.S.J. Diller, K. 2007. Petrologic constraints on the decompression history of magma prior to Vulcanian explosions at the Soufrière Hills volcano, Montserrat. *Journal of Volcanology and Geothermal Research*, **161**, 261-274.

Clarke, A.B. Ongaro, T.E. Belousov, A. 2015. Chapter 28 Vulcanian Eruptions. In: Sigurdsson, H. (ed.) *The Encyclopaedia of Volcanoes* Elsevier. 505-518.

Clocchiatti, R. Del Moro, A. Gioncada, A. Joron, J.L. Mosbah, M. Pinarelli, L. Sbrana, A. 1994. Assessment of a shallow magmatic system: the 1888-90 eruption, Vulcano Island, Italy. *Bulletin of Volcanology*, **56**, 466-486.

Colella, A. Hiscott, R. N. 1997. Pyroclastic surges of the Pleistocene Monte Guardia sequence (Lipari Island, Italy): depositional processes. *Sedimentology*, **44**, 47–66.

Connolly, J.A. Podladchikov, Y.Y. 2015. An analytical solution for solitary porosity waves: dynamic permeability and fluidization of nonlinear viscous and viscoplastic rock. *Geofluids*, **15**(1-2), 269-292.

Continisio, R. Ferrucci, F. Gaudiosi, G. Lo Bascio, D. Ventura, G. 1997. Malta Escarpment and Mt. Etna: Early stages of an asymmetric rifting process? Evidences from geophysical and geological data. *Acta Vulcanologica*, **9**, 39–47.

Cooper, G.F. Davidson, J.P. Blundy, J.D. 2016. Plutonic xenoliths from Martinique, Lesser Antilles: evidence for open system processes and reactive melt flow in island arc crust. *Contributions to Mineralogy and Petrology*, **171**, 1.

Cortés, J. (2016), Olive. https://vhub.org/resources/olive.

Costa, F. Dungan, M. 2005. Short time scales of magmatic assimilation from diffusion modeling of multiple elements in olivine. *Geology*, **33**(10), 837-840.

Costa, S. Masotta, M. Gioncada, A. Pistolesi, M. Bosch, D. Scarlato, P. 2020. Magma evolution at La Fossa volcano (Vulcano Island, Italy) in the last 1000 years: evidence from eruptive products and temperature gradient experiments. *Contributions to Mineralogy and Petrology*, **175**, 31.

Couch, S. Sparks, R.S.J. Carroll, M. 2003. The kinetics of degassing-induced crystallization at Soufriere Hills volcano, Montserrat. *Journal of Petrology*, **44**(8), 1477–1502.

Crisci, G.M. De Rosa, R. Lanzafame, G. Mazzuoli, R. Sheridan, M. F. Zuffa, G. G. 1981. Monte Guardia Sequence: a Late-Pleistocene Eruptive Cycle on Lipari (Italy). *Bulletin of Volcanology*, **44**, 241–255.

Crisci, G. M. Delibrias, G. De Rosa, R. Mazzuoli, R. Sheridan, M. F. 1983. Age and petrology of the Late-Pleistocene Brown Tuffs on Lipari, Italy. *Bulletin of Volcanology*, **46**, 381–391.

Crisci, G.M. De Rosa, R. Esperança, S. Mazzuoli, R. Sonnino, M. 1991. Temporal evolution of a three component system: the island of Lipari (Aeolian Arc, southern Italy). *Bulletin of Volcanology*, **53**, 207–221.

Dal Negro A. Carbonin S. Molin G.M. Cundari A. Piccirillo E.M. 1982. Intracrystalline cation distribution in natural clinopyroxenes of tholeiitic, transitional, and alkaline basaltic rocks. In: Saxena SK (ed) *Advances in physical geochemistry*, vol 2. Springer, Berlin Heidelberg New York, pp 117–150

Dal Negro, A. Carbonin, S. Domeneghetti, C. Molin, GM. Cundari, A. Piccirillo, E.M. 1984. Crystal chemistry and evolution of the clinopyroxenes in a suite of high-pressure ultramafic rocks from the Newer Volcanics of Victoria, Australia. *Contributions to Mineralogy and Petrology*, **86**, 221–229

Dal Negro, A. Molin, G.M. Salviulo, G. Secco, L. Cundari, A. Piccirillo, E.M. 1989. Crystal chemistry of clinopyroxenes and its petrogenetic significance: a new approach. In: Boriani A, Bonafede M, Piccardo GB, Vai GB (ed) Int Lithosphere Prog Mid Term Conf Accademia Naz Lincei, **80**, 271–295.

Davidson, J.P. 1985. Mechanisms of contamination in Lesser Antilles island arc magmas from radiogenic and oxygen isotope relationships. *Earth and Planetary Science Letters*, **72**, 163-174.

Davidson, J.P. 1986. Isotopic and Geochemical constraints on the petrogenesis of subduction-related lavas from Martinique, Lesser Antilles. *Journal of Geophysical Research*, **91**, 5943-5962.

Davidson, J. P. 1987. Crustal contamination versus subduction zone enrichment: Examples from the Lesser Antilles and implications for mantle source compositions of island arc volcanic-rocks, *Geochimica et Cosmochimica Acta*, **51**(8), 2185–2198.

Davidson, J., Turner, S., Handley, H., Macpherson, C., Dosseto, A., 2007. Amphibole 'sponge' in arc crust? *Geology*, **35**, 787–790.

Davidson, J.P. McMillan, N.J. Moorbath, S. Wörner, G. Russell, S.H. Lopez-Escobar, L. 1990. The Nevados de Payachata volcanic region (18° S/69° W, N. Chile) II. Evidence for widespread crustal involvement in Andean magmatism. *Contributions to Mineralogy and Petrology*, **105**, 412–432.

De Astis, G. 1995. Evoluzione Vulcanologica e Magmatologica dell'isola di Vulcano (Isole Eoile). PhD Thesis, Università degli studi di Bari.

De Astis, G. La Volpe, L. Peccerillo, A. Civetta, L. 1997. Volcanological and petrological evolution of Vulcano Island (Aeolian Arc, southern Tyrrhenian Sea). *Journal of Geophysical Research*, **102**(B4), 8021-8050.

De Astis, G. Peccerillo, A. Kempton, P. D. La Volpe, L. Wu, T. W. 2000. Transition from calc-alkaline to potassium-rich magmatism in subduction environments: geochemical and Sr, Nd, Pb isotopic constraints from the Island of Vulcano (Aeolian arc). *Contributions to Mineralogy and Petrology*, **139**, 684–703.

De Astis, G. Ventura, G, Vilardo, G. 2003. Geodynamic significance of the Aeolian volcanism (Southern Tyrrhenian Sea, Italy) in light of structural, seismological and geochemical data. *Tectonics*, **22**, 1040-1057.

De Astis, G. Dellino, P. La Volpe, L. Lucchi, F. Tranne, C. A. 2006. Geological map of the island of Vulcano (Aeolian Islands). University of Bari, University of Bologna and INGV. LAC, Firenze.

De Astis, G. Dellino, P. La Volpe, L. Lucchi, F. Tranne, C.A. 2007. Geological map of the Vulcano Island, 1:10,000 La Volpe L. & De Astis G (eds). From: Lucchi, F. Peccerillo, J. Keller, J. Tranne, C.A. Rossi, P.L. *The Aeolian Islands volcanoes*. Geological Society Memoirs, Geological Society, London.

De Astis, G. Lucchi, F. Dellino, P. La Voupe, L. Tranne, C.A. Frezzotti, M.L. Peccerillo, A. 2013. Geology, volcanic history and petrology of Vulcano (central Aeolian

archipelago). In: Lucchi, F. Peccerillo, J. Keller, J. Tranne, C.A. Rossi, P.L. *The Aeolian Islands volcanoes*. Geological Society Memoirs, Geological Society, London 281-349.

De Fino, M. La Volpe, L. Piccarreta, G. 1991. Role of magma mixing during the recent activity of La Fossa di Vulcano (Aeolian Islands, Italy). *Journal of Volcanology and Geothermal Research*, **48**, 385–398.

Dellino, P. La Volpe, L. 1995. Fragmentation versus transportation mechanisms in the pyroclastic sequence of Monte Pilato – Rocche Rosse (Lipari, Italy). *Journal of Volcanology and Geothermal Research*, **64**, 211–232.

Dellino, P. La Volpe, L. 1997. Stratigrafia, dinamiche eruttive e deposizionali, scenario eruttivo e valutazioni di pericolosita` a La Fossa di Vulcano. In: La Volpe, L. Dellino, P. Nuccio, M. Privitera, E. & Sbrana, A. (eds) Progetto Vulcano: Risultati dell'attivita` di ricerca 1993–1995. CNR – Gruppo Nazionale per La Vulcanologia, Felici Editore, Pisa, 214–237.

Dellino, P. Isaia, R. La Volpe, L. Orsi, G. 2001. Statistical analysis of textural data from complex pyroclastic sequences: implications for fragmentation processes of the Agnano-Monte Spina Tephra (4.1 ka), Phlegrean Fields, southern Italy. *Bulletin of Volcanology*, **63**, 443–461.

Del Moro, A. Gioncada, A. Pinarelli, L. Sbrana, A. Joron, J.L. 1998. Sr, Nd, and Pb isotope evidence for open system evolution at Vulcano, Aeolian Arc, Italy. *Lithos*, **43**, 81-106.

DePaolo, D. J. 1981. Trace-element and isotopic effects of combined wallrock assimilation and fractional crystallization. *Earth and Planetary Science Letters*, **53**, 189–202.

De Rosa, R. Sheridan, M. F. 1983. Evidence for magma mixing in the surge deposits of the Monte Guardia sequence, Lipari. *Journal of Volcanology and Geothermal Research*, **17**, 313–328.

De Rosa, R. Donato, P. Gioncada, A. Masetti, M. Santacroce, R. 2003. The Monte Guardia eruption (Lipari, Aeolian Islands): an example of a reversely zoned magma mixing sequence. *Bulletin of Volcanology*, **65**, 530–543.

De Rosa, R. Calanchi, N. Dellino, P.F. Francalanci, L. Lucchi, F. Rosi, M. Rossi, P.L. Tranne, C.A. 2004. 32nd International Geological Congress, Field Trip Guide Book – P42: Geology and volcanism of Stromboli, Lipari and Vulcano (Aeolian Islands, vol. 5. Firenze 20-28 August 2004).

Di Martino, C. Frezzotti, M. L. Lucchi, F. Peccerillo, A. Tranne, C. A. Diamond, L. W. 2010. Magma storage and ascent at Lipari Island (Aeolian archipelago, southern Italy) during the old stages (223–81 ka): role of crustal processes and tectonic influence. *Bulletin of Volcanology*, **72**, 1061–1076.

Di Martino, C. Forni, F. Frezzotti, M.L. Palmeri, R. Webster, J.D. Ayuso, R.A. Lucchi, F. Tranne, C.A. 2011. Formation of cordierite-bearing lavas during anatexis in the lower crust beneath Lipari Island (Aeolian arc, Italy). *Contribution to Mineralogy and Petrology*, **162**, 1011–1030.

Downs, B. Bartelmehs, K. 1997. Xtaldraw © programme

Druitt, T.H. Edwards, L. Mellors, R.M. Pyle, D.M. Sparks, R.S.J. Lanphere, M. Davies, M. Barreirio, B. 1999. *Santorini volcano*. Geological Society Memoir, 19.

Druitt, T.H. Young, S.R. Baptie, B. Bonadonna, C. Calder, E.S. Clarke, A.B. Cole, P.D. Harford, C.L. Herd, R.A. Luckett, R. Ryan, G. Voight, B. 2002. Episodes of cyclic Vulcanian explosive activity with fountain collapse at Soufrière Hills Volcano, Montserrat. In: Druitt, T.H. Kokelaar, B.P. (eds.). *The eruption of Soufrière Hills Volcano, Montserrat, from 1995 to 1999*. Geological Society Memoirs, Geological Society, London, 281–306.

Edmonds, M. Herd, R.A. 2007. A volcanic degassing event at the explosive-effusive transition. *Geophysical Research Letters*, **34**, L21310.

Druitt, T.H. Costa, F. Deloule, E. Dungan, M. Scaillet, B. 2012. Decadal to monthly timescales of magma transfer and reservoir growth at a caldera volcano. *Nature*, **482**(7383), 77-80.

Eiler, J.M. Farley, K.A. Valley, J.W. Stolper, E.M. Hauri, E.H. Craig, H. 1995. Oxygen isotope evidence against bulk recycled sediment in the mantle sources of Pitcairn Island lavas. *Nature*, **377**(6545), 138-141.

Eiler, J. Crawford, A. Elliott, T. Farley, K. Valley, J. Stolper, E. 2000. Oxygen Isotope Geochemistry of Oceanic-Arc Lavas. *Journal of Petrology*, **41**, 229-256.

Eiler, J. M. Carr, M.J. Reagan, M. Stopler, E. 2005. Oxygen isotope constraints on the sources of Central American arc lavas. *Geochemistry Geophysics Geosystems*, **6**, Q07007.

Ellam, R. M. 1986. The transition from calc-alkaline to potassic volcanism in the Aeolian islands, Southern Italy. Unpublished PhD thesis, The Open University, UK.

Ellam, R.M., Menzies, M.A., Hawkesworth, C.J., Leeman, W.P., Rosi, M., Serri, G., 1988. The transition from calc-alkaline to potassic orogenic magmatism in the Aeolian Islands, southern Italy. *Bulletin of Volcanology*, **50**, 386–398.

Ellam, R.M. Hawkesworth, C.J. Menzies, M.A. Rogers, N.W., 1989. The volcanism of Southern Italy: role of subduction and the relationship between potassic and sodic alkaline magmatism. *Journal of Geophysical Research: Solid Earth*, **94**(B4), 4589-4601.

Ellam, R.M. Harmon, R.S. 1990. Oxygen isotope constraints on the crustal contribution to the subduction-related magmatism of the Aeolian Islands, southern Italy. *Journal of Volcanology and Geothermal Research*, **44**, 105 – 122.

Elliott, T. Plank, T. Zindler, A. White, W. Bourdon, B. 1997. Element transport from slab to volcanic front at the Mariana arc. *Journal of Geophysical Research: Solid Earth*, **102**(B7), 14991-15019.

Esperança, S. Crisci, G. M. De Rosa, R. Mazzuoli, R. 1992. The role of the crust in the magmatic evolution of the island of Lipari (Aeolian Islands, Italy). *Contributions to Mineralogy and Petrology*, **112**, 450-462.

Fabbro, G.N. Druitt, T.H. Costa, F. 2017. Storage and eruption of silicic magma across the transition from dominantly effusive to caldera-forming states at an arc volcano (Santorini, Greece). *Journal of Petrology*, **58**(12), 2429-2464.

Fabbro, G.N. Druitt, T.H. Costa, F. 2018. Storage and eruption of silicic magma across the transition from dominantly effusive to caldera-forming states at an arc volcano (Santorini, Greece). *Journal of Petrology*, **58**, 2429–2464.

Faccenna, C. Mattei, M. Funiciello, R. Jolivet, L. 1997. Styles of back-arc extension in the Central Mediterranean: *Terra Nova,* **9**, 126–130.

Faccenna, C. Funiciello, F. Giardini, D. Lucente, P. 2001. Episodic back-arc extension during restricted mantle convection in the Central Mediterranean. *Earth and Planetary Science Letters*, **187**, 105-116.

Faraone, D. Molin, G.M. Zanazzi, P.F. 1988: Clinopyroxenes from Vulcano (Aeolian Islands, Italy): Crystal chemistry and cooling history. *Lithos,* **22**, 113-126.

Ferrari, L. Manetti, P. 1993. Geodynamic framework of the Tyrrhenian volcanism: a review. *Acta Vulcanologica*. **3**, 1–10.

Finetti, I. Morelli, C. 1973. Geophysical exploration of the Mediterranean Sea. *Bollettino di geofisica teorica ed applicata*, **15**, 263-341.

Finetti, I. 1982. Structure, stratigraphy and evolution of Central Mediterranean. *Bollettino di Geofi sica Teorica Applicata*, **24**, 247–315.

Fink, J.H. Malin, M.C. Anderson, S.W. 1990. Intrusive and extrusive growth of the Mount St Helens lava dome. *Nature,* **348**(6300), 435-437.

Forni, F. Lucchi, F. Peccerillo, A. Tranne, C.A. Rossi, P.L. Frezzotti, M.L. 2013. Stratigraphy and geological evolution of the Lipari volcanic complex (Central Aeolian

Archipelago) In: Lucchi, F. Peccerillo, J. Keller, J. Tranne, C.A. Rossi, P.L. *The Aeolian Islands volcanoes*. Geological Society Memoirs, Geological Society, London 213-279.

Forni, F. Ellis, B.S. Bachmann, O. Lucchi, F. Tranne, C.A. Agostini, S. Dallai, L. 2015. Erupted cumulate fragments in rhyolites from Lipari (Aeolian Islands). *Contributions to Mineralogy and Petrology*, **170**(5-6), p.49.

Forni, F. Petricca, E. Bachmann, O. Mollo, S. De Astis, G. Piochi, M. 2018. The role of magma mixing/mingling and cumulate melting in the Neapolitan Yellow Tuff caldera-forming eruption (Campi Flegrei, Southern Italy). *Contributions to Mineralogy and Petrology*, **173**, 45.

Francalanci, L. Taylor, S. R. Mcculloch, M. T. Woolhead, J. D. 1993. Geochemical and isotopic variations in the calc-alkaline rocks of Aeolian arc, southern Tyrrhenian Sea, Italy: constraints on magma genesis. *Contributions to Mineralogy and Petrology,* **113**, 300–313.

Francalanci, L. Avanzinelli, R. Petrone, C. M. Santo, A. 2004. Petrochemical and magmatological characteristics of the Aeolian Arc volcanoes, southern Tyrrhenian Sea, Italy: inferences on shallow level processes and magma source variations. *Periodico di Mineralogia,* **73**, 75–104.

Francalanci, L. Avanzinelli, R. Tommasini, S. Heuman, A. 2007. A west-east geochemical and isotopic traverse along the volcanism of the Aeolian Island arc, southern Tyrrhenian Sea, Italy: interferences on mantle source processes. *Geological Society of America Special Papers,* **418**, 235–263.

Francalanci, L. Lucchi, F. Keller, J. De Astis, G. Tranne, C.A. 2013. Eruptive, volcano-tectonic and magmatic history of the Stromboli volcano (north-eastern Aeolian archipelago). In: Lucchi, F. Peccerillo, J. Keller, J. Tranne, C.A. Rossi, P.L. *The Aeolian Islands volcanoes*. Geological Society Memoirs, Geological Society, London, 397-471.

Frazzetta, G. Lanzafame, G. Villari, L. 1982. Deformazioni e tettonica attiva a Lipari e Vulcano Eolie. *Mem. Soc. Geol. Ital.* **24**, 294–297.

Frazzetta, G. La Volpe, L. Sheridan, M. F. 1983. Evolution of the Fossa cone, Vulcano. *Journal of Volcanology and Geothermal Research*, **17**, 329–360.

Frazzetta, G. Gillot, P. Y. & La Volpe, L. 1985. The Island of Vulcano. IAVCEI Scientific Association Excursion Guidebook, 125–140.

Frezzotti, M. L. Peccerillo, A. 2004. Fluid inclusion and petrological studies elucidate reconstruction of magma conduits. *Transactions of the American Geophysical Union*, **85**, 157.

Frezzotti, M. L. Peccerillo, A. Bonelli, R. 2003. Magma ascent rates and depths of magma reservoirs beneath the Aeolian volcanic arc (Italy): inferences from fluid and melt inclusions in crustal xenoliths. In: Bodnar, B.&De Vivo, B. (eds) *Melt Inclusions in Volcanic Systems.* Elsevier, Amsterdam, 185–206.

Frezzotti, M. Peccerillo, A. Zanon, V. Nikogosian, I. 2004. Silica-rich Melts in Quartz Xenoliths from Vulcano Island and their Bearing on Processes of Crustal Anatexis and Crust - Magma Interaction beneath the Aeolian Arc, Southern Italy. *Journal of Petrology*, **45** (1), 3-26.

Fusillo, R. Di Traglia, F. Gioncada, A. Pistolesi, M. Wallace, P.J. Rosi, M. 2015. Deciphering post-caldera volcanism: insight into the Vulcanello (Island of Vulcano, Southern Italy) eruptive activity based on geological and petrological constraints. *Bulletin of Volcanology*, **77**, 76, 23

Gasparini, G. Iannaccone, G. Scandone, P. Scarpa, R. 1982. Seismotectonics of the Calabrian Arc. *Tectonophysics*, **84**, 267–286.

Gasparini, C. Iannaccone, G. Scarpa, R. 1985. Fault-plane solutions and seismicity of the Italian Peninsula. *Tectonophysics*, **110**, 59-78.

Gasparon, M. Hilton, D.R. Varne, R. 1994. Crustal contamination processes traced by helium isotopes: Examples from the Sunda arc, Indonesia. *Earth and Planetary Science Letters*, **126**(1-3), 15-22.

Gazel, E. Hayes, J.L. Hoernle, K. Kelemen, P. Everson, E. Holbrook, W.S. Hauff, F. Van Den Bogaard, P. Vance, E.A. Chu, S. Calvert, A.J. 2015. Continental crust generated in oceanic arcs. *Nature Geoscience*, **8**(4), 321-327.

Gertisser, R. Keller, J. 2000. From basalt to dacite: origin and evolution of the calc-alkaline series of Salina, Aeolian Arc, Italy. *Contributions to Mineralogy and Petrology*, **139**, 607–626.

Gertisser, R. Keller, J. 2003. Trace element and Sr, Nd, Pb and O isotope variations in medium-K and high-K volcanic rocks from Merapi Volcano, Central Java, Indonesia: evidence for the involvement of subducted sediments in Sunda Arc magma genesis. *Journal of Petrology*, **44**, 457–489.

Ghisetti, F. 1979. Relazioni tra strutture e fasi trascorrenti e distensive lungo i sistemi Messina-Fiumefreddo, Tindari-Letojanni e Alia- Malvagna (Sicilia nord-orientale): Uno studio microtettonic. *Geological Rom.* **18**, 23-58.

Giachetti, T. Druitt, T.H. Burgisser, A. Arbaret, L. Galven, C. 2010. Bubble nucleation, growth and coalescence during the 1997 vulcanian explosions of Soufrière Hills volcano,Montserrat. *Journal of Volcanology and Geothermal Research*, **193**(3–4), 215–231.

Giese, P. Morelli, C. 1973. La struttura della crosta terrestre in Italia. Publ. *Accad. Naz. Lincei*, **183**, 317-362.

Gill, J.B. 1981. *Orogenic andesites and plate tectonics*. Springer-Verlag. 390 pp.

Gillot, P. 1987. Historie volcanique des Iles Eoliennes: arc insulaire or complexe orogenique anulaire? Doc. Trav., Institut Géologique Albert-de-Lapparent, Paris, **11**, 35-42.

Gioncada, A. Clocchiatti, R. Sbrana, A. Bottazzi, P. Massare, D. Ottolini, L. 1998. A study of melt inclusions at Vulcano (Aeolian Islands, Italy): insights on the primitive magmas and on the volcanic feeding system. *Bulletin of Volcanology*, **60**, 286–306.

Gioncada, A. Mazzuoli, R. Bisson, M. Pareschi, M. T. 2003. Petrology of volcanic products younger than 42 ka on the Lipari-Vulcano complex (Aeolian Islands, Italy): an example of volcanism controlled by tectonics. *Journal of Volcanology and Geothermal Research*, **122**, 191–220.

Gioncada, A. Mazzuoli, R. Milton, A. J. 2005. Magma mixing at Lipari (Aeolian Islands, Italy): insights from textural and compositional features of phenocrysts. *Journal of Volcanology and Geothermal Research*, **145**, 97–118.

Gregory, R.T. Criss, R.E. 1986. Isotopic exchange in open and closed systems. In: Valley, J.W. Taylor, H.P. O'Neil, J.R. (Eds), Stable Isotopes in High Temperature Geological Processes. *Mineralogical Society of Americal Reviews*, **16**, 91-128.

Gregory, R.T. Criss, R.E. Taylor Jr, Hp>p 1989. Oxygen isotope exchange kinematics of mineral pairs in closed and open systems: applications to problems of hydrothermal alteration of igneous rocks and Precambrian iron formations. *Chemical Geology*, **75**, 1-42.

Gurenko, A.A. Bindeman, I.N. Chaussidon, M. 2011. Oxygen isotope heterogeneity of the mantle beneath the Canary Islands: insights from olivine phenocrysts. *Contributions to Mineralogy and Petrology*, **162**(2), 349-363.

Hammer, J.E. Cashman, K.V. Hoblitt, R.P. Newman, S. 1999. Degassing and microlite crystallisation during pre-climatic events of the 1991 eruption of Mt. Pinatubo, Philippines. *Bulletin of Volcanology*, **60**, 255-380.

Hammer, J.E. Cashman, K.V. Voight, B. 2000. Magmatic processes revealed by textural and compositional trends in Merapi dome lavas. *Journal of Volcanology and Geothermal Research*, **100**, 165-192.

Hammer, J.E. Rutherford, M.J. 2002 An experimental study of the kinetics of decompression-induced crystallization in silicic melt. *Journal of Geophysical Research*, **107**(B1): ECV-8).

Handley, H.K. Blichert-Toft, J. Gertisser, R. Macpherson, C.G. Turner, S.P. Zaennudin, A. Abdurrachman, M. 2014. Insights from Pb and O isotopes into along-arc variations in subduction inputs and crustal assimilation for volcanic rocks in Java, Sunda arc, Indonesia. *Geochimica et Cosmochimica Acta*, **139**, 205-226.

Harris, C. Smith, H.S. le Roex, A.P. 2000. Oxygen isotope composition of phenocrysts from Tristan da Cunha and Gough Island lavas: variation with fractional crystallization and evidence for assimilation. *Contributions to Mineralogy and Petrology*, **138**(2), 164-175.

Hawkesworth, C.J. Hammill, M. Gledhill, A.R. van Calsteren, O. Rogers, G. 1982. Isotope and trace element evidence for late stage intra-crustal melting in the high Andes. *Earth and Planetary Science Letters*, **58**, 240–54.

Hawkesworth, C. George, R. Turner, S. Zellmer, G. 2004. Time scales of magmatic processes. *Earth and Planetary Science Letters*, **218**(1-2), 1-16.

Hermann, J. Rubatto, D. 2009. Accessory phase control on the trace element signature of sediment melts in subduction zone. *Chemical Geology*, **265**, 512-526.

Hickey, R.L. Frey, F.A. Gerlach, D.C. Lopez-Escobar, L. 1986. Multiple sources for basaltic arc rocks from the southern volcanic zone of the Andes (34–41 S): trace element and isotopic evidence for contributions from subducted oceanic crust, mantle, and continental crust. *Journal of Geophysical Research: Solid Earth*, **91**(B6), 5963-5983.

Higgins, M.D. 2000. Measurement of crystal size distributions. *American Mineralogist*, **85**(9), 1105–1116.

Higgins, M.D. 2006. *Quantitative textural measurements in igneous and metamorphic petrology*. Cambridge University Press.

Higgins. M. D., 2010. Textural coarsening in igneous rocks. *International Geology Review*, **53**, 354-376.

Hildreth, W. Moorbath, S. 1988. Crustal contributions to arc magmatism in the Andes of Chile. *Contributions to Mineralogy and Petrology*, **98**, 455–489.

Hildreth W. Godoy E. Fierstein J. Singer B. 2010. Laguna del Maule Volcanic Field: Eruptive history of a Quaternary basalt-to-rhyolite distributed field on the Andean rangecrest in central Chile. Serv. *Nac. Geol. Miner. Boletin* **63**, 145p.

Hoblitt, R.P. Harmon, R.S. 1993. Bimodal density distribution of cryptodome dacite from the 1980 eruption of Mount St. Helens, Washington. *Bulletin of Volcanology*, **55**(6), 421–437.

Hollenstein, Ch., Kahle, H.G., Geiger, A., Jenny, S., Goes, S., Giardini, D., 2003. New GPS constraints on the Africa–Eurasia plate boundary zone in southern Italy. *Geophysical Research Letters,* **30**, 18.

Honnorez, J. Keller, J. 1968. Xenolithe in vulkanischen Gesteinen der Aolischen Inseln 1748 (Sizilien). *Geologische Rundschau*, **57**, 719-736.

Hyppolite, J. Angelier, J. Roure, F. 1994. A major change revealed by Quaternary stress patterns in the Southern Apennines. *Tectonophysics,* **230**, 199–210.

Isgett, S.J. Houghton, B.F. Fagents, S.A. Biass, S. Burgisser, A. Arbaret, L. 2017. Eruptive and shallow conduit dynamics during Vulcanian explosions: insights from the Episode IV block field of the 1912 eruption of Novarupta, Alaska. *Bulletin of Volcanology*, **79**,58.

Jacques, G., Hoernle, K., Gill, J., Hauff, F., Wehrmann, H., Garbe-Schönberg, D., van den Bogaard, P. Bindeman, I. Lara, L.E. 2013. Across-arc geochemical variations in the Southern Volcanic Zone, Chile (34.5–38.0 S): constraints on mantle wedge and slab input compositions. *Geochimica et Cosmochimica Acta,* **123**, 218-243.

James, D.E. 1981. The combined use of oxygen and radiogenic isotopes as indicators of crustal contamination. *Annual Review of Earth and Planetary Sciences*. **9**, 311-344.

Johnson, M. C. Plank, T. 1999. Dehydration and melting experiments constrain the fate of subducted sediments. *Geochemistry, Geophysics, Geosystems* **1**, 1999GC000014.

Keller, J. 1970. Die historischen Eruptionen von Vulcano und Lipari. *Zeitschrift der Deutschen Geologischen Gesellschaft*, **121**, 179–185.

Keller, J. 1980a. The island of Vulcano. *Rendiconti della Societa Italiana di Mineralogia e Petrologia*, **36**, 369-414.

Keller, J. 1980b. The island of Salina. *Rendiconti della Societa` Italiana di Mineralogia e Petrologia*, **36**, 489–524.

Keller, J. 1982. Mediterannean island arcs. In: Thorpe, R.S. (ed) *Andesites*. Wiley, Chichester, 307-325.

Keller, J. 2002. Lipari's fiery past: dating the medieval pumice eruption of Monte Pelato: International Conference 'The fire between air and water', UNESCO-Regione Siciliana, Lipari, September 29th – October 2nd, oral presentation.

Kennedy, B., Spieler, O., Scheu, B., Kueppers, U., Taddeucci, J., Dingwell, D.B., 2005. Conduit implosion during Vulcanian eruptions. *Geology*, **33**, 581–584.

Kessel, R. Schmidt, M.W. Ulmer, P. Pettke, T. 2005. Trace element signature of subduction-zone fluids, melts and supercritical liquids at 120–180 km depth. *Nature*, **437**(7059), 724-727.

Klaver, M. Matveev, S. Berndt, J. Lissenberg, C.J. Vroon, P.Z. 2017. A mineral and cumulate perspective to magma differentiation at Nisyros volcano, Aegean arc. *Contributions to Mineralogy and Petrology*, **172**, 1.

Krause, J. Brügmann, G.E. Pushkarev, E.V. 2007. Accessory and rock forming minerals monitoring the evolution of zoned mafic–ultramafic complexes in the Central Ural Mountains. *Lithos*, **95**, 19–42.

Krom, M.D. Michard, A. Cliff, R.A. Strohle, K. 1999. Sources of sediment to the Ionian Sea and western Levantine basin of the Eastern Mediterranean during S-1 sapropel times. *Marine Geology*, **160**, 45–61.

Kyser, T. K. O'Neil, J. R. Carmichael, I. S. E. 1981. Oxygen isotope thermometry of basic lavas and mantle nodules. *Contributions to Mineralogy and Petrology*, **77**, 11–23.

Laj, C. Rais, A. Surmont, J. Gillot, P. Y. Guillou, H. Kissel, C. Zanella, E. 1997. Changes of the geomagnetic field vector obtained from lava sequences on the island of Vulcano (Aeolian Islands, Sicily). *Physics of the Earth and Planetary Interiors*, **99**, 161–177.

Land, L.S. Lynch, F.L. 1996. $\delta^{18}O$ values of mudrocks: More evidence for an ^{18}O-buffered ocean. *Geochimica et Cosmochimica Acta*, **60**, 3347–3352.

Langmuir, C.H. Vocke Jr, R.D. Hanson, G.N. Hart, S.R. 1978. A general mixing equation with applications to Icelandic basalts. *Earth and Planetary Science Letters*, **37**(3), 380-392.

Lanzafame, G. & Bousquet, J. C. 1997. The Maltese escarpment and its extension from M. Etna to Aeolian Islands (Sicily): importance and evolution of a lithospheric discontinuity. *Acta Vulcanologica*, **9**, 121–135.

Le Bas, M.J. Le Maitre, R.W. Streckeisen, A. Zanettin, B. 1986. A chemical classification of volcanic rocks based on the total alkali-silica diagram. *Journal of Petrology*, **22**(7) 745-750.

Lee, C.T.A. Bachmann, O. 2014. How important is the role of crystal fractionation in making intermediate magmas? Insights from Zr and P systematics. *Earth and Planetary Science Letters*, **393**, 266-274.

Lofgren, G. (1974) An experimental study of plagioclase crystal morphology: isothermal crystallization. *Americal Journal of Science*, **274**(3), 243–273.

Lucchi, F. Tranne, C. A. De Astis, G. Keller, J. Losito, R. Morche, W. 2008. Stratigraphy and significance of Brown Tuffs on the Aeolian Islands (southern Italy). *Journal of Volcanology and Geothermal Research*, **177**, 49–70.

Lucchi, F. Tranne, C. A. Rossi, P. L. 2010. Stratigraphic approach to geological mapping of the late-Quaternary volcanic island of Lipari (Aeolian archipelago, Southern Italy). In: Groppelli, G. Viereck-Goette, L. (eds) *Stratigraphy and Geology of Volcanic Areas*. Geological Society of America, Boulder, Special Papers, **464**, 1–32.

Lucchi, F. Peccerillo, J. Keller, J. Tranne, C.A. Rossi, P.L. 2013a. *The Aeolian Islands volcanoes*. Geological Society Memoirs, Geological Society, London.

Lucchi, F. Gertisser, R. Keller, J. Forni, F. De Astis, G. Tranne, C.A. 2013b. Eruptive history and magmatic evolution of the island of Salina (central Aeolian archipelago). In: Lucchi, F. Peccerillo, J. Keller, J. Tranne, C.A. Rossi, P.L. *The Aeolian Islands volcanoes*. Geological Society Memoirs, Geological Society, London 155-211.

Lucchi, F. 2013c. Stratigraphic methodology for the geological mapping of volcanic areas: insights from the Aeolian archipelago (Southern Italy). In: Lucchi, F. Peccerillo, A. Keller, J. Tranne, C. A. Rossi, P. L. (eds) *The Aeolian Islands Volcanoes*. Geological Society, London, Memoirs, this volume, 37–53.

Lucchi, F. Keller, J. Tranne, C. A. 2013d. Regional stratigraphic correlations across the Aeolian archipelago (southern Italy). In: Lucchi, F. Peccerillo, A. Keller, J. Tranne, C. A. Rossi, P. L. (eds) *The Aeolian Islands Volcanoes*. Geological Society, London, Memoirs, 37, 57–81.

Lucchi, F. Peccerillo, A. Tranne, C. A. Keller, J. Rossi, P. L. 2013e. Geological history of the Panarea volcanic group (eastern Aeolian archipelago). In: Lucchi, F. Peccerillo, A. Keller, J. Tranne, C. A. Rossi, P. L. (eds) *The Aeolian Islands Volcanoes*. Geological Society, London, Memoirs, 37, 349–393.

Lucchi, F. Peccerillo, A. Tranne, C. A. Rossi, P. L. Donati, C. 2013f. Volcanism, calderas, and magmas of the Alicudi composite volcano (western Aeolian archipelago). In: Lucchi, F. Peccerillo, A. Keller, J. Tranne, C. A. Rossi, P. L. (eds) *The Aeolian Islands Volcanoes*. Geological Society, London, Memoirs, 37, 83–111.

Lucchi, F. Santo, A. Peccerillo, A. Tranne, C. A. Keller, J. 2013g. Volcanism, magmatism, volcano-tectonics and sea-level fluctuations in the geological history of Filicudi (western Aeolian archipelago). In: Lucchi, F. Peccerillo, A. Keller, J. Tranne, C. A. Rossi, P. L. (eds) *The Aeolian Islands Volcanoes*. Geological Society, London, Memoirs, 37, 113–153.

Malgarotto, C, Molin, G.M., Zanazzi, P.F. 1993: Crystal chemistry of clinopyroxenes of Filicudi and Salina (Aeolian Islands, Italy). Geothermometry and barometry. *European Journal of Mineralogy*, **5**, 915-923.

Mandarano, M., Paonita, A., Martelli,M., Viccaro,M., Nicotra, E., Millar, I.L., 2016. Revealing magma degassing below closed-conduit active volcanoes: geochemical features of volcanic rocks versus fumarolic fluids at Vulcano (Aeolian Islands, Italy). *Lithos*, **248-251**, 272–287.

Manoli S, Molin GM 1988. Crystallographic procedures in the study of experimental rocks: X-ray single-crystal structure refinement of C2/c clinopyroxene from Lunar 74275 high-pressure experimental basalt. *Mineralogy and Petrology*, **39**, 187–200.

Mantovani, E. Albarello, D. Tamburelli, C. Babbucci, D. 1996. Evolution of the Tyrrhenian basin and surrounding regions as a result of the Africa–Euroasia convergence. *Journal of Geodynamics*, **21** (1), 35–72.

Marsh, B.D. 1981. On the crystallinity, probability of occurrence, and rheology of lava and magma. *Contributions to Mineralogy and Petrology*, **78**(1), 85-98.

Marsh, B.D. 1988. Crystal size distribution (CSD) in rocks and the kinetics and dynamics of crystallization I. Theory. *Contributions to Mineralogy and Petrology*, **99**(3), 277–291.

Marsh, B.D. 1996. Solidification fronts and magmatic evolution. *Mineralogical Magazine*, **60**, 5–40.

Marsh, B. D., 1998. On the interpretation of Crystal Size Distributions in magmatic systems. *Journal of Petrology*, **39**, 553-599.

Marschall, H. R. Schumacher, J. C. 2012. Arc magmas sourced from mélange diapirs in subduction zones. *Nature Geoscience*, **5**(12), 862-867.

Martel, C. 2012. Eruption dynamics inferred from microlite crystallization experiments: application to Plinian and dome-forming eruptions of Mt. Pelée (Martinique, Lesser Antilles). *Journal of Petrology*, **53**(4), 699-725.

Martel, C. Pichavant, M. Bourdier, J-L. Traineau, H. Holtz, F. Scaillet, B. 1998. Magma storage conditions and control of eruption regime in silicic volcanoes: experimental evidence from Mt Pelée. *Earth and Planetary Science Letters*, **156**, 89-99.

Martin, H. Moyen, J-F, Guitreau, M. Blichert-Toft, J. Le Pennec, J-L. 2014. Why Archaean TTG cannot be generated by MORB melting in subduction zones. *Lithos*, **198-199**, 1–13.

Masotta, M. Mollo, S. Freda, C. Gaeta, M. Moore, G. 2013. Clinopyroxene–liquid thermometers and barometers specific to alkaline differentiated magmas. *Contributions to Mineralogy and Petrology*, **166**(6), 1545-1561.

Mattey, D. Lowry, D. Macpherson, C. 1994. Oxygen isotope composition of mantle peridotite. *Earth and Planetary Science Letters*, **128**, 231–241.

Mattia, M. Palano, M. Bruno, V. Cannavò, F. Bonaccorso, A. Gresta, S. 2008. Tectonic features of the Lipari-Vulcano complex (Aeolian archipelago, Italy) from 10 years of GPS data. *Terra Nova*, **20**(5), 370-377.

Mazzuoli, R. Tortorici, L. Ventura, G. 1995. Oblique rifting in Salina, Lipari and Vulcano Islands (Aeolian Islands, Southern Tyrrhenian Sea, Italy). *Terra Nova*, **7**, 444–452.

McCormick, M.P. Thomason, L.W. Trepte, C.R. 1995. Atmospheric effects of the Mt Pinatubo eruption. *Nature*, **373**, 399–404.

McKenzie, D.A.N. 1984. The generation and compaction of partially molten rock. *Journal of Petrology*, **25**(3), 713-765.

Melnik, O.E. Sparks, R.S.J., 2002. *Dynamics of magma ascent and lava extrusion at Soufrière Hills Volcano, Montserrat*. Geological Society Memoirs, Geological Society, London. 21, 153–171.

Melnik, O.E. Blundy, J.D. Rust, A.C. Muir, D.D. 2011. Subvolcanic plumbing systems imaged through crystal size distributions. *Geology*, **39**, 403-406.

Mercalli, G., Silvestri, O., 1891. Le eruzioni dell'Isola di Vulcano incominciate il 3 agosto 1888 e terminate il 22 marzo 1890, relazione scientifica. Annali dell'Ufficio Centrale di Metereologia e Geodinamica d'Italia **10**, 1–213.

Milano, G., Vilardo, G. & Luongo, G. 1994. Continental collision and basin opening in Southern Italy: a new plate subduction in the Tirrhenian Sea? *Tectonophysics*, **230**, 249–264.

Miller, D.M. Goldstein, S.L. Langmuir, C.H. 1994. Cerium/lead and lead isotope ra-tios in arc magmas and the enrichment of lead in the continents. *Nature*, **368**, 514–520.

Mock, A. Jerram, D.A. 2005. Crystal Size Distribution (CSD) in three dimensions: Insights from the 3D reconstruction of a highly porphyritic rhyolite. *Journal of Petrology*, **46**(8), 1525-1541.

Morche,W. 1988. Tephrochronologie derA ¨ olischen Inseln. Unpublished PhD thesis, Albert-Ludwigs-Universita¨t Freiburg, Germany.

Morelli, C. Giese, P. Cassinis, R. Colombi, B. Guerra, I. Luongo, G. Scarascia, S. Shutte, K.G. 1975. Crustal structure of Southern Italy: a seismic refraction profile between Puglia, Calabria and Sicily. *Bollettino di Geofisica Teorica e Applicata*. **17**, 183–210.

Morgan, D.J. Jerram, D.A. 2006. On estimating crystal shape for crystal size distribution analysis. *Journal of Volcanology and Geothermal Research*, **154**, 1–7.

Morgan, D.J. Blake, S. Rogers, N.W. DeVivo, B. Rolandi, G. Macdonald, R. Hawkesworth, C.J. 2004. Time scales of crystal residence and magma chamber volume from modelling of diffusion profiles in phenocrysts: Vesuvius 1944. *Earth and Planetary Science Letters*, **222**, 933–946.

Morimoto, N. 1988. Nomenclature of pyroxenes. *Mineralogy and Petrology*, **39**. 55-76.

Morrissey, M.M. Mastin, L.G. 2000. Vulcanian eruptions. In: Sigurdsson, H. (Ed.), *Encyclopedia of Volcanoes*. Academic Press, 463–476.

Muehlenbachs, K. 1986, Alteration of the oceanic crust and the ^{18}O history of seawater. In: Valley, J.W. Taylor, H.P. O'Neil, J.R. (eds.) Stable isotopes in high temperature geological processes: *Reviews in Mineralogy and Geochemistry* **16**: Washington, D.C., Mineralogical Society of America, 425–444.

Nazzareni S, Molin GM, Peccerillo A, Zanazzi PF 1998. Structural and chemical variations in clinopyroxenes from the island of Alicudi (Aeolian Arc) and their implications for the conditions of crystallization. European Journal of Mineralogy, 10:291–300.

Nazzareni, S. Molin GM, Peccerillo A, Zanazzi PF. 2001. Volcanological implications of crystal-chemical variations in clinopyroxenes from the Aeolian Arc, Southern Tyrrhenian Sea (Italy). *Bulletin of Volcanology*, **63**, 73–82.

Neri, G. Caccamo, D. Cocina, O. Montalto, A. 1991. Shallow earhquake features in the Southern Tyrrhenian region: geostructural and tectonic implications. *Bolletino Geofisica Teorica Applicata,* **33**, 47-60.

Neri, G. Barberi, G. Orecchio, B. Aloisi, M. 2002. Seismotomography of the crust in the transition zone between the southern Tyrrhenian and Sicilian tectonic domains. *Geophysical Research Letters,* **29** (23), 50-51..

Nimis, P. 1995. A clinopyroxene geobarometer for basaltic systems based on crystal structure modelling. *Contributions to Mineralogy and Petrology*, **121**, 115–125.

Nimis, P. 1999. Clinopyroxene geobarometry of magmatic rocks. Part 2. Structural geobarometers for basic to acid, tholeiitic and mildly alkaline magmatic systems. *Contributions to Mineralogy and Petrology*, **135**, 62–74.

Nimis, P. Taylor, W.R. 2000. Single clinopyroxene thermobarometry for garnet peridotites. Part I. Calibration and testing of a Cr-in-Cpx barometer and an enstatite-in-Cpx thermometer. *Contributions to Mineralogy and Petrology*, **139**, 541–554.

Nimis, P., Ulmer, P., 1998. Clinopyroxene geobarometry of magmatic rocks Part 1: An

expanded structural geobarometer for anhydrous and hydrous, basic and ultrabasic systems. *Contributions to Mineralogy and Petrology*, **133**, 122–135.

Nuccio, P.M., Paonita, A., Sortino, F., 1999. Geochemicalmodeling ofmixing betweenmagmatic and hydrothermal gases: the case of Vulcano Island, Italy. *Earth and Planetary Science Letters*, **167**, 321–333

Nicotra, E., Giuffrida, M., Viccaro, M., Donato, P., D'Oriano, C., Paonita, A., De Rosa, R., 2018. Timescales of pre-eruptive magmatic processes at Vulcano (Aeolian Islands, Italy) during the last 1000 years. *Lithos*, **316–317**, 347–365.

Palummo, F. Mollo, S. De Astis, G. Di Stefano, F. Nazzari, M. Scarlato, P. 2020. Petrological and geochemical modeling of magmas erupted at Vulcano Island in the period 54–8 ka: Quantitative constraints on the sub-volcanic architecture of the plumbing system. *Lithos*, **374-375**, 105715.

Paonita, A., Favara, R., Nuccio, P.M., Sortino, F., 2002. Genesis of fumarolic emissions as inferred by isotope mass balances: CO2 and water at Vulcano Island, Italy. *Geochimica et Cosmochimica Acta*, **66**, 759–772.

Paonita, A., Federico, C., Bonfanti, P., Capasso, G., Inguaggiato, S., Italiano, F., Madonia, P., Pecoraino, G., Sortino, F., 2013. The episodic and abrupt geochemical changes at La Fossa fumaroles (Vulcano Island, Italy) and related constraints on the dynamics, structure, and compositions of the magmatic system. *Geochimica et Cosmochimica Acta*, **120**, 158–178.

Patino, L.C., Carr, M.J. and Feigenson, M.D., 2000. Local and regional variations in central American arc lavas controlled by variations in subducted sediment input. *Contributions to Mineralogy and Petrology*, **138**(3), 265-283.

Peccerillo, A. 2002. Plio-Quaternary magmatism in central-southern Italy: a new classification scheme for volcanic provinces and its geodynamic implications. In: Barchi,

R. M. Cirilli, S. Minelli, C. (eds) *Geological and Geodynamic Evolution of the Apennines*. Bollettino della Societa` Geologica Italiana, Special volume, **1**, 113–127.

Peccerillo, A. 2005. *Plio-Quaternary Volcanism in Italy: Petrology, Geochemistry, Geodynamics*. Springer-Verlag Berlin, Germany.

Peccerillo, A. Taylor, S. R. 1976. Geochemistry of Eocene calc-alkaline volcanic rocks from the Kastamonu area, northern Turkey. *Contributions to Mineralogy and Petrology*, **58**, 63–81.

Peccerillo, A. Wu, T.W. 1992. Evolution of calc-alkaline magmas in continental arc volcanoes: evidence from Alicudi, Aeolian Arc (Southern Tyrrhenian Sea, Italy). *Journal of Petrology*, **33**, 1295–1315.

Peccerillo, A. Kempton, P. D. Harmon,R. S. Wu, T.W. Santo,A. P. Boyce, A. J. Tripodo, A. 1993. Petrological and geochemical characteristics of the Alicudi Volcano, Aeolian Island, Italy: implication for magma genesis and evolution. *Acta Vulcanologica*, **3**, 235–249.

Peccerillo, A. Dallai, L. Frezzotti, M. L. Kempton, P. D. 2004. Sr-Nd-Pb-O isotopic evidence for decreasing crustal contamination with ongoing magma evolution at Alicudi volcano (Aeolian Arc, Italy): implication for style of magma-crust interaction and mantle source compositions. *Lithos*, **78**, 217–233.

Peccerillo, A. Frezzotti, M. L. De Astis, G. Ventura, G. 2006. Modelling the magma 799 plumbing system of Vulcano (Aeolian Islands, Italy) by integrated fluid-inclusion 800 geobarometry, petrology, and geophysics. *Geology*, **34**, 17–20.

Peccerillo, A., De Astis, G., Faraone, D., Forni, F. & Frezzoti, M. L. 2013. Compositional variation of magmas in the Aeolian arc: implications for petrogenesis and geodynamics. In: Lucchi, F., Peccerillo, A., Keller, J., Tranne, C. A. & Rossi, P. L. (eds) *The Aeolian Islands Volcanoes*. Geological Society, London, Memoirs, 489–508.

Perugini, D. Valentini, L. Poli, G. 2007. Insights into magma chamber processes from the analysis of size distribution of enclaves in lava flows: a case study from Vulcano Island (Southern Italy). *Journal of Volcanology and Geothermal Research*, **166**, 193–203.

Perugini, D., De Campos, C.P., Petrelli, M., Dingwell, D.B., 2015. Concentration variance decay during magma mixing: a volcanic chronometer. *Scientific Reports*, **5**, 14225.

Petrone, C.M. Bugatti, G. Braschi, E. Tommasini, S. 2016. Pre-eruptive magmatic processes re-timed using a non-isothermal approach to magma chamber dynamics. *Nature communications*, **7**(1), 1-11.

Petrone, C.M. Braschi, E. Francalanci, L. Casalini, M. Tommasini, S. 2018. Rapid mixing and short storage timescale in the magma dynamics of a steady-state volcano. *Earth and Planetary Science Letters*, **492**, 206-221.

Pichler, H. 1976. Carta geologica dell'isola di Lipari. Istituto di Vulcanologia, CNR, LAC, Firenze.

Pichler, H. 1980. The island of Lipari. *Rendiconti della Societa` Italiana di Mineralogia e Petrologia*, **36**, 415–440.

Pinarelli, L. Gioncada, A. Capaccioni, B. Vaselli, O. Downes, H. 2019. Mantle source heterogeneity in subduction zones: constraints from elemental and isotope (Sr, Nd, and Pb) data on Vulcano Island, Aeolian Archipelago, Italy. *Mineralogy and Petrology*, **113** (1) 39-60.

Piochi, M. De Astis, G. Petrelli, M. Ventura, G. Sulpizio, R. Zanetti, A. 2009. Constraining the recent plumbing system of Vulcano (Aeolian Arc, Italy) by textural, petrological, and fractal analysis: The 1739 A.D. Pietre Cotte lava flow. *Geochemistry, Geophysics, Geosystems*, **10**, Q01009.

Plank, T. Langmuir, C.H. 1988. An evaluation of the global variations in the major element chemistry of arc basalts. *Earth and Planetary Science Letters*, **90**(4), 349-370.

Plank, T. Langmuir, C.H. 1993. Tracing trace elements from sediment input to volcanic output at subduction zones. *Nature*, **362**(6422), 739-743.

Plank, T. Langmuir, C.H. 1998. The chemical composition of subducting sediment and its consequences for the crust and mantle. *Chemical Geology*, **145**, 325–394.

Platz, T. Cronin, S.J. Cahsman, K.V. Stewart, R.B. Smith, I.E.M. 2007. Transition from effusive to explosive phases in andesite eruptions – A case-study from the AD1655 eruption of Mt. Taranaki, New Zealand. *Journal of Volcanology and Geothermal Research*, **161**, 15-34.

Polacci, M. Papale, P. Rosi, M. 2001. Textural heterogeneities in pumices from the climactic eruption of Mount Pinatubo, 15 June 1991, and implications for magma ascent dynamics. *Bulletin of Volcanology*, **63**, 83–97.

Preece, K. Barclay, J. Gertisser, R. Herd, R.A. 2013. Textural and micropetrological variations in the eruptive products of the 2006 domeforming eruption of Merapi volcano, Indonesia: implications for sub-surface processes. *Journal of Volcanology and Geothermal Research*, **261**, 98–120.

Preece, K. Gertisser, R. Barclay, J. Charbonnier S. Komorowski, J-C. Herd, R.A. 2016. Transitions between explosive and effusive phases during the cataclysmic 2010 eruption of Merapi volcano, Java, Indonesia. *Bulletin of Volcanology*, **78**, 54.

Putirka, K.D. 2005. Igneous thermometers and barometers based on plagioclase+ liquid equilibria: Tests of some existing models and new calibrations. *American Mineralogist*, **90**(2-3), 336-346.

Putirka, K.D., 2008. Thermometers and barometers for volcanic systems. *Reviews in Mineralogy and Geochemistry*, **69**, 61–120.

Putirka, K. Johnson, M. Kinzler, R. Longhi, J. Walker, D. 1996. Thermobarometry of mafic igneous rocks based on clinopyroxene-liquid equilibria, 0-30 kbar. *Contributions to Mineralogy and Petrology*, **123**, 92–108.

Putirka, K. Mikaelian, H. Ryerson, F. Shaw, H. 2003. New clinopyroxene-liquid thermobarometers for mafic, evolved, and volatile-bearing lava compositions, with applications to lavas from Tibet and the Snake River Plain, Idaho. *American Mineralogist*, **88**, 1542–1554.

Romagnoli, C. Casalbore, D. Bortoluzzi, G. Bosman, A. Chiocci, F.L. D'Oriano, F. Gamberi, F. Ligi, M. Marani, M. 2013. Bathy-morphological setting of the Aeolian islands. In: Lucchi, F. Peccerillo, A. Keller, J. Tranne, C. A. Rossi, P. L. (eds) *The Aeolian Islands Volcanoes*. Geological Society, London, Memoirs, 37, 27–36.

Rossi, S. Petrelli, M. Morgavi, D. González-García, D. Fischer, L.A. Vetere, F. Perugini, D. 2017. Exponential decay of concentration variance during magma mixing: Robustness of a volcanic chronometer and implications for the homogenization of chemical heterogeneities in magmatic systems. *Lithos*, **286-287**, 396–407.

Pontevivo, A. Panza, G. 2006. The Lithosphere-Asthenosphere System in the Calabrian Arc and Surrounding Seas – Southern Italy. *Pure and Applied Geophysics*, **163**, 1617–1659.

Rosenbaum, G. Gasparon, M. Lucente, F. P. Peccerillo, A. Miller,M S. 2008. Kinematics of slab tear faults during subduction segmentation and implications for Italian magmatism. *Tectonics*, **27**, TC2008.

Royet, J.P. 1991. Stereology: a method for analyzing images. *Progress in Neurobiology*, **37**(5), 433–474.

Ryan, J. G. Langmuir, C.H. 1993. The systematics of boron abundances in young volcanic rocks. *Geochimica et Cosmochimica Acta*, **57**(7), 1489–1498.

Salters, V.J. and Stracke, A., 2004. Composition of the depleted mantle. *Geochemistry, Geophysics, Geosystems*, **5**(5).

Santo, A. P. Peccerillo, A. 2008. Oxygen isotopic variations in the clinopyroxenes from the Filicudi volcanic rocks (Aeolian Islands Italy): implications for open-system magma evolution. *Open Mineralogy Journal*, **2**, 1–12.

Schneider, C.A. Rasband, W.S. Eliceiri, K.W. 2012. NIH image to ImageJ: 25 years of image analysis. *Nature Methods*, **9**(7), 671–675.

Schütte, K. 1978. Crustal structure of southern Italy. In: Closs, H. Roeder, D. Schmidt, K. eds. *Alps, Apennines and Hellenides*. Schweizerbart: Stuttgart, Germany, 315-327.

Scolamacchia, T. 1997. I depositi di wet surge di La Fossa (isola di Vulcano): studi per la ricostruzione della loro posizione stratigrafica e della genesi. Tesi di laurea. Universita` degli studi di Bari, 1–75.

Sharp, Z. D. 1990. A laser-based microanalytical method for the in situ determination of oxygen isotope ratios of silicates and oxides, *Geochimica et Cosmochimica Acta*, **54**, 1353–1357.

Sharp, Z.D. 2006. *Principles of stable isotope geochemistry*. 2nd edition.

Sheldrick, G.M. (1976): SHELX-76. *Program for crystal structure determination*. Univ. of Cambridge, Cambridge, England.

Sheppard, S.M.F. Harris, C. 1985. Hydrogen and oxygen isotope geochemistry of Ascension Island lavas and granites: variation with crystal fractionation and interaction with seawater. *Contributions to Mineralogy and Petrology*, **91**, 74-81

Silvestri, O. Mercalli, G. Grablowitz, G. Clerici, V. 1891. Le eruzioni dell'isola di Vulcano incominciate il 3 Agosto 1888 e terminate il 22 Marzo 1890. *Ann Uff Centr Meteor Geod* **10**: 212 pp.

Simon, L.A. Lécuyer, C. 2005. Continental recycling: The oxygen isotope point of view. *Geochemistry, Geophysics, Geosystems*, **6**(8).

Simmons, J.M. Cas, R.A.F. Druitt, T.H. Folkes, C.B. 2016. Complex variations during a caldera-forming Plinian eruption, including precursor deposits, thick pumice fallout, co-

ignimbrite breccias and climactic lag breccias: the 184 ka Lower pumice 1 eruption sequence, Santorini, Greece. *Journal of Volcanology and Geothermal Research*, **324**, 200–219.

Sisson, T.W. Grove, T.L. 1993. Experimental investigations of the role of H_2O in calc-alkaline differentiation and subduction zone magmatism. *Contributions to Mineralogy and Petrology*, **113**. 143-166.

Skora, S. Blundy, J. 2010. High-pressure hydrous phase relations of radiolarian clay and implications for the involvement of subducted sediment in arc magmatism. *Journal of Petrology*, **51**(11), 2211-2243.

Smet, I. De Muynck, D. Vanhaecke, F. Elburg, M. 2010. From volcanic rock powder to Sr and Pb isotope ratios: a fit-for-purpose procedure for multi-collector ICP–mass spectrometric analysis. *Journal of Analytical Atomic Spectrometry*, **25**(7), 1025-1032.

Smith, A. L. Roobol, M. J. 1990. Mount Pele¤e, *Martinique, A study of an Active Island-arc Volcano*. Geological Society of America, Memoirs **175**, 105 p.

Solano, J.M.S. Jackson, M.D. Sparks, R.S.J. Blundy, J.D. Annen, C. 2012. Melt segregation in deep crustal hot zones: a mechanism for chemical differentiation, crustal assimilation and the formation of evolved magmas. *Journal of Petrology*, **53**(10), 1999-2026.

Solìgo, M. De Astis, G. Delitala,M. C. La Volpe, L. Taddeucci, A. & Tuccimei, P. 2000. Uranium-series disequilibria in the products from Vulcano Island (Sicily, Italy): isotopic chronology and magmatological implications. *Acta Vulcanologica*, **12**, 49–59.

Spiegelman, M. Kelemen, P.B. Aharonov, E. 2001. Causes and consequences of flow organization during melt transport: The reaction infiltration instability in compactible media. *Journal of Geophysical Research: Solid Earth*, **106**(B2), 2061-2077.

Staudigel, H. Plank, T. White, B. Schminke, H.-U. 1996. Geochemical fluxes during seafloor alteration of the basaltic upper oceanic crust: DSDP Sites 417 and 418. In: Bebout,

G.E. (ed.) Subduction: Top to bottom: *American Geophysical Union Geophysical Monograph*, **96**, 19–38.

Stix, J. Calvache, M.L. Fischer, T.P. Gómez, D. 1993. A model of degassing at Galeras volcano, Colombia, 1988-1993. *Geology*, **21**, 963–967.

Stothers, R.B. 1984. The Great Tambora eruption in 1815 and its aftermath. *Science*, **224**, 1191–1198.

Sulpizio, R. De Rosa, R. Donato, P. 2008. The influence of variable topography on the depositional behaviour of pyroclastic density currents: the examples of the Upper Pollara eruption (The island of Salina, southern Italy). *Journal of Volcanology and Geothermal Research*, **175**, 367–385.

Sparks, R.S.J. 1997. Causes and consequences of pressurisation in lava dome eruptions. *Earth and Planetary Science Letters*, **150**(3–4), 177–189.

Tanguy, J. C. Le Goff, M. Principe, C. Arrighi, S. Chillemi, V. Paiotti, A. Le Delfa, S. Patanè, G. 2003. Archeomagnetic dating of Mediterranean volcanics of the last 2100 years: validity and limits. *Earth and Planetary Science Letters*, **211**, 111–124.

Thirlwall, M.F. Graham, A.M. Arculus, R.J. Harmon, R.S. Macpherson, C.G. 1996. Resolution of the effects of crustal assimilation, sediment subduction and fluid transport in island arc magmas; Pb–Sr–Nd–O isotope geochemistry of Grenada, Lesser Antilles. *Geochimica et Cosmochimica Acta*, **60**, 4785–4810.

Thorpe, R.S. Francis, P.W. O'Callaghan, L. 1984. Relative roles of source composition, fractional crystallisation and crustal contamination in the petrogenesis of Andean volcanic rocks. *Philosophical Transactions of the Royal Society of London A*, **310**, 675-692.

Tormey, D. Schuller, P. Lopez-Escobar, L. Frey, F. 1991. Uranium-thorium activities and disequilibrium in volcanic rocks from the Andes (33-46° S): petrogenetic constraints and environmental consequences. *Andean Geology*, **18**(2),165-175.

Tranne, C. A. Lucchi, F. Calanchi, N. Lanzafame, G. Rossi, P. L. 2002. Geological Map of the island of Lipari (Aeolian Islands) (scale 1:12 500). University of Bologna and INGV, LAC, Firenze.

Troll, V.R. Deegan, F.M. Jolis, E.M. Harris, C. Chadwick, J.P. Gertisser, R. Schwarzkopf, L.M. Borisova, A.Y. Bindeman, I.N. Sumarti, S. Preece, K. 2013. Magmatic differentiation processes at Merapi Volcano: inclusion petrology and oxygen isotopes. *Journal of Volcanology and Geothermal Research*, **261**, 38-49.

Trua, T. Serri, G. Marani, M. P. Rossi, P. L. Gamberi, F. Renzulli, A. 2004. Mantle domains beneath the southern Tyrrhenian: constraints from recent seafloor sampling and dynamic implications. *Periodico di Mineralogia*, **73**, 53–73.

Trua, T. Marani, M. P. Gamberi, F. 2011. Magmatic evidence for African mantle propagation into the southern Tyrrhenian backarc region. In: Beccaluva, L., Bianchini, G. & Wilson, M. (eds) Volcanism and Evolution of the African Lithosphere. *Geological Society of America, Boulder Special Paper* **478**, 307–331.

Turner, S. Foden, J. 2001. U, Th and Ra disequilibria, Sr, Nd and Pb isotopes and trace element variations in Sunda arc lavas: predominance of a subducted sediment component. *Contributions to Mineralogy and Petrology*, **142**, 43–57.

Turner, S.J. Langmuir, C.H. 2015. The global chemical systematics of arc front stratovolcanoes: Evaluating the role of crustal processes. *Earth and Planetary Science Letters*, **422**, 182-193.

Van Soest, M.C. Hilton, D.R. MacPherson, C.G. Mattey, D.P. 2002. Resolving sediment subduction and crustal contamination in the Lesser Antilles Island Arc: a combined He–O–Sr isotope approach. *Journal of Petrology*, **43**(1), 143-170.

Ventura, G. 1994. Tectonics, structural evolution and caldera Formation on Vulcano Island, Aeolian Archipelago, Southern Tyrrhenian Sea. *Journal of Volcanology and Geothermal Research*, **60**, 207–224.

Ventura, G. 1995. Relazioni fra tettonica e vulcanismo nelle isole del Tirreno Meridionale. PhD Thesis, University of Cosenza, Italy.

Ventura, G. 2013. Kinematics of the Aeolian volcanism (Southern Tyrrhenian Sea) from geophysical and geological data. In: Lucchi, F. Peccerillo, J. Keller, J. Tranne, C.A. Rossi, P.L. *The Aeolian Islands volcanoes*. Geological Society Memoirs, Geological Society, London, 3-11.

Ventura, G. Vilardo, G. Milano, G. Pino, N. 1999. Relationships among crustal structure, volcanism and strike-slip tectonics in the Lipari-Vulcano volcanic complex (Aeolian Islands, Southern Tyrrhenian Sea, Italy). *Physics of the Earth and Planetary Interiors*, **116**, 31-52.

Vetere, F., Petrelli, M., Morgavi, D., Perugini, D., 2015. Dynamics and time evolution of a shallow plumbing system: the 1739 and 1888–90 eruptions, Vulcano Island, Italy. *Journal of Volcanology and Geothermal Research*, **306**, 74–82.

Villemant, B. Boudon, G. 1998. Transition from dome-forming to plinian eruptive styles controlled by H2O and Cl degassing. *Nature*, **392**(6671), 65-69.

Voight, B. Elsworth, D. 2000. Instability and collapse of hazardous gas-pressurized lava domes. *Geophysical Research Letters*, **27**(1), 1-4.

Voltaggio, M. Branca, M. Tuccimei, P. Tecce, F. 1995. Leaching procedure used in dating young potassic volcanic rocks by the 226Ra/230Th method. *Earth Planetary and Science Letters*, **136**, 123–131.

Vroon, P.Z. Van Bergen, M.J. White, W.M. Varekamp, J.C. 1993. Sr-Nd-Pb isotope systematics of the Banda Arc, Indonesia: Combined subduction and assimilation of continental material. *Journal of Geophysical Research: Solid Earth*, **98**(B12), 22349-22366.

Wagner, G. A. Storzer, C. Keller, J. 1976. Spaltspurendatierung quarta¨rer Gesteinsgla¨ser aus dem Mittelmeerraum. *Neues Jahrbuch fu¨r Mineralogie Monatshefte*, **2**, 84–94.

Walker, G.P.L. 1969. The breaking of magma. *Geological Magazine*, **106** (2), 166-173.

Wang, C. Y., Hwang, W. T. & Shi, Y. 1989. Thermal evolution of a rift basin: the Tyrrhenian Sea. *Journal of Geophysical Research*, **94**, 3991–4006.

Westaway, R. 1993. Quaternary Uplift of Southern Italy. *Journal of Geophysical Research*, **98**, 741772.

Westercamp, D. Traineau, H. 1983. The past 5000 years of volcanic activity at Mt Pelée, Martinique (FWI): implications for assessment of volcanic hazards. *Journal of Volcanology and Geothermal Research*, **17**, 159-185.

Wilson, M., 1997. *Igneous Petrogenesis*. Chapman and Hall, London, pp. 1–456.

Wilson, M. Davidson, J. P. 1984. The relative roles of crust and upper mantle in the generation of oceanic island arc magmas. *Philosophical Transactions of the Royal Society of London A*, **310**, 661-674.

Winter, J.D., 2014. *Principles of igneous and metamorphic petrology*. Harlow, UK: Pearson education.

Wright, H.M., Cashman, K.V., Rosi, M. Cioni, R. 2007. Breadcrust bombs as indicators of Vulcanian eruption dynamics at Guagua Pichincha volcano, Ecuador. *Bulletin of Volcanology*, **69**(3), 281-300.

Yamagishi, H. Feebrey, C. 1994. Ballistic ejecta from the 1988–1989 andesitic Vulcanian eruptions of Tokachidake volcano, Japan: morphological features and genesis. *Journal of Volcanology and Geothermal Research*, **59**(4), 269-278.

Young, S.R. Sparks, R.S.J. Aspinall, W.P. Lynch, L.L. Miller, A.D. Robertson, R.E. Shepherd, J.B. 1998. Overview of the eruption of Soufriere Hills volcano, Montserrat, 18 July 1995 to December 1997. *Geophysical Research Letters*, **25**(18), 3389-3392.

Zamboni, D. Gazel, E. Ryan, J.G. Cannatelli, C. Lucchi, F. Atlas, Z.D. Trela, J. Mazza, S.E. De Vivo, B. 2016. Contrasting sediment melt and fluid signatures for magma

components in the Aeolian Arc: Implications for numerical modelling of subduction systems. *Geochemistry, Geophysics, Geosystems*, **17**(6), 2034-2053.

Zanchetta, G. Sulpizio, R. Roberts, N. Cioni, R. Eastwood, W.J. Siani, G. Caron, B. Paterne, M. Santacroce, R. 2011. Tephrostratigraphy, chronology and climatic events of the Mediterranean basin during the Holocene: an overview. *The Holocene*, **21**, 33–52.

Zanon, V. Nikogosian, I. 2004. Evidence of crustal melting events below the island of Salina (Aeolian arc, southern Italy). *Geological Magazine*, **141**(4), 525-540.

Zanon, V. Frezzotti, M.L. Peccerillo, A. 2003. Magmatic feeding system and crustal magma accumulation beneath Vulcano Island (Italy): evidence from fluid inclusion in quartz xenoliths. *Journal of Geophysical Research*, **108**, 2298-2301.

Zellmer, G. Annen, C. Charlier, B. George, R. Turner, S. Hawkesworth, C. 2005. Magma evolution and ascent at volcanic arcs: constraining petrogenetic processes through rates and chronologies. *Journal of Volcanology and Geothermal Research*, **140**, 171–191.

APPENDIX A – CHAPTER 2: La Fossa di Vulcano

Appendix A1 Sample List

Sample	Grid Reference			Unit	Location	Type
AI-17-004	33S	0496667	4251573	pn1	Port Beach	Pumice
AI-17-005	33S	0496667	4251573	pn1	Port Beach	Lava
AI-17-006	33S	0496667	4251573	pn3	Port Beach	Lava
AI-17-007	33S	0496667	4251573	pn3	Port Beach	Lava
AI-17-008	33S	0496398	4250565	pc2	Pietre Cotte lava flow	Enclave
AI-17-009	33S	0496398	4250565	pc2	Pietre Cotte lava flow	Lava
AI-17-010	33S	0496396	4250567	pc1	Fossa cone crater	Lithics
AI-17-011	33S	0496396	4250567	pc1	Fossa cone crater	Pumice
AI-17-012	33S	0496396	4250567	pc1	Fossa cone crater	Pumice
AI-17-013	33S	0496396	4250567	pc1	Fossa cone crater	Ash
AI-17-014	33S	0496396	4250567	pc1	Fossa cone crater	Pumice
AI-17-015	33S	0496396	4250567	pc1	Fossa cone crater	Lithics
AI-17-016	33S	0496396	4250567	pc1	Fossa cone crater	Pumice
AI-17-017	33S	0496396	4250567	pc1	Fossa cone crater	Pumice
AI-17-018	33S	0496396	4250567	pc1	Fossa cone crater	Pumice
AI-17-019	33S	0496396	4250567	pc1	Fossa cone crater	Scoria
AI-17-020	33S	0496396	4250567	pc1	Fossa cone crater	Pumice
AI-17-021	33S	0496396	4250567	pc1	Fossa cone crater	Pumice
AI-17-022	33S	0496396	4250567	pc1	Fossa cone crater	Pumice
AI-17-023	33S	0496396	4250567	pc1	Fossa cone crater	Pumice
AI-17-024	33S	0496396	4250567	pc1	Fossa cone crater	Pumice
AI-17-025	33S	0496396	4250567	pc1	Fossa cone crater	Pumice
AI-17-026	33S	0496396	4250567	pc1	Fossa cone crater	Pumice
AI-17-027	33S	0496396	4250567	pc1	Fossa cone crater	Pumice
AI-17-028	33S	0496279	4251369	pc2	Pietre Cotte lava flow	Enclave
AI-17-030	33S	0496099	4250933	ca2	NW flanks of Fossa cone	Pumice
AI-17-031	33S	0496099	4250933	ca2	NW flanks of Fossa cone	Pumice
AI-17-032	33S	0496099	4250933	ca2	NW flanks of Fossa cone	Pumice
AI-17-033	33S	0496099	4250933	ca2	NW flanks of Fossa cone	Pumice
AI-17-034	33S	0496099	4250933	ca2	NW flanks of Fossa cone	Pumice
AI-17-039	33S	0497279	4249822	gp2a	Close to Valle Roia	Pumice
AI-17-040	33S	0497279	4249822	gp2a	Close to Valle Roia	Scoria
AI-17-041	33S	0497578	4249950	pn1	Valle Roia	Ash
AI-17-042	33S	0497578	4249950	pn1	Valle Roia	Pumice
AI-17-044	33S	0497279	4249822	gp2a	Close to Valle Roia	Pumice
AI-17-045	33S	0496579	4249852	gp3b	Palizzi valley	Lava
AI-17-046	33S	0496559	4249994	pc1	Gully in the southern flanks	Pumice
AI-17-047	33S	0496559	4249994	gp2a	Gully in the southern flanks	Pumice

Sample	Grid Reference			Unit	Location	Type
AI-17-049	33S	0496559	4249994	gp2a	Gully in the southern flanks	Pumice
AI-17-050	33S	0496559	4249994	pc1	Gully in the southern flanks	Ash
AI-17-051	33S	0496559	4249994	pc1	Gully in the southern flanks	Ash
AI-17-052	33S	0496604	4250025	gp2a	Gully in the southern flanks	Pumice
AI-17-053	33S	0496604	4250025	ca2	Gully in the southern flanks	Enclave
AI-17-054	33S	0496623	4250087	gp2a	Gully in the southern flanks	Pumice
AI-17-055	33S	0496604	4250144	gp2b	Gully in the southern flanks	Lava
AI-17-056	33S	0496604	4250144	gp2b	Gully in the southern flanks	Enclave
AI-17-057	33S	0496679	4250147	gp2a	Gully in the southern flanks	Pumice
AI-17-058	33S	0496192	4251245	pc1	Gully close to pc2 lava flow	Pumice
AI-17-059	33S	0496192	4251245	pc1	Gully close to pc2 lava flow	Pumice
AI-17-060	33S	0496192	4251245	pc1	Gully close to pc2 lava flow	Pumice
AI-17-061	33S	0496192	4251245	pc1	Gully close to pc2 lava flow	Pumice
AI-17-062	33S	0496192	4251245	pc1	Gully close to pc2 lava flow	Pumice
AI-17-070	33S	0495218	4250810	gc1	Monte Lentia	Pumice
AI-17-071	33S	0495218	4250810	gc1	Monte Lentia	Ash
AI-17-072	33S	0495218	4250810	gc1	Monte Lentia	Ash
AI-17-073	33S	0495109	4250843	gp1a	Monte Lentia	Ash
AI-17-117	33S	0496245	4250204	gp2b	Base of gp2b lava	Lava
AI-17-118	33S	0496245	4250204	gp2b	Base of gp2b lava	Enclave
AI-17-119	33S	0496594	4251002	gc2	Bomb field	Bomb
AI-17-120	33S	0496594	4251002	gc2	Bomb field	Bomb
AI-17-121	33S	0496594	4251002	gc2	Bomb field	Bomb
AI-17-122	33S	0496594	4251002	gc2	Bomb field	Bomb
AI-17-123	33S	0496376	4250875	gc2	Bomb field	Bomb
AI-17-124	33S	0496376	4250875	gc2	Bomb field	Bomb
AI-17-125	33S	0496376	4250875	gc2	Bomb field	Bomb
AI-17-126	33S	0496376	4250875	gc2	Bomb field	Bomb
AI-18-056	33S	0496477	4249958	gp3a	Palizzi valley	Ash
AI-18-057	33S	0496477	4249958	gp3a	Palizzi valley	Pumice
AI-18-058	33S	0496545	4251501	pn2	Boat yard near Vulcano Porto	Ash
AI-18-059	33S	0496545	4251501	gp2a	Boat yard near Vulcano Porto	Pumice
AI-18-060				pn3	Punte Nere point	Lava
AI-18-061				?ca2	Punte Nere point	Ash
AI-18-068	33S	0496695	4251011	gc2	Bomb field	Bomb
AI-18-069	33S	0496702	4251018	gc2	Bomb field	Bomb
AI-18-070	33S	0496776	4250950	gc2	Bomb field	Bomb
AI-18-071	33S	0496718	4251008	gc2	Bomb field	Bomb
AI-18-072	33S	0496695	4251035	gc2	Bomb field	Bomb
AI-18-073	33S	0496610	4251011	gc2	Bomb field	Bomb
AI-18-074	33S	0496591	4250994	gc2	Bomb field	Bomb
AI-18-075	33S	0496598	4250975	gc2	Bomb field	Bomb
AI-18-076	33S	0496579	4251005	gc2	Bomb field	Bomb
AI-18-077	33S	0496531	4250975	gc2	Bomb field	Bomb
AI-18-078				gc2	Palizzi valley	Bomb

Appendix A2 Vulcano Mineral Chemical Dataset

Mineral chemical data for plagioclase, alkali feldspar, clinopyroxene and Fe-Ti oxides from La Fossa di Vulcano are included in the electronic appendix A2 for this thesis.

Appendix A3 Vulcano Thermometry

Thermometry results for clinopyroxene and feldspar are included in the electronic appendix A for this thesis.

Clinopyroxene Thermometers

As many of the clinopyroxenes from La Fossa di Vulcano are antecrystic and not always in equilibrium with their host melts, the thermometer used was the clinopyroxene composition thermometer, using equation 32d (Putirka 2008).

Plagioclase Thermometer

Temperature calculations for plagioclase phenocrysts have been performed using a plagioclase-liquid thermometer RiMG equation 26 (Putirka 2005). The results for temperature calculations using equation 23 are also illustrated in the electronic appendices.

Appendix A4 Olive Fractional Crystallisation Modelling

Olive (Cortés 2016) is a platform which produces simple mass balance fractionation models, by calculating changes in melt compositions using mass balance using weight proportions of known fractionated minerals in a melt. The Olive platform where you input the total melt (g), which is 100g and the total fractionated phases, 90g and the mineral proportions of fractionated phases. The mineral proportions were calculated using EMPA mineral data from La Fossa di Vulcano. A step-by-step model is then produced, illustrating the compositional changes of the melt as the different mineral phases fractionate. This can then be used to model fractional crystallisation of the melt.

Starting Composition

Major Element				**Mineral Proportions**	
Wt.%				**Mineral**	**Estimated Amount**
SiO_2	54.41	53.87		Fo	5.42
TiO_2	0.74	0.73		Fa	10.84
Al_2O_3	18.33	18.15		Wo	2.71
FeO	7.54	7.47		En	1.36
Fe_2O_3	0.63	0.62		Fs	0.27
MnO	0.15	0.15		Ab	24.39
MgO	3.43	3.39		An	27.1
CaO	6.63	6.56		Kfd	27.1
Na_2O	3.24	3.21		Mt	1.36
K_2O	4.44	4.39		Ap	1.36
P_2O_5	0.47	0.47			101.91
H_2O*	1.00	0.99			
Total	101.00	100.00			

*H2O is estimated based on Loss on Ignition

WET

Step	0	1	2	3	4	5	6	7	8	9	10	extract/step
SiO_2	53.86	53.96	54.08	54.24	54.43	54.69	55.04	55.57	56.2	57.42	59.83	53.15
TiO_2	0.73	0.8	0.89	1	1.14	1.33	1.59	1.97	2.6	3.79	6.81	0
Al_2O_3	18.15	18.04	17.9	17.73	17.52	17.23	16.83	16.24	15.2	13.2	7.51	19.43
Fe_2O_3	0.62	0.59	0.55	0.51	0.45	0.37	0.27	0.11	0.14	0.21	0.37	0.65
FeO	7.47	7.41	7.34	7.25	7.14	6.99	6.78	6.47	6.06	5.28	3.06	8
MnO	0.15	0.16	0.18	0.21	0.23	0.27	0.33	0.41	0.53	0.78	1.4	0
MgO	3.39	3.37	3.35	3.32	3.28	3.23	3.16	3.06	2.88	2.53	1.54	3.61
CaO	6.56	6.48	6.37	6.25	6.09	5.87	5.57	5.12	4.37	2.93	0.76	7.26
Na_2O	3.21	3.25	3.29	3.35	3.42	3.52	3.66	3.86	4.17	4.77	6.2	2.85
K_2O	4.39	4.38	4.37	4.35	4.33	4.3	4.26	4.2	4.09	3.87	3.17	4.54
P_2O_5	0.47	0.46	0.45	0.43	0.41	0.38	0.35	0.29	0.2	0.02	0.03	0.52
H_2O	1	1.1	1.21	1.36	1.55	1.8	2.15	2.66	3.49	5.1	9.15	0.02
mass	100	91	82	73	64	55	46	37	28.12	19.24	10.72	9
Total Dry	99	98.9	98.77	98.64	98.44	98.18	97.84	97.3	96.44	94.8	90.68	

DRY

Step	0	1	2	3	4	5	6	7	8	9	10
SiO_2	54.40	54.56	54.75	54.99	55.29	55.70	56.26	57.11	58.27	60.57	65.98
TiO_2	0.74	0.81	0.90	1.01	1.16	1.35	1.63	2.02	2.70	4.00	7.51
Al_2O_3	18.33	18.24	18.12	17.97	17.80	17.55	17.20	16.69	15.76	13.92	8.28
Fe_2O_3	0.63	0.60	0.56	0.52	0.46	0.38	0.28	0.11	0.15	0.22	0.41
FeO	7.55	7.49	7.43	7.35	7.25	7.12	6.93	6.65	6.28	5.57	3.37
MnO	0.15	0.16	0.18	0.21	0.23	0.28	0.34	0.42	0.55	0.82	1.54
MgO	3.42	3.41	3.39	3.37	3.33	3.29	3.23	3.14	2.99	2.67	1.70
CaO	6.63	6.55	6.45	6.34	6.19	5.98	5.69	5.26	4.53	3.09	0.84
Na_2O	3.24	3.29	3.33	3.40	3.47	3.59	3.74	3.97	4.32	5.03	6.84
K_2O	4.43	4.43	4.42	4.41	4.40	4.38	4.35	4.32	4.24	4.08	3.50
P_2O_5	0.47	0.47	0.46	0.44	0.42	0.39	0.36	0.30	0.21	0.02	0.03

APPENDIX B – CHAPTER 3: 1888 - 90 eruption

Appendix B1 Sample List

Sample Number	Island	Grid Reference			Unit	Location	Description
AI-17-119	VUL	33S	0496594	4251002	gc2	Bomb field at the top of the Fossa cone	Dense Bomb
AI-17-120	VUL	33S	0496594	4251002	gc2	Bomb field at the top of the Fossa cone	Dense Bomb
AI-17-121	VUL	33S	0496594	4251002	gc2	Bomb field at the top of the Fossa cone	Vesiculated Bomb
AI-17-122	VUL	33S	0496594	4251002	gc2	Bomb field at the top of the Fossa cone	Vesiculated Bomb
AI-17-123	VUL	33S	0496376	4250875	gc2	Bomb field at the top of the Fossa cone	Enclave in Dense Bomb
AI-17-124	VUL	33S	0496376	4250875	gc2	Bomb field at the top of the Fossa cone	Dense Bomb
AI-17-125	VUL	33S	0496376	4250875	gc2	Bomb field at the top of the Fossa cone	Dense Bomb
AI-17-126	VUL	33S	0496376	4250875	gc2	Bomb field at the top of the Fossa cone	Vesiculated Bomb
AI-18-068	VUL	33S	0496695	4251011	gc2	N valley at top of Fossa cone	Vesiculated Bomb
AI-18-069	VUL	33S	0496702	4251018	gc2	N valley at top of Fossa cone	Dense Bomb
AI-18-070	VUL	33S	0496776	4250950	gc2	N valley at top of Fossa cone	Vesiculated Bomb
AI-18-071	VUL	33S	0496718	4251008	gc2	N valley at top of Fossa cone	Vesiculated Bomb
AI-18-072	VUL	33S	0496695	4251035	gc2	N valley at top of Fossa cone	Dense Bomb
AI-18-073	VUL	33S	0496610	4251011	gc2	N valley at top of Fossa cone	Vesiculated Bomb
AI-18-074	VUL	33S	0496591	4250994	gc2	N valley at top of Fossa cone	Vesiculated Bomb
AI-18-075	VUL	33S	0496598	4250975	gc2	N valley at top of Fossa cone	Vesiculated Bomb
AI-18-076	VUL	33S	0496579	4251005	gc2	N valley at top of Fossa cone	Vesiculated Bomb
AI-18-077	VUL	33S	0496531	4250975	gc2	N valley at top of Fossa cone	Vesiculated Bomb
AI-18-078	VUL	33S	496477	4249958	gc2	Palizzi valley	Scoriaceous Bomb

Appendix B2 Textural Analysis Results

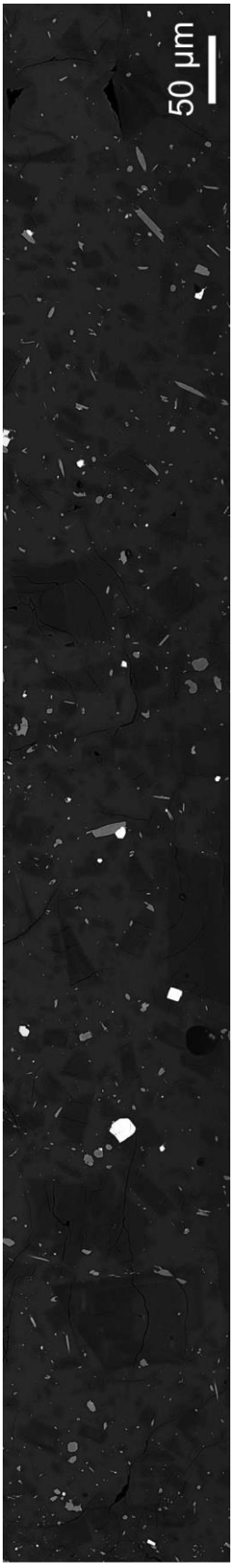

Sample: AI-17-120

Total Area	0.179	**Groundmass**	0.043	
Size Inter	**Data Set**	**Corr Factor**	**Mid Inter**	**ln (pop den)**
0.0631	10	0	0.1011	9.66
0.0398	38	0.03	0.0638	11.89
0.0251	65	0.07	0.0403	13.3
0.0158	113	0.08	0.0254	14.77
0.01	149	0.1	0.016	15.94
0.0063	268	0.09	0.0101	17.46
0.004	74	0.55	0.0064	16.42
Total	717			
ln (min PD)	**ln (max PD)**	**Crystal Number**	**Vol%**	
9.28	9.93	7.28E+02	11.95	
11.7	12.04	4.27E+03	17.59	
13.16	13.43	1.11E+04	11.49	
14.66	14.86	3.03E+04	7.887	
15.84	16.02	6.15E+04	4.017	
17.39	17.53	1.79E+05	2.935	
16.13	16.64	3.96E+04	0.163	

Sample: AI-17-122

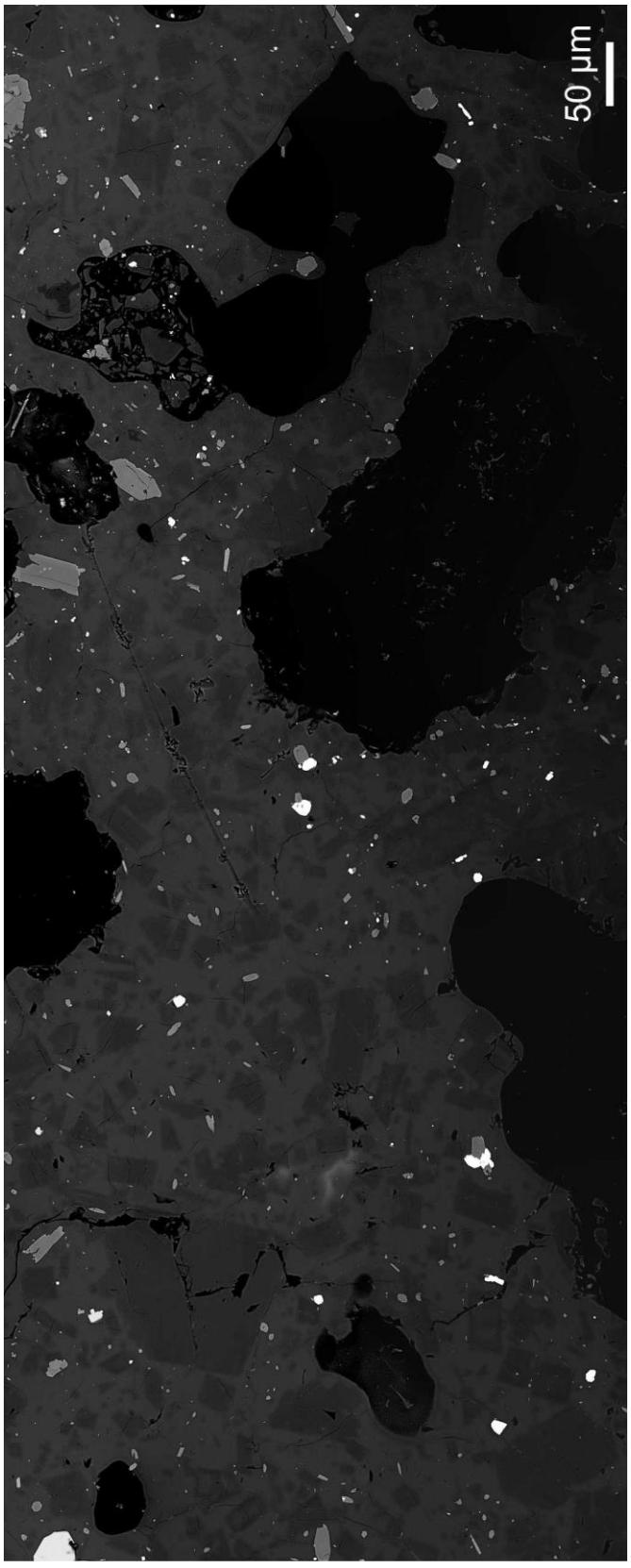

Total Area	0.265	
Pheno	0.012	
Vesicles	0.078	
GM	0.048	
Size Inter	**Data Set**	**Corr Fact**
0.0631	7	0
0.0398	31	0.03
0.0251	96	0.04
0.0158	140	0.1
0.01	162	0.14
0.0063	302	0.11
0.004	76	0.71
0.0025	15	0.4
Total	829	
Mid Inter	**ln (pop den)**	**ln (min PD)**
0.0809	9.64	9.17
0.051	12.02	11.82
0.0322	14.06	13.95
0.0203	15.3	15.2
0.0128	16.32	16.22
0.0081	17.9	17.83
0.0051	16.33	15.83
0.0032	16.35	15.79
ln (max PD)	**Crystal Number**	**Vol%**
9.96	575	7.545
12.19	3.92E+03	12.92
14.16	1.89E+04	15.67
15.39	4.13E+04	8.595
16.41	7.21E+04	3.771
17.96	2.21E+05	2.904
16.66	2.90E+04	0.095
16.7	1.86E+04	0.015

Sample: AI-18-068A

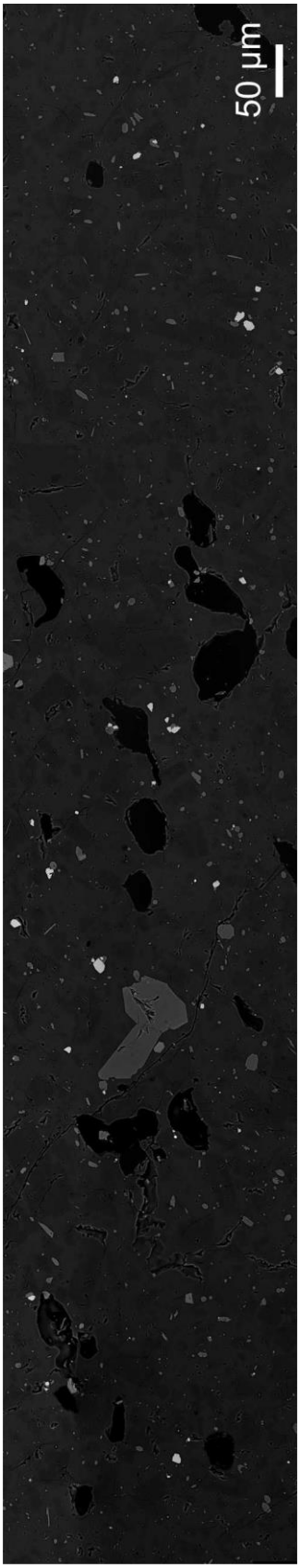

Total Area	0.419	**Pheno**	0.027	
Vesicles	0.023	**GM**	0.084	
Size Inter	**Data Set**	**Corr Fact**	**Mid Inter**	**ln (pop den)**
0.0631	30	0.04	0.1011	9.92
0.0398	66	0.05	0.0638	11.61
0.0251	115	0.07	0.0403	13.07
0.0158	216	0.07	0.0254	14.62
0.01	217	0.14	0.016	15.48
0.0063	260	0.14	0.0101	16.57
Total	904			
ln (min PD)	**ln (max PD)**	**Crystal Number**	**Vol%**	
9.71	10.09	9.44E+02	15.49	
11.47	11.73	3.24E+03	13.36	
12.96	13.16	8.78E+03	9.094	
14.54	14.69	2.62E+04	6.81	
15.39	15.55	3.88E+04	2.535	
16.49	16.64	7.31E+04	1.2	

Sample: AI-18-070

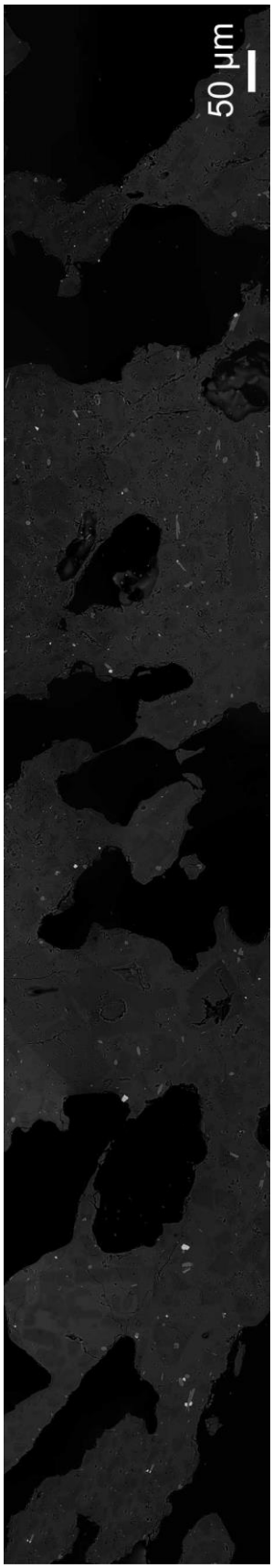

Total Area	0.721	**Pheno**	0.044	
Vesicles	0.299	**GM**	0.088	
Size Inter	**Data Set**	**Corr Fact**	**Mid Inter**	**ln (pop den)**
0.0631	29	0.02	0.0809	10.23
0.0398	65	0.06	0.051	11.91
0.0251	104	0.09	0.0322	13.27
0.0158	173	0.09	0.0203	14.7
0.01	162	0.17	0.0128	15.46
0.0063	218	0.15	0.0081	16.7
0.004	51	0.81	0.0051	14.7
0.0025	17	0.15	0.0032	15.99
Total	819			
ln (min PD)	**ln (max PD)**	**Crystal Number**	**Vol%**	
10.02	10.4	1.03E+03	13.54	
11.77	12.04	3.51E+03	11.58	
13.16	13.37	8.61E+03	7.131	
14.61	14.78	2.26E+04	4.7	
15.36	15.55	3.06E+04	1.598	
16.62	16.78	6.70E+04	0.879	
13.43	15.24	5.69E+03	0.018	
15.66	16.25	1.31E+04	0.01	

Sample: AI-18-072

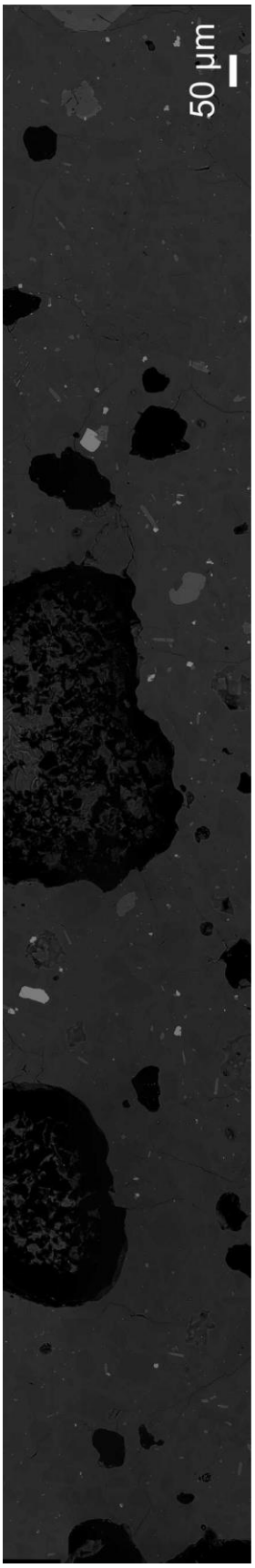

Total Area	0.848	**Pheno**	0.028	
Vesicles	0.206	**GM**	0.138	
Size Inter	**Data Set**	**Corr Fact**	**Mid Inter**	**ln (pop den)**
0.0631	57	0.01	0.0916	10.29
0.0398	86	0.08	0.0578	11.56
0.0251	170	0.07	0.0365	13.16
0.0158	209	0.11	0.023	14.24
0.01	134	0.26	0.0145	14.54
0.0063	68	0.51	0.0092	14.36
Total	724			

ln (min PD)	**ln (max PD)**	**Crystal Number**	**Vol%**
10.14	10.41	1.24E+03	17.29
11.43	11.67	2.78E+03	9.729
13.08	13.24	8.76E+03	7.706
14.16	14.32	1.63E+04	3.596
14.42	14.65	1.38E+04	0.766
14.07	14.58	7.29E+03	0.101

Sample: AI-18-074B

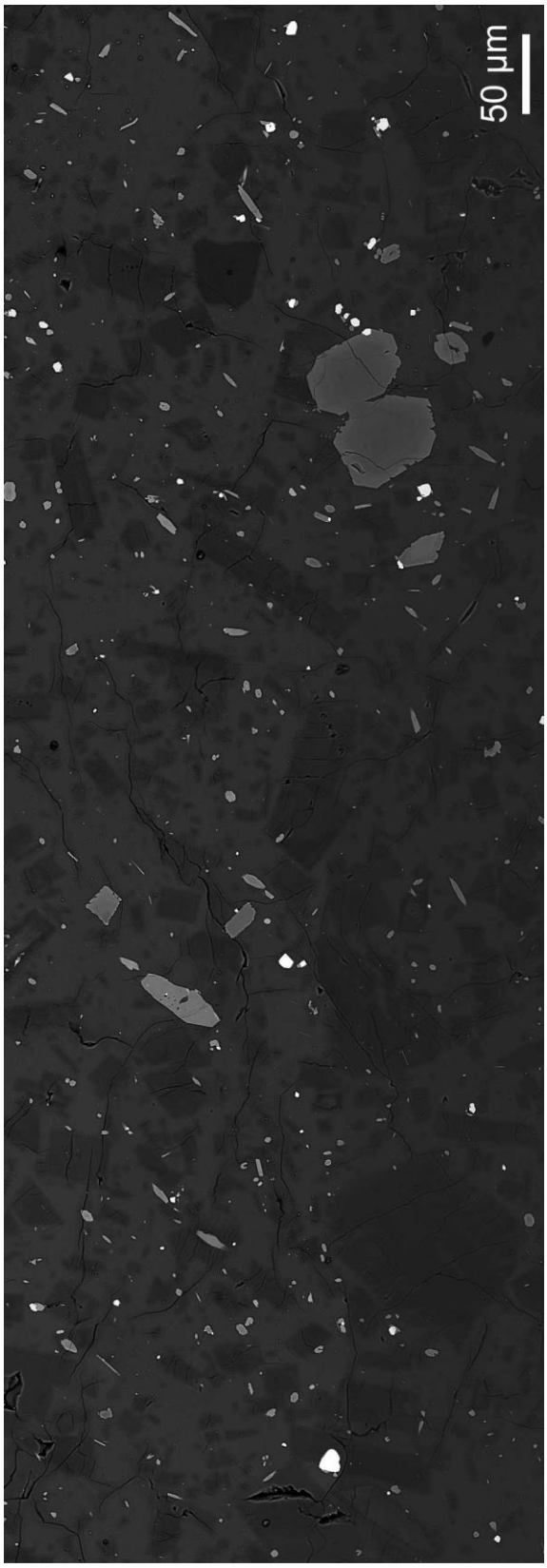

Total Area	0.344	
Pheno	0.026	
GM	0.076	
Size Inter	**Data Set**	**Corr Fact**
0.0631	18	0.03
0.0398	53	0.04
0.0251	106	0.07
0.0158	224	0.07
0.01	197	0.16
0.0063	293	0.12
0.004	78	0.67
Total	969	
Mid Inter	**ln (pop den)**	**ln (min PD)**
0.0809	9.94	9.66
0.051	11.93	11.78
0.0322	13.52	13.41
0.0203	15.19	15.12
0.0128	15.87	15.79
0.0081	17.24	17.17
0.0051	15.87	15.46
ln (max PD)	**Crystal Number**	**Vol%**
10.16	7.73E+02	10.14
12.07	3.57E+03	11.78
13.62	1.11E+04	9.158
15.26	3.70E+04	7.696
15.96	4.63E+04	2.419
17.3	1.14E+05	1.497
16.16	1.84E+04	0.06

Sample: AI-18-076

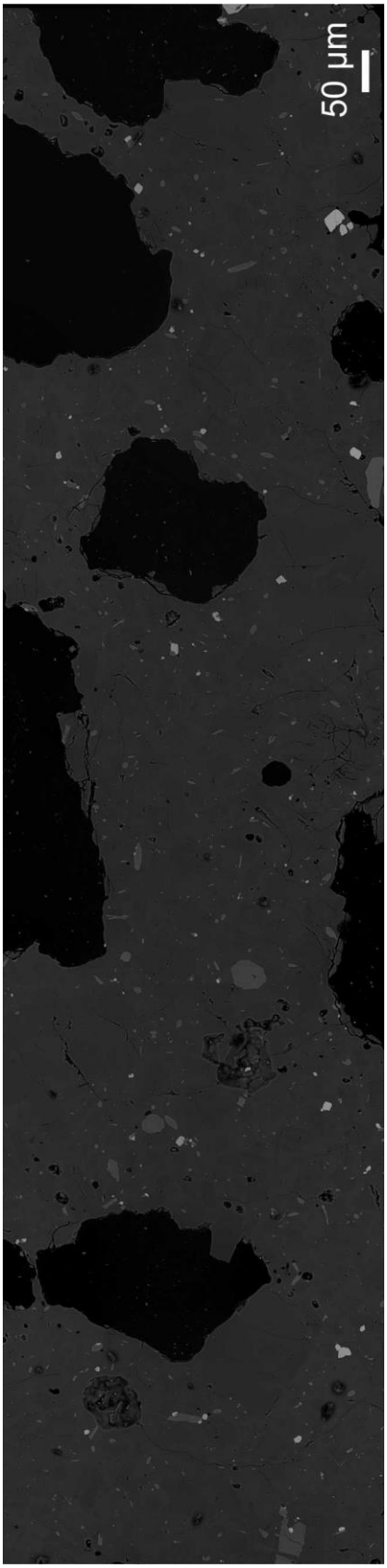

Total Area	0.787	
Pheno	0.076	
Vesicles	0.186	
GM	0.13	
Size Inter	**Data Set**	**Corr Fact**
0.0631	55	0.02
0.0398	81	0.08
0.0251	161	0.07
0.0158	213	0.1
0.01	126	0.26
0.0063	78	0.39
Total	714	
Mid Inter	**ln (pop den)**	**ln (min PD)**
0.1011	10.13	9.99
0.0638	11.38	11.25
0.0403	13	12.91
0.0254	14.16	14.08
0.016	14.37	14.24
0.0101	14.61	14.41
ln (max PD)	**Crystal Number**	**Vol%**
10.26	1.17E+03	19.25
11.49	2.57E+03	10.6
13.08	8.18E+03	8.472
14.24	1.65E+04	4.303
14.48	1.28E+04	0.836
14.78	1.04E+04	0.169

Sample: AI-18-078C

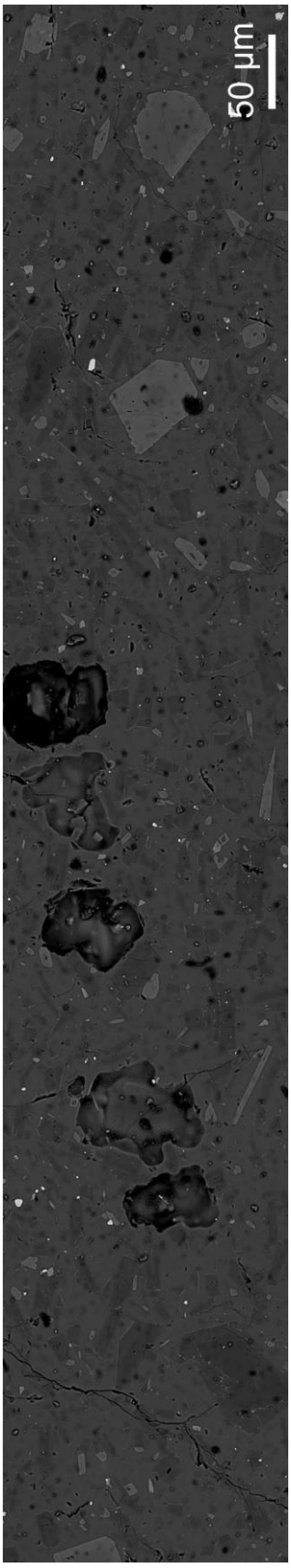

Total Area	0.198	**Pheno**	0.007	
Vesicles	0.014	**GM**	0.038	
Size Inter	**Data Set**	**Corr Fact**	**Mid Inter**	**ln (pop den)**
0.0398	54	0.01	0.1595	10.52
0.0251	130	0.02	0.1006	12.31
0.0158	148	0.05	0.0635	13.33
0.01	157	0.07	0.0401	14.29
0.0063	256	0.05	0.0253	15.72
0.004	133	0.14	0.016	15.88
0.0025	96	0.2	0.0101	16.41
0.0016	14	0.56	0.0064	14.81
Total	988			

ln (min PD)	**ln (max PD)**	**Crystal Number**	**Vol%**
10.37	10.65	2.72E+03	21.03
12.21	12.39	1.03E+04	19.93
13.24	13.41	1.80E+04	8.775
14.2	14.37	2.97E+04	3.637
15.65	15.78	7.81E+04	2.402
15.78	15.98	5.80E+04	0.448
16.28	16.53	6.22E+04	0.12
13.87	15.28	7.89E+03	0.003

Appendix C – CHAPTER 4: Central Aeolian arc

Appendix C1 Sample List

Island	Volcanic Centre		Unit	Sample		Major & Trace	Min Chem	O Isotopes	Sr Isotopes
Salina	Pollara	Punta di Perciato	pp2	SAL13/19	Lava	X	X	X	X
			pp2	SAL11-19	Lava		X		
		Lower Pollaara	pf	SAL16-2	Scoria	X	X	X	X
			pf	SAL16-5	Pumice	X	X	X	
		Upper Pollara	vp	UP	Pumice	X	X	X	
Lipari	Eruptive Epoch 8 - Southern Dome Field	Punta del Perciato	pe1	AI-17-080	Lava	X	X	X	X
			pe	AI-17-141	Pumice	X	X	X	
		Falcone	fa1	AI-17-136	Pumice		X		
			fa1	AI-17-137	Pumice		X		
			fa1	AI-17-138	Pumice	X		X	
			fa1	AI-17-138	Obsidian	X		X	
			fa1	AI-17-140	Pumice		X		
			fa2	AI-17-086	Lava	X		X	
			fa2	AI-17-088	Lava		X		
			fa3	AI-18-065	Dome	X		X	X
			fa3	AI-18-063	Enclave	X		X	
		Monte Guardia	gu	AI-17-002	Pumice		X		
			gu	AI-17-100	Pumice	X	X	X	
			gu	AI-17-102	Pumice		X		
			gu	AI-17-105	Pumice		X		
			gu	AI-17-108	Pumice		X		
			gu	AI-17-129	Pumice	X	X	X	
			gu	AI-17-131	Pumice		X		
			gi	AI-17-128	Lava		X		
			gi	AI-18-066	Lava	X		X	
	Northern Lipari	Gabellotto	vg	FBG	Pumice	X		X	
			vg	FBG-12	Obsidian	X		X	
			vg	FBG-72	Obsidian	X		X	
		Pomiciazzo	po	L10-016	Obsidian	X		X	
		Pilato	sa	Pilato	Pumice	X		X	
		Rocche Rosse	frr	RR	Obsidian	X		X	X
Vulcano	Lentia Complex	Lentia Dome	ml	V10-005	Lava	X		X	X
	La Fossa di Vulcano	Punte Nere	pn1	AI-17-041	Ash	X	X	X	
			pn2	AI-18-058	Ash	X	X	X	
			pn3	AI-17-006	Lava	X	X	X	
		Grotta dei Palizzi	gp1	AI-17-073	Ash	X	X	X	
			gp2a	AI-17-049	Pumice	X	X	X	X
			gp2b	AI-17-117	Obsidian	X	X	X	
			gp2b	AI-17-056	Enclave	X	X	X	
			gp3a	AI-18-056	Ash	X	X	X	
			gp3a	AI-18-057	Pumice	X	X	X	
			gp3b	AI-17-045	Lava	X	X	X	
		Caruggi	ca2	AI-17-034	Pumice	X	X	X	

Island	Volcanic Centre		Unit	Sample		Major & Trace	Min Chem	O Isotopes	Sr Isotopes
Vulcano	La Fossa di Vulcano	Pietre Cotte	pc1	AI-17-019	Scoria	X	X	X	
			pc1	AI-17-021	Pumice	X	X	X	
			pc1	AI-17-025	Pumice	X	X	X	
			pc2	AI-17-009	Obsidian	X	X	X	X
			pc2	AI-17-028	Enclave	X	X	X	X
		Gran Cratere	gc1	AI-17-070	Ash	X	X	X	
			gc2	AI-17-120	Bomb	X	X	X	
			gc2	AI-18-072	Bomb	X	X	X	
			gc2	AI-18-074	Bomb	X	X	X	
			gc2	AI-18-076	Bomb	X	X	X	
Crustal Xenoliths		Limestone		SAL17-3-3	Xenolith	X		X	
				SAL17-3-6	Xenolith	X		X	X
		Marble		SAL17-3-4	Xenolith	X		X	X
				Pollara026	Xenolith	X		X	
		Calc-Silicate		AI-18-051F	Xenolith	X		X	X
		Meta-sediment		SAL17-6-5	Xenolith	X		X	
				SAL17-6-6	Xenolith	X		X	X
		Quartzite		SAL17-3-7	Xenolith	X		X	
		Gneiss		SAL17-8-6	Xenolith	X		X	
				SAL17-8-7	Xenolith	X		X	X
				SA3A	Xenolith	X		X	X
		Granite		SA3C	Xenolith	X		X	X

Appendix C2 Salina and Lipari Mineral Chemical Data

Mineral chemical data for plagioclase, alkali feldspar, clinopyroxene and Fe-Ti oxides from Salina and Lipari are included in the electronic appendix C2 for this thesis.

Appendix C3 Modelling Parameters

Sr contents for the 'primary' magmas were estimated using existing literature data from De Astis *et al.* (2013), Forni *et al.* (2013) and Lucchi *et al.* (2013b) and references within. To calculate the primary magma compositions for Salina, Lipari and Vulcano, we assumed a parental SiO_2 content of 48 wt.% and MgO content of 8 wt.%.

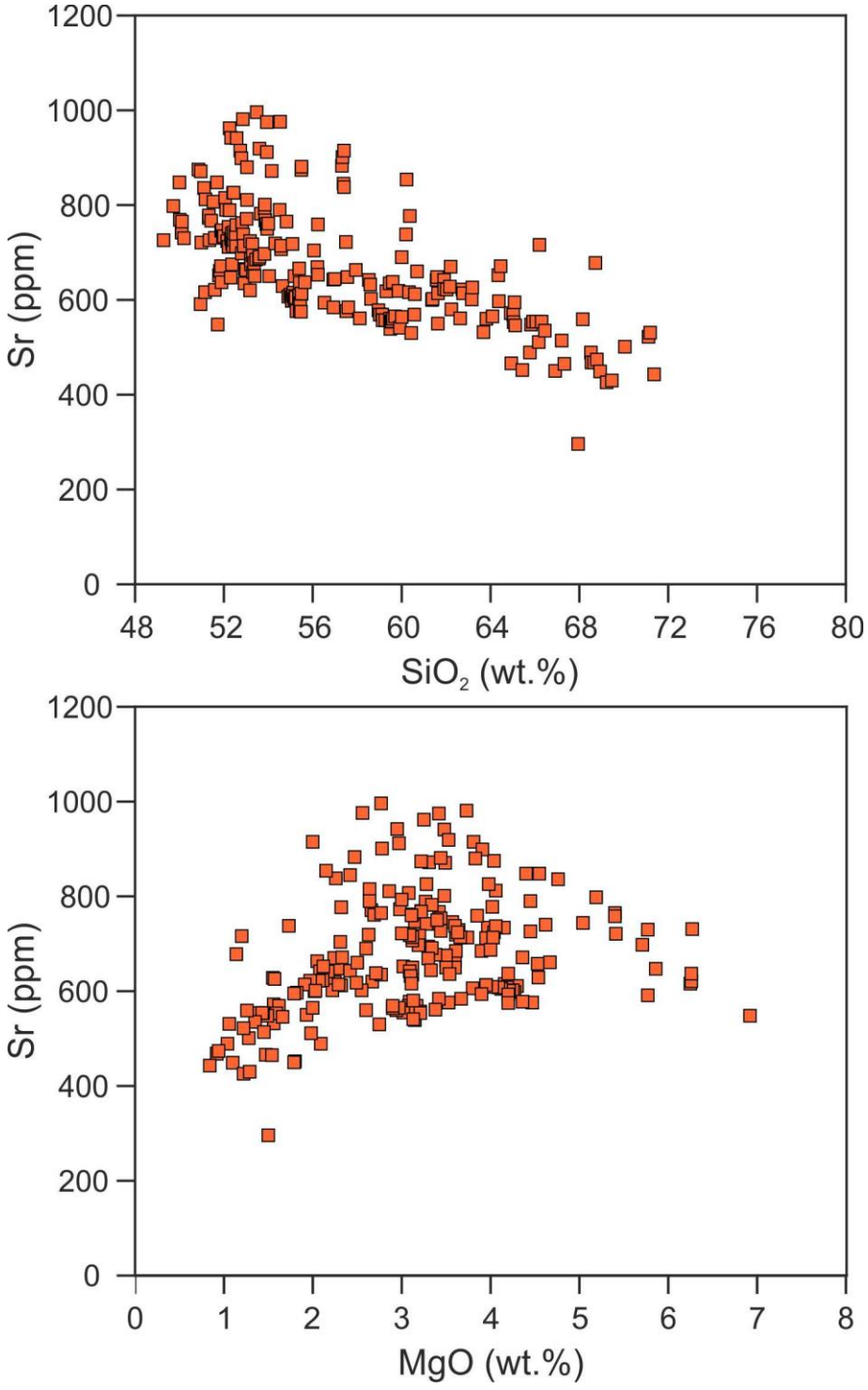

Fig. C3A: SiO_2 and MgO versus Sr for published whole-rock literature data from Salina to calculate Sr contents of primary magmas.

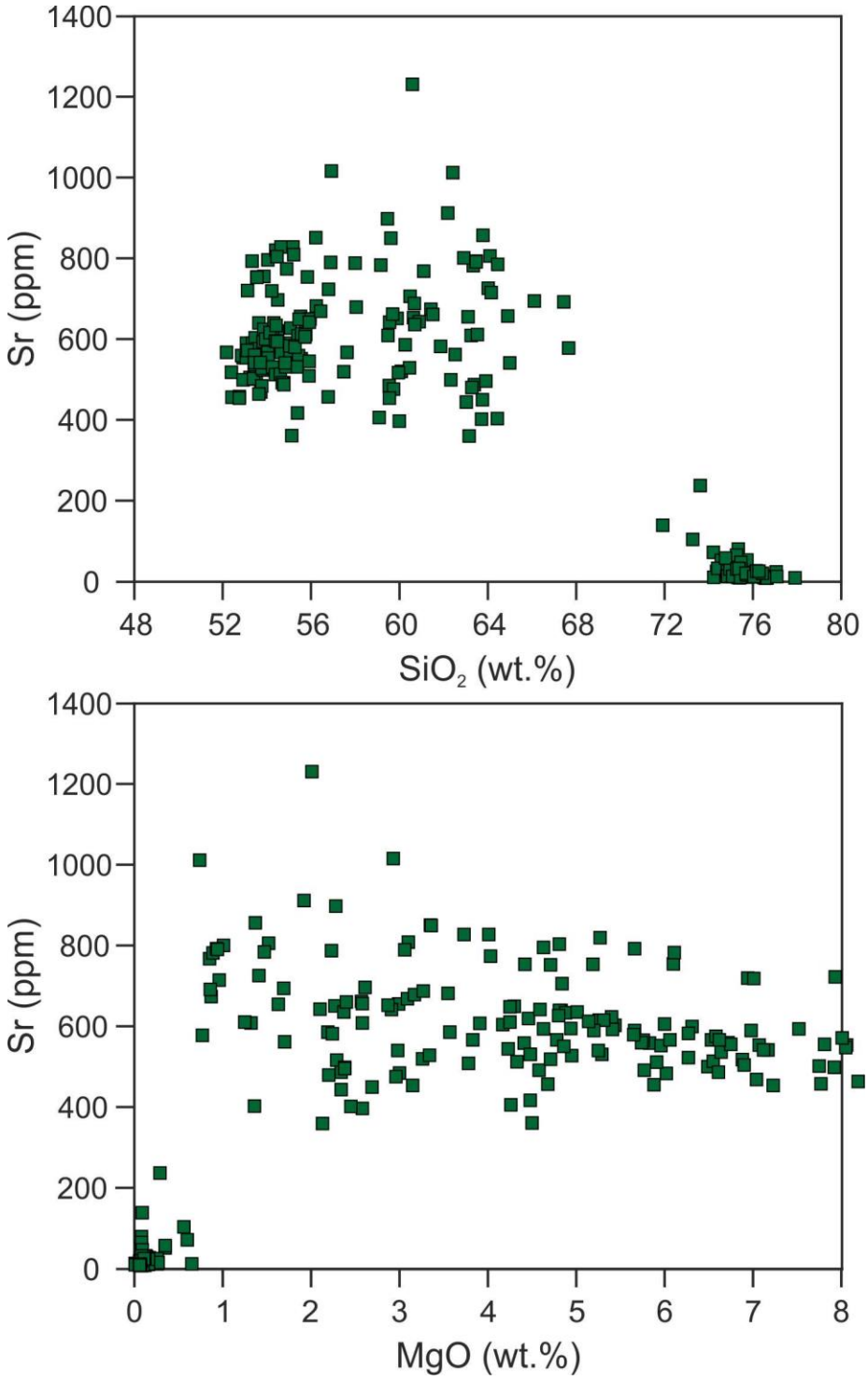

Fig. C3B: SiO_2 and MgO versus Sr for published whole-rock literature data from Lipari to calculate Sr contents of primary magmas.

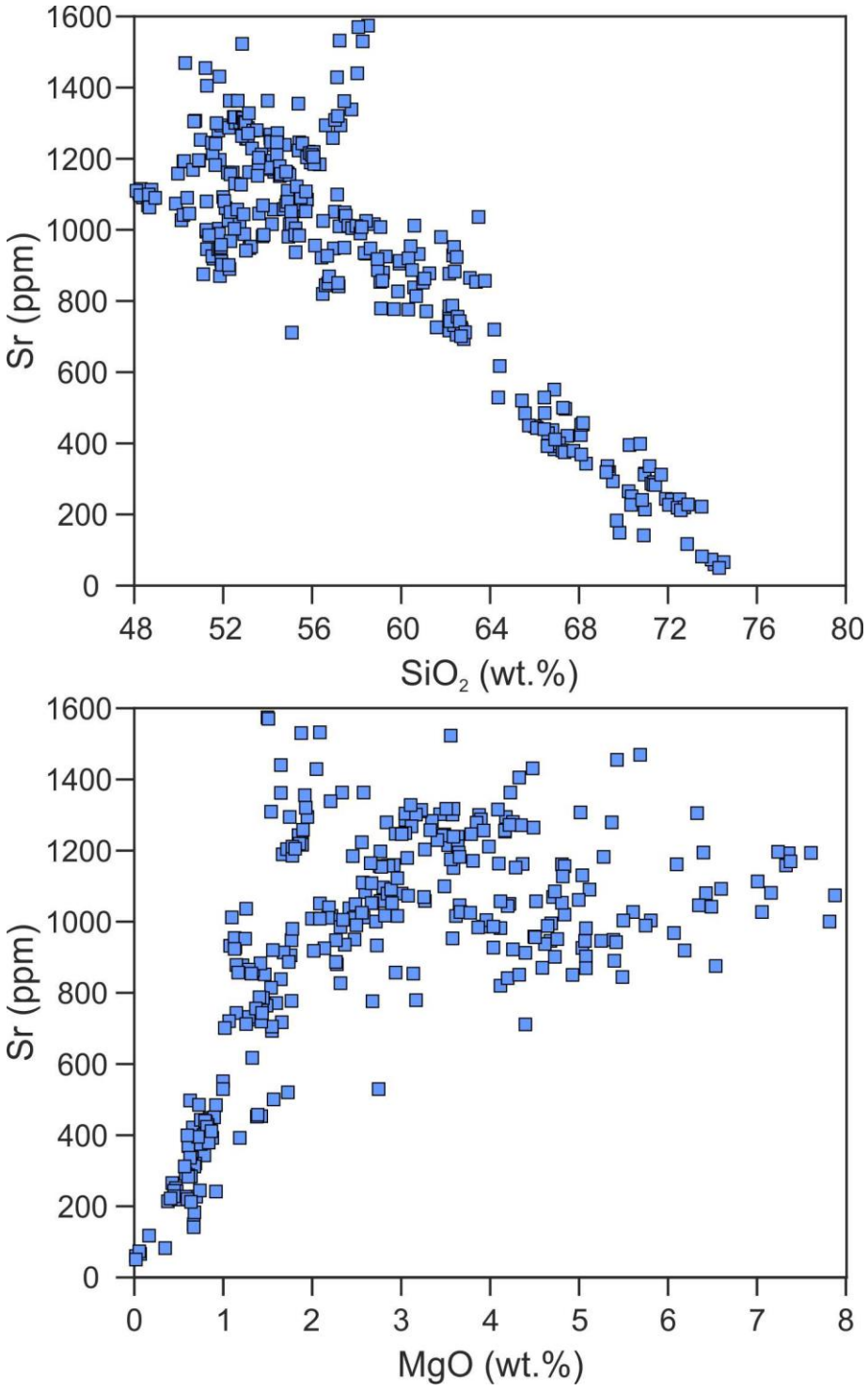

Fig. C3C: SiO_2 and MgO versus Sr for published whole-rock literature data from Vulcano to calculate Sr contents of primary magmas.

Appendix C4 Source Contamination Modelling Parameters

Bulk contamination mixing trends were modelled for the altered oceanic crust and subducted sediments. The inputs for bulk contamination and bulk contamination trends are summarised below.

		$\Delta^{18}O$	$^{87}Sr/^{86}Sr$	[Sr]	[O]
Krom *et al.* 1999	K1	20	0.71558	126.6	1
	K2	25	0.71558	126.6	1
	K3	20	0.71224	151	1
	K4	25	0.71224	151	1
	K5	20	0.71958	92.3	1
	K6	25	0.71958	92.3	1
AOC	AOC LAL	8	0.70744	130	1
	AOC LAA	8	0.70744	160	1
	AOC LAH	8	0.70744	220	1
	AOC HAL	10	0.70744	130	1
	AOC HAA	10	0.70744	160	1
	AOC HAH	10	0.70744	220	1
Mantle		5.75	0.703000	10	1

K1			K2			K3		
f(b)	$^{87}Sr/^{86}Sr_{mix}$	$\delta^{18}O_{mix}$	f(b)	$^{87}Sr/^{86}Sr_{mix}$	$\delta^{18}O_{mix}$	f(b)	$^{87}Sr/^{86}Sr_{mix}$	$\delta^{18}O_{mix}$
0.00	0.70300	5.75	0.00	0.70300	5.75	0.00	0.70300	5.75
0.05	0.70803	6.46	0.05	0.70803	6.71	0.05	0.70709	6.46
0.10	0.71035	7.18	0.10	0.71035	7.68	0.10	0.70879	7.18
0.15	0.71169	7.89	0.15	0.71169	8.64	0.15	0.70972	7.89
0.20	0.71256	8.60	0.20	0.71256	9.60	0.20	0.71030	8.60
0.25	0.71317	9.31	0.25	0.71317	10.56	0.25	0.71071	9.31
0.30	0.71362	10.03	0.30	0.71362	11.53	0.30	0.71100	10.03
0.35	0.71397	10.74	0.35	0.71397	12.49	0.35	0.71123	10.74
0.40	0.71425	11.45	0.40	0.71425	13.45	0.40	0.71141	11.45
0.45	0.71447	12.16	0.45	0.71447	14.41	0.45	0.71155	12.16
0.50	0.71466	12.88	0.50	0.71466	15.38	0.50	0.71167	12.88
0.55	0.71482	13.59	0.55	0.71482	16.34	0.55	0.71177	13.59
0.60	0.71495	14.30	0.60	0.71495	17.30	0.60	0.71185	14.30
0.65	0.71507	15.01	0.65	0.71507	18.26	0.65	0.71192	15.01
0.70	0.71517	15.73	0.70	0.71517	19.23	0.70	0.71198	15.73
0.75	0.71526	16.44	0.75	0.71526	20.19	0.75	0.71204	16.44
0.80	0.71534	17.15	0.80	0.71534	21.15	0.80	0.71209	17.15
0.85	0.71541	17.86	0.85	0.71541	22.11	0.85	0.71213	17.86
0.90	0.71547	18.58	0.90	0.71547	23.08	0.90	0.71217	18.58
0.95	0.71553	19.29	0.95	0.71553	24.04	0.95	0.71221	19.29
1.00	0.71558	20.00	1.00	0.71558	25.00	1.00	0.71224	20.00

K4			K5			K6		
f(b)	$^{87}Sr/^{86}Sr_{mix}$	$\delta^{18}O_{mix}$	f(b)	$^{87}Sr/^{86}Sr_{mix}$	$\delta^{18}O_{mix}$	f(b)	$^{87}Sr/^{86}Sr_{mix}$	$\delta^{18}O_{mix}$
0.00	0.70300	5.75	0.00	0.70300	5.75	0.00	0.70300	5.75
0.05	0.70709	6.71	0.05	0.70842	6.46	0.05	0.70842	6.71
0.10	0.70879	7.68	0.10	0.71139	7.18	0.10	0.71139	7.68
0.15	0.70972	8.64	0.15	0.71327	7.89	0.15	0.71327	8.64
0.20	0.71030	9.60	0.20	0.71457	8.60	0.20	0.71457	9.60
0.25	0.71071	10.56	0.25	0.71551	9.31	0.25	0.71551	10.56
0.30	0.71100	11.53	0.30	0.71623	10.03	0.30	0.71623	11.53
0.35	0.71123	12.49	0.35	0.71680	10.74	0.35	0.71680	12.49
0.40	0.71141	13.45	0.40	0.71726	11.45	0.40	0.71726	13.45
0.45	0.71155	14.41	0.45	0.71764	12.16	0.45	0.71764	14.41
0.50	0.71167	15.38	0.50	0.71796	12.88	0.50	0.71796	15.38
0.55	0.71177	16.34	0.55	0.71823	13.59	0.55	0.71823	16.34
0.60	0.71185	17.30	0.60	0.71846	14.30	0.60	0.71846	17.30
0.65	0.71192	18.26	0.65	0.71867	15.01	0.65	0.71867	18.26
0.70	0.71198	19.23	0.70	0.71884	15.73	0.70	0.71884	19.23
0.75	0.71204	20.19	0.75	0.71900	16.44	0.75	0.71900	20.19
0.80	0.71209	21.15	0.80	0.71914	17.15	0.80	0.71914	21.15
0.85	0.71213	22.11	0.85	0.71927	17.86	0.85	0.71927	22.11
0.90	0.71217	23.08	0.90	0.71938	18.58	0.90	0.71938	23.08
0.95	0.71221	24.04	0.95	0.71949	19.29	0.95	0.71949	24.04
1.00	0.71224	25.00	1.00	0.71958	20.00	1.00	0.71958	25.00
AOC LAL			AOC LAA			AOC LAH		
f(b)	$^{87}Sr/^{86}Sr_{mix}$	$\delta^{18}O_{mix}$	f(b)	$^{87}Sr/^{86}Sr_{mix}$	$\delta^{18}O_{mix}$	f(b)	$^{87}Sr/^{86}Sr_{mix}$	$\delta^{18}O_{mix}$
0.00	0.70300	5.75	0.00	0.70300	5.75	0.00	0.70300	5.75
0.05	0.70480	5.86	0.05	0.70503	5.86	0.05	0.70538	5.86
0.10	0.70562	5.98	0.10	0.70584	5.98	0.10	0.70615	5.98
0.15	0.70609	6.09	0.15	0.70628	6.09	0.15	0.70653	6.09
0.20	0.70640	6.20	0.20	0.70655	6.20	0.20	0.70676	6.20
0.25	0.70661	6.31	0.25	0.70674	6.31	0.25	0.70691	6.31
0.30	0.70676	6.43	0.30	0.70687	6.43	0.30	0.70701	6.43
0.35	0.70689	6.54	0.35	0.70698	6.54	0.35	0.70709	6.54
0.40	0.70698	6.65	0.40	0.70706	6.65	0.40	0.70716	6.65
0.45	0.70706	6.76	0.45	0.70712	6.76	0.45	0.70721	6.76
0.50	0.70712	6.88	0.50	0.70718	6.88	0.50	0.70725	6.88
0.55	0.70718	6.99	0.55	0.70722	6.99	0.55	0.70728	6.99
0.60	0.70722	7.10	0.60	0.70726	7.10	0.60	0.70731	7.10
0.65	0.70726	7.21	0.65	0.70730	7.21	0.65	0.70733	7.21
0.70	0.70730	7.33	0.70	0.70732	7.33	0.70	0.70736	7.33
0.75	0.70733	7.44	0.75	0.70735	7.44	0.75	0.70737	7.44
0.80	0.70736	7.55	0.80	0.70737	7.55	0.80	0.70739	7.55
0.85	0.70738	7.66	0.85	0.70739	7.66	0.85	0.70740	7.66
0.90	0.70740	7.78	0.90	0.70741	7.78	0.90	0.70742	7.78
0.95	0.70742	7.89	0.95	0.70743	7.89	0.95	0.70743	7.89
1.00	0.70744	8.00	1.00	0.70744	8.00	1.00	0.70744	8.00

The contribution from AOC fluids and subducted sediments were calculated using the range of published values. The contribution from AOC fluids was modelled using experimental studies by Kessel *et al.* (2005) for aqueous fluids at 700°C, 800°C and 900°C. Sr concentrations for the altered oceanic crust range are 130 ppm, 160 ppm and 220 ppm and $\delta^{18}O$ values of +8‰ and +10‰.

Kessel *et al.* 2005 800° Aqueous Fluid			
D	1.9	1SD	0.43
	Low	Avg	High
	L	A	H
$\delta^{18}O$	8	10	
$^{87}Sr/^{86}Sr$			0.70744
[Sr]	130	160	220
[Sr]	247	304	418

AOC		$\delta^{18}O$	$^{87}Sr/^{86}Sr$	[Sr]	[O]
	AHL	10	0.70744	247	1
	AHH	10	0.70744	418	1
	LHL	8	0.70744	247	1
	LHH	8	0.70744	418	1
Mantle		5.75	0.703000	10	1

AHL			AHH		
f(b)	$^{87}Sr/^{86}Sr_{mix}$	$\delta^{18}O_{mix}$	f(b)	$^{87}Sr/^{86}Sr_{mix}$	$\delta^{18}O_{mix}$
0.00	0.70300	5.75	0.00	0.70300	5.75
0.05	0.70551	5.96	0.05	0.70605	5.96
0.10	0.70625	6.18	0.10	0.70665	6.18
0.15	0.70661	6.39	0.15	0.70691	6.39
0.20	0.70682	6.60	0.20	0.70705	6.60
0.25	0.70696	6.81	0.25	0.70714	6.81
0.30	0.70706	7.03	0.30	0.70721	7.03
0.35	0.70713	7.24	0.35	0.70725	7.24
0.40	0.70719	7.45	0.40	0.70729	7.45
0.45	0.70723	7.66	0.45	0.70731	7.66
0.50	0.70727	7.88	0.50	0.70734	7.88
0.55	0.70730	8.09	0.55	0.70735	8.09
0.60	0.70732	8.30	0.60	0.70737	8.30
0.65	0.70735	8.51	0.65	0.70738	8.51
0.70	0.70736	8.73	0.70	0.70739	8.73
0.75	0.70738	8.94	0.75	0.70740	8.94
0.80	0.70740	9.15	0.80	0.70741	9.15
0.85	0.70741	9.36	0.85	0.70742	9.36
0.90	0.70742	9.58	0.90	0.70743	9.58
0.95	0.70743	9.79	0.95	0.70743	9.79
1.00	0.70744	10.00	1.00	0.70744	10.00
LHL			LHH		
f(b)	$^{87}Sr/^{86}Sr_{mix}$	$\delta^{18}O_{mix}$	f(b)	$^{87}Sr/^{86}Sr_{mix}$	$\delta^{18}O_{mix}$
0.00	0.70300	5.75	0.00	0.70300	5.75
0.05	0.70551	5.86	0.05	0.70605	5.86
0.10	0.70625	5.98	0.10	0.70665	5.98
0.15	0.70661	6.09	0.15	0.70691	6.09
0.20	0.70682	6.20	0.20	0.70705	6.20
0.25	0.70696	6.31	0.25	0.70714	6.31
0.30	0.70706	6.43	0.30	0.70721	6.43
0.35	0.70713	6.54	0.35	0.70725	6.54
0.40	0.70719	6.65	0.40	0.70729	6.65
0.45	0.70723	6.76	0.45	0.70731	6.76
0.50	0.70727	6.88	0.50	0.70734	6.88
0.55	0.70730	6.99	0.55	0.70735	6.99
0.60	0.70732	7.10	0.60	0.70737	7.10
0.65	0.70735	7.21	0.65	0.70738	7.21
0.70	0.70736	7.33	0.70	0.70739	7.33
0.75	0.70738	7.44	0.75	0.70740	7.44
0.80	0.70740	7.55	0.80	0.70741	7.55
0.85	0.70741	7.66	0.85	0.70742	7.66
0.90	0.70742	7.78	0.90	0.70743	7.78
0.95	0.70743	7.89	0.95	0.70743	7.89
1.00	0.70744	8.00	1.00	0.70744	8.00

Kessel et al 2005 700° Aqueous Fluid			
D	0.34	1SD	0.17
	Low	Avg	High
	L	A	H
$\delta^{18}O$	7.7	9.96	19.2
$^{87}Sr/^{86}Sr$	0.70364	0.70475	0.70744
[Sr]	130	160	220
[Sr]	44.2	54.4	74.8

AOC		$\delta^{18}O$	$^{87}Sr/^{86}Sr$	[Sr]	[O]
	HLL	19.2	0.70364	44.2	1
	ALL	9.96	0.70364	44.2	1
	HAL	19.2	0.70475	44.2	1
	HAH	19.2	0.70475	74.8	1
	AAL	9.96	0.70475	44.2	1
	AAH	9.96	0.70475	74.8	1
	HHL	19.2	0.70744	44.2	1
	AHL	9.96	0.70744	44.2	1
Mantle		5.75	0.703000	10	1

HLL			ALL		
f(b)	$^{87}Sr/^{86}Sr_{mix}$	$\delta^{18}O_{mix}$	f(b)	$^{87}Sr/^{86}Sr_{mix}$	$\delta^{18}O_{mix}$
0.00	0.70300	5.75	0.00	0.70300	5.75
0.05	0.70312	6.42	0.05	0.70312	5.96
0.10	0.70321	7.10	0.10	0.70321	6.17
0.15	0.70328	7.77	0.15	0.70328	6.38
0.20	0.70334	8.44	0.20	0.70334	6.59
0.25	0.70338	9.11	0.25	0.70338	6.80
0.30	0.70342	9.79	0.30	0.70342	7.01
0.35	0.70345	10.46	0.35	0.70345	7.22
0.40	0.70348	11.13	0.40	0.70348	7.43
0.45	0.70350	11.80	0.45	0.70350	7.64
0.50	0.70352	12.48	0.50	0.70352	7.86
0.55	0.70354	13.15	0.55	0.70354	8.07
0.60	0.70356	13.82	0.60	0.70356	8.28
0.65	0.70357	14.49	0.65	0.70357	8.49
0.70	0.70358	15.17	0.70	0.70358	8.70
0.75	0.70360	15.84	0.75	0.70360	8.91
0.80	0.70361	16.51	0.80	0.70361	9.12
0.85	0.70362	17.18	0.85	0.70362	9.33
0.90	0.70362	17.86	0.90	0.70362	9.54
0.95	0.70363	18.53	0.95	0.70363	9.75
1.00	0.70364	19.20	1.00	0.70364	9.96

HAL			HAH			AAL		
f(b)	$^{87}Sr/^{86}Sr_{mix}$	$\delta^{18}O_{mix}$	f(b)	$^{87}Sr/^{86}Sr_{mix}$	$\delta^{18}O_{mix}$	f(b)	$^{87}Sr/^{86}Sr_{mix}$	$\delta^{18}O_{mix}$
0.00	0.70300	5.75	0.00	0.70300	5.75	0.00	0.70300	5.75
0.05	0.70333	6.42	0.05	0.70349	6.42	0.05	0.70333	5.96
0.10	0.70358	7.10	0.10	0.70379	7.10	0.10	0.70358	6.17
0.15	0.70377	7.77	0.15	0.70400	7.77	0.15	0.70377	6.38
0.20	0.70392	8.44	0.20	0.70414	8.44	0.20	0.70392	6.59
0.25	0.70404	9.11	0.25	0.70425	9.11	0.25	0.70404	6.80
0.30	0.70415	9.79	0.30	0.70433	9.79	0.30	0.70415	7.01
0.35	0.70423	10.46	0.35	0.70440	10.46	0.35	0.70423	7.22
0.40	0.70431	11.13	0.40	0.70446	11.13	0.40	0.70431	7.43
0.45	0.70437	11.80	0.45	0.70450	11.80	0.45	0.70437	7.64
0.50	0.70443	12.48	0.50	0.70454	12.48	0.50	0.70443	7.86
0.55	0.70448	13.15	0.55	0.70458	13.15	0.55	0.70448	8.07
0.60	0.70452	13.82	0.60	0.70461	13.82	0.60	0.70452	8.28
0.65	0.70456	14.49	0.65	0.70463	14.49	0.65	0.70456	8.49
0.70	0.70460	15.17	0.70	0.70466	15.17	0.70	0.70460	8.70
0.75	0.70463	15.84	0.75	0.70468	15.84	0.75	0.70463	8.91
0.80	0.70466	16.51	0.80	0.70469	16.51	0.80	0.70466	9.12
0.85	0.70468	17.18	0.85	0.70471	17.18	0.85	0.70468	9.33
0.90	0.70471	17.86	0.90	0.70472	17.86	0.90	0.70471	9.54
0.95	0.70473	18.53	0.95	0.70474	18.53	0.95	0.70473	9.75
1.00	0.70475	19.20	1.00	0.70475	19.20	1.00	0.70475	9.96
AAH			HHL			AHL		
f(b)	$^{87}Sr/^{86}Sr_{mix}$	$\delta^{18}O_{mix}$	f(b)	$^{87}Sr/^{86}Sr_{mix}$	$\delta^{18}O_{mix}$	f(b)	$^{87}Sr/^{86}Sr_{mix}$	$\delta^{18}O_{mix}$
0.00	0.70300	5.75	0.00	0.70300	5.75	0.00	0.70300	5.75
0.05	0.70349	5.96	0.05	0.70384	6.42	0.05	0.70384	5.96
0.10	0.70379	6.17	0.10	0.70446	7.10	0.10	0.70446	6.17
0.15	0.70400	6.38	0.15	0.70495	7.77	0.15	0.70495	6.38
0.20	0.70414	6.59	0.20	0.70533	8.44	0.20	0.70533	6.59
0.25	0.70425	6.80	0.25	0.70564	9.11	0.25	0.70564	6.80
0.30	0.70433	7.01	0.30	0.70591	9.79	0.30	0.70591	7.01
0.35	0.70440	7.22	0.35	0.70613	10.46	0.35	0.70613	7.22
0.40	0.70446	7.43	0.40	0.70632	11.13	0.40	0.70632	7.43
0.45	0.70450	7.64	0.45	0.70648	11.80	0.45	0.70648	7.64
0.50	0.70454	7.86	0.50	0.70662	12.48	0.50	0.70662	7.86
0.55	0.70458	8.07	0.55	0.70675	13.15	0.55	0.70675	8.07
0.60	0.70461	8.28	0.60	0.70686	13.82	0.60	0.70686	8.28
0.65	0.70463	8.49	0.65	0.70696	14.49	0.65	0.70696	8.49
0.70	0.70466	8.70	0.70	0.70705	15.17	0.70	0.70705	8.70
0.75	0.70468	8.91	0.75	0.70713	15.84	0.75	0.70713	8.91
0.80	0.70469	9.12	0.80	0.70720	16.51	0.80	0.70720	9.12
0.85	0.70471	9.33	0.85	0.70727	17.18	0.85	0.70727	9.33
0.90	0.70472	9.54	0.90	0.70733	17.86	0.90	0.70733	9.54
0.95	0.70474	9.75	0.95	0.70739	18.53	0.95	0.70739	9.75
1.00	0.70475	9.96	1.00	0.70744	19.20	1.00	0.70744	9.96

Kessel et al 2005 900° Aqueous Fluid			
D	21.1	1SD	3
	Low	Avg	High
	L	A	H
$\delta^{18}O$	7.7	9.96	19.2
$^{87}Sr/^{86}Sr$	0.70364	0.70475	0.70744
[Sr]	130	160	220
[Sr]	2743	3376	4642

AOC		$\delta^{18}O$	$^{87}Sr/^{86}Sr$	[Sr]	[O]
	HLL	19.2	0.70364	2743	1
	ALL	9.96	0.70364	2743	1
	HAL	19.2	0.70475	2743	1
	HAH	19.2	0.70475	4642	1
	AAL	9.96	0.70475	2743	1
	AAH	9.96	0.70475	4642	1
	HHL	19.2	0.70744	2743	1
	AHL	9.96	0.70744	2743	1
Mantle		5.75	0.703000	10	1

HLL			ALL		
f(b)	$^{87}Sr/^{86}Sr_{mix}$	$\delta^{18}O_{mix}$	f(b)	$^{87}Sr/^{86}Sr_{mix}$	$\delta^{18}O_{mix}$
0	0.703	5.75	0.00	0.70300	5.75
0.05	0.703599	6.42	0.05	0.70360	5.96
0.1	0.70362	7.10	0.10	0.70362	6.17
0.15	0.703627	7.77	0.15	0.70363	6.38
0.2	0.703631	8.44	0.20	0.70363	6.59
0.25	0.703633	9.11	0.25	0.70363	6.80
0.3	0.703635	9.79	0.30	0.70363	7.01
0.35	0.703636	10.46	0.35	0.70364	7.22
0.4	0.703637	11.13	0.40	0.70364	7.43
0.45	0.703637	11.80	0.45	0.70364	7.64
0.5	0.703638	12.48	0.50	0.70364	7.86
0.55	0.703638	13.15	0.55	0.70364	8.07
0.6	0.703638	13.82	0.60	0.70364	8.28
0.65	0.703639	14.49	0.65	0.70364	8.49
0.7	0.703639	15.17	0.70	0.70364	8.70
0.75	0.703639	15.84	0.75	0.70364	8.91
0.8	0.703639	16.51	0.80	0.70364	9.12
0.85	0.70364	17.18	0.85	0.70364	9.33
0.9	0.70364	17.86	0.90	0.70364	9.54
0.95	0.70364	18.53	0.95	0.70364	9.75
1	0.70364	19.20	1.00	0.70364	9.96

HAL			HAH			AAL		
f(b)	$^{87}Sr/^{86}Sr_{mix}$	$\delta^{18}O_{mix}$	f(b)	$^{87}Sr/^{86}Sr_{mix}$	$\delta^{18}O_{mix}$	f(b)	$^{87}Sr/^{86}Sr_{mix}$	$\delta^{18}O_{mix}$
0.00	0.70300	5.75	0.00	0.70300	5.75	0.00	0.70300	5.75
0.05	0.70464	6.42	0.05	0.70468	6.42	0.05	0.70464	5.96
0.10	0.70469	7.10	0.10	0.70472	7.10	0.10	0.70469	6.17
0.15	0.70471	7.77	0.15	0.70473	7.77	0.15	0.70471	6.38
0.20	0.70472	8.44	0.20	0.70474	8.44	0.20	0.70472	6.59
0.25	0.70473	9.11	0.25	0.70474	9.11	0.25	0.70473	6.80
0.30	0.70474	9.79	0.30	0.70474	9.79	0.30	0.70474	7.01
0.35	0.70474	10.46	0.35	0.70474	10.46	0.35	0.70474	7.22
0.40	0.70474	11.13	0.40	0.70474	11.13	0.40	0.70474	7.43
0.45	0.70474	11.80	0.45	0.70475	11.80	0.45	0.70474	7.64
0.50	0.70474	12.48	0.50	0.70475	12.48	0.50	0.70474	7.86
0.55	0.70474	13.15	0.55	0.70475	13.15	0.55	0.70474	8.07
0.60	0.70475	13.82	0.60	0.70475	13.82	0.60	0.70475	8.28
0.65	0.70475	14.49	0.65	0.70475	14.49	0.65	0.70475	8.49
0.70	0.70475	15.17	0.70	0.70475	15.17	0.70	0.70475	8.70
0.75	0.70475	15.84	0.75	0.70475	15.84	0.75	0.70475	8.91
0.80	0.70475	16.51	0.80	0.70475	16.51	0.80	0.70475	9.12
0.85	0.70475	17.18	0.85	0.70475	17.18	0.85	0.70475	9.33
0.90	0.70475	17.86	0.90	0.70475	17.86	0.90	0.70475	9.54
0.95	0.70475	18.53	0.95	0.70475	18.53	0.95	0.70475	9.75
1.00	0.70475	19.20	1.00	0.70475	19.20	1.00	0.70475	9.96
AAH			HHL			AHL		
f(b)	$^{87}Sr/^{86}Sr_{mix}$	$\delta^{18}O_{mix}$	f(b)	$^{87}Sr/^{86}Sr_{mix}$	$\delta^{18}O_{mix}$	f(b)	$^{87}Sr/^{86}Sr_{mix}$	$\delta^{18}O_{mix}$
0.00	0.70300	5.75	0.00	0.70300	5.75	0.00	0.70300	5.75
0.05	0.70468	5.96	0.05	0.70715	6.42	0.05	0.70715	5.96
0.10	0.70472	6.17	0.10	0.70730	7.10	0.10	0.70730	6.17
0.15	0.70473	6.38	0.15	0.70735	7.77	0.15	0.70735	6.38
0.20	0.70474	6.59	0.20	0.70738	8.44	0.20	0.70738	6.59
0.25	0.70474	6.80	0.25	0.70739	9.11	0.25	0.70739	6.80
0.30	0.70474	7.01	0.30	0.70740	9.79	0.30	0.70740	7.01
0.35	0.70474	7.22	0.35	0.70741	10.46	0.35	0.70741	7.22
0.40	0.70474	7.43	0.40	0.70742	11.13	0.40	0.70742	7.43
0.45	0.70475	7.64	0.45	0.70742	11.80	0.45	0.70742	7.64
0.50	0.70475	7.86	0.50	0.70742	12.48	0.50	0.70742	7.86
0.55	0.70475	8.07	0.55	0.70743	13.15	0.55	0.70743	8.07
0.60	0.70475	8.28	0.60	0.70743	13.82	0.60	0.70743	8.28
0.65	0.70475	8.49	0.65	0.70743	14.49	0.65	0.70743	8.49
0.70	0.70475	8.70	0.70	0.70743	15.17	0.70	0.70743	8.70
0.75	0.70475	8.91	0.75	0.70743	15.84	0.75	0.70743	8.91
0.80	0.70475	9.12	0.80	0.70744	16.51	0.80	0.70744	9.12
0.85	0.70475	9.33	0.85	0.70744	17.18	0.85	0.70744	9.33
0.90	0.70475	9.54	0.90	0.70744	17.86	0.90	0.70744	9.54
0.95	0.70475	9.75	0.95	0.70744	18.53	0.95	0.70744	9.75
1.00	0.70475	9.96	1.00	0.70744	19.20	1.00	0.70744	9.96

The composition of the subducting Ionian sediments using Ionian sediment core data for boreholes KC01, UM35 and KC01 and UM35 combined from Krom *et al.* (1999). For the models, $\delta^{18}O$ values used are +20‰ and +25‰ (Land & Lynch 1996). The partition coefficient for Sr used is 2.78 ± 0.08 using experimental studies on clays, with a melt fraction of 29.5% at 800°C (Skora & Blundy 2010). The degree of melting is 20% to 30% for sediments (Hermann & Rubatto 2009).

Borehole: KC01 (Krom *et al.* 1999)

	$\delta^{18}O$	$^{87}Sr/^{86}Sr$	[Sr]	[O]
HLL	25	0.71224	38	1
AAL	20	0.71558	38	1
HAL	25	0.71558	38	1
HAH	25	0.71558	67	1
AAL	20	0.71558	38	1
AAH	20	0.71558	67	1
HHL	25	0.71958	38	1
AHL	20	0.71958	38	1

HLL			AAL			HAL		
f(b)	$^{87}Sr/^{86}Sr_{mix}$	$\delta^{18}O_{mix}$	f(b)	$^{87}Sr/^{86}Sr_{mix}$	$\delta^{18}O_{mix}$	f(b)	$^{87}Sr/^{86}Sr_{mix}$	$\delta^{18}O_{mix}$
0	0.70300	5.75	0	0.70300	5.75	0	0.70300	5.75
0.05	0.70454	6.71	0.05	0.70510	6.46	0.05	0.70510	6.71
0.1	0.70575	7.68	0.1	0.70674	7.18	0.1	0.70674	7.68
0.15	0.70671	8.64	0.15	0.70806	7.89	0.15	0.70806	8.64
0.2	0.70751	9.60	0.2	0.70914	8.60	0.2	0.70914	9.60
0.25	0.70817	10.56	0.25	0.71004	9.31	0.25	0.71004	10.56
0.3	0.70873	11.53	0.3	0.71080	10.03	0.3	0.71080	11.53
0.35	0.70921	12.49	0.35	0.71146	10.74	0.35	0.71146	12.49
0.4	0.70963	13.45	0.4	0.71202	11.45	0.4	0.71202	13.45
0.45	0.70999	14.41	0.45	0.71252	12.16	0.45	0.71252	14.41
0.5	0.71032	15.38	0.5	0.71296	12.88	0.5	0.71296	15.38
0.55	0.71061	16.34	0.55	0.71335	13.59	0.55	0.71335	16.34
0.6	0.71086	17.30	0.6	0.71371	14.30	0.6	0.71371	17.30
0.65	0.71110	18.26	0.65	0.71402	15.01	0.65	0.71402	18.26
0.7	0.71131	19.23	0.7	0.71431	15.73	0.7	0.71431	19.23
0.75	0.71150	20.19	0.75	0.71457	16.44	0.75	0.71457	20.19
0.8	0.71167	21.15	0.8	0.71480	17.15	0.8	0.71480	21.15
0.85	0.71183	22.11	0.85	0.71502	17.86	0.85	0.71502	22.11
0.9	0.71198	23.08	0.9	0.71522	18.58	0.9	0.71522	23.08
0.95	0.71211	24.04	0.95	0.71541	19.29	0.95	0.71541	24.04
1	0.71224	25.00	1	0.71558	20.00	1	0.71558	25.00
HAH			AAL			AAH		
f(b)	$^{87}Sr/^{86}Sr_{mix}$	$\delta^{18}O_{mix}$	f(b)	$^{87}Sr/^{86}Sr_{mix}$	$\delta^{18}O_{mix}$	f(b)	$^{87}Sr/^{86}Sr_{mix}$	$\delta^{18}O_{mix}$
0	0.70300	5.75	0	0.70300	5.75	0	0.70300	5.75
0.05	0.70629	6.71	0.05	0.70510	6.46	0.05	0.70629	6.46
0.1	0.70838	7.68	0.1	0.70674	7.18	0.1	0.70838	7.18
0.15	0.70983	8.64	0.15	0.70806	7.89	0.15	0.70983	7.89
0.2	0.71089	9.60	0.2	0.70914	8.60	0.2	0.71089	8.60
0.25	0.71170	10.56	0.25	0.71004	9.31	0.25	0.71170	9.31
0.3	0.71234	11.53	0.3	0.71080	10.03	0.3	0.71234	10.03
0.35	0.71286	12.49	0.35	0.71146	10.74	0.35	0.71286	10.74
0.4	0.71329	13.45	0.4	0.71202	11.45	0.4	0.71329	11.45
0.45	0.71364	14.41	0.45	0.71252	12.16	0.45	0.71364	12.16
0.5	0.71395	15.38	0.5	0.71296	12.88	0.5	0.71395	12.88
0.55	0.71422	16.34	0.55	0.71335	13.59	0.55	0.71422	13.59
0.6	0.71445	17.30	0.6	0.71371	14.30	0.6	0.71445	14.30
0.65	0.71465	18.26	0.65	0.71402	15.01	0.65	0.71465	15.01
0.7	0.71483	19.23	0.7	0.71431	15.73	0.7	0.71483	15.73
0.75	0.71499	20.19	0.75	0.71457	16.44	0.75	0.71499	16.44
0.8	0.71513	21.15	0.8	0.71480	17.15	0.8	0.71513	17.15
0.85	0.71526	22.11	0.85	0.71502	17.86	0.85	0.71526	17.86
0.9	0.71538	23.08	0.9	0.71522	18.58	0.9	0.71538	18.58
0.95	0.71548	24.04	0.95	0.71541	19.29	0.95	0.71548	19.29
1	0.71558	25.00	1	0.71558	20.00	1	0.71558	20.00

HHL			AHL		
f(b)	$^{87}Sr/^{86}Sr_{mix}$	$\delta^{18}O_{mix}$	f(b)	$^{87}Sr/^{86}Sr_{mix}$	$\delta^{18}O_{mix}$
0	0.70300	5.75	0	0.70300	5.75
0.05	0.70577	6.71	0.05	0.70577	6.46
0.1	0.70793	7.68	0.1	0.70793	7.18
0.15	0.70966	8.64	0.15	0.70966	7.89
0.2	0.71109	9.60	0.2	0.71109	8.60
0.25	0.71227	10.56	0.25	0.71227	9.31
0.3	0.71328	11.53	0.3	0.71328	10.03
0.35	0.71414	12.49	0.35	0.71414	10.74
0.4	0.71489	13.45	0.4	0.71489	11.45
0.45	0.71555	14.41	0.45	0.71555	12.16
0.5	0.71613	15.38	0.5	0.71613	12.88
0.55	0.71665	16.34	0.55	0.71665	13.59
0.6	0.71711	17.30	0.6	0.71711	14.30
0.65	0.71753	18.26	0.65	0.71753	15.01
0.7	0.71790	19.23	0.7	0.71790	15.73
0.75	0.71825	20.19	0.75	0.71825	16.44
0.8	0.71856	21.15	0.8	0.71856	17.15
0.85	0.71885	22.11	0.85	0.71885	17.86
0.9	0.71911	23.08	0.9	0.71911	18.58
0.95	0.71935	24.04	0.95	0.71935	19.29
1	0.71958	25.00	1	0.71958	20.00

Borehole: UM35 (Krom *et al.* 1999)

	$\delta^{18}O$	$^{87}Sr/^{86}Sr$	[Sr]	[O]
HLL	25	0.71355	35	1
ALL	20	0.71355	35	1
HAL	25	0.718595	35	1
HAH	25	0.718595	87	1
AAL	20	0.718595	35	1
AAH	20	0.718595	87	1
HHL	25	0.72348	35	1
AHL	20	0.72348	35	1

HLL			ALL			HAL		
f(b)	$^{87}Sr/^{86}Sr_{mix}$	$\delta^{18}O_{mix}$	f(b)	$^{87}Sr/^{86}Sr_{mix}$	$\delta^{18}O_{mix}$	f(b)	$^{87}Sr/^{86}Sr_{mix}$	$\delta^{18}O_{mix}$
0	0.703	5.75	0	0.703	5.75	0	0.703	5.75
0.05	0.704629	6.7125	0.05	0.704629	6.4625	0.05	0.705408	6.7125
0.1	0.705935	7.675	0.1	0.705935	7.175	0.1	0.707339	7.675
0.15	0.707006	8.6375	0.15	0.707006	7.8875	0.15	0.708922	8.6375
0.2	0.7079	9.6	0.2	0.7079	8.6	0.2	0.710244	9.6
0.25	0.708658	10.5625	0.25	0.708658	9.3125	0.25	0.711363	10.5625
0.3	0.709308	11.525	0.3	0.709308	10.025	0.3	0.712324	11.525
0.35	0.709872	12.4875	0.35	0.709872	10.7375	0.35	0.713158	12.4875
0.4	0.710366	13.45	0.4	0.710366	11.45	0.4	0.713888	13.45
0.45	0.710802	14.4125	0.45	0.710802	12.1625	0.45	0.714532	14.4125
0.5	0.71119	15.375	0.5	0.71119	12.875	0.5	0.715106	15.375
0.55	0.711537	16.3375	0.55	0.711537	13.5875	0.55	0.715619	16.3375
0.6	0.71185	17.3	0.6	0.71185	14.3	0.6	0.716081	17.3
0.65	0.712133	18.2625	0.65	0.712133	15.0125	0.65	0.7165	18.2625
0.7	0.71239	19.225	0.7	0.71239	15.725	0.7	0.71688	19.225
0.75	0.712625	20.1875	0.75	0.712625	16.4375	0.75	0.717228	20.1875
0.8	0.712841	21.15	0.8	0.712841	17.15	0.8	0.717547	21.15
0.85	0.713039	22.1125	0.85	0.713039	17.8625	0.85	0.71784	22.1125
0.9	0.713223	23.075	0.9	0.713223	18.575	0.9	0.718111	23.075
0.95	0.713392	24.0375	0.95	0.713392	19.2875	0.95	0.718362	24.0375
1	0.71355	25	1	0.71355	20	1	0.718595	25
HAH			AAL			AAH		
f(b)	$^{87}Sr/^{86}Sr_{mix}$	$\delta^{18}O_{mix}$	f(b)	$^{87}Sr/^{86}Sr_{mix}$	$\delta^{18}O_{mix}$	f(b)	$^{87}Sr/^{86}Sr_{mix}$	$\delta^{18}O_{mix}$
0	0.703	5.75	0	0.703	5.75	0	0.703	5.75
0.05	0.707913	6.7125	0.05	0.705408	6.4625	0.05	0.707913	6.4625
0.1	0.710683	7.675	0.1	0.707339	7.175	0.1	0.710683	7.175
0.15	0.712461	8.6375	0.15	0.708922	7.8875	0.15	0.712461	7.8875
0.2	0.713699	9.6	0.2	0.710244	8.6	0.2	0.713699	8.6
0.25	0.71461	10.5625	0.25	0.711363	9.3125	0.25	0.71461	9.3125
0.3	0.715309	11.525	0.3	0.712324	10.025	0.3	0.715309	10.025
0.35	0.715862	12.4875	0.35	0.713158	10.7375	0.35	0.715862	10.7375
0.4	0.716311	13.45	0.4	0.713888	11.45	0.4	0.716311	11.45
0.45	0.716682	14.4125	0.45	0.714532	12.1625	0.45	0.716682	12.1625
0.5	0.716994	15.375	0.5	0.715106	12.875	0.5	0.716994	12.875
0.55	0.71726	16.3375	0.55	0.715619	13.5875	0.55	0.71726	13.5875
0.6	0.71749	17.3	0.6	0.716081	14.3	0.6	0.71749	14.3
0.65	0.71769	18.2625	0.65	0.7165	15.0125	0.65	0.71769	15.0125
0.7	0.717866	19.225	0.7	0.71688	15.725	0.7	0.717866	15.725
0.75	0.718022	20.1875	0.75	0.717228	16.4375	0.75	0.718022	16.4375
0.8	0.718161	21.15	0.8	0.717547	17.15	0.8	0.718161	17.15
0.85	0.718286	22.1125	0.85	0.71784	17.8625	0.85	0.718286	17.8625
0.9	0.718399	23.075	0.9	0.718111	18.575	0.9	0.718399	18.575
0.95	0.718502	24.0375	0.95	0.718362	19.2875	0.95	0.718502	19.2875
1	0.718595	25	1	0.718595	20	1	0.718595	20

HHL			AHL		
f(b)	$^{87}Sr/^{86}Sr_{mix}$	$\delta^{18}O_{mix}$	f(b)	$^{87}Sr/^{86}Sr_{mix}$	$\delta^{18}O_{mix}$
0	0.703	5.75	0	0.703	5.75
0.05	0.706162	6.7125	0.05	0.706162	6.4625
0.1	0.708698	7.675	0.1	0.708698	7.175
0.15	0.710777	8.6375	0.15	0.710777	7.8875
0.2	0.712513	9.6	0.2	0.712513	8.6
0.25	0.713983	10.5625	0.25	0.713983	9.3125
0.3	0.715245	11.525	0.3	0.715245	10.025
0.35	0.71634	12.4875	0.35	0.71634	10.7375
0.4	0.717298	13.45	0.4	0.717298	11.45
0.45	0.718145	14.4125	0.45	0.718145	12.1625
0.5	0.718898	15.375	0.5	0.718898	12.875
0.55	0.719572	16.3375	0.55	0.719572	13.5875
0.6	0.720179	17.3	0.6	0.720179	14.3
0.65	0.720729	18.2625	0.65	0.720729	15.0125
0.7	0.721228	19.225	0.7	0.721228	15.725
0.75	0.721685	20.1875	0.75	0.721685	16.4375
0.8	0.722103	21.15	0.8	0.722103	17.15
0.85	0.722489	22.1125	0.85	0.722489	17.8625
0.9	0.722844	23.075	0.9	0.722844	18.575
0.95	0.723174	24.0375	0.95	0.723174	19.2875
1	0.72348	25	1	0.72348	20

Borehole: KC01 + UM35 (Krom *et al.* 1999)

	$\delta^{18}O$	$^{87}Sr/^{86}Sr$	[Sr]	[O]
HLL	25	0.71224	35	1
AAL	20	0.717169	35	1
HAL	25	0.717169	35	1
HAH	25	0.717169	67	1
AAL	20	0.717169	35	1
AAH	20	0.717169	67	1
HHL	25	0.72348	35	1
AHL	20	0.72348	35	1

HLL			ALL			HAL		
f(b)	$^{87}Sr/^{86}Sr_{mix}$	$\delta^{18}O_{mix}$	f(b)	$^{87}Sr/^{86}Sr_{mix}$	$\delta^{18}O_{mix}$	f(b)	$^{87}Sr/^{86}Sr_{mix}$	$\delta^{18}O_{mix}$
0	0.703	5.75	0	0.703	5.75	0	0.703	5.75
0.05	0.704427	6.71	0.05	0.704427	6.46	0.05	0.705188	6.71
0.1	0.705571	7.68	0.1	0.705571	7.18	0.1	0.706942	7.68
0.15	0.706509	8.64	0.15	0.706509	7.89	0.15	0.708381	8.64
0.2	0.707292	9.60	0.2	0.707292	8.60	0.2	0.709581	9.60
0.25	0.707955	10.56	0.25	0.707955	9.31	0.25	0.710599	10.56
0.3	0.708525	11.53	0.3	0.708525	10.03	0.3	0.711472	11.53
0.35	0.709018	12.49	0.35	0.709018	10.74	0.35	0.712229	12.49
0.4	0.709451	13.45	0.4	0.709451	11.45	0.4	0.712892	13.45
0.45	0.709833	14.41	0.45	0.709833	12.16	0.45	0.713478	14.41
0.5	0.710173	15.38	0.5	0.710173	12.88	0.5	0.713999	15.38
0.55	0.710477	16.34	0.55	0.710477	13.59	0.55	0.714465	16.34
0.6	0.710751	17.30	0.6	0.710751	14.30	0.6	0.714885	17.30
0.65	0.710999	18.26	0.65	0.710999	15.01	0.65	0.715265	18.26
0.7	0.711224	19.23	0.7	0.711224	15.73	0.7	0.715611	19.23
0.75	0.71143	20.19	0.75	0.71143	16.44	0.75	0.715927	20.19
0.8	0.711619	21.15	0.8	0.711619	17.15	0.8	0.716217	21.15
0.85	0.711793	22.11	0.85	0.711793	17.86	0.85	0.716483	22.11
0.9	0.711953	23.08	0.9	0.711953	18.58	0.9	0.716729	23.08
0.95	0.712102	24.04	0.95	0.712102	19.29	0.95	0.716957	24.04
1	0.71224	25.00	1	0.71224	20.00	1	0.717169	25.00
HAH			AAL			AAH		
f(b)	$^{87}Sr/^{86}Sr_{mix}$	$\delta^{18}O_{mix}$	f(b)	$^{87}Sr/^{86}Sr_{mix}$	$\delta^{18}O_{mix}$	f(b)	$^{87}Sr/^{86}Sr_{mix}$	$\delta^{18}O_{mix}$
0	0.703	5.75	0	0.703	5.75	0	0.703	5.75
0.05	0.706703	6.71	0.05	0.705188	6.46	0.05	0.706703	6.46
0.1	0.709059	7.68	0.1	0.706942	7.18	0.1	0.709059	7.18
0.15	0.710689	8.64	0.15	0.708381	7.89	0.15	0.710689	7.89
0.2	0.711884	9.60	0.2	0.709581	8.60	0.2	0.711884	8.60
0.25	0.712797	10.56	0.25	0.710599	9.31	0.25	0.712797	9.31
0.3	0.713518	11.53	0.3	0.711472	10.03	0.3	0.713518	10.03
0.35	0.714102	12.49	0.35	0.712229	10.74	0.35	0.714102	10.74
0.4	0.714584	13.45	0.4	0.712892	11.45	0.4	0.714584	11.45
0.45	0.714989	14.41	0.45	0.713478	12.16	0.45	0.714989	12.16
0.5	0.715334	15.38	0.5	0.713999	12.88	0.5	0.715334	12.88
0.55	0.715632	16.34	0.55	0.714465	13.59	0.55	0.715632	13.59
0.6	0.715891	17.30	0.6	0.714885	14.30	0.6	0.715891	14.30
0.65	0.716118	18.26	0.65	0.715265	15.01	0.65	0.716118	15.01
0.7	0.71632	19.23	0.7	0.715611	15.73	0.7	0.71632	15.73
0.75	0.7165	20.19	0.75	0.715927	16.44	0.75	0.7165	16.44
0.8	0.716661	21.15	0.8	0.716217	17.15	0.8	0.716661	17.15
0.85	0.716807	22.11	0.85	0.716483	17.86	0.85	0.716807	17.86
0.9	0.716939	23.08	0.9	0.716729	18.58	0.9	0.716939	18.58
0.95	0.717059	24.04	0.95	0.716957	19.29	0.95	0.717059	19.29
1	0.717169	25.00	1	0.717169	20.00	1	0.717169	20.00

HHL			AHL		
f(b)	$^{87}Sr/^{86}Sr_{mix}$	$\delta^{18}O_{mix}$	f(b)	$^{87}Sr/^{86}Sr_{mix}$	$\delta^{18}O_{mix}$
0	0.703	5.75	0	0.703	5.75
0.05	0.706162	6.71	0.05	0.706162	6.46
0.1	0.708698	7.68	0.1	0.708698	7.18
0.15	0.710777	8.64	0.15	0.710777	7.89
0.2	0.712513	9.60	0.2	0.712513	8.60
0.25	0.713983	10.56	0.25	0.713983	9.31
0.3	0.715245	11.53	0.3	0.715245	10.03
0.35	0.71634	12.49	0.35	0.71634	10.74
0.4	0.717298	13.45	0.4	0.717298	11.45
0.45	0.718145	14.41	0.45	0.718145	12.16
0.5	0.718898	15.38	0.5	0.718898	12.88
0.55	0.719572	16.34	0.55	0.719572	13.59
0.6	0.720179	17.30	0.6	0.720179	14.30
0.65	0.720729	18.26	0.65	0.720729	15.01
0.7	0.721228	19.23	0.7	0.721228	15.73
0.75	0.721685	20.19	0.75	0.721685	16.44
0.8	0.722103	21.15	0.8	0.722103	17.15
0.85	0.722489	22.11	0.85	0.722489	17.86
0.9	0.722844	23.08	0.9	0.722844	18.58
0.95	0.723174	24.04	0.95	0.723174	19.29
1	0.72348	25.00	1	0.72348	20.00